



HAL
open science

Performance Analysis and PAPR Reduction Techniques for Filter-Bank based Multi-Carrier Systems with Non-Linear Power Amplifiers

Sri Satish Krishna Chaitanya Bulusu

► **To cite this version:**

Sri Satish Krishna Chaitanya Bulusu. Performance Analysis and PAPR Reduction Techniques for Filter-Bank based Multi-Carrier Systems with Non-Linear Power Amplifiers. Networking and Internet Architecture [cs.NI]. Conservatoire national des arts et metiers - CNAM, 2016. English. NNT : 2016CNAM1042 . tel-01401456

HAL Id: tel-01401456

<https://theses.hal.science/tel-01401456>

Submitted on 23 Nov 2016

HAL is a multi-disciplinary open access archive for the deposit and dissemination of scientific research documents, whether they are published or not. The documents may come from teaching and research institutions in France or abroad, or from public or private research centers.

L'archive ouverte pluridisciplinaire **HAL**, est destinée au dépôt et à la diffusion de documents scientifiques de niveau recherche, publiés ou non, émanant des établissements d'enseignement et de recherche français ou étrangers, des laboratoires publics ou privés.

École doctorale Informatique, Télécommunication et Électronique de Paris

Laboratoire LAETITIA/CEDRIC

THÈSE DE DOCTORAT

présentée par : Sri Satish Krishna Chaitanya BULUSU

soutenue le : 29 avril 2016

pour obtenir le grade de : Docteur du Conservatoire National des Arts et Métiers

Spécialité : Radiocommunications

Performance Analysis and PAPR Reduction Techniques for Filter-Bank based Multi-Carrier Systems with Non-Linear Power Amplifiers

THÈSE DIRIGÉE PAR

M. ROVIRAS Daniel
M. SHAIEK Hmaied

Professeur, CNAM, France
Maitre de conférences, CNAM, France

RAPPORTEURS

M. BAUDOUIN Geneviève
M. LOUET Yves

Professeur, ESIEE, France
Professeur, Supelec, France

EXAMINATEURS

M. HELARD Jean-François
M. MARTINOD Laurent
M. ZAYANI Rafik

Professeur, INSA Rennes, France
Ingénieur, CASSIDIAN, France
Maitre de conférences, ISI-Tunis, Tunisie

Declaration of Authorship

I, **BULUSU Sri Satish Krishna Chaitanya**, declare that this doctoral thesis titled, 'Performance Analysis and PAPR Reduction Techniques for Filter-Bank based Multi-Carrier Systems with Non-Linear Power Amplifiers' and the work presented in it are my own. I confirm that:

- This work was done wholly or mainly while in candidature for a research degree at this University.
- Where any part of this thesis has previously been submitted for a degree or any other qualification at this University or any other institution, this has been clearly stated.
- Where I have consulted the published work of others, this is always clearly attributed.
- Where I have quoted from the work of others, the source is always given. With the exception of such quotations, this thesis is entirely my own work.
- I have acknowledged all main sources of help.
- Where the thesis is based on work done by myself jointly with others, I have made clear exactly what was done by others and what I have contributed myself.

Signed:

Date: 29/04/2016

© Copyright 2016 by **Sri Satish Krishna Chaitanya BULUSU**
All rights reserved

“Āno bhadrā kṛtavo yantu viśvataḥ”

“Que de nobles pensées nous viennent de toutes les directions”

“Let noble thoughts come to us, from all directions”

- Ṛg vedam

Dedicated to my mother...

Acknowledgements

It is with great pleasure that I acknowledge several of the many people who have supported me on my journey through the Ph.D. program. They provided me with so many of the things that I needed: from some, I received technical support; from some, professional and academic advice; from some, friendship; from some, love; and from some, a combination of these things. So, I would like to express my gratitude to these people without whom this dissertation would not have been completed. To the people mentioned here, and to many others who are not, I extend my sincere, deepest, heartfelt gratitude.

This acknowledgment would be incomplete, without mentioning my most beloved supervisor, Professor Daniel ROVIRAS. Thus spake Issac newton, “*If I have seen further, it is by standing on the shoulders of giants*”. This is the quote, which flashes in my mind, when I think of my professor. He is indeed a giant; Alas! I am no Newton, but a dwarf with full of quenching thirst for knowledge. So, may be I should stick to the one said by Bernard de Chartes, “*nanos gigantum humeris insidentes*”. If I have made any scientific contribution in this dissertation, it is by his cordial support and relentless inspiration. As a matter of fact, he indeed was more like a friend, guide and philosopher than a mere supervisor. Even at times, when I posed some stupid questions, he would answer me with utmost patience and lucidity. One thing, which I have learnt from him is that imagination, organization and proper expression of ideas is vital to any research work; to make it more fruitful. Apart from his scientific outlook, to my utmost delight and surprise, he is a painter of his own sort. Whenever possible, I used to have very interesting conversations about art in general with him, which I shall cherish for many years to come. A mere thanks to him, is nothing but an escape. Perhaps, I should continue with scientific zeal and contribute more to my field.

Then, I would like to thank my co-supervisor, Assistant Professor Hmaied SHAIK, who continuously supported my work and ideas throughout my PhD studies at CNAM. Whenever I needed, Hmaied always made himself available and put a great deal of time and effort into our joint work. I am very indebted to his constructive comments and guidance in my work throughout this dissertation. His close guidance and efforts had prepared me for making this dissertation more purposeful. I am grateful to him for allowing me to work with absolute freedom, and for adroitly stepping in to advise when the need arose. I would consider myself lucky to be working along with him.

I would also like to thank my jury committee members, Professor Geneviève BAUDOIN, Professor Yves LOUET, Dr. Laurent MARTINOD, Professor Jean-François HELARD and Assistant Professor Rafik ZAYANI for serving on my committee and for helping to improve my dissertation with their thoughtful critiques.

I would like to thank my group members: Rostom ZAKARIA, Yahia MEDJAHDI, Ali

KABALAN, Juwendo DENIS, Marwa CHAMI, Hanen BOUHADDA, Rémi CHAUVAT, Salma HAMDIA, Wosen KASSA and Yannick PAUGAM, for useful technical discussions and worthy collaborations.

There are many people who have influenced and inspired me since childhood and especially, throughout my graduate studies and thesis research over the years. One among them, to whom I am ever grateful is, Mr. Bhaskar Ramamurthi, the director of IIT Madras, who gave me such a nice opportunity to work with intense theoretical learning accompanied by practical approach. His support and guidance during my years at IIT Madras remain to be some of the most cherished moments in my life.

I have no words but a humble thanks to Thales group and French ministry of external affairs for providing me with Thales-MAE scholarship in 2007, to pursue my masters at Eurécom. It opened up unvisited chests of knowledge in the field of mobile communications and increased my passion for learning. I, being a francophile, feel very proud to be associated with the French cultural, historical and linguistic legacy and its administrative process. So, had I not been a recipient of that prestigious scholarship, I would have never fulfilled my dreams about higher studies and associating with France.

I would not have been here, had it not been by the support of my family. So, last but not the least, I am thankful to my family in India, who have done such great sacrifices to keep me at this position. They showed me that I am not, and never have been, alone in my endeavors. They are the source of unending love and support. Whatever hardships they have endured, they would always keep me at bay, to make sure that I succeed. I seek humble blessings from them.

Abstract

This thesis is part of the European FP7 - ICT 318362 EMPHATIC project (Enhanced Multicarrier Techniques for Professional Ad-Hoc and Cell-Based Communications) including various European universities and two main industrial partners: THALES Communications Security and CASSIDIAN. The EMPHATIC objective is to develop, evaluate and demonstrate the capability of enhanced multi-carrier techniques to make better use of the existing radio frequency bands in providing broadband data services in coexistence with narrowband legacy services. The project addresses the Professional Mobile Radio (PMR) application. The main idea is to analyze the viability of broadband systems based on filter bank multi-carrier (FBMC) clubbed with offset quadrature amplitude modulation (OQAM) in the context of the future 5th Generation (5G) radio access technology (RAT).

Increasingly, the FBMC-OQAM systems are gaining appeal in the probe for advanced multi-carrier modulation (MCM) waveforms for future communication systems. This advanced modulation scheme offers numerous advantages such as excellent frequency localization in its power spectral density (PSD), a robustness to phase noise, frequency offsets and also to the multi-user asynchronism; making it more appealing than OFDM for PMR, cognitive radio (CR) and 5G RAT. However, like any other MCM technique, FBMC-OQAM suffers from high PAPR. When the power amplifier (PA) non-linearity, which is realistic radio-frequency impairment, is taken into account; the good frequency localization property is severely compromised, due to the spectral regrowth.

The first objective of this PhD thesis is, to predict the extent of the spectral regrowth in FBMC-OQAM systems, due to the PA non-linearity. The second objective is to probe techniques for FBMC-OQAM systems, such as PAPR reduction and PA linearization, in order to mitigate the NL effects of PA. By cumulant analysis, spectral regrowth prediction has been done for FBMC-OQAM systems. Also, some algorithms for PAPR

reduction, which are based on probabilistic approach and adding signal methods, have been proposed. The coexistence capability of the FBMC-OQAM based broadband system with the narrowband PMR systems in the presence of PA has been analyzed and it has been found that coexistence is possible, provided there is a symbiotic combination of PA Input Back-off (IBO), PAPR reduction and PA linearization. Finally, a novel PA linearization technique has been proposed for FBMC-OQAM.

Résumé

Cette thèse a été effectuée dans le cadre du projet européen FP7 - ICT 318362 EM-PHATIC (Enhanced Multicarrier Techniques for Professional Ad-Hoc and Cell-Based Communications). Plusieurs universités européennes et deux partenaires industriels: THALES Communications Security et CASSIDIAN ont participé à ce projet. L'objectif de ce projet est de développer, d'évaluer et de démontrer les apports des techniques multi-porteuses avancées, permettant une meilleure utilisation des bandes de fréquences radio existantes en fournissant des services de données à large bande, en coexistence avec les services traditionnels à bande étroite. Le projet porte sur l'application de radiocommunications mobiles professionnelles (Professional Mobile Radio : PMR). L'idée principale de ce projet est d'analyser la viabilité des systèmes à large bande utilisant des bancs de filtres (Filter Bank Multi Carrier : FBMC) conjointement avec une modulation d'amplitude en quadrature avec décalage (Offset Quadrature Amplitude Modulation : OQAM) dans le cadre de la 5ème génération (5G) des systèmes radio-mobiles.

La modulation FBMC-OQAM se positionne comme candidate potentielle pour les futurs systèmes de communication. Cette modulation avancée offre de nombreux avantages tels que l'excellente localisation fréquentielle de sa densité spectrale de puissance (DSP), une robustesse au bruit de phase, aux décalages de fréquence ainsi qu'à l'asynchronisme entre les utilisateurs. Ces atouts, la rendent plus attrayante qu'OFDM pour l'application PMR, la radio cognitive (CR) et la 5G. Cependant, comme toute autre technique de modulation muti-porteuses, FBMC-OQAM souffre d'un facteur de crête ou d'un PAPR (pour Peak to Average Power Ratio) élevé. Lorsque l'amplificateur de puissance (AP), utilisé au niveau de l'émetteur, est opéré proche de sa zone non-linéaire (NL), ce qui est le cas dans la pratique, la bonne localisation fréquentielle de la DSP du système FBMC/OQAM est sérieusement compromise, en raison des remontées spectrales.

Le premier objectif de cette thèse est de prédire l'étendue des remontées spectrales dans

les systèmes FBMC-OQAM, introduites par la non-linéarité de l'AP. Le deuxième objectif de ce travail est de proposer des techniques, pour les systèmes FBMC-OQAM, permettant la réduction du PAPR et la linéarisation de l'AP, afin d'atténuer les effets NL. L'utilisation des cumulants, a permis de prédire les remontées spectrales pour les signaux FBMC-OQAM après amplification NL. En outre, certains algorithmes de réduction du PAPR, basées sur des approches probabilistes et des techniques d'ajout de signaux, ont été proposés. La capacité de coexistence du système à large bande utilisant FBMC-OQAM avec des systèmes PMR à bande étroite en présence de PA a été analysée et il a été démontré que la coexistence est possible, à condition qu'il y ait une bonne combinaison entre le recul du signal à l'entrée de l'AP (Input Back-Off : IBO), la réduction du PAPR et la linéarisation de l'AP. Enfin, une nouvelle technique de linéarisation de l'AP a été proposée pour le système FBMC-OQAM.

Résumé des travaux de thèse

Introduction

Contexte et motivation

Les premiers systèmes de communication numériques étaient basés sur des modulations Mono-porteuse. Avec l'essor des systèmes de communication mobiles avec des canaux fortement sélectifs en fréquence, les modulations multi-porteuses (MCM) ont montré leur intérêt grâce à une égalisation fréquentielle simplifiée. Jusqu'à ce jour, la modulation OFDM (Multiplexage par division de fréquences orthogonales) est la plus répandue des schémas de MCM. Néanmoins, l'OFDM souffre de perte d'efficacité spectrale à cause du préfixe cyclique, de sensibilité aux décalages Doppler [1, 2] et d'une mauvaise localisation fréquentielle. Ces inconvénients ont ainsi motivé les chercheurs à trouver de nouvelles solutions alternatives pour la couche physique, notamment avec des MCM ayant de meilleures localisations fréquentielles que l'OFDM. Une des solutions proposées est la modulation FBMC-OQAM (Modulation multi-porteuse à base de banc de filtres avec offset QAM) Saltzberg [3] (également appelée parfois, OFDM/OQAM ou SMT) qui sera étudiée tout au long de cette thèse.

Les systèmes des technologies de l'information et de la communication (ICT) contribuent aux émissions mondiales de gaz à effet de serre qui devraient presque doubler, et atteindre environ 4% d'ici 2020. Mettre davantage l'accent sur les communications vertes est l'une des grandes priorités de l'ITU pour 2020, afin de diminuer de 30% les émissions de carbone par appareil [4]. Ainsi, la consommation énergétique est devenue un défi clé au cours des dernières années. Selon plusieurs études [4, 5], le secteur des TIC est responsable de 2% à 10% de la consommation énergétique mondiale et plusieurs projets portés, tant par des industriels que des universitaires, tentent de réduire la consommation d'énergie des appareils électroniques.

Les amplificateurs de puissance sont l'un des composants les plus coûteux et qui consomment le plus d'énergie dans les systèmes de communication. L'amplificateur de puissance (AP) représente plus de 60% de la consommation d'énergie totale d'un émetteur [6]. Il est donc important d'opter pour des techniques permettant d'augmenter le rendement énergétique et de réduire les effets non linéaires (NL) des AP. Ces techniques visent deux objectifs : la réduction du facteur de crête (PAPR) des signaux transmis et la linéarisation des AP.

Project EMPHATIC

Cette thèse s'inscrit dans le cadre du projet européen FP7 EMPHATIC (Enhanced Multicarrier Techniques for Professional Ad-Hoc and Cell-Based Communications, <http://www.ict-emphatic.eu/>). Son objectif est de démontrer l'apport des systèmes MCM FBMC-OQAM pour la PMR et tout particulièrement la coexistence avec les services existants à bande étroite avec les services large bande MCM. En effet, ces deux types de services doivent utiliser les mêmes bandes de fréquences radio existantes tout en permettant la coexistence.

Objectifs de la thèse

Dans cette thèse, l'impact des AP non-linéaires sur la performance des systèmes FBMC-OQAM sera étudié:

- Nous étudierons, en particulier, les remontées de puissance hors bande (OOB) grâce à l'utilisation des cumulants,
- Nous proposerons de nouvelles techniques de réduction du PAPR adaptées aux systèmes FBMC-OQAM et étudierons les complexités de mise en œuvre,
- Nous étudierons la coexistence d'un système large bande de type FBMC-OQAM avec des systèmes bande étroite en présence d'AP non linéaires,
- Nous proposerons enfin de nouvelles techniques de linéarisation des AP adaptées aux modulations FBMC-OQAM.

Les systèmes FBMC-OQAM et les amplificateurs de puissance

Introduction

La modulation FBMC-OQAM est perçue comme une alternative intéressante à l'OFDM, pour les systèmes radio-mobiles de 5ème génération (5G). Elle présente de nombreuses caractéristiques attrayantes telles qu'une excellente localisation fréquentielle avec une densité spectrale de puissance (DSP) avec des lobes latéraux très atténués et une robustesse améliorée pour les décalages de fréquence porteuse. Ce chapitre présente un état de l'art des différents concepts qui vont être utilisés tout au long de cette thèse.

Introduction à la modulation FBMC-OQAM

Dans un système FBMC-OQAM, nous transmettons des symboles réels toutes les demi-périodes symbole (la période symboles étant classiquement la durée d'un symbole complexe émis) [7]. Dans le mapping OQAM, un symbole complexe en entrée est mappé dans deux symboles réel et imaginaire pur qui seront transmis avec un offset de $\frac{T}{2}$ d'où l'appellation Offset QAM. Ce mapping est réalisé de façon à ce que, deux symboles sur la même porteuse soient successivement réels et imaginaires pur. De plus, les symboles adjacents entre deux sous porteuses sont aussi réels ou imaginaires pur. Ces symboles réels ou imaginaires sont mis en forme par un filtre prototype ayant une bonne localisation fréquentielle. Le filtre prototype a une réponse impulsionnelle (RI) $h(t)$ de longueur égale à KT où T est la période des symboles complexes émis. Les filtres prototypes utilisés dans cette thèse sont les filtres PHYDYAS et IOTA. Les réponses impulsionnelles et

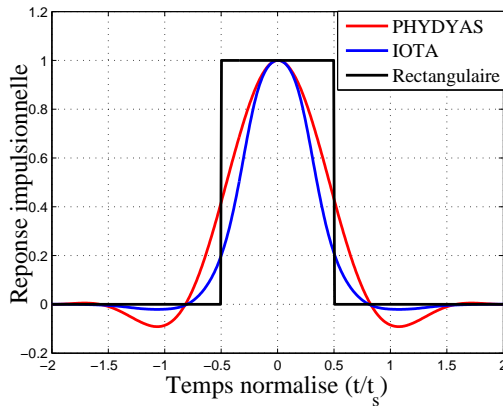


FIGURE 1: Comparaison de la réponse impulsionnelle des filtres PHYDYAS, IOTA et rectangulaire.

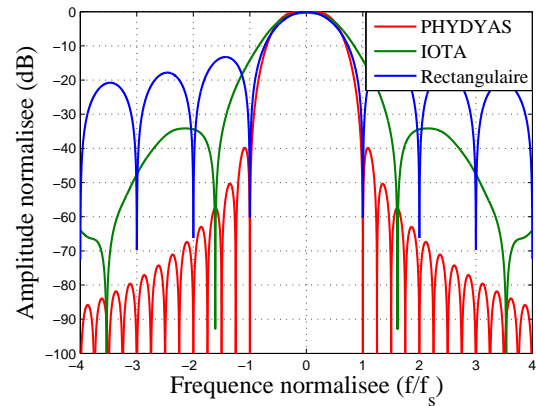


FIGURE 2: Comparaison de la DSP des filtres PHYDYAS, IOTA et rectangulaire.

DSP sont indiquées dans les Fig. 1 et Fig. 2. La durée de la réponse impulsionnelle $h(t)$ du FBMC-OQAM, cause des chevauchements des symboles successifs. Il est évident d'après la Fig. 3 que le profil de puissance moyenne du filtre FBMC-OQAM couvre plus de $4.5T$, alors que dans le cas de l'OFDM, elle s'étend sur T seulement.

Introduction aux amplificateurs de puissance non linéaire

La fonction de transfert d'un AP peut être divisée en deux zones : linéaire et non linéaire. La région NL présente une haute efficacité énergétique, mais le signal amplifié sera distordu. Afin de limiter la distorsion du signal, le AP est généralement exploité dans sa région linéaire avec une faible efficacité énergétique. Ceci est réalisé en augmentant le recul en entrée ou input back-off (IBO), qui est défini comme le rapport entre la

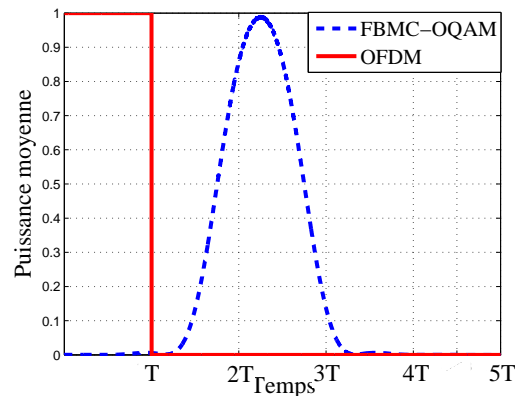


FIGURE 3: Illustration du profil de puissance moyenne de l'OFDM et des FBMC-OQAM.

puissance moyenne du signal d'entrée et la puissance de saturation.

Le signal de sortie de l'AP peut être modélisé grâce aux caractéristiques AM/AM et AM/PM de l'AP. Dans cette thèse nous nous sommes limités aux AP sans mémoire dont les modélisations sont présentées ci-après.

Modèle polynomiale

Le AP non-linéaire est modélisé comme un polynôme d'ordre impair avec coefficients complexes.

Modèle limiteur

La caractéristique AM/AM du limiteur parfait (Soft Enveloppe Limiter SEL) [8] est présentée dans la Fig. 4.

Modèle de Rapp

La caractéristique AM/AM du modèle de Rapp est présentée dans la Fig. 4, où p est le facteur d'arrondi.

Modèle de Saleh

Les caractéristiques AM/AM et AM/PM du modèle de Saleh sont illustrées dans les Fig. 5 et Fig. 6.

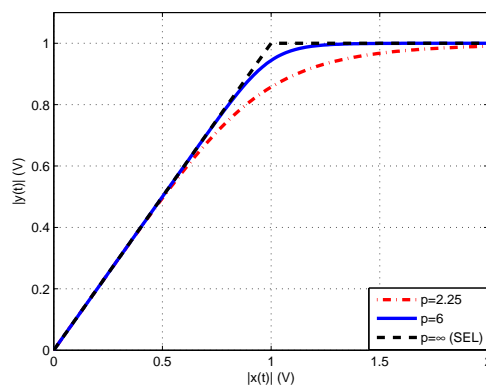


FIGURE 4: AM/AM conversion des modèles SEL et Rapp.

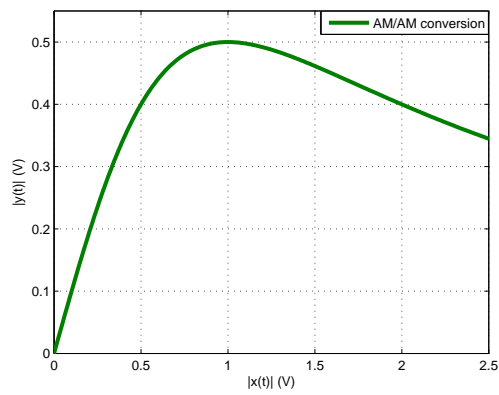


FIGURE 5: AM/AM conversion du modèle de Saleh.

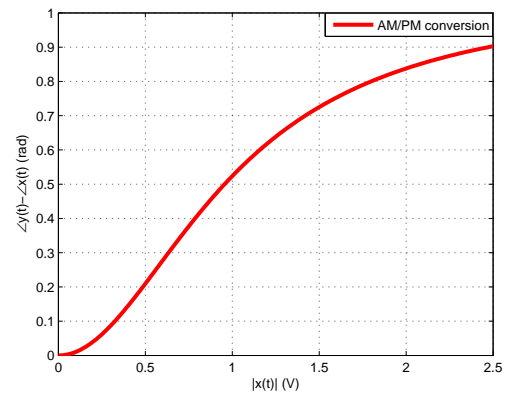


FIGURE 6: AM/PM conversion du modèle de Saleh.

Conclusion

Dans ce chapitre, nous avons introduit les concepts de base de la modulation FBMC-OQAM et des amplificateurs de puissance qui seront pris en considération dans cette thèse.

Prédiction des remontées spectrales pour une modulation FBMC-OQAM avec analyse par les cumulants

Introduction

Il existe de nombreuses méthodes pour prédire les remontées spectrales liées à un traitement NL. Dans cette thèse nous utilisons les cumulants pour y parvenir. Le modèle d'AP utilisé dans cette analyse est le modèle de Saleh [9]. Toutefois, l'étude reste valide pour les autres modèles de l'AP.

Prédiction des remontées spectrales

Tout d'abord, nous avons besoin de construire un modèle polynomial de l'AP à partir de ses caractéristiques de conversion AM/AM et AM/PM. Les coefficients du polynôme seront nécessaires pour calculer le spectre avec les cumulants. Pour obtenir ce modèle polynomial, il est suffisant de se concentrer sur des polynômes d'ordre impair [10]. Une fois le modèle polynomial obtenu nous pouvons prédire les remontées spectrales du signal après amplification.

La prédiction des remontées spectrales d'un signal FBMC-OQAM avec 128 sous-porteuse et des symboles complexes 4-QAM amplifiée par un AP suivant le modèle de Saleh est présenté sur les Fig. 7 et Fig. 8. On peut constater sur ces figures, qu'en fonction de l'IBO il faut utiliser des ordres de polynômes plus ou moins grands afin d'avoir une

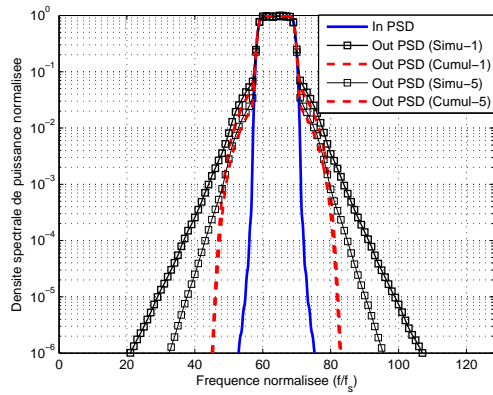


FIGURE 7: Prédiction de remontées spectrales avec IBO=1, 5 dB pour NL ordre 3.

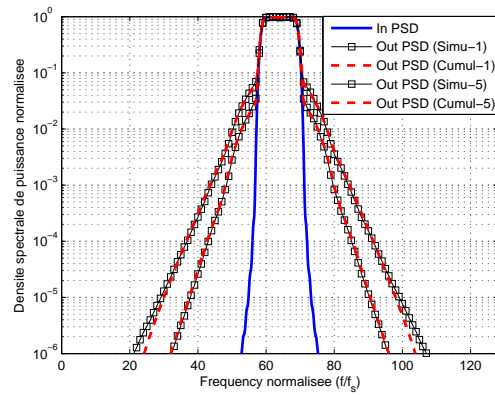


FIGURE 8: Prédiction de remontées spectrales avec IBO=1, 5 dB pour NL ordre 11.

bonne estimation du spectre. Plus l'IBO est petit (AP opéré proche de la saturation) plus l'ordre du polynôme doit être élevé.

Conclusion

Dans ce chapitre, il a été montré qu'en utilisant une décomposition polynomiale avec un ordre suffisamment élevé, il est possible de prédire les remontées spectrales avec la technique des cumulants. Plus l'ordre du polynôme sera élevé, meilleure sera la prédiction du spectre. Plus l'AP est opéré proche de la saturation plus l'ordre du polynôme devra être élevé pour une bonne approximation du spectre.

Les techniques de réduction du PAPR pour les systèmes FBMC-OQAM

Introduction

Le PAPR d'un signal est une variable aléatoire, qui est un paramètre pratique permettant de quantifier la sensibilité de ce signal vis-à-vis de l'amplification par un AP NL. Le PAPR d'un signal est égal au rapport de sa puissance de crête sur sa puissance moyenne. Étant une technique multi-porteuses, la modulation FBMC- OQAM souffre d'un PAPR élevé. Pour contrer cela, nous devons mettre en œuvre des techniques de réduction du PAPR, afin d'exploiter l'AP plus efficacement du point de vue du rendement énergétique. La fonction de densité cumulative complémentaires (CCDF) du PAPR est le paramètre généralement utilisé pour analyser le PAPR.

Les techniques de réduction du PAPR utilisées pour OFDM

Etat de l'art

Avec les systèmes de communication muti-porteuses, la réduction du PAPR est un des problèmes clé qui doit être résolu efficacement avec une complexité raisonnable. Des techniques de réduction du PAPR existent pour la modulation OFDM. Les plus populaires sont les Techniques de clipping [11], Tone Injection (TI) [12], Tone Reservation (TR) [13], Active Constellation Extension (ACE) [14], Partial Transmit Sequence (PTS) [15], Selected Mapping (SLM) [16] et block coding [17]. La comparaison de la majorité des techniques susmentionnées peut être trouvée dans [18] et [19].

Technique du Selected Mapping (SLM)

Dans la technique SLM, nous générons tout d'abord, U vecteurs de rotation. Le vecteur de symboles complexes d'entrée est multiplié par ces U vecteurs de rotation de phase, avant la modulation FBMC-OQAM. La technique SLM consiste à identifier le vecteur de rotation qui donne un signal ayant le plus faible PAPR. L'indice de ce vecteur de rotation de phase est ainsi envoyé au récepteur comme information supplémentaire (CSI) à l'aide d'un mot binaire composée de $\log_2 U$ bits. Une caractéristique majeure de la technique SLM est qu'elle ne modifie pas les performances en termes de BER ou d'OOB.

Technique de Tone Reservation (TR)

L'idée derrière la TR est d'utiliser un sous ensemble de sous porteuses (les tones réservés, PRT) afin d'annuler les pics du signal émis et ainsi minimiser son PAPR. Ces sous-porteuses ou tones ne sont pas porteurs d'information utile et sont, bien sûr, disjoints des sous porteuses de données (data tones, DTs).

Ainsi, le signal résultant qui sera transmis est donné par

$$x(t) = d(t) + c(t), 0 \leq t < \infty \quad (1)$$

Où, $c(t)$ est le signal d'annulation de crête et $d(t)$ est le signal généré par les sous-porteuses de données. L'objectif de la technique TR est de calculer les valeurs optimales des tones réservés afin de minimiser le PAPR. Ceci peut être réalisé en utilisant des algorithmes d'optimisation convexe comme QCQP [20], POCS [21] ou par recherche de gradient [20], etc. Néanmoins, trouver l'emplacement optimal des PRT est un problème difficile qui a un fort impact sur les performances de toute technique TR.

Les techniques de réduction du PAPR adaptées aux modulations FBMC-OQAM

Les techniques classiques, proposées pour l'OFDM, ne peuvent pas être appliquées directement au FBMC-OQAM à cause du chevauchement de la RI qui s'étend sur KT . Dernièrement, plusieurs techniques de réduction du PAPR ont été proposées pour le FBMC-OQAM: Overlapped SLM [22], Sliding window TR [23], Iterative clipping [24, 25], Improved SLM [26], Multi-block Joint optimization PTS [27], ACE [28], ACE avec TR [29]

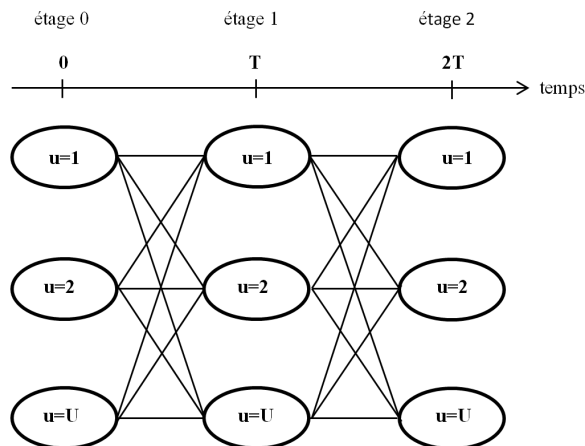


FIGURE 9: Schéma du treillis entre 3 étages avec 3 états.

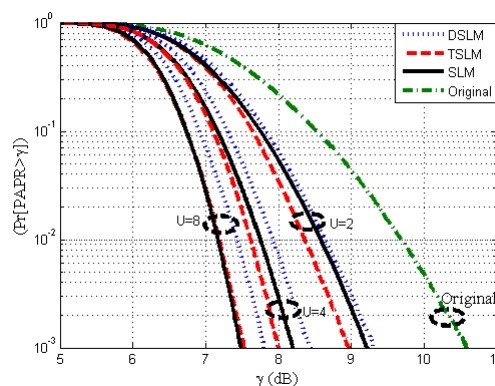


FIGURE 10: CCDF du PAPR pour FBMC-OQAM avec DSLM et TSLM et OFDM avec SLM.

Dispersive selected mapping (DSLMM)

DSLMM est une approche de type symbole par symbole pour la réduction du PAPR. La technique DSLMM pour FBMC est assez proche de la technique classique SLM pour l'OFDM sauf que nous prenons en compte les symboles passés (recouvrement lié à la longueur de la RI) afin de générer le signal dans le domaine temporel [22].

Trellis-based selected mapping (TSLMM)

DSLMM est une approche sous-optimale car elle travaille symbole par symbole. Une approche globale optimale serait nécessaire mais, afin d'éviter la recherche exhaustive de plus de U^M vecteurs de rotations possibles, nous avons proposé une solution quasi-optimale faisant appel à la programmation dynamique utilisant un treillis. TSLMM est une approche basée sur un treillis qui permet de trouver les vecteurs de rotation optimaux en prenant en compte plusieurs symboles successifs. Le treillis est constitué d'étages successifs correspondants aux différents vecteurs de symboles complexes émis. Chaque étage du treillis est subdivisé en plusieurs états correspondant chacun à l'un des U vecteurs de rotation. Un chemin entre deux états possède une métrique qui est une fonction du PAPR du signal obtenu avec les rotations de l'état d'origine et final. Un schéma de treillis avec 3 étages et 3 états ($U = 3$), est représenté sur la Fig. 9. Les performances de DSLMM et TSLMM sont affichées sur la Fig. 10, où nous pouvons remarquer que la réduction du PAPR de la modulation FBMC-OQAM avec TSLMM est supérieure au FBMC-OQAM avec DSLMM et à l'OFDM avec SLM classique.

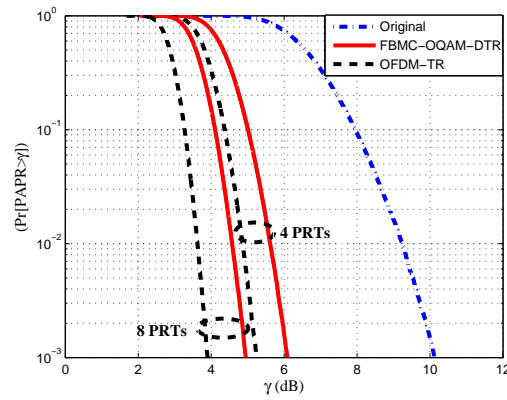


FIGURE 11: CCDF du PAPR pour FBMC-OQAM avec DTR et OFDM avec TR.

Dispersive TR

Pour la modulation FBMC OQAM, la technique dite “dispersive TR” (DTR) a été proposée. Cette technique tient compte du chevauchement des symboles, lié à la longueur de la RI, pour le calcul du signal $d(t)$. Pour identifier les emplacements optimaux des PRT, une technique basée sur la méthode du noyau a été proposée. Les performances en termes de réduction du PAPR de la technique DTR sont présentées sur la Fig. 11. En outre, sur cette même figure, il peut être remarqué que la modulation FBMC-OQAM avec DTR est devancée par le TR classique appliqué à la modulation OFDM.

Conclusion

La modulations FBMC-OQAM ayant un PAPR élevé, il est nécessaire de mettre en œuvre des techniques de réduction du PAPR performantes et de faible complexité. Les techniques classiques disponibles pour l’OFDM ne peuvent pas être appliquées directement du fait de la longueur de la RI des filtres prototypes. En prenant en compte la structure même du signal FBMC-OQAM avec des symboles qui se chevauchent, trois nouvelles techniques de réduction du PAPR ont été proposées et validées : DSLM, TSLM et DTR.

Coexistence entre système FBMC-OQAM et systèmes PMR bande étroite

Introduction

TETRA (TErrestrial TRunked RAdio) et TETRAPOL sont les deux principaux standards de la PMR en Europe. Un effort important est déployé afin d'étendre les services offerts vers des services de type large bande [30]. Néanmoins, le manque de spectre disponible complique le déploiement. Dans le contexte de la PMR, ce chapitre étudie la possible coexistence, sur la même bande de fréquence des services historiques bande étroite de la PMR avec les services large bande MCM basés sur une couche physique de type FBMC-OQAM.

Scénario PMR typique de coexistence avec masques de réception du standard TEDS

La puissance du signal interféreur peut être représentée en fonction du décalage fréquentiel entre la fréquence porteuse nominale (à savoir la fréquence centrale) du système TEDS et la fréquence porteuse de l'interfereur le plus proche. Le niveau de brouillage global peut être défini comme étant le niveau maximal d'interférence que pourrait supporter un récepteur TEDS afin de garantir une certaine qualité de service. Le rayonnement OOB du système large bande LTE doit respecter le masque spécifié par le standard TEDS. Nous analysons la possibilité de déployer un système de MCM de type LTE dans une bande de fréquence de 1.4 MHz réservée à la PMR (située dans la bande des 400 MHz) en

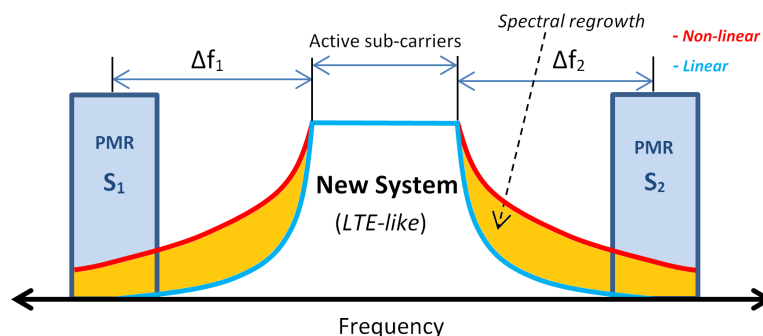


FIGURE 12: Coexistence d'un système à large bande avec des utilisateurs bande étroite PMR.

présence d'un AP non linéaire. Comme cela est illustré sur la Fig. 12, un problème typique de la coexistence peut être une situation où le système à large bande doit respecter les contraintes imposées par des dispositifs déjà existants et opérationnels de PMR, S_1 et S_2 , qui sont situés dans la bande de fréquence allouée et séparés par un intervalle spectral donné. L'objectif est de loger le système large bande de type LTE entre les deux systèmes S_1 et S_2 , tout en respectant les contraintes de brouillage. Le rayonnement hors bande du système de type LTE doit être inférieur au niveau d'interférence destructive de système PMR existant.

Analyse des interférences dans le scenario de coexistence

Les simulations sont faites avec 128 sous-porteuses modulées par des symboles 4 QAM dans un système MCM de type LTE avec 1.4 MHz de bande qui doit coexister avec des systèmes PMR bande étroite de largeur de bande 25 kHz. Nous considérons un cas réaliste de AP modélisé par un modèle de Rapp avec $p = 2.25$. L'impact de l'IBO sur l'interférence efficace est indiquée dans la Fig. 13, où on observe qu'un IBO de 21 dB est nécessaire pour respecter le masque TEDS. Si maintenant, nous considérons un AP parfaitement linéarisé (modèle du limiteur parfait) on peut voir sur la Fig. 14 qu'un IBO de 11.7 dB est nécessaire pour respecter le masque TEDS. Afin de comprendre l'impact de la réduction du PAPR, nous avons appliqué la technique DTR au signal FBMC-OQAM avant amplification de puissance. Sur la Fig. 15 il peut être remarqué que, pour un nombre de porteuses réservées de $R = 8$, respectivement de $R = 16$, le masque TEDS peut être respecté pour des valeurs de l'IBO de 6.7 dB et 5.6 dB respectivement.

Maintenant, nous allons supposer que l'AP a été linéarisé de façon imparfaite. Cela correspond à un AP ayant une conversion AM/AM intermédiaire entre le limiteur parfait ($p = \infty$) et le modèle de Rapp fortement non linéaire avec $p = 2.25$. Pour les simulations suivantes la valeur de $p = 6$ a été choisie pour modéliser un AP imparfaitement linéarisé. Sur la Fig. 16, il peut être remarqué que pour un nombre de porteuses réservées $R =$

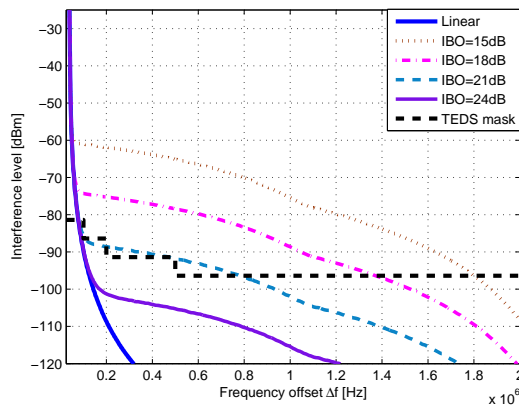


FIGURE 13: Interférence effective du système FBMC-OQAM avec un modèle Rapp AP avec $p = 2.25$.

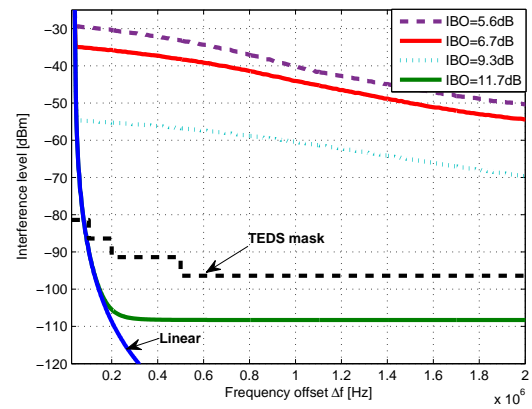


FIGURE 14: Interférence effective du système FBMC-OQAM avec un AP parfaitement linéarisé.

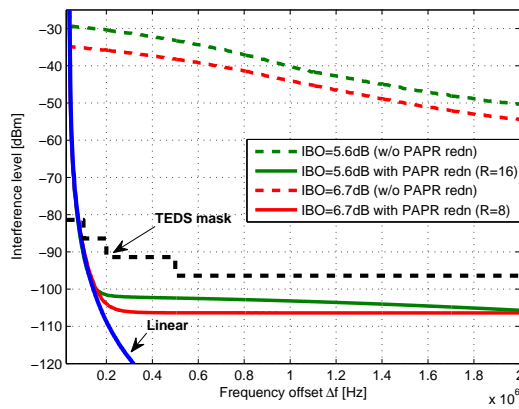


FIGURE 15: Interférence effective du système FBMC-OQAM avec un AP parfaitement linéarisé.

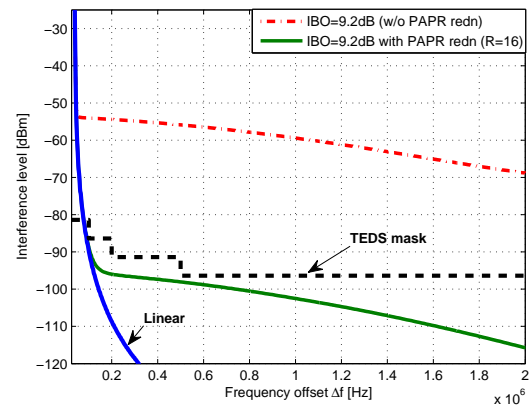


FIGURE 16: Interférence effective du système FBMC-OQAM avec un AP modérément linéarisé (modèle Rapp avec $p = 6$).

16, le masque TEDS peut être respecté pour des valeurs de l'IBO de 9.2 dB avec une réduction du PAPR.

Conclusion

Dans ce chapitre, nous avons testé plusieurs scénarios de coexistence d'utilisateurs PMR à bande étroite avec des utilisateurs large bande de type LTE en présence d'AP non linéaires. Nous avons montré qu'un choix judicieux de l'IBO et de technique de réduction du PAPR assure le respect du masque défini par la standard TEDS et donc la coexistence entre utilisateurs large bande, de type LTE, et utilisateurs à bande étroite. Différents scénarios de AP non-linéarité ont été étudiés. Les résultats des simulations suggèrent

qu'un système FBMC-OQAM peut encore coexister avec les systèmes PMR/PPDR, quand il y a atténuation NL appropriée.

Techniques de linéarisation des amplificateurs de puissance pour les modulations FBMC-OQAM

Introduction aux techniques de linéarisation de AP

Il existe de nombreuses techniques de linéarisation d'amplificateurs de puissance non linéaires. Les différentes techniques de la littérature sont des techniques dites de : Feedback, Feedforward, Dynamic biasing, Envelope elimination and restoration (EER), Linear amplification with NL components (LINC), Prédistorsion analogique ou numérique et prédistorsion adaptative.

Prédistorsion est le terme générique donné à des techniques qui visent à linéariser un AP en apportant les modifications appropriées à l'amplitude et la phase du signal d'entrée. Dans cette thèse, nous nous concentrerons principalement sur les prédistorsions numériques (DPD).

Techniques de DPD adaptées aux modulations FBMC-OQAM

Récemment, une DPD adaptative basée sur des réseaux neuronaux, a été proposée pour des modulations FBMC-OQAM, dans [31]. L'évaluation expérimentale de DPD avec les systèmes FBMC-OQAM a été faite dans [32].

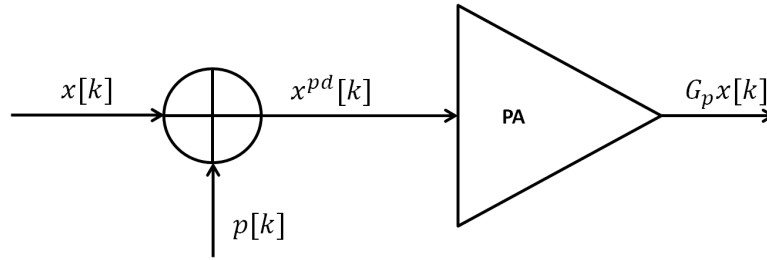


FIGURE 17: Illustration de la DPD en tant que méthode d'ajout de signal.

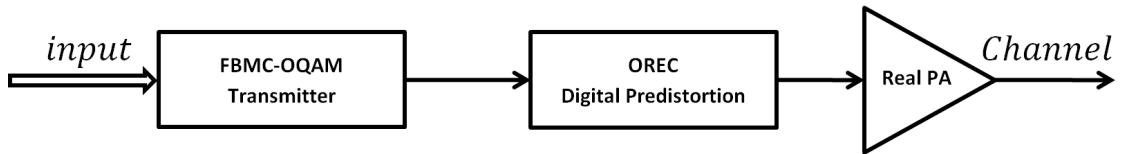


FIGURE 18: Illustration d'un système FBMC-OQAM avec technique OREC-DPD.

Prédistorsion par ajout de signal

Si les effets de la mémoire de l'AP sont négligeables, la prédistorsion peut être considérée comme une technique d'ajout de signal pour les signaux OFDM. L'illustration de la DPD en tant que technique d'ajout de signal est présentée sur la Fig. 17.

Technique de prédistorsion numérique proposée: Overlapped-Recursive Error Correcting

Dans ce chapitre, nous proposons une nouvelle technique de DPD adaptée aux signaux FBMC-OQAM. Cette technique est baptisée Overlapped-Recursive Error Correcting (OREC-DPD), car elle prend en compte le chevauchement des symboles FBMC-OQAM. La manière selon laquelle le chevauchement des symboles antérieurs est pris en considération est similaire à celle des techniques proposées pour la réduction du PAPR. Cependant, cette DPD se fait en bande de base, ce qui implique qu'il faut préalablement modéliser le vrai AP afin d'effectuer sa linéarisation. L'illustration d'un système FBMC-OQAM OREC-DPD est représentée sur la Fig. 18.

Analyse de la technique de linéarisation OREC-DPD

Les simulations sont effectuées pour 10^5 symboles FBMC-OQAM avec des porteuses modulées par des symboles 4QAM et 64 sous-porteuses. Le facteur de sur échantillonnage choisi est de $L = 4$. Le filtre prototype utilisé est celui de PHYDYAS. Dans l'analyse,

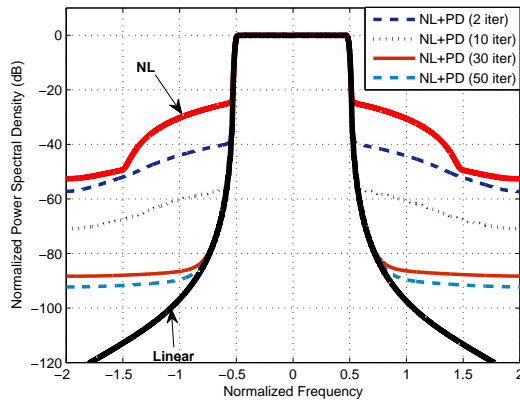


FIGURE 19: Impact du nombre d'itérations, $\lambda = 0.1$ et $IBO=5$ dB.

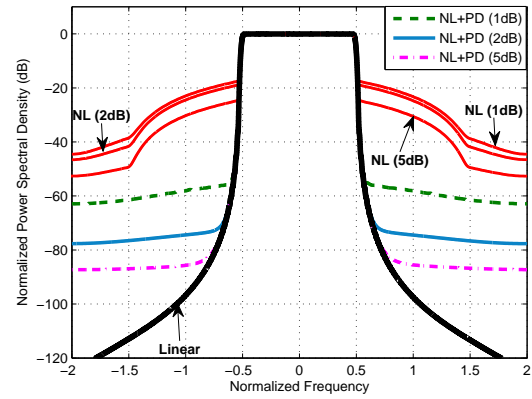


FIGURE 20: Impact de l'IBO, $p = 2.25$ dB.

nous considérons un AP modélisé par le modèle de Rapp avec $p = 2.25$. En outre, nous fixons $\lambda = 0.1$ dans notre analyse de linéarisation. Sur la Fig. 19 nous pouvons voir que la performance de linéarisation est améliorée avec le nombre d'itérations. L'impact de l'IBO sur la technique OREC-DPD a été simulé pour différentes valeurs de l'IBO. Sur la Fig. 20, on peut remarquer que les valeurs d'IBO élevées aboutissent à de meilleures performances de linéarisation.

Conclusion

Le but du travail décrit dans ce chapitre est de contribuer au domaine de la linéarisation des AP non linéaires. Une nouvelle technique de DPD, à savoir OREC-DPD a été proposée pour les modulations FBMC-OQAM et les résultats de simulation montrent qu'elle est très efficace dans la linéarisation des AP.

Conclusion

Contributions

Cette thèse a été réalisée dans le cadre du projet européen FP7 EMPHATIC. Tout au long de cette thèse, nous avons passé en revue et étudié certains aspects importants liés à l'étude des effets des amplificateurs de puissance non linéaires sur les signaux FBMC-OQAM. Une étude avec prédiction de l'OOB a été présentée avec la technique des cumulants. Successivement, nous avons fait trois propositions originales pour la réduction du PAPR, à savoir : DSLM, TSLM et DTR. En outre, nous avons montré qu'un système large bande de type LTE basé sur une couche physique FBMC-OQAM permet la coexistence avec les systèmes PMR bande étroite. Enfin, une proposition nouvelle pour la linéarisation des AP avec modulations FBMC-OQAM, appelée OREC-DPD, a été réalisée.

Les perspectives futures

Bien sûr, de nombreuses idées sont apparues au fil de l'avancement des travaux de thèse et nous pensons qu'il serait intéressant par exemple d'examiner les aspects ci-après:

- Etudier les différentes techniques avec des modèles de AP avec mémoire,
- Réaliser l'optimisation conjointe de la réduction du PAPR et de la DPD adaptée au FBMC-OQAM,
- Etudier les différentes techniques proposées dans cette thèse avec d'autres formes d'onde post-OFDM,

- Etudier l'impact d'une limitation de la puissance sur les tones réservés avec la méthode DTR.

Contents

Declaration of Authorship

Acknowledgements	i
Abstract	iii
Résumé	v
Contents	xxviii
List of Figures	xxxiii
List of Tables	xxxvii
Abbreviations	xxxviii
Symbols	xli
1 Introduction	1
1.1 Background and motivation	1
1.2 Project EMPHATIC	4
1.3 Thesis objectives	4
1.4 Thesis outline	5
1.5 Publications	7
2 FBMC-OQAM systems and power amplifiers	9
2.1 Introduction	9
2.2 Brief overview of OFDM system	10
2.3 Introduction to a FBMC-OQAM system	11
2.3.1 OQAM mapping	14
2.3.2 Poly-phase filtering	16
2.3.3 Discrete-time representation	17
2.3.4 FBMC-OQAM modulation as matrix operation	17
2.3.5 Prototype filter	20

2.3.5.1	PHYDYAS filter	20
2.3.5.2	IOTA filter	22
2.3.6	Transmultiplexer impulse response of PHYDYAS and IOTA prototype filters	23
2.3.7	Orthogonality in real domain	24
2.3.8	Overlapping nature of FBMC-OQAM symbols	26
2.4	Introduction to non-linear power amplifiers	27
2.4.1	Linearity and power efficiency tradeoff in a PA	29
2.4.2	Analytical representation of a PA	29
2.4.3	AM/AM and AM/PM characteristics	30
2.4.4	Some PA models	31
2.4.4.1	Polynomial model	31
2.4.4.2	Soft envelope limiter	32
2.4.4.3	Rapp model	33
2.4.4.4	Saleh model	34
2.4.5	Spectral regrowth of non-linearly amplified MCM signals	35
2.5	Need for mitigation of NL effects of PA	36
2.5.1	PAPR analysis of MCM signals	39
2.5.1.1	Complementary cumulative density function of PAPR	41
2.5.1.2	Need for oversampling	41
2.5.2	PA linearization	42
2.6	Conclusion	42
3	Spectral regrowth prediction for FBMC-OQAM systems using cumulant analysis	44
3.1	Introduction	44
3.2	Introduction to cumulants	45
3.2.1	Definition of cumulants	46
3.2.2	Cumulants and moments relation	46
3.2.3	Joint cumulants	47
3.2.4	Properties of cumulants	48
3.2.4.1	Additivity	48
3.2.4.2	Homogeneity	48
3.2.4.3	Semi-variance	48
3.2.4.4	Gaussian random variable	49
3.2.5	Cumulants of a random process	49
	Gaussian case:	50
	Independent and identically distributed case:	50
	Symmetrical case:	51
	Complex case:	51
3.3	Spectral prediction by cumulants	51
3.4	Simulation results for PSD prediction	54
3.4.1	Polynomial fitting	54
3.4.2	Spectral regrowth prediction in the case of a single user	55
3.4.3	Spectral regrowth prediction in a cognitive radio context	55
3.5	Conclusion	56

4	PAPR reduction techniques for FBMC-OQAM systems	59
4.1	Introduction	59
4.2	PAPR reduction techniques suggested for OFDM	60
4.2.1	State of the art	60
4.2.2	Clipping	60
4.2.3	Selected Mapping	61
4.2.4	Partial transmitting sequence	62
4.2.5	Tone reservation	63
4.2.6	Tone Injection	65
4.2.7	Active Constellation Extension	66
4.2.8	Block coding	66
4.3	PAPR reduction techniques suggested for FBMC-OQAM	66
4.4	Dispersive SLM	67
4.4.1	DSL _M algorithm	68
4.4.2	Simulation results with DSL _M	70
4.4.2.1	Impact of variation of T_0 duration	70
4.4.2.2	Impact of size of U	72
4.4.2.3	Impact of FFT size	73
4.4.2.4	Comparison of OS _{LM} and DSL _M	73
4.4.3	Sub-optimality of the symbol-by symbol approach	74
4.5	Trellis-based SLM	75
4.5.1	Exhaustive search	76
4.5.2	Dynamic programming	76
4.5.3	TSL _M algorithm	78
4.5.4	Computational complexity analysis of DSL _M and TSL _M	80
4.5.4.1	Derivation of computational complexities in DSL _M and TSL _M	80
4.5.4.2	Comparison of computational complexities of TSL _M and MBJO-PTS	82
4.5.5	Simulation Results with TSL _M	84
4.5.5.1	Impact of variation of T_0 duration	85
4.5.5.2	Impact of choice of the metric function	86
4.5.5.3	Impact of variation in prototype filter	87
4.5.5.4	Impact of FFT size	88
4.5.5.5	Impact of size of U	88
4.5.5.6	Comparison of TSL _M and MBJO-PTS schemes	90
4.6	Dispersive TR	91
4.6.0.1	Determination of \mathcal{B} for FBMC-OQAM	92
4.6.0.2	DTR Algorithm	93
4.6.1	Simulation Results	96
4.6.1.1	Impact of variation of T_0 duration	96
4.6.1.2	Impact of variation in prototype filter	97
4.6.1.3	Impact of size of \mathcal{B}	98
4.6.1.4	Impact of FFT size	99
4.6.1.5	Impact of PRT locations	100
4.7	Overview of proposed PAPR reduction schemes	101
4.8	Conclusion	102

5	Coexistence capability of FBMC-OQAM Systems with PMR Systems	103
5.1	Introduction	103
5.2	PMR systems	105
5.3	TEDS reception mask	106
5.4	System model in a typical coexistence scenario	108
5.5	Interference analysis of the coexistence scenario	110
5.5.1	Coexistence scenario in a linear case	110
5.5.2	Coexistence scenario in a NL case	111
5.5.2.1	Scenario 1: Realistic model without PAPR reduction	111
5.5.2.2	Scenario 2: Perfectly linearized model without PAPR reduction	111
5.5.2.3	Scenario 3: Perfectly linearized model with PAPR reduction	112
5.5.2.4	Scenario 4: Moderately linearized model with PAPR reduction	113
5.6	Proposed solution for PMR coexistence	114
5.7	Conclusion	115
6	PA linearization techniques for FBMC-OQAM systems	117
6.1	Background	117
6.2	Introduction to PA linearization techniques	119
6.2.1	Power backoff	119
6.2.2	Feedback	120
6.2.3	Feedforward	120
6.2.4	Dynamic biasing	121
6.2.5	Envelope elimination and restoration	121
6.2.6	Linear amplification with NL components	121
6.2.7	Predistortion	122
6.2.8	Adaptive predistortion	123
6.3	Digital predistortion techniques suggested for FBMC-OQAM	123
6.3.1	State of the art	123
6.3.2	Predistortion by signal addition	124
6.3.3	Overlapped-Recursive Error Correcting Digital Predistortion	125
6.3.4	Non-collaborative PAPR reduction	127
6.4	Linearization analysis	128
6.4.1	Impact of number of iterations Q	129
6.4.2	Impact of knee factor p	130
6.4.3	Impact of polynomial model mismatch	131
6.4.3.1	Negative mismatch ($p_{real} - p_{model} < 0$)	132
6.4.3.2	Positive mismatch ($p_{real} - p_{model} > 0$)	133
6.4.4	Impact of IBO	133
6.4.5	Impact of non-collaborative PAPR reduction	134
6.5	Conclusion	135
7	Conclusion	137
7.1	Background and motivation	137
7.2	Contributions	138

7.3 Future Perspectives	140
Bibliography	151
Vita	152

List of Figures

1	Comparaison de la réponse impulsionnelle des filtres PHYDYAS, IOTA et rectangulaire.	xi
2	Comparaison de la DSP des filtres PHYDYAS, IOTA et rectangulaire.	xi
3	Illustration du profil de puissance moyenne de l'OFDM et des FBMC-OQAM.	xi
4	AM/AM conversion des modèles SEL et Rapp.	xii
5	AM/AM conversion du modèle de Saleh.	xiii
6	AM/PM conversion du modèle de Saleh.	xiii
7	Prédiction de remontées spectrales avec IBO=1, 5 dB pour NL ordre 3.	xv
8	Prédiction de remontées spectrales avec IBO=1, 5 dB pour NL ordre 11.	xv
9	Schéma du treillis entre 3 étages avec 3 états.	xviii
10	CCDF du PAPR pour FBMC-OQAM avec DSLM et TSLM et OFDM avec SLM.	xviii
11	CCDF du PAPR pour FBMC-OQAM avec DTR et OFDM avec TR.	xix
12	Coexistence d'un système à large bande avec des utilisateurs bande étroite PMR.	xxi
13	Interférence effective du système FBMC-OQAM avec un modèle Rapp AP avec $p = 2.25$	xxi
14	Interférence effective du système FBMC-OQAM avec un AP parfaitement linéarisé.	xxi
15	Interférence effective du système FBMC-OQAM avec un AP parfaitement linéarisé.	xxi
16	Interférence effective du système FBMC-OQAM avec un AP modérément linéarisé (modèle Rapp avec $p = 6$).	xxi
17	Illustration de la DPD en tant que méthode d'ajout de signal.	xxiv
18	Illustration d'un système FBMC-OQAM avec technique OREC-DPD.	xxiv
19	Impact du nombre d'itérations, $\lambda = 0.1$ et IBO=5 dB.	xxv
20	Impact de l'IBO, $p = 2.25$ dB.	xxv
1.1	Illustration of frequency responses of OFDM and FBMC-OQAM.	3
2.1	Multicarrier transmitter.	10
2.2	FBMC-OQAM transmitter.	13
2.3	FBMC-OQAM receiver.	13

2.4	Time-frequency phase-space lattice representation of a FBMC-OQAM system.	14
2.5	Comparison of impulse response for PHYDYAS and rectangular filters.	21
2.6	Comparison of analytical PSD for PHYDYAS and rectangular filters.	21
2.7	Comparison of impulse response for IOTA and rectangular filters.	22
2.8	Comparison of analytical PSD for IOTA and rectangular filters.	22
2.9	Illustration of mean power profile of OFDM and FBMC-OQAM symbols.	26
2.10	Illustration of FBMC-OQAM transmission chain along with PA.	27
2.11	Impact of AM/PM conversion on QPSK constellation I/Q diagram.	30
2.12	SEL and Rapp model AM/AM conversion characteristics.	33
2.13	Saleh model AM/AM conversion characteristic.	34
2.14	Saleh model AM/PM conversion characteristic.	34
2.15	Spectral regrowth in PSD in a OFDM system with Saleh model of PA.	35
2.16	Spectral regrowth in PSD in a OFDM system with Saleh model of PA.	35
2.17	PA nonlinear behavior.	37
2.18	Linearized PA and input signal with low PAPR.	39
2.19	A FBMC-OQAM symbol with PAPR of 15.27 dB.	40
2.20	CCDF of PAPR of a 64-tone FBMC-OQAM signal w.r.t L	41
3.1	AM/AM conversion of Saleh Model and its polynomial fitting of orders 3, 7, 11 and 15.	53
3.2	AM/PM conversion of Saleh Model and its polynomial fitting of orders 3, 7, 11 and 15.	53
3.3	PSD Prediction with IBO=1 dB.	54
3.4	PSD Prediction with IBO=3 dB.	56
3.5	PSD Prediction with IBO=1 dB (3 different active Sub-bands).	57
3.6	Zoomed version of Fig. 3.5	58
4.1	Illustration of past symbol overlap on the m^{th} FBMC-OQAM symbol.	68
4.2	CCDF of PAPR plot for FBMC-OQAM symbols with partial PAPR calculated over $[T_a, T_b) = \{[0, T), [T, 3T), [0, 4T)\}$ with $U = 4$ to illustrate the impact of variation of T_0 duration on the DSLM scheme.	71
4.3	CCDF of PAPR plot for FBMC-OQAM symbols with PAPR calculated over $[2T, 4T)$ with $U = \{2, 4, 8\}$ to illustrate the impact of size of U on the DSLM scheme in comparison with SLM scheme for OFDM.	72
4.4	CCDF of PAPR plot for FBMC-OQAM symbols with PAPR calculated over $[2T, 4T)$ with $U = 4$ and $N = \{64, 128\}$ to illustrate the impact of FFT size on the DSLM scheme.	73
4.5	CCDF of PAPR plot for FBMC-OQAM symbols with PAPR calculated over $[2T, 4T)$ with $U = \{2, 4, 8\}$ with DSLM and OSLM schemes.	74
4.6	Illustration of the trellis diagram between M stages composed of U states.	75
4.7	CCDF of PAPR for FBMC-OQAM symbols with partial PAPR calculated over different T_0 , $U = 2$ and PHYDYAS filter.	85
4.8	CCDF of PAPR for FBMC-OQAM symbols with partial PAPR calculated over $[2T, 4T)$, $U = 2$ and different metric functions.	86
4.9	CCDF of PAPR plot for FBMC-OQAM symbols with PAPR calculated over $[2T, 4T)$ with $U = 8$ with PHYDYAS and IOTA filters.	87

4.10	CCDF of PAPR plot for FBMC-OQAM symbols with PAPR calculated over $[2T, 4T)$ with $U = 4$ and $N = \{64, 128\}$ to illustrate the impact of FFT size on the TSLM scheme.	88
4.11	CCDF of PAPR for FBMC-OQAM symbols with partial PAPR calculated over $[2T, 4T)$ with $U = 2, 4, 8$ and PHYDYAS filter.	89
4.12	CCDF of PAPR for FBMC-OQAM symbols with PAPR calculated over $[2T, 4T)$ with $U = 8$ with PHYDYAS.	90
4.13	Illustration of DTR kernel for FBMC-OQAM with 64 sub-carriers.	94
4.14	CCDF of PAPR plot for FBMC-OQAM symbols with PAPR calculated over $[T, 3T)$, $[T, 4T)$ and $[2T, 3T)$ with 8 PRTs (i.e. $R = 8$).	96
4.15	CCDF of PAPR plot for FBMC-OQAM symbols with PAPR calculated over $[T, 3T)$ with size of PRT set, $R = 8$	97
4.16	CCDF of PAPR plot for FBMC-OQAM symbols with PAPR calculated over $[T, 3T)$ with size of PRT set, $R = \{4, 8, 16\}$	98
4.17	CCDF of PAPR plot for FBMC-OQAM symbols with PAPR calculated over $[T, 3T)$ with $R = \{8, 32\}$ for $N = \{64, 256\}$ respectively.	99
4.18	Illustration of DTR kernel for FBMC-OQAM with 256 sub-carriers.	99
4.19	CCDF of PAPR plot for FBMC-OQAM symbols with PAPR calculated over $[T, 3T)$ with 8 PRTs (i.e. $R=8$) for various PRT locations.	100
5.1	Coexistence of a LTE-like broadband system with narrowband PMR users.	106
5.2	The location of LTE mobile station and narrowband mobile station near a base station in our coexistence scenario.	109
5.3	Interference performances for OFDM and FBMC-OQAM with linear PA.	110
5.4	Impact of IBO on the effective interference of FBMC-OQAM system with a realistic PA model (Rapp model with $p = 2.25$).	112
5.5	Impact of IBO on the effective interference of FBMC-OQAM system with a perfectly linearized PA.	113
5.6	Impact of PAPR reduction on the effective interference of FBMC-OQAM system with a perfectly linearized PA.	114
5.7	Impact of PAPR reduction on the effective interference of FBMC-OQAM system with a moderately linearized PA.	115
6.1	Illustration of analog and digital predistortion scheme to linearize a PA, where LO is the local oscillator.	122
6.2	Illustration of DPD as an adding signal method.	124
6.3	Illustration of a FBMC-OQAM system along with OREC-DPD scheme.	125
6.4	Detailed illustration of OREC-DPD block.	126
6.5	Illustration of PAPR reduction by DTR followed by OREC-DPD.	128
6.6	Impact of number of iterations on the OREC-DPD algorithm with $\lambda = 0.1$ and IBO=5 dB.	129
6.7	Impact of PA non-linearity on the OREC-DPD algorithm, for $p = \{1, 1.5, 2.25\}$ and IBO=5 dB.	130
6.8	Impact of negative mismatch of PA modeling on the OREC-DPD algorithm, for $p_{real} = 2.25$ and IBO=5 dB.	131
6.9	Impact of positive mismatch of PA modeling on the OREC-DPD algorithm, for $p_{real} = 2.25$ and IBO=5 dB.	132
6.10	Illustration of IBO on OREC-DPD scheme with $p = 2.25$ dB.	133

6.11 Illustration of impact of PAPR (DTR with $R = 8$) on OREC-DPD scheme with $p = 2.25$ dB.	134
---	-----

List of Tables

2.1	Transmultiplexer impulse response using PHYDYAS filter	23
2.2	Transmultiplexer impulse response using IOTA filter	24
2.3	Transmultiplexer impulse response after OQAM decision	25
4.1	Computational complexity comparison of the SLM algorithms	80
4.2	Computational complexity in DSLM	82
4.3	Computational complexity in TSLM	82
4.4	Computational complexity in MBJO-PTS	83
4.5	CCDF of PAPR at 10^{-3} value (in dB)	89
4.6	Computational complexities of the TSLM and MBJO-PTS w.r.t. complex multiplications and additions	91
4.7	CCDF of PAPR at 10^{-3} value (in dB)	99
4.8	Overview of different novel PAPR reduction techniques proposed for FBMC- OQAM	101
5.1	25 <i>kHz</i> –TEDS receiver blocking levels and mask	108
5.2	LTE Physical layer parameters	109
5.3	IBO requirements to reach the TEDS spectrum mask for FBMC-OQAM system with bandwidth corresponding to 72 active LTE subcarriers. SSPA model with different values of knee factor p with and without DTR based PAPR mitigation.	114
6.1	Impact of Digital Predistortion	118
6.2	Spectral regrowth for FBMC-OQAM when OREC-DPD is implemented with and without DTR based PAPR mitigation, before amplified by a Rapp model PA with $p = 2.25$	135

Abbreviations

3GPP	3rd Generation Partnership Project
5G	5th Generation
ACE	Active Constellation Extension
AFB	Analysis Filter Bank
AM/AM	Amplitude-to-Amplitude
AM/PM	Amplitude-to-Phase
BER	Bit Error Rate
BW	Band Width
CCDF	Complementary Cumulative Density Function
CMT	Cosine Multi-Tone
CP	Cyclic Prefix
CR	Cognitive Radio
DC	Direct Current
DFT	Discrete Fourier Transform
DC	Dynamic Programming
DPD	Digital Pre Distortion
DC	Data Tone
DTR	Dispersive Tone Reservation
DSLm	Dispersive SeLected Mapping
ETSI	European Telecommunications Standards Institute
FBMC	Filter-Bank Multi-Carrier

FFT	F ast F ourier T ransform
FMT	F iltered M ulti- T one
IB	I n- B and
IBO	I nput B ack- O ff
IDFT	I nverse D iscrete F ourier T ransform
IEEE	I nstitute of E lectrical and E lectronic E ngineers
IFFT	I nverse F ast F ourier T ransform
IOTA	I sotropic O rthogonal T ransform A lgorithm
ITU	I nternational T elecommunications U nion
LTE	L ong T erm E volution
LS	L east- S quares
MCM	M ulti- C arrier M odulation
OFDM	O rthogonal F requency D ivision M ultiplexing
OOB	O ut O f B and
OQAM	O ffset Q uadrature A mplitude M odulation
OSLM	O verlapped S elected M apping
PA	P ower A mplifier
PAM	P ulse A mplitude M odulation
PAPR	P eak-to- A verage P ower R atio
PHYDYAS	P HYsical Layer for D Ynamic Spectrum A ces S C ognitive R adio
PMR	P ersonal M obile R adio
PPDR	P ublic P rotection and D isaster R elief
PPN	P oly- P hase N etwork
PRT	P eak R eserved T one
PSD	P ower S pectral D ensity
PTS	P artial T ransmit S cheme
QAM	Q uadrature A mplitude M odulation
QCQP	Q uadratically C onstrained Q uadratic P rograming
QPSK	Q uadrature P hase S hift K eying
RAT	R adio A ccess T echnology
RF	R adio- F requency
SEL	S oft E nvelope L imiter
SFB	S ynthesis F ilter B ank

SLM	SeLected Mapping
SMT	Staggered Multi-Tone
SNR	Signal-to-Noise Ratio
SSPA	Solid State Power Amplifier
TR	Tone Reservation
TSLM	Trellis-based SeLected Mapping
TWTA	Travelling Wave Tube Amplifier

Symbols

Mathematical notations used in this dissertation

$\sin(\cdot)$	Sine function
$\cos(\cdot)$	Cosine function
e	Euler's number (also Napier's constant)
\mathbb{N}	Set of natural numbers
\mathbb{C}	Set of complex numbers
j	$\sqrt{-1}$
$(\cdot)^\top$	Transpose operator
\mathbf{X}_m	Vector
$\{\mathbf{X}_m\}_{m=0}^{M-1}$	$\{\mathbf{X}_0, \mathbf{X}_1, \dots, \mathbf{X}_{M-1}, \}$
$\widehat{\mathbf{X}}_m$	Oversampled vector
$(\cdot)^*$	Complex conjugate
$\text{diag}(\cdot)$	Diagonal matrix
$\langle \cdot \rangle$	Inner product
$\Re\{\cdot\}$	Real part of a complex number
$\ln[\cdot]$	Natural logarithm (logarithm to base e)
$\log_2(\cdot)$	Logarithm to base 2
$\log(\cdot)$ or $\log_{10}(\cdot)$	Logarithm to base 10
$\mathbb{E}[\cdot]$	Expectation operator
$ \cdot $	Modulus
$\angle(\cdot)$	Angle

$\ \cdot\ _2$ or $\ \cdot\ $	Euclidean norm
$\ \cdot\ _\infty$	Infinite norm
$\ \cdot\ _p$	p^{th} norm
$Proba(\cdot)$	Probability function
$(\cdot)!$	Factorial operator
\star	Convolution
$\arg \min$	Argument of the minimum
\odot Point-to-point multiplication	
$\mathcal{F}_N^{-1}\{\cdot\}$	N -point IFFT transform
$(\cdot)^c$	Complement set
$\lfloor \cdot \rfloor$	Floor function
Notations applicable in all Chapters	
N	Number of sub-carriers
M	Number of complex symbols vectors
$\mathcal{G}(\cdot)$	FBMC-OQAM modulation function
T	Symbol period
L	Oversampling factor
K	Prototype filter overlapping factor
L_h	Length of prototype filter
F_k	Frequency coefficients of prototype filter
A	Normalization factor
$x(t)$	Continuous-time FBMC-OQAM signal
$x[k]$	Discrete-time FBMC-OQAM signal
$h(t)$	Continuous-time prototype filter impulse response
$h[k]$	Discrete-time prototype filter impulse response
$H(Z)$	Transfer function of prototype filter impulse response
\mathbf{X}_m	m^{th} FBMC-OQAM input symbol vector
$X_{m,n}$	m^{th} input symbol on n^{th} sub-carrier
$a_{m',n}$	FBMC-OQAM symbol on n^{th} sub-carrier

	at instant $mT/2$
$\varphi_{m',n}$	Phase term on n^{th} sub-carrier
	at instant $mT/2$
$x_m(t)$	m^{th} FBMC-OQAM symbol in continuous-time
$x_m[k]$	m^{th} FBMC-OQAM symbol in discrete-time
$\hat{\mathbf{X}}_m$	Oversampled m^{th} FBMC-OQAM input symbol vector
$\mathbf{Z}_{(p,q)}$	Zero matrix or null matrix of order $p \times q$
\mathcal{M}	Mapping matrix of order $LN \times LN$
\mathcal{Q}_{LN}	IDFT matrix of order $LN \times LN$
\mathcal{Q}	Scaled IDFT matrix (i.e. \mathcal{Q}_{LN} scaled by \sqrt{LN})
\mathcal{H}	Prototype filter matrix of order $KLN \times LN$
$\Phi_{PHYDYAS}(f)$	PSD of FBMC-OQAM with PHYDYAS prototype filter
$\Phi_{IOTA}(f)$	PSD of FBMC-OQAM with IOTA prototype filter
$P_{avg}[x(t)]$	Average power of $x(t)$
η	Power efficiency of a PA
P_{DC}	DC Input power of a PA
P_{out}	RF Output power of a PA
IBO	IBO of a PA
ρ	IBO coefficient
$\dot{x}(t)$	Input signal of a PA
$y(t)$	Output signal of a PA
$G(\cdot)$	Complex gain function of a PA
$\mathcal{A}(\cdot)$	Amplification function
$\phi_{\dot{x}(t)}$	Phase of $\dot{x}(t)$
$F_a(\cdot)$	AM/AM characteristic
$F_p(\cdot)$	AM/PM characteristic
Υ	An integer; where $2\Upsilon + 1$

a_{2k+1}	is the order of polynomial model k^{th} complex coefficient of the polynomial model
v_{sat}	Input saturation level of a PA
p	Knee factor in Rapp model of PA
$PAPR_{x(t)}$	Continuous PAPR of $x(t)$
$PAPR_{x[k]}$	Discrete PAPR of $x[k]$
$CCDF_{x[k]}(\gamma)$	CCDF of $x[k]$ for a given threshold γ
$Proba(.)$	Probability function

Notations specific to Chapter 2

f_k	Sub-carrier frequencies
T_{ofdm}	Symbol duration of OFDM
Δ	Duration of CP
F	Frequency spacing
$i(t)$	Continuous-time OFDM signal
$c_{m,n}$	OFDM symbol on n^{th} sub-carrier at instant mT
$f(t)$	Rectangular time window
$g(t)$	Gaussian pulse signal
$z_{\alpha,\nu_0,\tau_0}(t)$	Extended Gaussian function
α	Spreading factor of EGF
$\lambda_{m',n}(t)$	Time-shifted version of $h(t)$
$r_{m'_0,n_0}$	Demodulated FBMC-OQAM signal before OQAM decision
$ju_{m'_0,n_0}$	Imaginary interference term of $r_{m'_0,n_0}$
$a_{m'_0,n_0}$	Demodulated FBMC-OQAM signal after OQAM decision
IBO_{lin}	IBO of a PA in linear scale
α_a, α_p	Amplitude related parameters in Saleh model
β_a, β_p	Phase related parameters in Saleh model

P_{in}	Input power of a PA
P_1	An arbitrary input power level
P_{out}	Output power of a PA
P_{mean}	Mean input power of a PA
P_{sat}	Saturation power of a PA

Notations specific to Chapter 3

$\mathcal{C}(t)$	Cumulant-generating function
S	Random variable
$\kappa_n(S)$	n^{th} order cumulant of S
$\mathbb{E}(e^{tS})$	Moment-generating function
$m_n(S)$	n^{th} raw moment of S
\mathbf{p}	Partition of a set
$ \mathbf{p} $	Number of parts in the partition \mathbf{p}
\mathbf{B}	Block in a partition \mathbf{p}
B_m	m^{th} Bell number
$S(t)$	Random process
τ	Delay
$m_{is}(\tau)$	i^{th} order raw moment of $s(t)$
$\kappa_{is}(\tau)$	i^{th} order cumulant of $s(t)$
σ	Mean of $s(t)$
μ	Variance of $s(t)$
δ	Kronecker delta function
$\kappa_{2s}(t)$	Auto-covariance function of $s(t)$
$S_{2s}(f)$	PSD of $s(t)$
β_{2m+1}	m^{th} constant coefficient in $\kappa_{2y}(t)$

Notations specific to Chapter 4

α_o	Clipping threshold
$x_c(t)$	Clipped signal
U	Number of phase rotation vectors in SLM
$\phi^{(u)}$	u^{th} complex phase rotation vector
$\phi_k^{(u)}$	k^{th} element of $\phi^{(u)}$

ψ_k	Phase of $\phi_k^{(u)}$
u_{min}	Optimal phase rotation vector
V	Number of sub-block partitions in PTS
W	Number of phase candidates in a sub-block
$e^{j\omega(i,v)}$	Phase factor for v^{th} sub-block partition
$\mathcal{F}_N^{-1}\{\cdot\}$	N-point IFFT transform
$\mathcal{O}(\cdot)$	Order of computational complexity
$d(t)$	Data signal
$c(t)$	Peak cancellation signal
$D[n]$	DT set
$C[n]$	PRT set
\mathcal{B}	PRT locations set
R	Length of \mathcal{B}
\mathcal{K}	Peak reduction kernel
δ	Unit impulse symbol
n_0	Maximum of the Dirac-type kernel
$\mathcal{O}(\cdot)$	Order of complexity
ν	Constellation enlargement factor in TI
d_{min}	Minimum distance between two constellation points
p	Distance between constallements in TI
$x_m^{(u)}(t)$	Rotated FBMC-OQAM symbol overlapped by past symbols
$\mathbf{X}_m^{(u_{min})}$	Optimal rotation index for \mathbf{X}_m
$PAPR_{(T_0)}^{(u)}$	Partial PAPR of $x_m^{(u)}(t)$ over T_0
T_0	Arbitrary time interval used in partial PAPR calculation
T_a	Lower limit of the time interval ($T_a \geq 0$)
T_b	Upper limit of the time interval ($T_b \geq 4.5T$)
Θ	Set of optimal rotation vectors
$\zeta_{(m \Rightarrow m+1)}^{(u,v)}$	Trellis path between u^{th} state in m^{th} stage and v^{th} state in $(m+1)^{th}$ stage

$\Gamma_{(m,m+1)}^{(u,v)}$	Path metric related to the trellis path $\zeta_{(m \Rightarrow m+1)}^{(u,v)}$
$f(\cdot)$	Convex function
$\Psi_{(u,m)}$	State metric in the trellis path at u^{th} state in m^{th} stage
$x_m^{(u)}(t)$	Rotated m^{th} FBMC-OQAM signal
$x_{m,m+1}^{(u,v)}(t)$	Jointly modulated rotated m^{th} and $(m+1)^{th}$ signals
$\lambda(v, m)$	State matrix in the trellis at v^{th} state in m^{th} stage
c_{rot}	Complexity related to phase rotations in DSLM or TSLM
c_{mod}	Complexity related to FBMC-OQAM modulation in DSLM or TSLM
c_{met}	Complexity related to metric calculation in DSLM or TSLM
d	Number of successive symbol intervals
$c_{DSL M}$	Complexity related to DSLM
$c_{TSL M}$	Complexity related to TSLM
\hat{c}_{rot}	Complexity related to phase rotations in MBJO-PTS
\hat{c}_{mod}	Complexity related to FBMC-OQAM modulation in MBJO-PTS
\hat{c}_{met}	Complexity related to metric calculation in MBJO-PTS
c_{MBJO}	Complexity related to MBJO-PTS
U_{root}	U value for TSLM to have fairly same complexity as in MBJO-PTS
Δ	Discriminant in equation (4.45)
\mathbf{D}_m	m^{th} DT in DTR
\mathbf{C}_m	m^{th} PRT in DTR
$\dot{o}_m(t)$	Signal generated by past overlapping symbols on m^{th} symbol

$\hat{c}_m(t)$ Optimal peak cancellation signal for m^{th} symbol

Notations specific to Chapter 5

I Inteference power in given bandwidth $[f_1, f_2]$

S_{dBm} Receiver sensitivity

E_S/N_0 Signal-to-noise ratio

B Blocking level

R_m TEDS reception mask level

ν_{dB} Efficiency loss

NF Noise figure

T_0 Reference temperature for receiver noise

NF Noise figure

W Bandwidth of TEDS receiver

k Boltzmann constant

N_d Number of data symbols in a TEDS slot

N_t Number of total symbols in a TEDS slot

R_s Symbol rate

S_c Number of subcarriers in the considered bandwidth

Notations specific to Chapter 6

$x^{pd}[k]$ Predistorted signal

$p[k]$ Predistortion function

G_p Linear gain

$p_m^{(q)}[n]$ Accumulative partial predistortion signal at end of q^{th} iteration

$y^{(q)}[n]$ Output signal of PA at end of q^{th} iteration

$e^{(q)}[n]$ Predistortion error signal at end of q^{th} iteration

λ Convergence rate

Chapter 1

Introduction

1.1 Background and motivation

The wireless (mobile) communication system took time to evolve to where it is today, changed drastically since Guglielmo Marconi first demonstrated radio's ability to provide continuous contact with ships sailing the English channel. Nowadays, in a world of high mobility, transmission system speed and capacity are essential components to maintain communication and connectivity among remote people all around the world. The early digital communication systems were based on single carrier modulation. Generally, by reducing the symbol duration, we can increase the bit rate of a transmission system. However, the presence of a multipath channel introduces intersymbol interference (ISI) requiring complex equalization. Multicarrier modulation (MCM) is a good alternative in order to counteract the multipath fading effects. In multicarrier communications the data is transmitted over many frequencies instead of a single carrier, dividing the wideband frequency selective communication channel into several subbands with mildly selective fading. The subcarriers are generally selected to be orthogonal, in such a way that their spectra overlap but without causing interference to the other subcarriers. The bandwidth of each subchannel is smaller than coherence bandwidth of the propagation channel. It means, the maximum delay spread of the channel is much lower than the

symbol duration. Consequently, each subchannel experiences a flat fading and the ISI in each subchannel becomes very small.

Till date, Orthogonal Frequency Division Multiplexing (OFDM) is the most widespread MCM scheme. Nevertheless, OFDM suffers from loss of spectral efficiency due to cyclic prefix insertion. Moreover, it is highly sensitive to residual frequency and timing offsets that can be generated by a defective synchronization as well as the Doppler effect [1, 2]. The use of a rectangular impulse response in OFDM causes large sidelobes at each subcarrier. Thus, the subchannels at the edge of the transmission bandwidth could be a source of interference for other neighboring systems [33]. The severity of high peak-to-average power ratio (PAPR) in OFDM can be seen from the 3rd generation partnership project (3GPP) specification for 4th generation (4G) long term evolution (LTE); where in the physical layer uplink (UL), the single carrier-frequency division multiple access (SC-FDMA) has been chosen instead of OFDM, owing to the high PAPR of the later. These drawbacks have motivated researchers to develop alternative solutions and some enhanced physical layers based on filter bank processing, have been proposed. Filter-bank based multi-carrier (FBMC) have a long history in telecommunication research. FBMC uses a frequency well-localized pulse shaping for each subcarrier, which reduces significantly the (OOB) out-of-band leakage, thus a higher number of subcarriers can be used within the allocated frequency band. There are mainly three FBMC techniques that have been studied in the literature: filtered multitone (FMT) [34–36], offset quadrature amplitude modulation (QAM) [3] (also called staggered multitone (SMT) [37]), and cosine modulated multitone (CMT) [38, 39]. This dissertation focuses on the Saltzberg’s scheme [3] called FBMC-OQAM (also called FBMC/OQAM, OFDM/OQAM or SMT). An efficient discrete Fourier transform (DFT) implementation of this modulation method has been proposed by Hirosaki [40]. Fig. 1.1 shows the frequency response comparison between OFDM and FBMC-OQAM system comprising of prototype filter designed by Bellanger [41]. Saltzberg showed, in [3], that by introducing a shift of half the symbol period between the in-phase and quadrature components of QAM symbols, it is possible to achieve a baud-rate spacing between adjacent subcarrier channels and still recover the information symbols free of ISI and intercarrier interference (ICI). Thus, each subcarrier is modulated with an offset QAM (OQAM) and the orthogonality conditions are considered only to the real field [7]. Indeed, the data at the receiver side is carried only by the real (or imaginary) components of the signal, and the imaginary (or real) parts appear as interference terms.

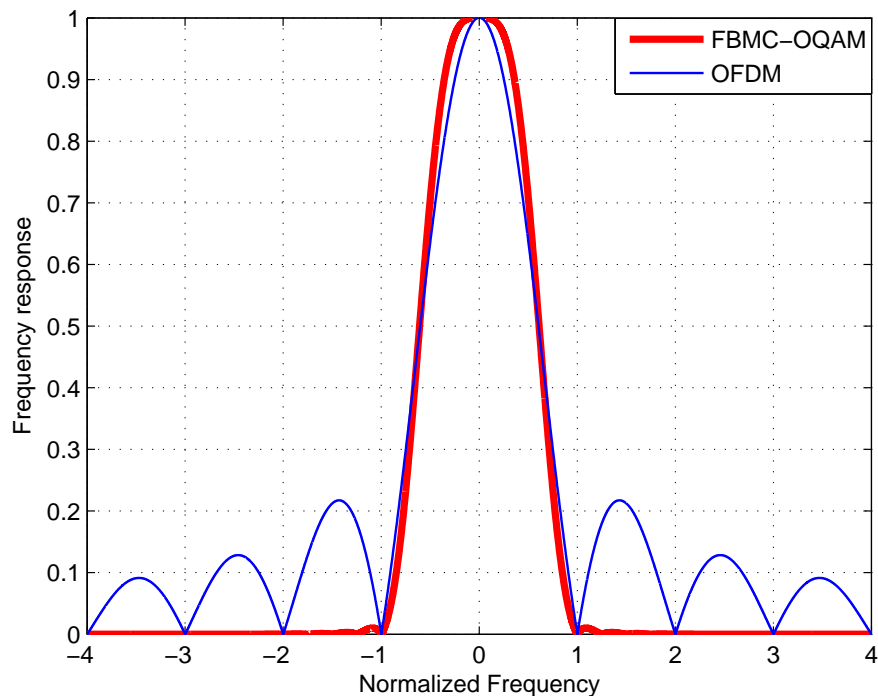


FIGURE 1.1: Illustration of frequency responses of OFDM and FBMC-OQAM.

Nowadays, energy crisis and global warming problems are hanging over everyone's head, urging much research work on energy saving. It is coming to a consensus that the information and communication technologies (ICT) industry has emerged as one of the major contributors to the CO₂ emission and world power consumption. According to the International Telecommunications Union (ITU), carbon emission related to ICT is about 2% of the worldwide emissions, which is comparable to the emissions by all commercial airplanes or one quarter of the emissions by all vehicles around the world. But, telecommunications usage is expected to expand rapidly over the coming decade; especially in developing countries. If nothing is done, the ICT contribution to global greenhouse gas emissions is projected to nearly double, i.e. about 4% by 2020. Putting an increasing emphasis on green communications, one of the main agendas of the ITU by 2020, is to cut short the carbon emissions per device by 30% [4].

Also, energy consumption has become a key challenge in the last few years. According to several studies [4, 5], the ICT sector alone is responsible of a percentage which varies widely from 2% to 10% of the worldwide energy consumption and several projects, both from industries and universities, are trying to reduce the power consumption of electronic devices. The power consumption helps to define the battery life for mobile

communications systems [42].

Power amplifiers are one of the most expensive and most power-consuming devices in the communication systems. Power amplifier (PA) represents more than 60% of the total power consumption at transmitter [6]. Thus, it is imperative to improve the amplifier efficiency for reducing the energy consumption in the communication systems. For this purpose, the contemporary modern communication systems need to operate PA at near saturation level. Unfortunately, PA is an analog component and is inherently non-linear (NL). So, it is important to opt for techniques to diminish the NL effects. These techniques are broadly classified into two categories. The former one aim at PAPR reduction and the later one tries to linearize the PA.

Being a MCM technique, FBMC-OQAM suffer from high PAPR and the reduction of this remains to be one of the most crucial issues that need to be solved effectively with a reasonable complexity. The main objective of this thesis is to analyze the impact of PA non-linearities on FBMC-OQAM systems and propose mitigating techniques in this regard, with a prime focus on PAPR reduction.

1.2 Project EMPHATIC

This thesis is part of the European FP7 project EMPHATIC (Enhanced Multicarrier Techniques for Professional Ad-Hoc and Cell-Based Communications, <http://www.ict-emphatic.eu/>) including various European universities and two main industrial partners: THALES Communications Security and CASSIDIAN. The EMPHATIC objective is to develop, evaluate and demonstrate the capability of enhanced multicarrier techniques to make better use of the existing radio frequency bands in providing broadband data services in coexistence with narrowband legacy services.

1.3 Thesis objectives

In this dissertation, the impact of PA non-linearities on the performance of FBMC-OQAM systems, especially in OOB, is studied and the mitigation techniques are addressed with novel proposals. As a matter of fact, we would like to:

- Predict the spectral regrowth in non-linearly amplified FBMC-OQAM systems using cumulant analysis.
- Propose novel PAPR reduction techniques suited for FBMC-OQAM systems and study their computational complexities.
- Investigate the co-existence capabilities of a FBMC-OQAM system working on non-linear devices.
- Propose novel PA linearization techniques for FBMC-OQAM systems.

1.4 Thesis outline

The thesis dissertation is written as follows: **Chapter 1** is the current chapter, presenting the background motivation, thesis objective along with outline.

Chapter 2, is devoted to introduce the background and the state of the art related to the different concepts to be used throughout this thesis. A very brief overview of OFDM system is provided. Then, the fundamental theory of FBMC-OQAM system is given with much emphasis on transmitter side. In that aspects such as the OQAM mapping, polyphase filtering, discrete-time representation, FBMC-OQAM modulation as matrix operation, prototype filtering, orthogonality and overlapping nature have been discussed. Non-linear aspects of PAs are studied in terms of analytical representation and conversion characteristics. Then, some memoryless models are presented. Finally, the need for mitigation of non-linear PA effects is pondered and the prevailing methods to achieve that has been discussed.

Chapter 3 deals with spectral regrowth prediction for FBMC-OQAM systems using cumulant analysis. A brief introduction of cumulants is given and the aspect of spectral prediction by cumulants is presented. Some characteristic properties of cumulants has been displayed. How a polynomial model of the PA is achieved by polynomial fitting of its conversion characteristics, is shown. Then, the usage of cumulants as a tool to derive closed-form expression for the auto-covariance function of PA output in terms of auto-covariance function of its input is putforward. Simulation results are presented to show the efficiency of using the cumulants for spectral regrowth prediction.

In **Chapter 4**, different PAPR reduction techniques suggested for OFDM are discussed. Then, a state-of-art of PAPR reduction techniques for FBMC-OQAM is presented. FBMC-OQAM by virtue of having an overlapping signal structure cannot afford to have the conventional PAPR reduction schemes that have been effectively applied for OFDM systems. How this impacts the PAPR reduction in FBMC-OQAM systems, is clearly presented with theory and results. In this chapter, we propose three novel PAPR reduction techniques suited for FBMC-OQAM. The aspects of symbol-by-symbol approach and trellis-based approach are discussed. Also, their computational complexities have been derived, which can be extended to any probabilistic schemes. While, two techniques are probabilistic ones and the last one is an adding signal technique.

In **Chapter 5**, the co-existence capabilities of FBMC-OQAM system with Professional Mobile Radio system is analyzed taking into account the implications of PA non-linearities. It is a fact that in the recent literature, the suggestion that LTE-like FBMC-OQAM system working on linear devices can coexist in PMR band, while conventional OFDM-based LTE system fails; is recalled. The need to take into account the RF impairments in radio communication systems, such as the non-linear nature of PAs and how they add severe hindrance in the coexistence aspect is elaborately presented. Also, in this chapter, we address this issue and show that LTE-like FBMC-OQAM system working on non-linear devices can still coexist with PMR systems. However, keeping in mind energy efficiency, the need for PAPR reduction and PA linearization is highlighted. The analysis in this chapter has inculcated interest on the issue of PA linearization and the same is dealt in the succeeding Chapter 6.

Chapter 6 studies the PA linearization aspects. Different classes of PA linearization techniques that have been suggested for OFDM has been discussed, with much focus on digital predistortion. Then, a state-of-art of PA linearization techniques for FBMC-OQAM is presented. Similar to that of PAPR reduction, even in predistortion, the need to take into account the overlapping nature of FBMC-OQAM is putforward. The feasibility to view the predistortion as an adding signal technique has been presented. In this chapter, we propose a novel DPD technique suited for FBMC-OQAM. Apart from displaying the capabilities of this linearization techniques, we demonstrate that PAPR reduction before linearization shows tremendous impact on the energy efficiency and

diminishing the OOB spectral regrowth. An abstract idea has been pondered that both PAPR reduction and PA linearization can be combined by an adding signal operation which yields to joint optimization. It means both of these can be done at one stretch by adding a signal, which not only reduces PAPR but also linearizes the PA.

Chapter 7 draws the final conclusions by highlighting the main contributions of this dissertation. Possible future research are provided at the end.

1.5 Publications

Some publications have resulted from work contained in or related to this thesis. Below is a comprehensive list of this work:

Journals

[J1]. **K. C. Bulusu**, M. Renfors, J. Yli-Kaakinen, H. Shaiek, and D. Roviras, “Enhanced Multicarrier Techniques for Narrowband and Broadband PMR Systems,” *Wiley Transactions on Emerging Telecommunications Technologies*, May 2016.

[J2]. **K. C. Bulusu**, H. Shaiek, and D. Roviras, “Reducing the PAPR in FBMC-OQAM Signals by Trellis-based SLM Technique,” *Eurasip Journal on Advances in Signal Processing* (Submitted).

Conferences

[C1]. **K. C. Bulusu**, H. Shaiek, and D. Roviras, “Impact of HPA Non-linearity on Coexistence of FBMC-OQAM Systems with PMR/PPDR Systems,” *IEEE Vehicular Technologies Conference*, May 2016.

[C2]. **K. C. Bulusu**, H. Shaiek, and D. Roviras, “Reduction of PAPR of FBMC-OQAM Signals by Dispersive Tone Reservation Technique,” *12th IEEE International Symposium on Wireless Communication Systems*, Aug. 2015.

[C3]. **K. C. Bulusu**, H. Shaiek, and D. Roviras, “Potency of Trellis-based SLM over

symbol-by-symbol approach in reducing PAPR for FBMC-OQAM Signals,” *IEEE International Conference on Communications*, Jun. 2015.

[C4]. **K. C. Bulusu**, H. Shaiek, and D. Roviras, “Prediction of Spectral Regrowth for FBMC-OQAM system using Cumulants,” *IEEE International Conference on Wireless and Mobile Computing, Networking and Communications*, pp. 402-406, Oct. 2014.

[C5]. **K. C. Bulusu**, H. Shaiek, D. Roviras, and R. Zayani, “PAPR Reduction for FBMC-OQAM Systems using Dispersive SLM Technique,” *11th IEEE International Symposium on Wireless Communication Systems*, pp. 568-572, Aug. 2014.

Book Chapters

[B1]. **K. C. Bulusu**, H. Shaiek, D. Roviras et al, *Chapter.5 in Orthogonal waveforms and filter banks for future communication systems*,” Elsevier/Academic Press, 2016 (In progress).

Technical reports

[T1]. **K. C. Bulusu**, H. Shaiek, D. Roviras et al, “Reduction of PAPR and non linearities effects,” *Technical contribution report in the deliverable D3.3 - European ICT- 318362 EMPhAtiC FP7 project*, pages 110, 2014.

[T2]. **K. C. Bulusu**, H. Shaiek, D. Roviras et al, “Energy-efficient power controls and interference mitigation (first issue),” *Technical contribution report in the deliverable D2.1 - French ANR-14-CE28-0026-02 ACCENT5 project*, 2015.

Chapter 2

FBMC-OQAM systems and power amplifiers

2.1 Introduction

FBMC-OQAM is seen as an interesting alternative to OFDM, for 5th generation (5G) radio access technology (RAT). The exponential increase in data traffic in coming years prompts design of a new 5G RAT with an aim to achieve 10 Gbps upper data rate and sub-ms latency [43]. FBMC-OQAM is an attractive candidate to become 5G radio waveform. It has many attractive features such as, excellent frequency localization, a power spectral density (PSD) with very low side lobes and improved robustness to carrier frequency offsets. In fact, FBMC-OQAM can deal with the channel frequency selectivity without any guard interval requirement. Armed with these properties, FBMC-OQAM seems to be more suitable candidate as the radio waveform for 5G RAT than OFDM, especially for asynchronous devices [44]. This chapter introduces the background and the state of the art related to the different concepts to be used throughout this thesis.

This chapter is organized as follows: The section 2.2 gives very brief overview of OFDM system. In section 2.3, the fundamental theory of FBMC-OQAM system is presented; where, some concepts such as OQAM mapping, polyphase filtering, discrete-time and

matrix representation, prototype filter design, real-domain orthogonality and signal structure are dealt with. Later in section 2.4, the PA non-linearities are discussed in terms of conversion characteristics and memoryless behavioral models. Finally, section 2.5 highlights the need to mitigate the NL effects of PA by PAPR reduction and PA linearization. Section 2.6 concludes this chapter.

2.2 Brief overview of OFDM system

The OFDM is the most widespread modulation among all the multicarrier modulations. In general, the idea of MCM is to divide the transmitted bit stream into different sub-streams and send them, after mapping, over different orthogonal subchannels centered at different subcarrier frequencies f_k , with $k = 0, 1, \dots, N - 1$. The number N of sub-streams is chosen sufficiently large to insure that each subchannel has a bandwidth less than the coherence bandwidth of the channel. Fig. 2.1 illustrates a multicarrier transmitter. The transmitter and receiver of the classical OFDM systems are constituted of

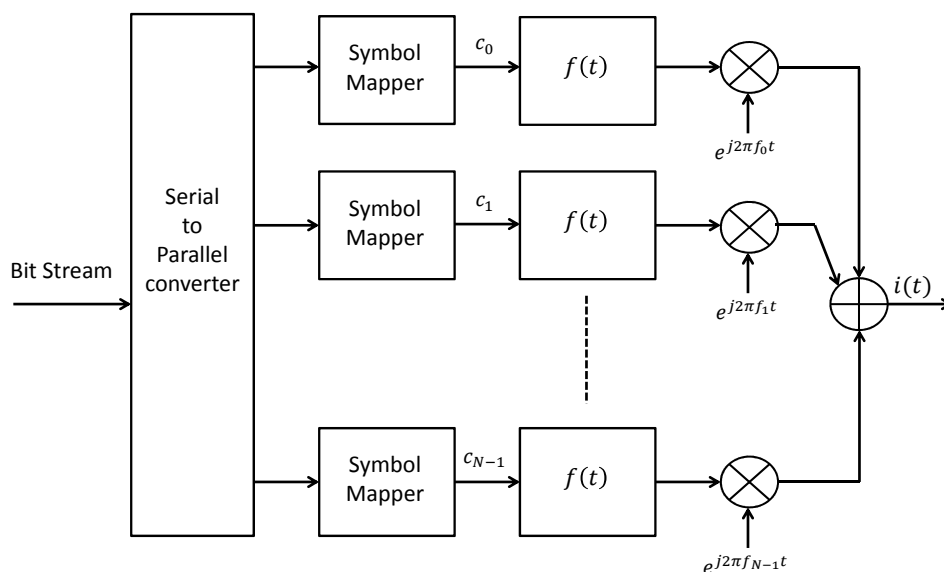


FIGURE 2.1: Multicarrier transmitter.

inverse fast Fourier transform (IFFT) and fast Fourier transform (FFT) respectively. Therefore, OFDM is based on overlapping sinc function type subcarrier spectra, where the adjacent subcarriers are at the nulls of the sinc function. The constellation symbols

are mapped with N sub-carriers and the modulated signal can be represented in time domain as,

$$i(t) = \sum_{m=-\infty}^{+\infty} \sum_{n=0}^{N-1} c_{m,n} f(t - mT) e^{j\frac{2\pi}{T} n(t - mT)} \quad (2.1)$$

where

- T is the OFDM symbol time period,
- $c_{m,n}$ is the transmitted complex-valued symbol on n^{th} sub-carrier at instant mT ,
- $f(t)$ is a rectangular time window.

The PSD of a single sub-carrier OFDM signal is given below,

$$\Phi_{OFDM}(f) = T \left(\frac{\sin(\pi f T)}{\pi f T} \right)^2 \quad (2.2)$$

Most of the advantages of OFDM arise from the use of the IFFT block, easing the signal generation, receiver signal separation, channel equalization and ability to cope with severe channel conditions, by adding a cyclic prefix (CP). If Δ is the duration of CP, then the CP-OFDM data symbols are transmitted every $T_{ofdm} = T + \Delta$. These symbols are uniformly spread along the frequency axis at the spacing $F = 1/T$. The symbol density of a CP-OFDM system is

$$\frac{1}{T_{ofdm} F} = \frac{T}{T + \Delta} \leq 1 \quad (2.3)$$

Since, we always need a cyclic prefix to avoid the interference in the presence of a frequency selective propagation channel, the CP-OFDM can only achieve a symbol density lower than one. Nevertheless, OFDM suffers from spectral efficiency loss (due to CP), sensitivity to Doppler shift and frequency synchronization problems, and susceptibility to power amplifier characteristics.

2.3 Introduction to a FBMC-OQAM system

Usage of a filter-bank is a computationally efficient way to implement a large number of filters that are well localized in time and frequency, in order to separate the sub-channels. According to polyphase decomposition theory, a filter-bank can be implemented through

the filters' poly-phase decomposition associated with the FFT. A FBMC MCM system can be described by a synthesis-analysis filter bank i.e. a trans-multiplexer. The synthesis filter-bank (SFB) is composed of all the parallel transmit filters known as poly-phase network (PPN), which is the set of the so-called prototype filters, with the IFFT to divide the bandwidth in N sub-channels for transmission. The inverse operation in reversed order is realized in the receiver by the analysis filter-bank (AFB) consisting of all the matched receive filters, to recover the transmitted data. So, SFB and AFB implement the systems' modulator and the demodulator, respectively.

Albeit, the usage of these efficient filters to separate the sub-channels, instead of the rectangular window, imposes the use of a real modulation to maintain the orthogonality between sub-carriers, since the trans-multiplexer impulse response is non-unitary due to interference from the neighboring sub-channels and time instants. Thus, the FBMC system has to transmit a real symbol every half OFDM symbol duration, yielding to the so-called FBMC-OQAM system.

Efficient digital implementation of the FBMC-OQAM system through polyphase structures and DFT was first introduced by Bellanger [45] and later studied by Hirosaki [40]. The implementation of FBMC-OQAM transmitter and receiver systems over N subcarriers, has been shown in Fig. 2.2 and Fig. 2.3. Assuming $H(Z)$ is the transfer function of the discrete-time impulse response of prototype filter $h[k]$, using polyphase decomposition, we have

$$\begin{aligned} H(Z) &= \sum_{k=0}^{LN-1} h[k]Z^{-k} \\ &= \sum_{m=0}^{N-1} H_m(Z^N)Z^{-m} \end{aligned} \quad (2.4)$$

where

$$H_m(Z^N) = \sum_{l=0}^{L-1} h_{lN+m}Z^{-lN} \quad (2.5)$$

where L denotes the oversampling factor.

Let us consider that we need to transmit $M \times N$ complex input symbols in a FBMC-OQAM system over N tones. We denote the real and imaginary parts of the m^{th} symbol over n^{th} tone as R_m^n and I_m^n respectively. These complex symbols can be written as

$$X_{m,n} = R_m^n + j.I_m^n, \quad 0 \leq n \leq N-1, \quad 0 \leq m \leq M-1 \quad (2.6)$$

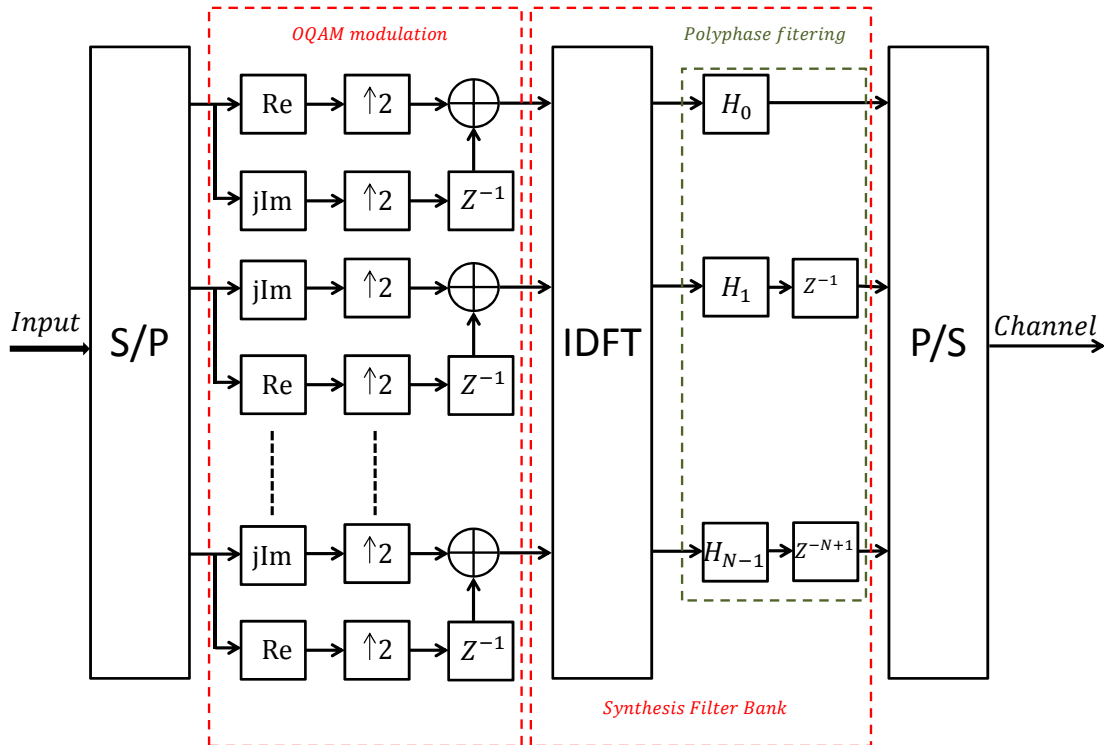


FIGURE 2.2: FBMC-OQAM transmitter.

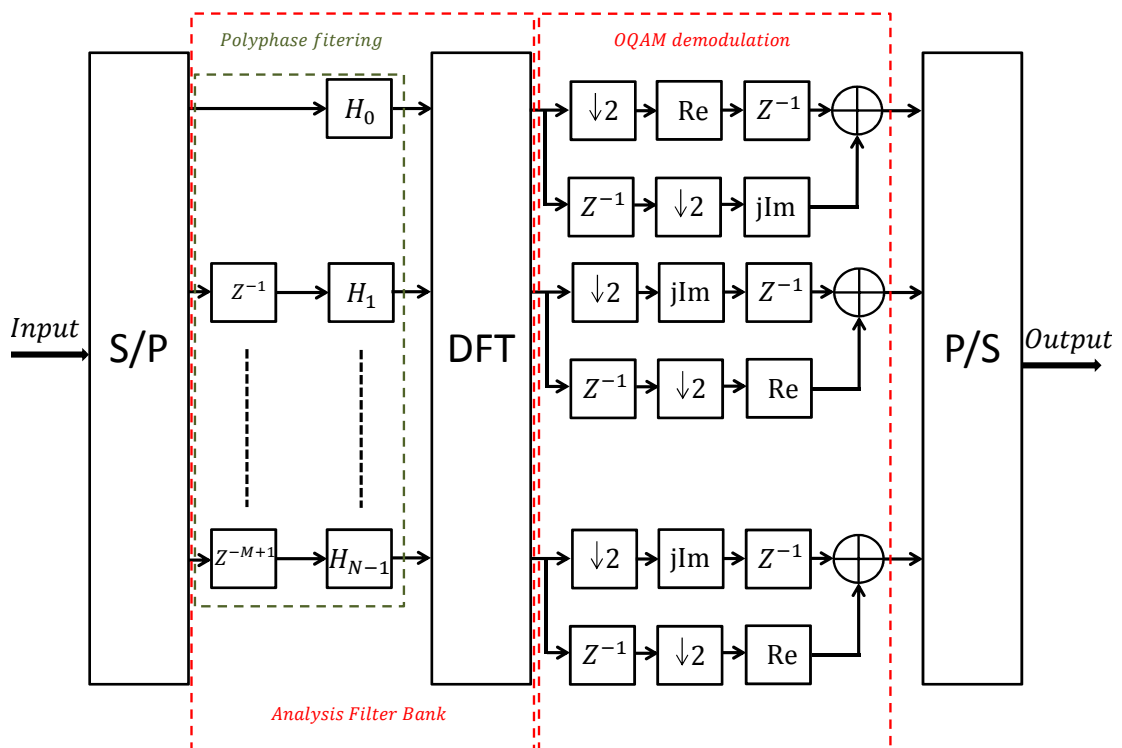


FIGURE 2.3: FBMC-OQAM receiver.

In a FBMC-OQAM system, we transmit real symbols at interval $\frac{T}{2}$, where T is the symbol period [7]. The m^{th} input symbol vector, which is a collection of N complex input symbols can be written as

$$\mathbf{X}_m = (X_{m,0}, X_{m,1}, \dots, X_{m,N-1})^T, \quad 0 \leq m \leq M-1 \quad (2.7)$$

where, $(\cdot)^T$ is the transpose operator.

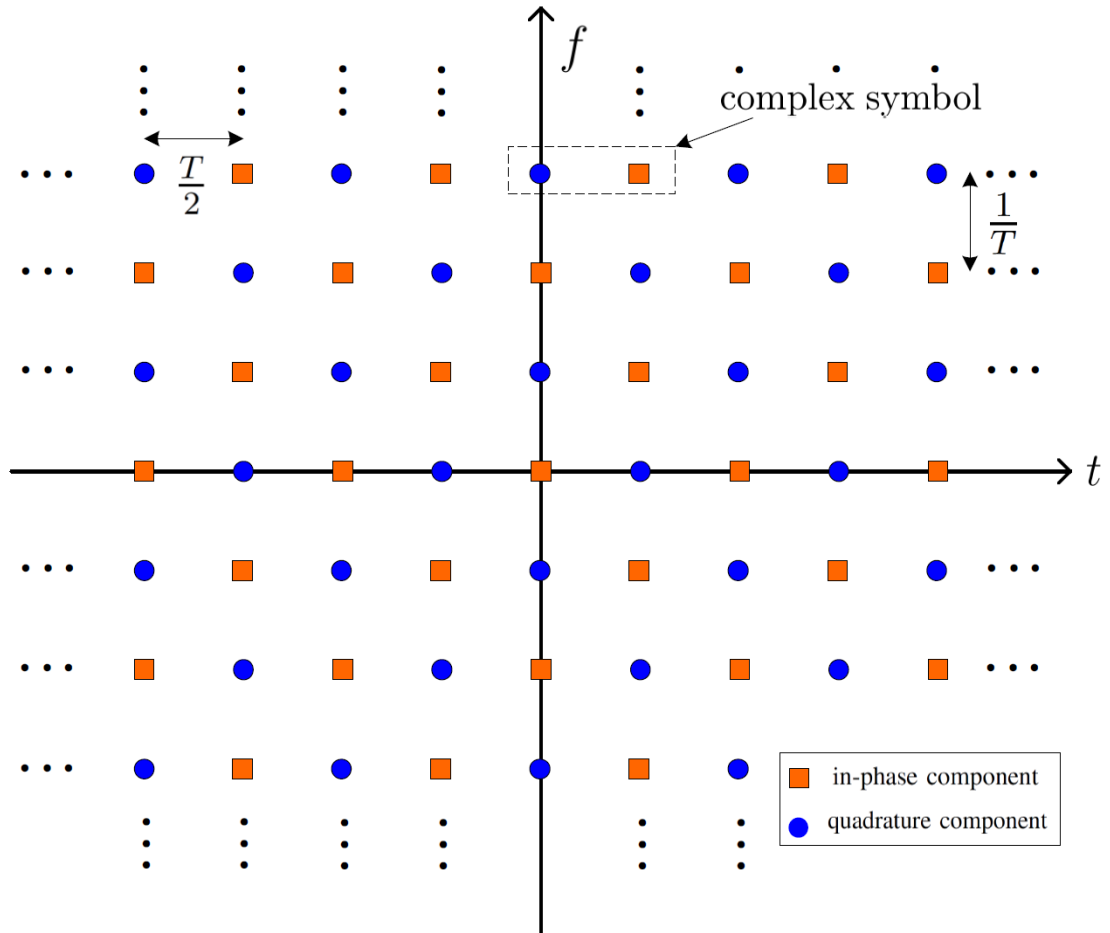


FIGURE 2.4: Time-frequency phase-space lattice representation of a FBMC-OQAM system.

2.3.1 OQAM mapping

In [3], Saltzberg showed that with the introduction of a shift of half the symbol period between the in-phase and quadrature components of QAM symbols, it is possible to achieve a baud-rate spacing between adjacent subcarrier channels and still recover

the information symbols free of ISI and ICI. So, each subcarrier is modulated with an OQAM and the orthogonality conditions are considered only in the real field [7].

In OQAM mapping, in order to keep adjacent carriers orthogonal, real and pure imaginary values alternate on successive carrier frequencies and on successive transmitted symbols for a given carrier at the transmitter side. The time-frequency phase-space lattice is a very useful tool that can be used to compare the different multi-carrier schemes [46]. A lattice is defined by the symbol period and the sub-carrier spacing of the system and the same associated with FBMC-OQAM system is illustrated in Fig. 2.4. For $0 \leq m' \leq 2M - 1$, the OQAM mapping of the complex input symbol vectors $\{\mathbf{X}_m\}_{m=0}^{M-1}$ into real symbol $\{a_{m',n}\}_{m'=0}^{2M-1}$ is done as shown below

$$\begin{aligned}
 a_{m',n} &= \begin{cases} R_{\lfloor \frac{m'}{2} \rfloor}^n & m' \text{ is even, } n \text{ is even} \\ I_{\lfloor \frac{m'}{2} \rfloor}^n & m' \text{ is odd, } n \text{ is even} \\ I_{\lfloor \frac{m'}{2} \rfloor}^n & m' \text{ is even, } n \text{ is odd} \\ R_{\lfloor \frac{m'}{2} \rfloor}^n & m' \text{ is odd, } n \text{ is odd} \end{cases} \quad (2.8) \\
 &= \begin{cases} (1 - \delta) \cdot R_{\lfloor \frac{m'}{2} \rfloor}^n + j\delta \cdot I_{\lfloor \frac{m'}{2} \rfloor}^n & m' \text{ is even} \\ \delta \cdot R_{\lfloor \frac{m'}{2} \rfloor}^n + (1 - \delta) \cdot I_{\lfloor \frac{m'}{2} \rfloor}^n & m' \text{ is odd} \end{cases} \\
 &= [(1 - \theta)(1 - \delta) + \theta\delta] \cdot R_{\lfloor \frac{m'}{2} \rfloor}^n + [(1 - \theta)\delta + \theta(1 - \delta)] \cdot I_{\lfloor \frac{m'}{2} \rfloor}^n
 \end{aligned}$$

where, $\theta = m'$ modulo 2 and $\delta = n$ modulo 2. e.g. $a_{0,0} = R_0^0, a_{0,1} = I_0^1, a_{1,0} = I_0^0$ and $a_{1,1} = R_0^1$. To avail maximize spectral efficiency of the OQAM modulation, the symbol period T is halved. Thus, the data at the receiver side, carries the real (or imaginary) components of the signal, and the imaginary (or real) parts appear as interference terms. For two successive subcarrier, the time-offset of $\frac{T}{2}$ is introduced onto the real part for the first one and onto the imaginary part for the second one, so that N has to be even. The mathematical implication of this staggering rule in [38] with a phase term $\varphi_{m',n}$ defined as

$$\varphi_{m',n} = \begin{cases} 0 & m' + n \text{ is even} \\ \frac{\pi}{2} & m' + n \text{ is odd} \end{cases} \quad (2.9)$$

2.3.2 Poly-phase filtering

After this OQAM mapping, the real symbols undergo poly-phase filtering that involves IFFT transformations along with filtering by a SFB. We denote the prototype filter impulse response as $h(t)$ and its length depends on its filter overlapping factor K , which is KT . The obtained continuous-time base-band FBMC-OQAM signal $x(t)$ can be written as [47]

$$x(t) = \mathcal{G}\{\{\mathbf{X}_m\}_{m=0}^{M-1}\} \quad (2.10)$$

$$= \mathcal{G}\{\mathbf{X}_0, \mathbf{X}_1, \dots, \mathbf{X}_{M-1}\} \quad (2.11)$$

$$= \sum_{m'=0}^{2M-1} \sum_{n=0}^{N-1} a_{m',n} h(t - m'T/2) e^{j\frac{2\pi}{T}nt} e^{j\varphi_{m',n}} \quad (2.12)$$

where

- $x(t) \neq 0$ from $t = [0, (M - \frac{1}{2})T + KT)$,
- $\mathcal{G}\{\cdot\}$ is the FBMC-OQAM modulation function.

Let $x_m(t)$ be the m^{th} FBMC-OQAM symbol that is obtained after the modulation of the corresponding m^{th} input symbol vector \mathbf{X}_m .

$$x_m(t) = \mathcal{G}\{\mathbf{X}_m\} \quad (2.13)$$

Then, the continuous-time signal for all the M input signal vectors at the FBMC-OQAM transmitter output can also be written as

$$x(t) = \sum_{m=0}^{M-1} x_m(t - mT), 0 \leq t < \infty \quad (2.14)$$

2.3.3 Discrete-time representation

A discrete-time base-band FBMC-OQAM signal $x[k]$ oversampled by L times, can be written as

$$x[k] = \mathcal{G}\{\widehat{\mathbf{X}}_0, \widehat{\mathbf{X}}_1, \dots, \widehat{\mathbf{X}}_{M-1}\} \quad (2.15)$$

$$= \sum_{m'=0}^{2M-1} \sum_{n=0}^{N-1} a_{m',n} h[k - m' \frac{LN}{2}] e^{j \frac{2\pi}{LN} nk} e^{j \varphi_{m',n}} \quad (2.16)$$

$$= \sum_{m=0}^{M-1} x_m[k - mLN] \quad (2.17)$$

where, $x[k] \neq 0$ from $0 \leq k \leq (M + K - 0.5)LN - 1$ and $\widehat{\mathbf{X}}_m$, for $0 \leq m \leq M - 1$, is the oversampled input symbol vector that is obtained by inserting $(L - 1) \times N$ zeros in the middle of the \mathbf{X}_m as

$$\widehat{\mathbf{X}}_m = (X_{m,0}, \dots, X_{m, \frac{N}{2}-1}, \underbrace{0, \dots, 0}_{(L-1) \times N}, X_{m, \frac{N}{2}}, \dots, X_{m, N-1})^T \quad (2.18)$$

Also, $x_m[k]$ is the oversampled m^{th} FBMC-OQAM symbol in discrete-time that is obtained after the modulation of the corresponding oversampled input symbol vector $\widehat{\mathbf{X}}_m$.

$$x_m[k] = \mathcal{G}\{\widehat{\mathbf{X}}_m\} \quad (2.19)$$

2.3.4 FBMC-OQAM modulation as matrix operation

For the purpose of ease, we define four matrices, namely, prototype filter matrix \mathcal{H} , scaled IDFT matrix \mathcal{Q} , OQAM mapping matrix \mathcal{M} and zero matrix $\mathcal{Z}_{p,q}$ as shown below. The zero matrix or null matrix $\mathcal{Z}_{(p,q)}$ is a matrix of order $p \times q$, with all its entries being zero, for p, q being natural numbers. Some examples of zero matrices are

$$\mathcal{Z}_{(1,1)} = [0], \quad \mathcal{Z}_{(2,1)} = \begin{bmatrix} 0 \\ 0 \end{bmatrix}, \quad \mathcal{Z}_{(2,2)} = \begin{bmatrix} 0 & 0 \\ 0 & 0 \end{bmatrix}, \quad \mathcal{Z}_{(2,3)} = \begin{bmatrix} 0 & 0 & 0 \\ 0 & 0 & 0 \end{bmatrix} \quad (2.20)$$

The mapping matrix \mathcal{M} is square diagonal matrix of order $LN \times LN$ given by

$$\begin{aligned} \mathcal{M} &= \text{diag}\{1, -1, 1, -1, \dots, 1, -1\} \\ &= \begin{bmatrix} 1 & 0 & \dots & 0 & 0 \\ 0 & -1 & \dots & 0 & 0 \\ \vdots & \vdots & \ddots & \vdots & \vdots \\ 0 & 0 & \dots & 1 & 0 \\ 0 & 0 & \dots & 0 & -1 \end{bmatrix}_{LN \times LN} \end{aligned} \quad (2.21)$$

We recall that a $LN \times LN$ order IDFT matrix \mathcal{Q}_{LN} is defined as

$$\begin{aligned} \mathcal{Q}_{LN} &= \frac{1}{\sqrt{LN}} e^{j \frac{2\pi}{LN} p \cdot q} \quad 0 \leq p, q \leq LN - 1 \\ &= \frac{1}{\sqrt{LN}} \begin{bmatrix} 1 & 1 & \dots & 1 \\ 1 & e^{j \frac{2\pi}{LN}} & \dots & e^{j \frac{2\pi}{LN}(LN-1)} \\ 1 & e^{j \frac{2\pi}{LN} 2} & \dots & e^{j \frac{2\pi}{LN} 2(LN-1)} \\ \vdots & \vdots & \ddots & \vdots \\ 1 & e^{j \frac{2\pi}{LN} p} & \dots & e^{j \frac{2\pi}{LN} p(LN-1)} \\ \vdots & \vdots & \ddots & \vdots \\ 1 & 0 & \dots & 1 \\ 1 & e^{j \frac{2\pi}{LN}(LN-1)} & \dots & e^{j \frac{2\pi}{LN}(LN-1)(LN-1)} \end{bmatrix}_{LN \times LN} \end{aligned} \quad (2.22)$$

Note that the normalization factor in front of the sum ($\frac{1}{\sqrt{LN}}$) is merely a convention and differ in some treatments. However, the ($\frac{1}{\sqrt{LN}}$) choice here makes the resulting IDFT matrix unitary, which is convenient in many circumstances. Some examples of IDFT matrices are

$$\mathcal{Q}_1 = [1], \quad \mathcal{Q}_2 = \frac{1}{\sqrt{2}} \begin{bmatrix} 1 & 1 \\ 1 & -1 \end{bmatrix}, \quad \mathcal{Q}_4 = \frac{1}{2} \begin{bmatrix} 1 & 1 & 1 & 1 \\ 1 & j & -1 & -j \\ 1 & -1 & 1 & -1 \\ 1 & -j & -1 & j \end{bmatrix} \quad (2.23)$$

Then, the scaled IDFT matrix \mathcal{Q} is nothing but a order IDFT matrix \mathcal{Q}_{LN} , that is scaled by \sqrt{LN} and its order is $LN \times LN$. That is

$$\mathcal{Q} = \sqrt{LN} \mathcal{Q}_{LN} \quad (2.24)$$

The prototype filter matrix \mathcal{H} is a rectangular matrix of order $KLN \times LN$ that is defined by

$$\mathcal{H} = \begin{bmatrix} h_1 & 0 & \dots & 0 \\ 0 & h_2 & \dots & 0 \\ \vdots & \vdots & \ddots & \vdots \\ 0 & 0 & \dots & h_{LN} \\ h_{LN+1} & 0 & \dots & 0 \\ 0 & h_{LN+2} & \dots & 0 \\ \vdots & \vdots & \ddots & \vdots \\ 0 & 0 & \dots & h_{2LN} \\ \vdots & \vdots & \ddots & \vdots \\ h_{(K-1)LN+1} & 0 & \dots & 0 \\ 0 & h_{(K-1)LN+2} & \dots & 0 \\ \vdots & \vdots & \ddots & \vdots \\ 0 & 0 & \dots & h_{KLN} \end{bmatrix}_{KLN \times LN} \quad (2.25)$$

In equation (2.25), h_i , for $1 \leq i \leq KLN$ represents the samples of the prototype impulse response with a oversampling factor of L .

We recall that the input symbol vector \mathbf{X}_m can be seen as a column matrix of order $N \times 1$. Thus, the oversampled input symbol vector $\widehat{\mathbf{X}}_m$ is a column matrix of order $LN \times 1$. The OQAM mapping of $\widehat{\mathbf{X}}_m$ can be seen as a matrix operation, which results in two matrices \mathcal{X}_e and \mathcal{X}_o , namely, the even and odd input matrices as given below

$$\mathcal{X}_e = \frac{1}{2}(\widehat{\mathbf{X}}_m + \mathcal{M}\widehat{\mathbf{X}}_m^*) \quad (2.26)$$

$$\mathcal{X}_o = \frac{1}{2}(\widehat{\mathbf{X}}_m - \mathcal{M}\widehat{\mathbf{X}}_m^*) \quad (2.27)$$

where, $\widehat{\mathbf{X}}_m^*$ is the complex conjugate of $\widehat{\mathbf{X}}_m$ and the \mathcal{X}_e , \mathcal{X}_o are column matrices of order $LN \times 1$. Then, the polyphase filtering operation can be represented as shown below

$$x_e = \mathcal{H}\mathcal{Q}\mathcal{X}_e \quad (2.28)$$

$$x_o = \mathcal{H}\mathcal{Q}\mathcal{X}_o \quad (2.29)$$

where, x_e , x_o are even and odd FBMC-OQAM data frames that are column matrices of order $KLN \times 1$. Finally, the $x_m[k]$ in equation (2.17) can be represented as column matrix x_m of order $(K + 0.5)LN \times 1$, which is nothing but a time-staggered addition of x_e and x_o by $\frac{LN}{2}$, which is shown below

$$x_m = \left[x_e \parallel \mathcal{Z}_{\left(\frac{LN}{2}, 1\right)} \right] + \left[\mathcal{Z}_{\left(\frac{LN}{2}, 1\right)} \parallel x_o \right] \quad (2.30)$$

where, \parallel is the matrix concatenation. The equation (2.30) can also be written as below

$$x_m = \frac{1}{2} \begin{bmatrix} \mathcal{H} & \mathcal{Z}_H \\ \mathcal{Z}_H & \mathcal{H} \end{bmatrix} \cdot \begin{bmatrix} \mathcal{Q} & \mathcal{Z}_Q \\ \mathcal{Z}_Q & \mathcal{Q} \end{bmatrix} \cdot \begin{bmatrix} X_e \\ X_e \end{bmatrix} \quad (2.31)$$

where, the zero matrices $\mathcal{Z}_H = \mathcal{Z}_{\left(\frac{LN}{2}, LN\right)}$ and $\mathcal{Z}_Q = \mathcal{Z}_{(LN, LN)}$.

2.3.5 Prototype filter

In the literature, various prototype filters are designed for their corresponding applications. The study of prototype functions and filters is of a particular interest for FBMC-OQAM, because it represents an important degree of freedom w.r.t. OFDM [48]. Excellent frequency localization is the most characteristic property of FBMC-OQAM systems. To have more localized sub-carriers, FBMC-OQAM waveforms utilize a more advanced prototype filter design. The prototype filters that is more often used in this thesis is PHYDYAS filter. Nevertheless, Isotropic orthogonal transform algorithm (IOTA) filter has also been used few times, in order to study the impact of prototype filter.

2.3.5.1 PHYDYAS filter

It is the one designed in the physical layer for dynamic spectrum access and cognitive radio (PHYDYAS) European project [49]. This prototype filter was introduced by Belanger in [41]. The design is based on the frequency sampling technique, which gives the advantage of using a closed-form representation that includes only a few adjustable design parameters. Here onwards, it will be referred as PHYDYAS filter, in this dissertation. The most significant parameter is the duration of the impulse response of the prototype filter L_h , which is dependent on prototype filter overlapping factor, K .

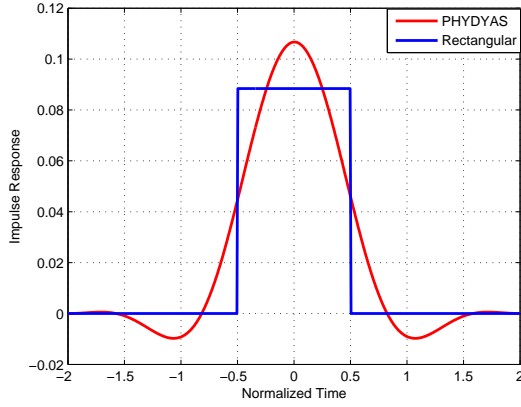


FIGURE 2.5: Comparison of impulse response for PHYDYAS and rectangular filters.

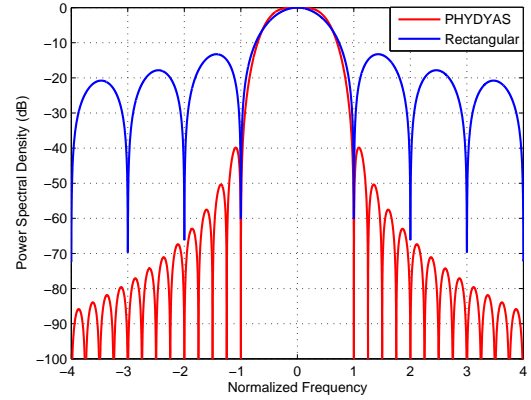


FIGURE 2.6: Comparison of analytical PSD for PHYDYAS and rectangular filters.

The design starts with the determination of $L_h = KLN$ desired frequency coefficients F_k , $0 < k < L_h - 1$ takes values

$$\begin{aligned} F_0 &= 1, F_1 = 0.97195983, F_2 = \frac{1}{\sqrt{2}} \\ F_3 &= \sqrt{1 - F_1^2}, F_k = 0, 4 < k < L_h - 1 \end{aligned} \quad (2.32)$$

For an overlapping factor of $K = 4$, the impulse response of the PHYDYAS prototype filter is given by [41]

$$h(t) = \begin{cases} \frac{1}{\sqrt{A}} \left[F_0 + 2 \sum_{k=1}^{K-1} (-1)^k F_k \cos\left(\frac{2\pi kt}{KT}\right) \right], & t \in [0, KT] \\ 0, & \text{elsewhere} \end{cases} \quad (2.33)$$

where, A is the normalization factor

$$\begin{aligned} A &= \int_0^{KT} \left[1 + 2 \sum_{k=1}^{K-1} (-1)^k F_k \cos\left(\frac{2\pi kt}{KT}\right) \right]^2 dt \\ &= KT \left[1 + 2 \sum_{k=1}^{K-1} (-1)^k F_k^2 \right] \end{aligned} \quad (2.34)$$

The analytical PSD of FBMC-OQAM system with PHYDYAS prototype filter is given by [50]

$$\Phi_{PHYDYAS}(f) = [F(f)]^2 \quad (2.35)$$

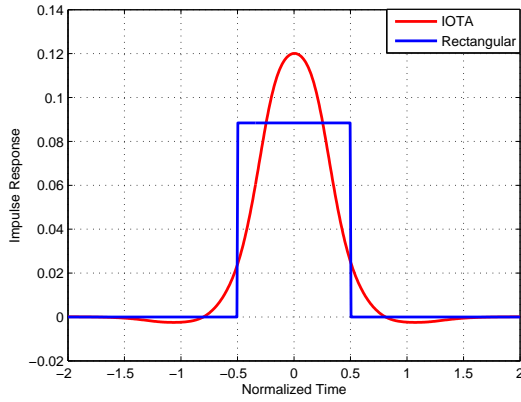


FIGURE 2.7: Comparison of impulse response for IOTA and rectangular filters.

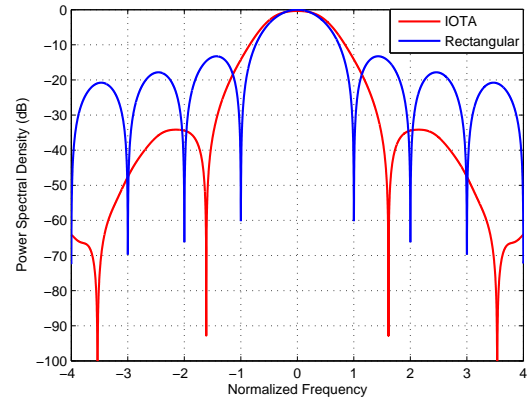


FIGURE 2.8: Comparison of analytical PSD for IOTA and rectangular filters.

where $F(f)$ is the square root of the PHYDYAS filter frequency response given by

$$F(f) = \sum_{k=-(K-1)}^{k=K-1} F_k \frac{\sin(\pi(f - \frac{k}{NK})NK)}{NK \sin(\pi(f - \frac{k}{NK}))} \quad (2.36)$$

In Fig. 2.5 and Fig. 2.6, we can have a glance of the impulse responses and PSD for PHYDYAS and rectangular filters, respectively. Also, from Fig. 2.6, it can be noticed that the frequency localization of the PHYDYAS filter is highly superior to that of the rectangular one used in OFDM system.

2.3.5.2 IOTA filter

The most well-localized pulse shape in the time-frequency domain, according to the Heisenberg-Gabor uncertainty principle [51], is the Gaussian pulse $g(t) = e^{-\pi t^2}$. It is invariant through the Fourier transform. However, it does not satisfy the real orthogonality condition. Therefore, an algorithm was introduced by Alard in [47] converting the Gaussian pulse to an orthogonalized pulse. This obtained orthogonalized pulse shape is called IOTA prototype function. Also, IOTA prototype function is a special case of extended Gaussian function (EGF). The EGF is defined in time in [52].

$$z_{\alpha, \nu_0, \tau_0}(t) = \frac{1}{2} \sum_{k=0}^{\infty} d_{k, \alpha, \nu_0} \left[g_{\alpha} \left(t + \frac{k}{\nu_0} \right) + g_{\alpha} \left(t - \frac{k}{\nu_0} \right) \right] \sum_{l=0}^{\infty} d_{l, 1/\alpha, \tau_0} \cos \left(2\pi l \frac{t}{\tau_0} \right) \quad (2.37)$$

TABLE 2.1: Transmultiplexer impulse response using PHYDYAS filter

	m'_0-4	m'_0-3	m'_0-2	m'_0-1	m'_0	m'_0+1	m'_0+2	m'_0+3	m'_0+4
$n_0 - 3$	0	0	0	0	0	0	0	0	0
$n_0 - 2$	0	0.0006	-0.0001	0	0	0	-0.0001	0.0006	0
$n_0 - 1$	0.0054	0.0429j	-0.125	-0.2058j	0.2393	0.2058j	-0.125	-0.0429j	0.0054
n_0	0	-0.0668	0.0002	0.5644	1	0.5644	0.0002	-0.0668	0
$n_0 + 1$	0.0054	-0.0429j	-0.125	0.2058j	0.2393	-0.2058j	-0.125	0.0429j	0.0054
$n_0 + 2$	0	0.0006	-0.0001	0	0	0	-0.0001	0.0006	0
$n_0 + 3$	0	0	0	0	0	0	0	0	0

where, $g_\alpha(t) = (2\alpha)^{1/4}e^{-\pi\alpha t^2}$ and α is the spreading factor. The computation of the real coefficients d_{k,α,ν_0} is detailed in [52]. Originally the EGFs have been derived in closed form by Le Floch et al. [47] using the IOTA. The IOTA prototype function is obtained by setting $\nu_0 = \tau_0 = 1/\sqrt{2}$ and $\alpha = 1$. Note that the IOTA prototype function is identical to its Fourier transform. Thereby, IOTA is equally localized in time and frequency domains. Its excellent time localization implies that it is less sensitive than the square root raised cosine filter to time truncation [7]. The analytical PSD of FBMC-OQAM system with IOTA prototype filter is given by [50]

$$\Phi_{IOTA}(f) = [z_{1,\sqrt{2},\sqrt{2}}]^2 \quad (2.38)$$

We can have a glance of the impulse responses and PSD for IOTA and rectangular filters, in Fig. 2.7 and Fig. 2.8, respectively. From Fig. 2.6 and Fig. 2.8, one can infer that FBMC system with PHYDYAS possess better frequency localization compared to the one with IOTA. In the same manner, From Fig. 2.5 and Fig. 2.7, we understand that IOTA is well localized in time domain compared to PHYDYAS.

2.3.6 Transmultiplexer impulse response of PHYDYAS and IOTA prototype filters

A transmultiplexer of a communication system is nothing but its transmitter and receiver connected back-to-back. The PHYDYAS and IOTA transmultiplexer impulse responses are displayed in Table 2.1 and Table 2.2 respectively. In these two tables, each row represents a sequence of the impulse response corresponding to a given subchannel. Row n_0 is the subchannel response that satisfies the Nyquist criteria. The other rows correspond to the impulse responses of the interference filters due to the overlapping of the neighboring subchannels $\{n_0 - 3, n_0 - 2, n_0 - 1, n_0, n_0 + 1, n_0 + 2, n_0 + 3\}$.

TABLE 2.2: Transmultiplexer impulse response using IOTA filter

	m'_0-4	m'_0-3	m'_0-2	m'_0-1	m'_0	m'_0+1	m'_0+2	m'_0+3	m'_0+4
$n_0 - 3$	-0.0001	0.0004j	0.0016	-0.0103j	-0.0182	0.0103j	0.0016	-0.0004j	-0.0001
$n_0 - 2$	0	0.0016	0	-0.0381	0	-0.0381	0	0.0016	0
$n_0 - 1$	0.0013	-0.0103j	-0.0380	0.2280j	0.4411	-0.2280j	-0.0380	0.0103j	0.0013
n_0	-0.0007	-0.0183	0	0.4411	1	0.4411	0	-0.0183	-0.0007
$n_0 + 1$	0.0013	0.0103j	-0.0380	-0.2280j	0.4411	0.2280j	-0.0380	-0.0103j	0.0013
$n_0 + 2$	0	0.0016	0	-0.0381	0	-0.0381	0	0.0016	0
$n_0 + 3$	-0.0001	-0.0004j	0.0016	0.0103j	-0.0182	-0.0103j	0.0016	0.0004j	-0.0001

2.3.7 Orthogonality in real domain

Let us denote the shifted versions of $h(t)$ in time and frequency as $\lambda_{m',n}(t)$, which can be given as

$$\lambda_{m',n}(t) = h(t - m'T/2)e^{j\frac{2\pi}{T}nt} e^{j\varphi_{m',n}} \quad (2.39)$$

So, equation (2.12) can be rewritten as

$$x(t) = \sum_{m'=0}^{2M-1} \sum_{n=0}^{N-1} a_{m',n} \lambda_{m',n}(t) \quad (2.40)$$

Let the received signal be $r(t)$. In a distortion-free noise-less channel, the demodulated signal $r_{m'_0,n_0}$ at the time instant m'_0 on the subcarrier n_0 is given by

$$\begin{aligned} r_{m'_0,n_0} &= \langle x(t), \lambda_{m'_0,n_0}(t) \rangle \\ &= \int_{-\infty}^{+\infty} x(t) \lambda_{m'_0,n_0}^*(t) dt \\ &= \sum_{m'=0}^{2M-1} \sum_{n=0}^{N-1} a_{m',n} \int_{-\infty}^{+\infty} \lambda_{m',n}(t) \lambda_{m'_0,n_0}^*(t) dt \\ &= a_{m'_0,n_0} + \underbrace{\sum_{\substack{m' \\ (m',n) \neq (m'_0,n_0)}} \sum_n a_{m',n} \int_{-\infty}^{+\infty} \lambda_{m',n}(t) \lambda_{m'_0,n_0}^*(t) dt}_{\text{intrinsic interference term, } ju_{m'_0,n_0}} \end{aligned} \quad (2.41)$$

where, \langle, \rangle is inner product operations. According to [41], the prototype filter has to be designed such that the intrinsic interference term, denoted by $ju_{m'_0,n_0}$, is orthogonal to the real-valued useful symbol $a_{m'_0,n_0}$. i.e. the intrinsic interference term is purely

TABLE 2.3: Transmultiplexer impulse response after OQAM decision

	m'_0-4	m'_0-3	m'_0-2	m'_0-1	m'_0	m'_0+1	m'_0+2	m'_0+3	m'_0+4
$n_0 - 2$	0	0	0	0	0	0	0	0	0
$n_0 - 1$	0	0	0	0	0	0	0	0	0
n_0	0	0	0	0	1	0	0	0	0
$n_0 + 1$	0	0	0	0	0	0	0	0	0
$n_0 + 2$	0	0	0	0	0	0	0	0	0

imaginary.

$$ju_{m'_0, n_0} = \sum_{\substack{m' \\ (m', n) \neq (m'_0, n_0)}} \sum_n a_{m', n} \underbrace{\int_{-\infty}^{+\infty} \lambda_{m', n}(t) \lambda_{m'_0, n_0}^*(t) dt}_{\Psi_{\Delta m', \Delta n}} \quad (2.42)$$

The orthogonality constraint for FBMC-OQAM is relaxed being limited only to the real field, while for OFDM it has to be satisfied in the complex field. This is due to the fact that, it is theoretically proven with the Balian Low theorem, see [53], that it is not possible to get a prototype function being well-localized in time and frequency, and satisfying simultaneously both orthogonality condition and a symbol density of one. Therefore, in order to meet these objectives, we must relax the orthogonality condition and restrict it to the real field. Then, to be able to recover the data at the receiver side, the transmitted data must be real-valued (or purely imaginary) chosen from a pulse amplitude modulation (PAM) constellation instead of a QAM one. Consequently, one of the characteristics of FBMC-OQAM is that the demodulated transmitted symbols are accompanied by interference terms caused by the neighboring transmitted data in time-frequency domain. The coefficients $\Psi_{\Delta m', \Delta n}$ can be understood by the transmultiplexer impulse responses given in Table 2.1 and Table 2.2 for PHYDYAS and IOTA prototype filters, respectively. Also, from these two tables, the frequency localization of FBMC-OQAM system with PHYDYAS filter and time localization of IOTA filter can also be observed. A perfect reconstruction of the transmitted real symbols $a_{m', n}$ is obtained by taking the real part (OQAM decision) of the demodulated signal $r_{m', n}$.

$$\begin{aligned} \hat{a}_{m', n} &= \Re\{r_{m'_0, n_0}\} \\ &= a_{m'_0, n_0} \end{aligned} \quad (2.43)$$

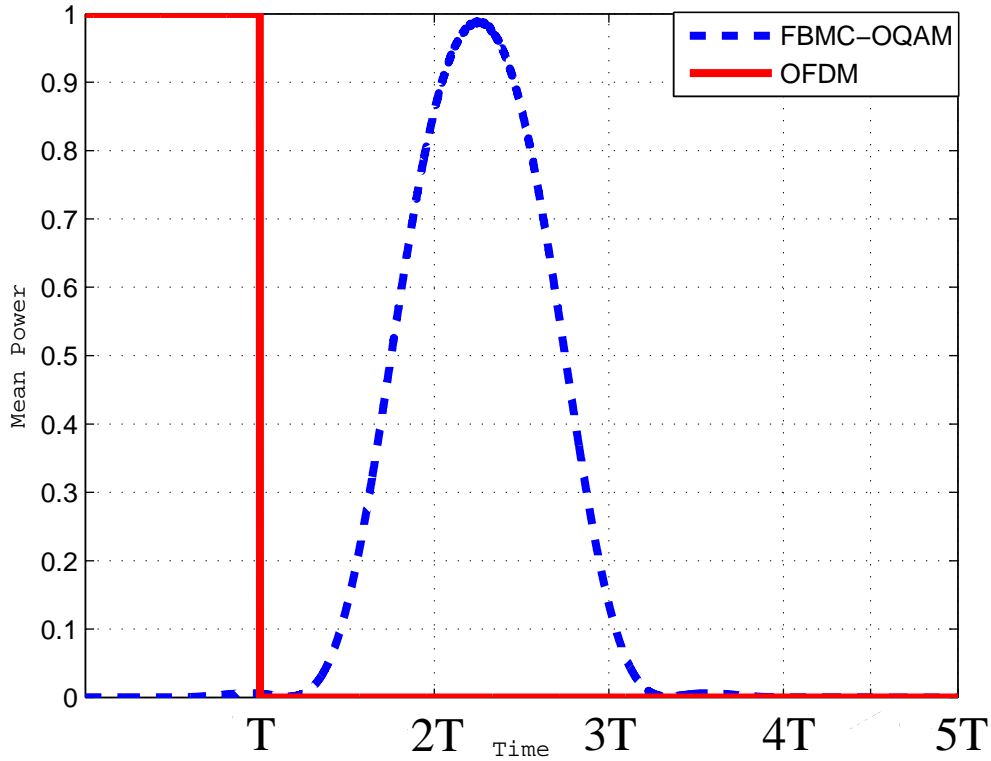


FIGURE 2.9: Illustration of mean power profile of OFDM and FBMC-OQAM symbols.

The OQAM decision has been summarized in Table 2.3. From equation (2.41), we can infer that the orthogonality of FBMC-OQAM symbols depends solely on the pulse shape of prototype filter. By introducing $T/2$ delay between the in-phase and the quadrature components of every complex symbol, the orthogonality between carriers is maintained in FBMC-OQAM.

2.3.8 Overlapping nature of FBMC-OQAM symbols

The duration of $h(t)$ impacts the FBMC-OQAM signal, causing adjacent FBMC-OQAM symbols to overlap. In PHYDYAS filter, most of the energy of $h(t)$ lies within the main lobe. In order to elucidate the overlapping nature, one need to get to know about the mean power profile of a FBMC-OQAM signal, which is defined as

$$P_{avg}[x(t)] = \mathbb{E}[|x(t)|^2] \quad (2.44)$$

where, $\mathbb{E}[\cdot]$ is the expectation operator. Due to time-dispersive nature, the real and imaginary parts of the symbol have an offset of $\frac{T}{2}$ and both parts have a span of $4T$, which is directly linked to the length of $h(t)$. It is evident from Fig. 2.9 that the power profile of the FBMC-OQAM symbols spans over $4.5T$, where as in the case of OFDM, it spans over T . Unlike OFDM, we can also observe that most of the energy of a FBMC-OQAM symbol lies in its succeeding two symbols rather than its own period interval.

2.4 Introduction to non-linear power amplifiers

The PA is one of the key component in the wireless mobile communication systems. It allows the transmitted signal to compensate for the attenuation caused by free space propagation. Unfortunately, it is an analog component and is inherently NL. This is due to the fact that the amplifier circuits are constructed from active components such as transistors, which are NL in nature.

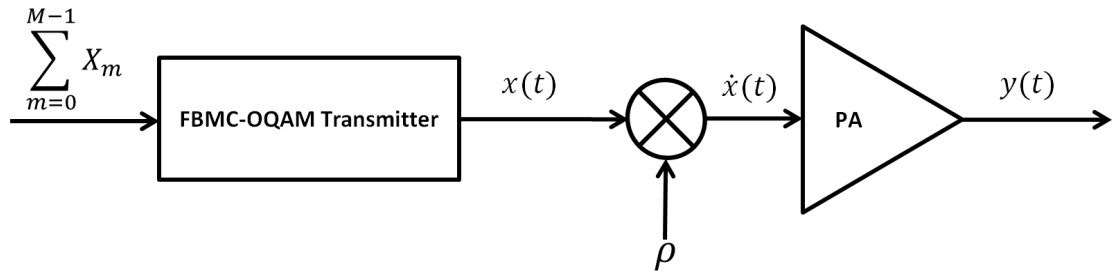


FIGURE 2.10: Illustration of FBMC-OQAM transmission chain along with PA.

A typical illustration of a FBMC-OQAM transmission system in the presence of a PA, is shown in Fig. 2.10. So, if we have to transmit M symbols $\{\mathbf{X}_m\}_{m=0}^{M-1}$ in a FBMC-OQAM system, then we recall that we perform FBMC-OQAM modulation as per equation (2.12) to obtain the baseband signal $x(t)$. Considering the transfer function of the PA, one can distinguish into two zones, linear and non-linear one. In the linear zone, the signal is amplified with very good linearity; albeit, with low energy efficiency. On the contrary, the NL region has high energy efficiency, but the amplified signal is distorted. The concept of energy efficiency can be understood by defining the power efficiency of a PA η , which is defined as the part of direct current (DC) power that is converted to radio-frequency (RF) power, i.e. the ratio of the RF output power to DC input power and is

given by

$$\eta = \frac{P_{out}}{P_{DC}} \quad (2.45)$$

This NL amplification causes OOB interference due to spectral leakage into the neighboring channels and degrade the bit error rate (BER) due to warped and clustered symbol constellation at the receiver, which is known as in-band (IB) distortion. In order to get rid of the signal distortion, the PA is made to operate in its linear region with low efficiency. This means that the signal peaks should be within this region. This can be realized by increasing the input back-off (IBO), which can be achieved by decreasing the mean power of the input signal $x(t)$. Instead of directly feeding $x(t)$ into the PA, we apply an IBO, by multiplying with a coefficient ρ , in order to obtain $\dot{x}(t)$.

$$\dot{x}(t) = \rho \cdot x(t) \quad (2.46)$$

When, we amplify $\dot{x}(t)$, we obtain $y(t)$, which is the base-band equivalent of PA output respectively in continuous-time. Definition of ρ can be better comprehended after defining IBO. The IBO of a PA, often expressed in dB, is a measure of how far one must reduce the input power in order mostly remain in the linear region. It can be defined as the ratio between the saturation power to the mean power of the input signal that delivers desired linearity as given below

$$IBO = 10 \cdot \log_{10} \left[\frac{v_{sat}^2}{\mathbb{E}[|\dot{x}(t)|^2]} \right] \quad (2.47)$$

where v_{sat} is the input saturation level or saturation voltage of PA. Without loss of generality, we fix it to 1 V. Now, we define ρ as

$$\rho = \frac{v_{sat}}{\sqrt{IBO_{lin} * \mathbb{E}[|x(t)|^2]}} \quad (2.48)$$

where IBO_{lin} is IBO in linear scale given by $10^{\frac{IBO}{10}}$. There is an increasing emphasis on green communications, which aims at cutting short the carbon emissions in future communication systems. To achieve this, it is imperative to improve the amplifier efficiency for reducing the energy consumption in the communication systems. This means that the PA has to operate at near saturation region, i.e. very low IBO.

2.4.1 Linearity and power efficiency tradeoff in a PA

Power efficiency and amplifier linearity are two key parameters, which play a significant role in the design of modern power amplifiers. It is critical in the design in minimizing the cost of operating transmitter sites such as cell phone based stations and prolonging battery life in portable wireless devices. It is well known that driving the amplifier into its non-linear region, e.g. Class C operation, may improve efficiency, but it will also lead to increased distortion. The impact of the PA on transceiver performance is twofold. First, because it consumes the lion's share of the power budget, the power efficiency of the entire system is improved almost exactly to the extent that such improvement is made with the PA. In a cellular phone, efficiency leads to longer battery lifetimes. In a base station, efficiency can mean reduced thermal management problems. Second, the PA, in large part, determines the transceiver's ability to use the spectrum efficiently. Narrowing the question to "circuit realizations based on NL, three-terminal devices," we can at least say that no one has yet found a way to achieve this elusive goal. For reasons that may as well be fundamental, then, linearity and power efficiency are competing design objectives. The intriguing question is: do linearity and power efficiency tradeoff for fundamental reasons? It may be impossible to answer that question definitively.

2.4.2 Analytical representation of a PA

Generally, the PA models are classified into two categories: memory-less models or models with memory. The scope of this thesis is confined to the memory-less PA models. We denote, the PA input saturation level as v_{sat} and without loss of generality fix it to 1 V, in our analysis. Ideally speaking, a PA is supposed to conserve the input signal waveform (i.e. no distortion). Thus, in an ideal PA, the output signal $y(t)$ is an amplified input signal $\dot{x}(t)$ with a linear gain. However, in a NL PA model with a complex gain function $G(\cdot)$, the output signal $y(t)$ can be represented as

$$\begin{aligned} y(t) &= \mathcal{A}\{\dot{x}(t)\} \\ &= G(\dot{x}(t))e^{j\phi_{\dot{x}(t)}} \end{aligned} \tag{2.49}$$

where, $\mathcal{A}\{\cdot\}$ is the amplification function and $\phi_{\dot{x}(t)}$ is the phase of the input signal $\dot{x}(t)$.

2.4.3 AM/AM and AM/PM characteristics

The conversion characteristics or the transfer functions of the PA represent the relation between its input and output. The amplitude-to-amplitude (AM/AM) characteristic is the measure of AM/AM conversion in PA, by reflecting the relationship between the amplitude of its output voltage (denoted by $|y(t)|$) as a function of its input $|\dot{x}(t)|$.

Similarly, amplitude-to-phase (AM/PM) characteristic is the measure of AM/PM conversion in PA, which shows the deviation of the phase of the output voltage $\phi_y(t)$, w.r.t. the magnitude of the input voltage $|\dot{x}(t)|$. It is a critical parameter because undesired phase deviation causes analog signal degradation, or increased BER in digital communication systems. While it is easy to measure the BER of a digital communication

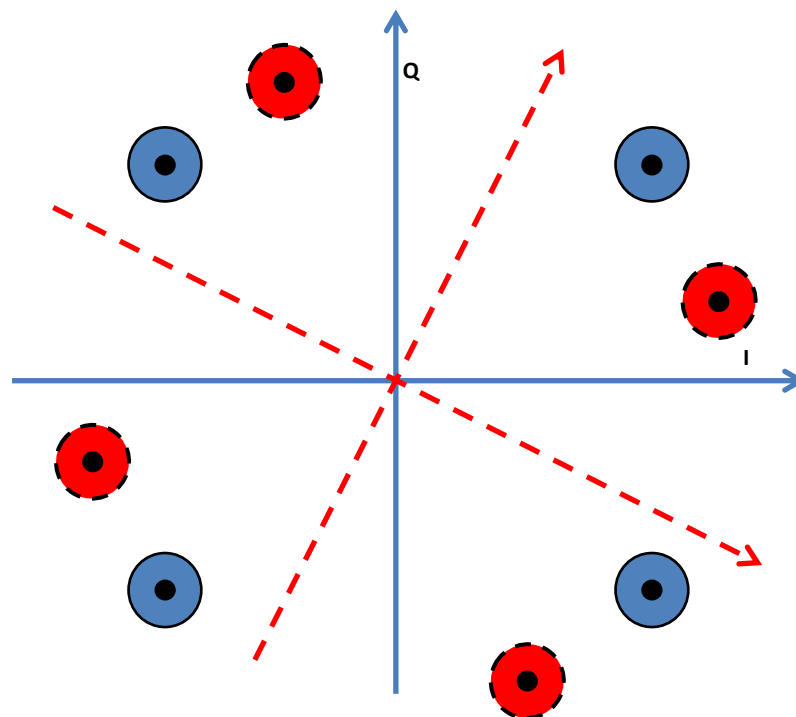


FIGURE 2.11: Impact of AM/PM conversion on QPSK constellation I/Q diagram.

system, this measurement alone does not help you understand the underlying causes of bit errors. It is important to quantify AM/PM conversion in communication systems. Fig. 2.11 gives an idea about the typical impact of AM/PM conversion for a QPSK constellation, where the original and distorted constellation points are shown in blue and red color respectively in the I/Q diagram. In general, even though, the AM/AM characteristic has a typical shape for all amplifiers, the AM/PM characteristic changes accordingly with the design of each amplifier. The complex gain function of the PA can

be represented in terms of the AM/AM and AM/PM characteristics.

Thus, the complex gain of the output signal $y(t)$, which is $G(\dot{x}(t))$ can be behaviorally modeled as a function of the input voltage $|\dot{x}(t)|$ as

$$G(\dot{x}(t)) = F_a(|\dot{x}(t)|).e^{jF_p(|\dot{x}(t)|)} \quad (2.50)$$

where, $F_a(\cdot)$ and $F_p(\cdot)$ are the AM/AM and AM/PM characteristics respectively.

2.4.4 Some PA models

The study of non-linearities and their effects in communication systems can be carried out through the analytical treatment of models that are conceived to approach the fundamental physical nature of devices and channels. Such treatment, often based on solving non-trivial sets of differential equations (normally untractable by algebraic means), lead us to seek the aid of numeric methods and further simplifications to face the almost unbeatable mathematical challenges therein involved. Hence, higher-level transference models, normally referred to as ‘behavioral’ models, are required for producing testable characterizations of non-linearities by providing good accuracy at a reasonable complexity for analysis as well as simulation purposes. All of these models use a limited number of parameters that are adjustable by means of fitting procedures to represent the input-output functional relationship of a given real system.

2.4.4.1 Polynomial model

The polynomial model can be seen as the simplest way to model the behavior of a PA as a nonlinear system and is widely used. In polynomial model, for any measured or modeled PA, we can approximate its input output conversion characteristics as

$$\begin{aligned} y(t) &= \sum_{k=0}^{\Upsilon} a_{2k+1} [\dot{x}(t)]^{k+1} [\dot{x}^*(t)]^k \\ &= \dot{x}(t) \sum_{k=0}^{\Upsilon} a_{2k+1} |\dot{x}(t)|^{2k} \\ &= \left[\sum_{k=0}^{\Upsilon} a_{2k+1} |\dot{x}(t)|^{2k+1} \right] e^{j\phi_{\dot{x}(t)}} \\ &= G(|\dot{x}(t)|) e^{j\phi_{\dot{x}(t)}} \end{aligned} \quad (2.51)$$

where

- $2\Upsilon + 1$ is the order of the polynomial model,
- $\{a_{2k+1}\}_{k=0}^{\Upsilon}$ are the complex coefficients of the polynomial model,
- the complex gain $G(|\dot{x}(t)|) = \left[\sum_{k=0}^{\Upsilon} a_{2k+1} |\dot{x}(t)|^{2k} \right]$.

The AM/AM conversion is actually a polynomial, consisting of monomials of odd degrees [10]. In [54], this approximation was compared to full ranking polynomial and the conclusion is that both approaches give the same performance in terms of base-band modeling of PA non-linearity. Least-squares (LS) algorithm is used to perform polynomial approximation. In case of absence of AM/PM conversion, the coefficients $\{a_{2k+1}\}_{k=0}^{\Upsilon}$ will be real. It can be inferred from equation (2.51), that the complex gain $G(|\dot{x}(t)|)$, is a function of the input amplitude $|\dot{x}(t)|$ only. Once the AM/AM and AM/PM characteristics of the PA are known, it is possible to extract the coefficients $\{a_{2k+1}\}_{k=0}^{\Upsilon}$. We know that, the PA amplitude gain (AM/AM conversion) $|G(|\dot{x}(t)|)| = |y(t)|/|\dot{x}(t)|$ and the output phase distortion (AM/PM conversion) $\angle G(|\dot{x}(t)|) = \angle y(t) - \angle \dot{x}(t)$, yielding the complex gain $G(|\dot{x}(t)|) = |G(|\dot{x}(t)|)|e^{j\angle G(|\dot{x}(t)|)}$. A least squares fit with respect to (w.r.t.) the regressors $\{1, |\dot{x}(t)|^2, |\dot{x}(t)|^4, \dots, |\dot{x}(t)|^{2\Upsilon}\}$ yields to polynomial coefficients $a_1, a_3, a_5, \dots, a_{2\Upsilon+1}$ for the polynomial model.

2.4.4.2 Soft envelope limiter

In a soft envelope limiter (SEL) [8], up to an input saturation level v_{sat} , this power amplifier model assumes a linear conversion characteristic; beyond which, the amplified output signal is clipped to v_{sat} . It has to be noted that SEL amplifier model is used for modeling a PA with a perfect predistortion system. So, the global transfer function of the predistortion followed by the PA is an envelope limiter, which can be described by following AM/AM and AM/PM characteristics [8]

$$F_a(|\dot{x}(t)|) = \begin{cases} |\dot{x}(t)|, & |\dot{x}(t)| \leq |v_{sat}| \\ |v_{sat}|, & |\dot{x}(t)| > |v_{sat}| \end{cases} \quad (2.52)$$

$$F_p(|\dot{x}(t)|) = 0 \quad (2.53)$$

AM/AM conversion characteristic of SEL model is shown in Fig. 2.12.

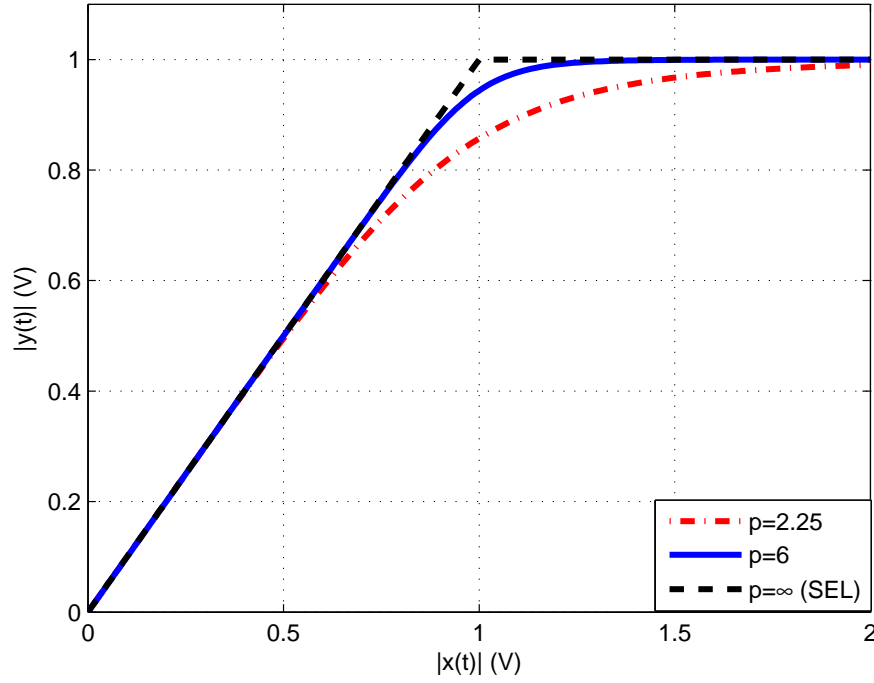


FIGURE 2.12: SEL and Rapp model AM/AM conversion characteristics.

2.4.4.3 Rapp model

The Rapp model is commonly used for modeling the Solid State Power Amplifiers (SSPA) and was presented in [55]. SSPA is composed of several stages of amplification based on transistors and is used for low-power terrestrial radio transmissions. Rapp model exhibits only AM/AM conversion and does not apply a phase change to the input signal. The AM/AM and AM/PM conversion characteristics of the Rapp model are

$$F_a(|\dot{x}(t)|) = \frac{|\dot{x}(t)|}{\left(1 + \left(\frac{|\dot{x}(t)|}{v_{sat}}\right)^{2p}\right)^{\frac{1}{2p}}} \quad (2.54)$$

$$F_p(|\dot{x}(t)|) = 0 \quad (2.55)$$

Where, p is the knee factor, which controls the smoothness of transition from the linear region to the saturation region. It is clear from the AM/AM conversion characteristic illustrated in the Fig. 2.12; that as the value of knee factor increases, the SSPA model approaches the SEL one.

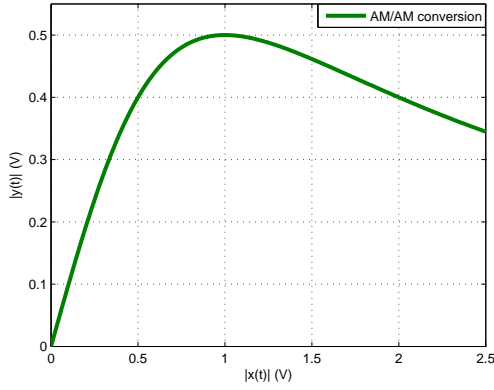


FIGURE 2.13: Saleh model AM/AM conversion characteristic.

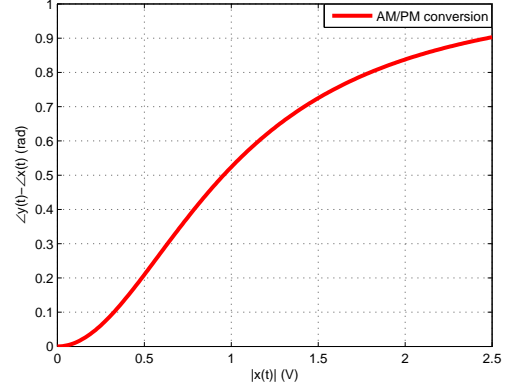


FIGURE 2.14: Saleh model AM/PM conversion characteristic.

2.4.4.4 Saleh model

Saleh model is generally used for modeling traveling wave tube amplifiers (TWTA) [9]. As evident in the name, TWTA has microwave tubes and is mainly used in satellite communications and can deliver high power amplification. Saleh model has been mainly used in several works dealing with the impact of non-linearities in OFDM systems [56]. The AM/AM and AM/PM conversion characteristics of Saleh model has been shown in Fig. 2.13 and Fig. 2.14 respectively. According to this model, the AM/AM and AM/PM conversion characteristics can be expressed as follows:

$$F_a(|\dot{x}(t)|) = \frac{\alpha_a |\dot{x}(t)|}{1 + \beta_a |\dot{x}(t)|^2} \quad (2.56)$$

$$F_p(|\dot{x}(t)|) = \frac{\alpha_p |\dot{x}(t)|^2}{1 + \beta_p |\dot{x}(t)|^2} \quad (2.57)$$

where α_a and β_a are the parameters to decide the NL amplitude distortion level, and α_p and β_p are phase displacements. In the literature we also found the following equations (2.58) and (2.59), for the modeling the AM/AM and AM/PM conversion characteristics of TWTA

$$F_a(|\dot{x}(t)|) = \frac{v_{sat}^2 |\dot{x}(t)|}{v_{sat}^2 + |\dot{x}(t)|^2} \quad (2.58)$$

$$F_p(|\dot{x}(t)|) = \frac{\phi_o \cdot |\dot{x}(t)|^2}{v_{sat}^2 + |\dot{x}(t)|^2} \quad (2.59)$$

Where, ϕ_o is a phase constant related to saturation point. ϕ_o controls the maximum phase distortion introduced by this PA model. Its clear that both versions of above

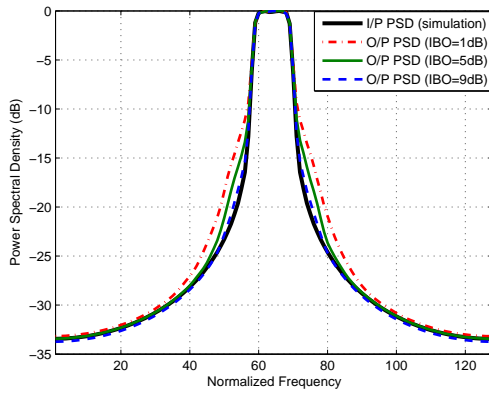


FIGURE 2.15: Spectral regrowth in PSD in a OFDM system with Saleh model of PA.

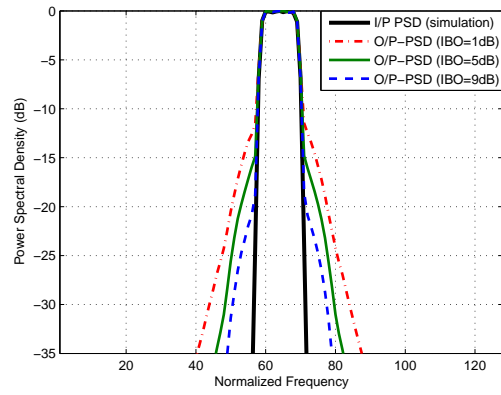


FIGURE 2.16: Spectral regrowth in PSD in a OFDM system with Saleh model of PA.

equations allow the modeling of PA exhibiting both NL amplitude and phase distortion. However, in this dissertation, we will refer to this model as Saleh model by 2.58 and (2.59).

2.4.5 Spectral regrowth of non-linearly amplified MCM signals

Intermodulation products, or spurs, can develop within the analog and digital transmitters in combined systems using high-level injection. In some cases, spurs can result in sub-optimal signal quality or even cause stations to interfere with each other's signals. The term spectral regrowth was coined to describe inter-modulation products generated when a digital transmitter is added to an analog transmission system. This can be observed on a spectrum analyzer or a power spectral density plot. In general, passing of a non-constant envelope modulated signal through a NL system generates undesirable spectral products. The MCM signals are more susceptible to intermodulation distortion and hence can create large spectral regrowth components as a results of passing through a NL PA.

To summarize, when a modulated signal passes through a NL system, its bandwidth is broadened by odd-order non-linearities. This broadening is caused by the creation of mixing products between the individual frequency components of the modulated signal spectrum. In any modern communication system, the spectral regrowth is of typical concern in the transmitter side. Within the transmitter, spectral regrowth is typically caused by the most NL component of the transmit chain. This component is almost always the PA.

Spectral regrowth can cause several problems in a communication system. Perhaps, most important problem of all is creating interference with adjacent channels. As a matter of fact, the spectrum is a very precious commodity. Therefore, the channels are tightly packed together in order to maximize the efficiency of the spectrum usage. Excessive spectral regrowth can cause interference with the adjacent channels and this is the primary reason why standards formulated by regulated bodies, require conformance to a spectral mask.

Spectral regrowth in typical OFDM and FBMC-OQAM systems with a NL PA has been displayed in Fig. 2.15 and Fig. 2.16 respectively. As evident from Fig. 2.15, OFDM system shows meager spectral regrowth. Albeit, the intriguing aspect is that of FBMC-OQAM system shown in Fig. 2.16, which seems to be very very sensitive to PA non-linearity. Even with high IBO=9 dB, we can still see non-negligible spectral regrowth. This explains the gravity of the situation in a communication system, when RF impairments are taken into consideration.

2.5 Need for mitigation of NL effects of PA

Signals with high amplitude fluctuations, as in the case of MCM systems, pose a tough challenge to the RF design of PAs. The power consumption helps define the battery life for mobile communications systems [57]. PA represents more than 60% of the total power consumption at transmitter [58]. So, the PA linearity and energy efficiency are two vital parameters in the context of the signals with strong fluctuations, as evident in MCM techniques. In order to get rid of the amplified signal distortion, the PA is made to operate in its linear region, which has very poor energy efficiency. The presence of high peaks cause IB and OOB interferences when the MCM signals are passed through a PA, which does not have enough linear range. The fluctuation of the signal envelope can be well understood by its PAPR. The PAPR is a random variable, which is a convenient parameter in measuring the sensitivity of a NL PA, when a non-constant envelop input need to be transmitted. Low values of PAPR are synonymous with a transmitted signal with a power always very close to its mean power while high PAPR values indicate that the instantaneous power can be very high compared to the average one. The PAPR of the continuous-time base-band signal $x(t)$ transmitted during a symbol period T is

defined by,

$$PAPR_{x(t)} = \frac{\max_{0 \leq t \leq T} |x(t)|^2}{\frac{1}{T} \int_0^T |x(t)|^2 dt} \quad (2.60)$$

The PAPR definition in equation (2.60) is also known as the Peak-to-Mean Envelope Power Ratio (PMEPR) [59]. A general presentation of the terminology in use can be found in [60]. Also, PAPR is square of *crest factor*, which is defined as the ratio of peak amplitude of a waveform to its RMS value.

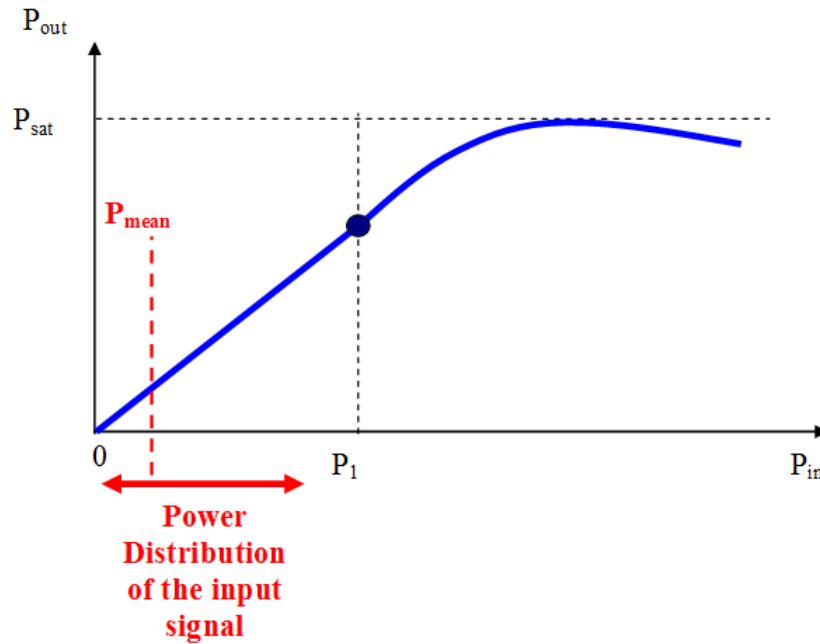


FIGURE 2.17: PA nonlinear behavior.

PA at the emitter side can be quasi linear for a certain part of the input powers, P_{in} , (from 0 to P_1 , see Fig. 2.17) and NL for input powers larger than P_1 . Furthermore, the output power, P_{out} , of a PA is limited to a saturation power P_{sat} (Fig. 2.17).

If the input power is always lower than P_1 , the PA is operated in its quasi linear region and the high PAPR of the MCM signal will not have any influence on the quality of the transmission. This is illustrated in Fig. 2.17 by an input signal with a mean power equal to P_{mean} and a certain distribution of the input power around P_{mean} . Nevertheless, this situation has a high cost in terms of energy efficiency: operating a PA with a very low mean input power gives a low mean output power compared to P_{sat} . Especially for mobile applications with batteries, it is necessary to increase the power efficiency. Real

PA communication systems will then be operated as close as possible to the saturation point in order to increase the power efficiency. By doing that, two negative effects will appear:

- if the PA is operated in its NL region, the output signal spectrum will be broadened compared to the input one,
- distortions will occur in the transmitted signal causing transmission errors.

FBMC-OQAM systems have, like classical OFDM multi-carrier signals, a high PAPR. For FBMC-OQAM signals, spectral broadening is perhaps a more important drawback compared to OFDM. The latter has a decreasing spectrum following the sinc function (sinus cardinal function) because of the rectangular shaping filter used. On the contrary, FBMC-OQAM signals exhibit a very strong decrease in the frequency domain due to their shaping filters. If NL PA are used, the advantage of FBMC-OQAM compared to OFDM related to the frequency localization can be highly diminished. It is thus of prime importance with FBMC-OQAM to fight against NL amplification effects. Concerning distortions induced by the NL PA, it is also important to limit and correct them. Looking at Fig. 2.17, we can view several axes of progression concerning the NL effects of the PA:

- we can increase the PA linear area using PA linearization. This is equivalent to increase P_1 towards P_{sat} (see illustration on figure 2.18),
- we can decrease the distribution of high values of the instantaneous power of the transmitted signal. This is equivalent to lowering the PAPR of the transmitted MCM signal,
- we can also correct NL distortion at the receiver side.

Increasing the PA linearity together with PAPR minimization permits to increase power efficiency by increasing the mean power of the input signal, P_{mean} , very close to P_{sat} . If the PA is perfectly linearized and if the PAPR is reduced to 0 dB (instantaneous power always very close to P_{mean}), the power efficiency can be very close to one. Furthermore, if the input signal is always in the linear region of the PA, the spectral regrowth will be

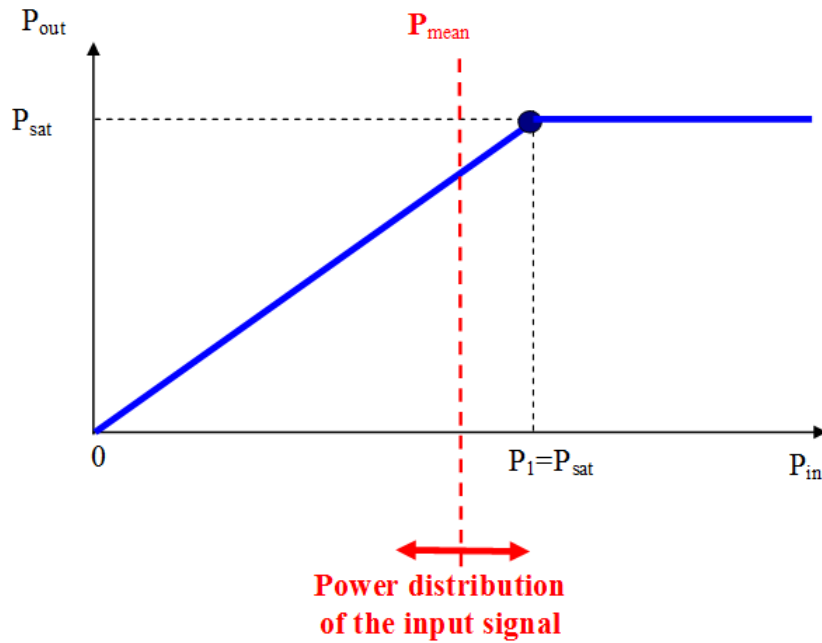


FIGURE 2.18: Linearized PA and input signal with low PAPR.

limited. Thus, minimizing the impact of NL effects of PA is obligatory and the most prevailing methods in literature, to deal with this are, (i) operation of the PA with sufficient IBO, (ii) reduction of the input signal peaks and (iii) linearization of PA.

2.5.1 PAPR analysis of MCM signals

MCM signals exhibit a high PAPR because of the central limit theorem. In fact, the transmitted signal is a sum of independent signals (the different carriers) with same probability density function. When the number of sub-carriers is sufficiently large (larger than few tens, for example), central limit theorem can be applied and the probability density function of real and imaginary parts of the MCM signal follow a Gaussian law giving high values of the PAPR. The distribution of the transmitted power is not very important as far as linear systems are used in the transmission chain. Since PA is NL, it is imperative to opt for PAPR reduction techniques. Generally, at the baseband level, the implementation of modems is in digital domain; leading to specific definitions for discrete-time signals. The PAPR of a MCM system with N tones is defined as [16]

$$PAPR_{x[k]} = \frac{\|x[k]\|_{\infty}^2}{\|x[k]\|_2^2}, \quad 0 \leq k \leq N - 1 \quad (2.61)$$

where, $\|\cdot\|_2$ and $\|\cdot\|_\infty$ denote Euclidean and infinite norm respectively, which are given below

$$\|x[k]\|_2 = \sqrt{\sum_{k=0}^{N-1} |x[k]|^2} \quad (2.62)$$

$$\|x[k]\|_\infty = \max_{0 \leq k \leq N-1} |x[k]| \quad (2.63)$$

In general, any p^{th} norm of a vector $x[k]$ is given by

$$\|x[k]\|_p = \left[\sum_{k=0}^{N-1} |x[k]|^p \right]^{1/p} \quad (2.64)$$

Where, p is a natural number. Fig. 2.19 illustrates the extent of deviation of peak-voltage of a single FBMC-OQAM symbol from its rms voltage, where its PAPR is 15.27 dB. This explains the necessity of PAPR reduction.

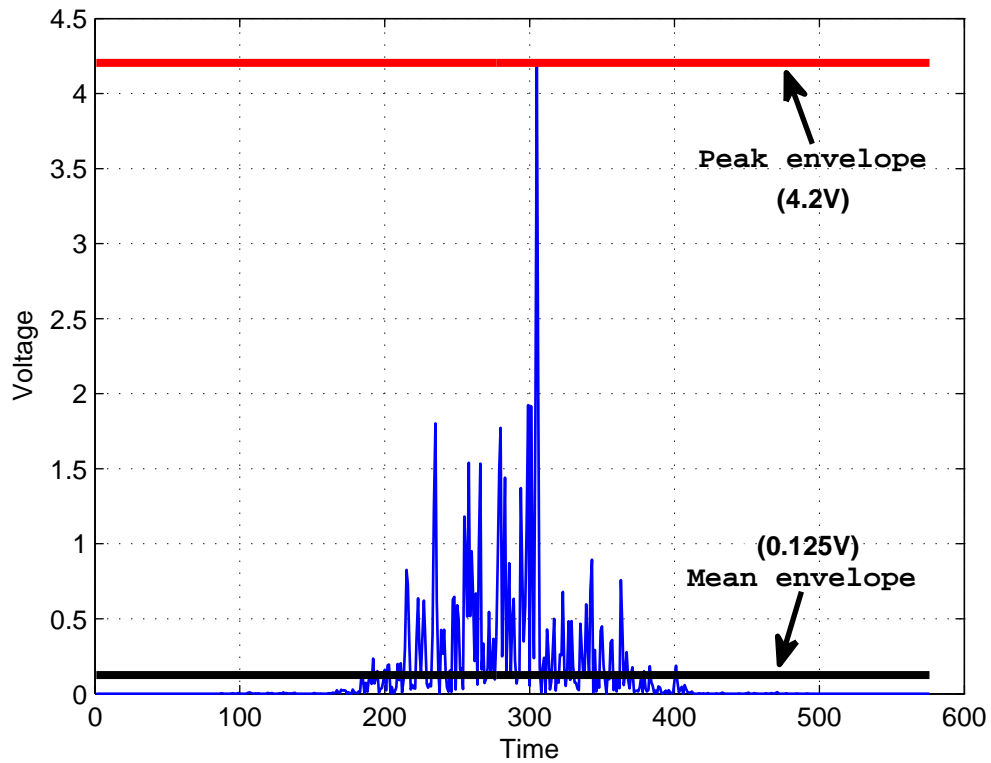


FIGURE 2.19: A FBMC-OQAM symbol with PAPR of 15.27 dB.

2.5.1.1 Complementary cumulative density function of PAPR

The complementary cumulative density function (CCDF) of PAPR is a useful parameter to analyze the PAPR, which is defined as the probability that the PAPR of the discrete-time signal $x[k]$ exceeds beyond a given threshold that is denoted by γ (in dB)

$$CCDF_{x[k]}(\gamma) = \text{Proba}\{PAPR_{x[k]} \geq \gamma\} \quad (2.65)$$

where, $\text{Proba}(\cdot)$ denotes probability function.

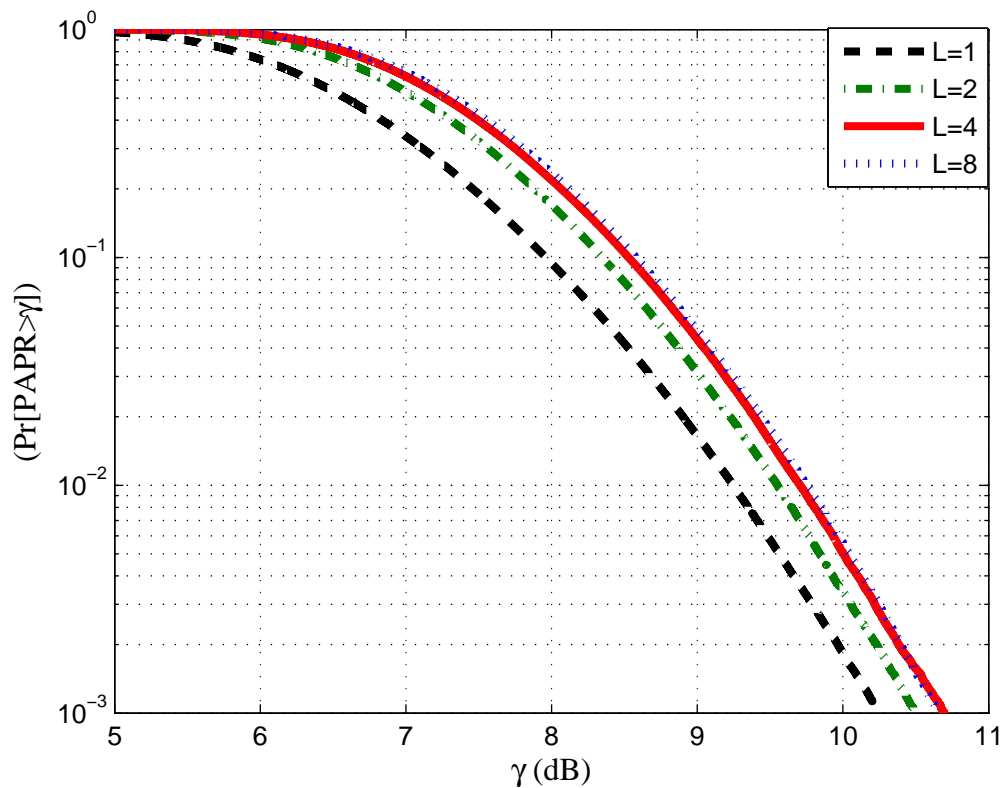


FIGURE 2.20: CCDF of PAPR of a 64-tone FBMC-OQAM signal w.r.t L .

2.5.1.2 Need for oversampling

Generally, most of the existing reduction PAPR techniques can be implemented on discrete-time signals. If we sample a MCM signal at Nyquist rate, then we may miss some peaks. So, it is advisable to perform oversampling. In [13], it was shown that, it was shown that beyond an oversampling factor $L = 4$, we cannot improve further in

approximating the PAPR of the continuous-time signal. The impact of oversampling in a FBMC-OQAM system can be well understood from Fig. 2.20. Based on results shown in Fig. 2.20, it is clear that an oversampling factor of 4 is sufficient to ensure good approximation of the PAPR for a FBMC-OQAM signal.

2.5.2 PA linearization

Non-linearity of PA is due to the fact that the amplifier circuits are constructed from active components such as transistors, which are NL in nature. Thus, PA linearization involves in reducing the NL distortion due to PA. Linearization permits PA efficiency and linear amplification at Transmitter. However, there is a tradeoff between linearity and efficiency. In this dissertation, we throw some light on digital pre-distortion techniques for FBMC-OQAM systems and possibility for joint optimization of PAPR reduction and digital predistortion. PA linearization for FBMC-OQAM systems is dealt in detail in the Chapter 6.

2.6 Conclusion

In this chapter, we have introduced the basic concepts of two MCM techniques that will be considered in this dissertation. The first technique is the well-known OFDM technique considered in the 3G and 4G systems. However the second technique is a filter-bank based technique involving offset-QAM that is introduced to ensure better frequency localization compared to the OFDM one. FBMC-OQAM is a post-OFDM waveform technique offering numerous advantages such as excellent frequency localization, robustness to asynchronism among users, etc. This chapter provides the fundamental theory of FBMC-OQAM systems. Among other, we have discussed regarding the dissimilarities in the signal structure of OFDM and FBMC-OQAM in this chapter.

FBMC-OQAM system suffers from high PAPR by being a MCM technique. This poses a severe challenge to the RF design of PAs. Some PA models had been introduced in this chapter. These models are mainly of the memoryless types and completely determined by their AM/AM and AM/PM conversion characteristics. To maintain energy efficiency, PA need to operate at near saturation region and cope up with the NL effects.

In order to reduce NL effects of PA, many approaches can be applied; such as PAPR

reduction and PA linearization. Actually, NL mitigation at the receiver side also exists, but is beyond the scope of this dissertation. The PAPR reduction and PA linearization techniques should be applied to signals with judicious choice of IBO.

Chapter 3

Spectral regrowth prediction for FBMC-OQAM systems using cumulant analysis

3.1 Introduction

Unlike OFDM, FBMC-OQAM has extremely concentrated frequency localization. This is compromised when realistic RF impairments are taken into account; as shown in [61]. When a signal with time-varying envelope passes through a NL PA, spectral regrowth appears at the PA output. Spectral regrowth causes adjacent channel interference (ACI), which is very tightly controlled by regulatory bodies for many over-the-air applications. Indeed, the spectral regrowth of FBMC-OQAM and OFDM is very similar when the PA distorts the transmitted waveform. Prediction of spectral regrowth for a prescribed level of PA non-linearity can be very helpful for designing communication systems. Given the PA conversion characteristics, it is desirable to be capable to predict offline (i.e. without running time-domain simulations), whether the PA can be used to amplify certain types of signals. Through polynomial model of PA, we are able to derive a closed-form expression for the output auto-covariance function, whose Fourier transform (FT) yields to the PSD, for any stationary input. There are two popular methods for spectral regrowth analysis, where we can derive a closed-form expression for the auto-covariance

function of the PA output. The first method is based on cumulants and the later one is based on Price's theorem [62]. However since the latter involves integral calculus, it may sometime involve difficulty in determining the integration constant which will impact the closed-form expression derivation. Considering only AM/AM conversion, analysis of the nonlinear spectral re-growth in band-limited offset-QPSK systems using cumulants [63] and in FBMC-OQAM systems for cognitive radio context using Price theorem [64], has been done. In a scenario where AM/PM conversion is to be taken into account, it becomes complicated to predict the PSD using the Price theorem. Due to these two reasons, the cumulant-based method seems to be more adequate for PSD prediction.

Once the PA model is known i.e. its AM/AM and AM/PM characteristics are available then we can do polynomial approximation for those characteristics. In order to derive a closed-form expression based on cumulants, we need the coefficients of the polynomial. The PA model used in this analysis is the Saleh one [9]. However, the study remains valid for any other PA model. Already, the spectral regrowth prediction for OFDM systems based on cumulants was done in [65]. In this thesis, a similar approach has been extended to FBMC-OQAM systems.

This chapter is organized as follows: In Section 3.2, the cumulants are introduced. Their properties are discussed, along with their relevance to the power spectrum. In Section 3.3, the methodology is presented to predict the PA output PSD based on cumulants. Then, in Section 3.4, simulation results are presented for a PA with Saleh model and also in a cognitive radio (CR) context. Finally, the Section 3.5 concludes the chapter.

3.2 Introduction to cumulants

Cumulants are used generally for derivation of closed-form expressions. Because of their interesting properties they are used as an alternative to the moments of a distribution. Cumulants were first introduced by Thorvald N. Thiele, who called them as *semi-invariants* [66]. They were first called *cumulants* in a paper by Ronald Fisher and John Wishart [67]. Cumulants are of interest for a variety of reasons and in some cases, theoretical treatments of problems in terms of cumulants are simpler than those using moments.

3.2.1 Definition of cumulants

The cumulants κ of any random variable S can be defined via the cumulant-generating function $\mathcal{C}(t)$, which is natural logarithm of the moment generating function.

$$\begin{aligned}\mathcal{C}(t) &= \ln[\mathbb{E}(e^{tS})] \\ &= \sum_{n=1}^{\infty} \kappa_n(S) \frac{t^n}{n!}\end{aligned}\tag{3.1}$$

where, $\ln[\cdot]$ is the natural logarithm and $\kappa_n(S)$ is the n^{th} order cumulant of S . The expansion in equation (3.1) is a Maclaurin series. We know that, the n^{th} order raw moment (i.e. *moment about zero*), m_n can be obtained by differentiating the moment-generating function $\mathbb{E}(e^{tS})$ by n times and evaluating the result at $t = 0$

$$\begin{aligned}m_n(S) &= \left. \frac{\partial^n}{\partial t^n} \mathbb{E}(e^{tS}) \right|_{t=0} \\ &= \mathbb{E}(S^n)\end{aligned}\tag{3.2}$$

Similarly, the n^{th} order cumulant, κ_n can be obtained by differentiating the cumulant-generating function $\mathcal{C}(t)$ by n times and evaluating the result at $t = 0$

$$\kappa_n(S) = \left. \frac{\partial^n}{\partial t^n} \mathcal{C}(t) \right|_{t=0}\tag{3.3}$$

Cumulant of a random variable is also called a ‘Ursell function’ or ‘connected correlation function’ as it can often be obtained by summing over connected Feynman diagrams (the sum over all Feynman diagrams gives the correlation functions) [68].

3.2.2 Cumulants and moments relation

If S is a random variable with mean μ and variance σ^2 , then $\kappa_n(S)$ can be represented as a n^{th} degree polynomial containing the first n raw moments, $m_n(S)$

$$\kappa_1(S) = m_1(S) = \mu\tag{3.4}$$

$$\kappa_2(S) = m_2(S) - m_1(S)^2 = \sigma^2\tag{3.5}$$

$$\kappa_n(S) = m_n(S) - \sum_{r=1}^{n-1} \binom{n-1}{r-1} \kappa_r(S) m_{n-r}(S)\tag{3.6}$$

where, $\binom{n-1}{r-1} = \frac{(n-1)!}{(r-1)!(n-r)!}$.

3.2.3 Joint cumulants

The joint cumulant of several random variables S_1, S_2, \dots, S_m is defined by

$$\kappa(S_1, S_2, \dots, S_m) = \sum_{\mathbf{p}} (|\mathbf{p}| - 1)! (-1)^{|\mathbf{p}|-1} \prod_{\mathbf{B} \in \mathbf{p}} \mathbb{E} \left(\prod_{i \in \mathbf{B}} S_i \right) \quad (3.7)$$

where

- partition \mathbf{p} runs through the list of all partitions of S_1, S_2, \dots, S_m ,
- $|\mathbf{p}|$ is number of parts in the partition \mathbf{p} ,
- the sum is over all partitions \mathbf{p} of the set $1, \dots, m$ of indices,
- $\mathbf{B} \in \mathbf{p}$, i.e. \mathbf{B} runs through the whole list of “blocks” of the partition \mathbf{p} .

For example

$$\kappa(S_1) = \mathbb{E}(S_1) \quad (3.8)$$

$$\kappa(S_1, S_2) = \mathbb{E}(S_1 S_2) - \mathbb{E}(S_1) \mathbb{E}(S_2) \quad (3.9)$$

$$\begin{aligned} \kappa(S_1, S_2, S_3) &= \mathbb{E}(S_1 S_2 S_3) - \mathbb{E}(S_1 S_2) \mathbb{E}(S_3) - \mathbb{E}(S_1 S_3) \mathbb{E}(S_2) \\ &\quad - \mathbb{E}(S_2 S_3) \mathbb{E}(S_1) + 2 \mathbb{E}(S_1) \mathbb{E}(S_2) \mathbb{E}(S_3) \end{aligned} \quad (3.10)$$

It can be noted that equations (3.8), (3.9) are nothing but *mean* and *co-variance* respectively. Number of total possible partitions in equations (3.8), (3.9) and (3.10) are 1, 2 and 5 respectively. In general, if there are m random variables, then, total number of possible partitions is m^{th} Bell number B_m . In combinatorial mathematics, the Bell numbers count the number of partitions of a set and they satisfy a recurrence relation involving binomial coefficients

$$B_{m+1} = \sum_{i=0}^m \binom{m}{i} B_i \quad (3.11)$$

Starting with $B_0 = B_1 = 1$, the first ten Bell numbers are 1, 1, 2, 5, 15, 52, 203, 877, 4140, 21147 . . .

3.2.4 Properties of cumulants

Cumulants exhibit some characteristic properties as mentioned below

3.2.4.1 Additivity

Suppose S_1, S_2, \dots, S_m are m independent random variables, each having n^{th} cumulant. Then $S = \sum_i S_i$ has n^{th} cumulant, and

$$\kappa_n(S) = \sum_i \kappa_n(S_i) \quad (3.12)$$

i.e. the n^{th} cumulant of a sum of independent random variables is simply the sum of the n^{th} cumulants of the summands. It means, the cumulants accumulate and hence the name ‘cumulants’.

3.2.4.2 Homogeneity

Suppose S is a random variable with a n^{th} cumulant. Then for any constant $c \in \mathbb{R}$, cS has a n^{th} cumulant and

$$\kappa_n(cS) = c^n \kappa_n(S) \quad (3.13)$$

3.2.4.3 Semi-variance

The first cumulant is ‘shift-equivariant’ and all the others are ‘shift-invariant’; hence the original name of *semi – variants*. Then, for any constant c

$$\kappa_i(S + c) = \begin{cases} \kappa_i(S) + c, & i = 1 \\ \kappa_i(S), & i \geq 2 \end{cases} \quad (3.14)$$

3.2.4.4 Gaussian random variable

If S is a Gaussian random variable with mean μ and variance σ^2 , then

$$\kappa_i(S) = \begin{cases} \mu, & i = 1 \\ \sigma^2, & i = 2 \\ 0, & i \geq 3 \end{cases} \quad (3.15)$$

Since the first and second cumulants of any random variables are its mean and variance (see equations (3.8) and (3.9)), the Gaussian random variables have the simplest possible cumulants.

3.2.5 Cumulants of a random process

If $s(t)$ is a random process then, we denote its i^{th} order cumulant as

$$\kappa_{is}(\boldsymbol{\tau}) = \kappa\{s(t), s(t + \tau_1), \dots, s(t + \tau_{i-1})\} \quad (3.16)$$

where $\boldsymbol{\tau} = (\tau_1, \tau_2, \dots, \tau_{i-1})$ and $\tau_1, \tau_2, \dots, \tau_{i-1}$ are delays applied to $s(t)$. Similarly, its i^{th} order moment at delay $\boldsymbol{\tau}$ is defined as

$$m_{is}(\boldsymbol{\tau}) = m\{s(t)s(t + \tau_1)\dots s(t + \tau_{i-1})\} \quad (3.17)$$

General definitions and properties of cumulants can be found in [69]. For e.g. if $s(t)$ is zero-mean, then

$$\begin{aligned} \kappa_{4s}(\tau_1, \tau_2, \tau_3) &= \kappa\{s(t), s(t + \tau_1), s(t + \tau_2), s(t + \tau_3)\} \\ &= E[s(t)s(t + \tau_1)s(t + \tau_2)s(t + \tau_3)] - E[s(t)s(t + \tau_1)]E[s(t + \tau_2)s(t + \tau_3)] \\ &\quad - E[s(t)s(t + \tau_2)]E[s(t + \tau_1)s(t + \tau_3)] - E[s(t)s(t + \tau_3)]E[s(t + \tau_1)s(t + \tau_2)] \\ &= m_{4s}(\tau_1, \tau_2, \tau_3) - m_{2s}(\tau_1)m_{2s}(\tau_3 - \tau_2) - m_{2s}(\tau_2)m_{2s}(\tau_3 - \tau_1) \\ &\quad - m_{2s}(\tau_3)m_{2s}(\tau_2 - \tau_1) \end{aligned} \quad (3.18)$$

Although it may apparently be seem that cumulants are more tedious than moments, they possess important properties, which do not hold for moments.

Gaussian case: If $s(t)$ is a Gaussian random process with mean μ and variance σ^2 , then $\kappa_{is}(\boldsymbol{\tau}) \forall k > 3, \forall \boldsymbol{\tau}$. But, for moments in general, we don't have $m_{is}(\boldsymbol{\tau}) = 0, \forall \boldsymbol{\tau}$ for $i > 3$, even if $s(t)$ is Gaussian. Therefore, a cumulant in a higher-order than second can be used for the measurement of non-Gaussianity or non-normality of time sequence. By putting $\kappa_{4s}(\tau_1, \tau_2, \tau_3) = 0$, into the 4th order cumulant in equation (3.18), we obtain

$$m_{4s}(\tau_1, \tau_2, \tau_3) = m_{2s}(\tau_1)m_{2s}(\tau_2 - \tau_3) + m_{2s}(\tau_2)m_{2s}(\tau_1 - \tau_3) + m_{2s}(\tau_3)m_{2s}(\tau_1 - \tau_2) \quad (3.19)$$

This is one form of the Gaussian moment theorem [70] based on which references [71–73] derive the closed-form expressions. As cumulants are the higher-order generalization of covariance functions; they can naturally be used as a tool to derive closed-form expression for the auto-covariance functions

Independent and identically distributed case: In probability theory and statistics, a sequence or other collection of random variables is independent and identically distributed (i.i.d.), if each random variable has the same probability distribution as the others and all are mutually independent. So, if $s(t)$ is an i.i.d. process then its i^{th} order cumulant is a multidimensional Dirac functions [74], given by

$$\kappa_{is}(\boldsymbol{\tau}) = \kappa_{is}(\mathbf{0}) \cdot \delta(\boldsymbol{\tau}), \forall i, \forall \boldsymbol{\tau} \quad (3.20)$$

where δ is the Kronecker delta function. However, for $i > 2$, $m_{is}(\boldsymbol{\tau})$ is not a delta function in general. If $s(t)$ is zero mean and i.i.d. with variance σ^2 , then it is also wide-sense stationary (WSS). This property implies that cumulants, but not moments, characterize independence.

For a WSS process $s(t)$, its PSD can be defined as the FT of its auto-covariance function $\kappa_{2s}(t)$:

$$S_{2s}(f) = \int_{-\infty}^{+\infty} \kappa_{2s}(\tau) e^{-j2\pi f\tau} d\tau \quad (3.21)$$

Symmetrical case: If $s(t)$ is a zero-mean random process having a symmetrical distribution, then

$$\kappa_{is}(\boldsymbol{\tau}) = 0, \forall i \text{ odd}, \forall \boldsymbol{\tau} \quad (3.22)$$

This property also holds for moments, i.e. $m_{is}(\boldsymbol{\tau}) = 0, \forall i \text{ odd}$.

Complex case: If $s(t)$ is a complex random process, then we can conjugate any copy of s in the cumulant expression and obtain different versions of the i^{th} -order cumulant. For $i = 2$ for example, we define the auto-covariance function as

$$\begin{aligned} \kappa_{2s}(\tau) &= \kappa\{s(t), s^*(t + \tau)\} \\ &= \kappa\{s^*(t), s(t + \tau)\} \end{aligned} \quad (3.23)$$

3.3 Spectral prediction by cumulants

We recall that $\dot{x}(t)$ and $y(t)$ are the base-band equivalent of PA input and output respectively in continuous-time respectively. Let us assume that $\dot{x}(t)$ is zero-mean, Gaussian and i.i.d process. Under this assumption $\kappa_{2\dot{x}}(\tau)$ is real-valued and even i.e. $\kappa_{2\dot{x}}(\tau) = \kappa_{2\dot{x}}(-\tau)$. As a result, the input PSD $S_{2\dot{x}}(f)$ is real-valued and non-negative. For high number of sub-carriers, we can assume the FBMC-OQAM signal to a Gaussian process as evident from central limit theorem. The auto-covariance function of the PA output $y(t)$, denoted by $\kappa_{2y}(\tau)$ is same as its auto-correlation function, since $y(t)$ is zero-mean and can be written as

$$\begin{aligned} \kappa_{2y}(\tau) &= \kappa\{y(t)y^*(t + \tau)\} \\ &= \mathbb{E}[y(t)y^*(t + \tau)] \end{aligned} \quad (3.24)$$

by substituting the polynomial model given in equation (2.51) in the above equation (3.24) gives

$$\begin{aligned} \kappa_{2y}(\tau) &= \kappa \left[\sum_{k=0}^{\Upsilon} a_{2k+1} [\dot{x}(t)]^{k+1} [\dot{x}^*(t)]^k \sum_{l=0}^{\Upsilon} a_{2l+1}^* [\dot{x}^*(t + \tau)]^{l+1} [\dot{x}(t + \tau)]^l \right] \\ &= \sum_{k=0}^{\Upsilon} \sum_{l=0}^{\Upsilon} a_{2k+1} a_{2l+1}^* \kappa([\dot{x}(t)]^{k+1} [\dot{x}^*(t)]^k [\dot{x}^*(t + \tau)]^{l+1} [\dot{x}(t + \tau)]^l) \end{aligned} \quad (3.25)$$

The expected value term in equation (3.25) is one-dimensional higher-order cumulant of $\dot{x}(t)$ at delay

$$\underbrace{(0, 0, \dots, 0)}_{2k}, \underbrace{\tau, \tau, \dots, \tau}_{2l+1} \quad (3.26)$$

This implies that by knowing the joint, multi-dimensional probability density function (PDF) of $\dot{x}(t)$, then the theoretical value of this cumulant can be calculated. However, if $\dot{x}(t)$ is not i.i.d. then its PDF is rarely known and hence we have to probe for alternate ways to compute $\kappa_{2y}(\tau)$. The closed-form expressions for both Gaussian and non-Gaussian random processes has been derived in [75]. Since, $\dot{x}(t)$ is symmetrical, the equation (3.25) can be expanded as

$$\begin{aligned} \kappa_{2y}(\tau) &= \sum_{k=0}^{\Upsilon} |a_{2k+1}|^2 \cdot \kappa\{[\dot{x}(t)]^{k+1} [\dot{x}^*(t)]^k, [\dot{x}^*(t+\tau)]^{k+1} [\dot{x}(t+\tau)]^k\} \\ &+ \sum_{\substack{k,l=0 \\ k \neq l}}^{\Upsilon} 2 \cdot \Re[a_{2k+1} a_{2l+1}^*] \cdot \kappa\{[\dot{x}(t)]^{k+1} [\dot{x}^*(t)]^k, [\dot{x}^*(t+\tau)]^{l+1} [\dot{x}(t+\tau)]^l\} \end{aligned} \quad (3.27)$$

We recall that $\Re[\cdot]$ is the real part of the complex term. For Gaussian process, all cumulants of order greater than 2, gets vanished. Thus, the equation (3.27) can be simplified and expressed in terms of $\kappa_{2\dot{x}}(\tau)$ for a $(2\Upsilon + 1)^{th}$ polynomial order non-linearity as [65]

$$\kappa_{2y}(\tau) = \sum_{m=0}^{\Upsilon} \beta_{2m+1} |\kappa_{2\dot{x}}(\tau)|^{2m} \kappa_{2\dot{x}}(\tau) \quad (3.28)$$

where the constant coefficient β_{2m+1} is given as

$$\beta_{2m+1} = \frac{1}{m+1} \left| \sum_{k=m}^{\Upsilon} a_{2k+1} \binom{k}{m} (k+1)! [\kappa_{2\dot{x}}(0)]^{2m} \right|^2 \quad (3.29)$$

The spectral regrowth prediction algorithm has been given below

Step 1-Extraction of polynomial coefficients: Initially, we have to obtain the PA conversion characteristics; based on which we compute the complex gain $G(|\dot{x}(t)|)$. For a given odd NL order $2\Upsilon + 1$, the polynomial coefficients $\{a_{2k+1}\}_{k=0}^{\Upsilon}$ can be extracted

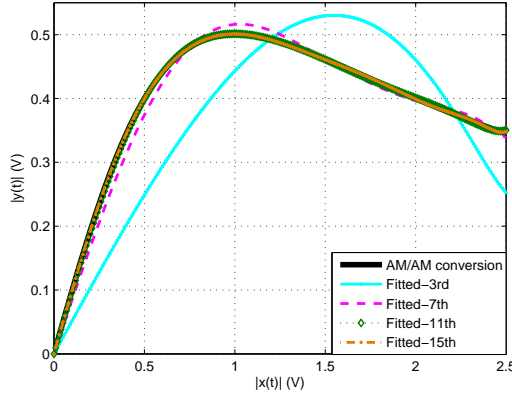


FIGURE 3.1: AM/AM conversion of Saleh Model and its polynomial fitting of orders 3, 7, 11 and 15.

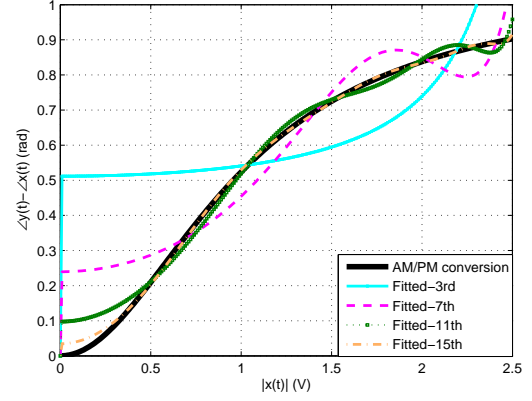


FIGURE 3.2: AM/PM conversion of Saleh Model and its polynomial fitting of orders 3, 7, 11 and 15.

from $G(|\dot{x}(t)|)$ by polynomial fitting based on LS method. We recall the equation (2.51) for polynomial model

$$y(t) = \sum_{k=0}^{\Upsilon} a_{2k+1} [\dot{x}(t)]^{k+1} [\dot{x}^*(t)]^k$$

Step 2-Derivation of closed-form expression: Derive closed-form expression for $\kappa_{2y}(\tau)$ in terms of the polynomial coefficients $\{a_{2k+1}\}_{k=0}^{\Upsilon}$ as per equation (3.28).

Step 3-Calculation of PA output PSD: The FT of $\kappa_{2y}(\tau)$, obtained from equation (3.28), yields to the PSD of the amplified signal $S_{2y}(f)$ and is given by

$$\begin{aligned} S_{2y}(f) &= \int_{-\infty}^{+\infty} \kappa_{2y}(\tau) e^{-j2\pi f\tau} d\tau \\ &= \int_{-\infty}^{+\infty} \sum_{m=0}^{\Upsilon} \beta_{2m+1} |\kappa_{2\dot{x}}(\tau)|^{2m} \kappa_{2\dot{x}}(\tau) e^{-j2\pi f\tau} d\tau \\ &= \sum_{m=0}^{\Upsilon} \beta_{2m+1} \underbrace{S_{2\dot{x}}(f) \star S_{2\dot{x}}(f) \star \dots \star S_{2\dot{x}}(f)}_{m+1} \star \underbrace{S_{2\dot{x}}(-f) \star S_{2\dot{x}}(-f) \star \dots \star S_{2\dot{x}}(-f)}_m \end{aligned} \quad (3.30)$$

where \star denotes convolution. It has to be noted that, as $S_{2\dot{x}}(f)$ is symmetric, i.e. $S_{2\dot{x}}(f) = S_{2\dot{x}}(-f)$, the $S_{2y}(f)$ is also symmetric as well.

We call this approach as spectral prediction, because, the knowledge of input PSD $S_{2\dot{x}}(f)$ and the polynomial coefficients allows the prediction of the $S_{2y}(f)$. Once we are able to model the PA (or obtain the AM/AM and AM/PM conversion measurements),

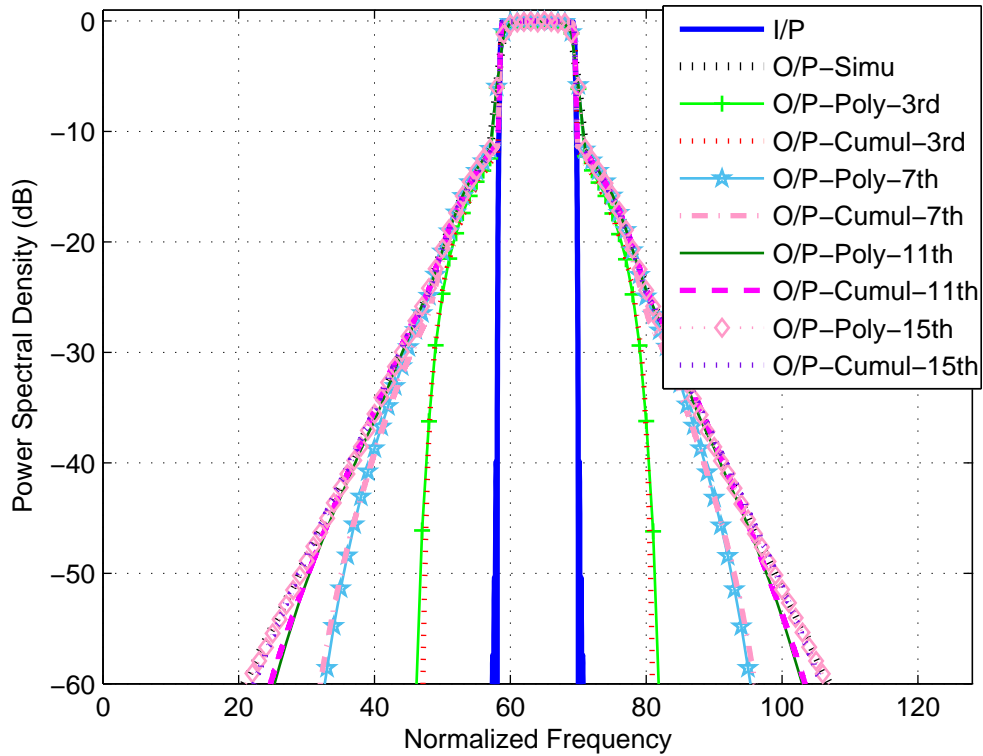


FIGURE 3.3: PSD Prediction with IBO=1 dB.

then, we can pre-calculate the complex coefficients from polynomial approximation. The input auto-correlation function $\kappa_{2i}(\tau)$ can be calculated based on analytical PSD of a FBMC-OQAM signal from the equation (2.35).

3.4 Simulation results for PSD prediction

Simulation is done for 1000 FBMC-OQAM symbols with 128 total Sub-carriers. PHY-DYAS prototype filter and Saleh model of PA has been used in the simulations. We remind that the conversion characteristics of Saleh model have been defined in equations (2.58) and (2.59).

3.4.1 Polynomial fitting

The AM/AM and AM/PM characteristics of Saleh model along with different orders of polynomial fitting, are given in Fig. 3.1 and Fig. 3.2. In these figures, we also plot the

conversion characteristics obtained after polynomial fitting with polynomials of order 3, 7, 11 and 15 respectively.

3.4.2 Spectral regrowth prediction in the case of a single user

In the legends of the PSD plots, 'Input' is the FBMC-OQAM signal input PSD, 'Output-Simu' is the simulated PSD based on real Saleh model, 'Output-Poly-3rd', 'Output-Poly-7th', 'Output-Poly-11th' and 'Output-Poly-15th' are the simulated output PSDs based on polynomial approximation with 3rd, 7th, 11th and 15th order non-linearity respectively (i.e. the PA model is the polynomial approximated model and the spectral regrowth is the simulated corresponding PSD). Similarly, 'Output-Cumul-3rd', 'Output-Cumul-7th', 'Output-Cumul-11th' and 'Output-Cumul-15th' are the analytical PSDs calculated using cumulants for respective polynomial approximations for different orders of non-linearity. Fig. 3.3 and Fig. 3.4 present the simulations results done with IBO values of 1 dB and 3 dB having 10 active sub-carriers each. We can observe that with IBO of 3 dB the 11th order polynomial gives result very close to simulated PSD, while for IBO of 1 dB it is necessary to take the 15th order polynomial fitting to have a similar behavior.

3.4.3 Spectral regrowth prediction in a cognitive radio context

In a CR context, multiple primary users can occupy the spectrum. A typical scenario in this CR context have been considered, where, three users are operating on closely spaced sub-bands. The information signals of these three users are amplified at an IBO of 1 dB. The details of active sub-bands for the three users are given below,

- User 1: 30th to 40th sub-carrier,
- User 2: 45th to 50th sub-carrier,
- User 2: 52nd to 57th sub-carrier.

The simulation results for PSD prediction when 3 users share neighboring sub-carriers is shown in Fig. 3.5. For more detail, we show the zoomed version in Fig. 3.6. In this typical CR scenario, we can notice that despite operating the PA at an IBO=1 dB, the prediction

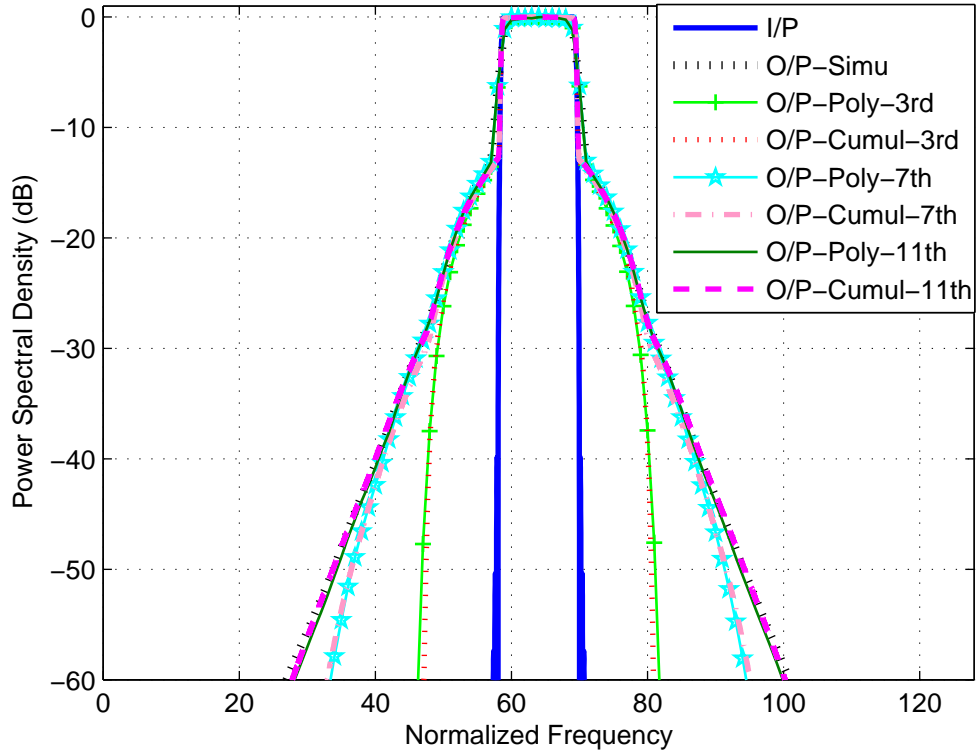


FIGURE 3.4: PSD Prediction with IBO=3 dB.

of the PSD is well achieved up to -20 dB, -25 dB and -33 dB with polynomial fittings of orders 3^{rd} , 7^{th} and 11^{th} respectively. The reason for choosing thinner sub-bands for the three users is because that when the band of active sub-carriers tends to be thinner, we need higher-order polynomial fitting to predict the output PSD accurately.

3.5 Conclusion

Power amplifiers are inherently NL and this non-linearity generates spectral regrowth in digitally modulated signals. The extent of spectral regrowth is tightly controlled by regulatory bodies. This chapter focuses on the prediction of PSD regrowth for FBMC-OQAM systems in presence of NL PA. The advantage of FBMC-OQAM systems over OFDM ones in terms of spectrum localization is lost due to non-linearity of PA and it becomes important to predict the PSD regrowth of the amplified FBMC-OQAM signal. Cumulants are used as a tool to derive closed-form expression and can be good usage in this context. Real communication signals are in general, non-Gaussian. However, due

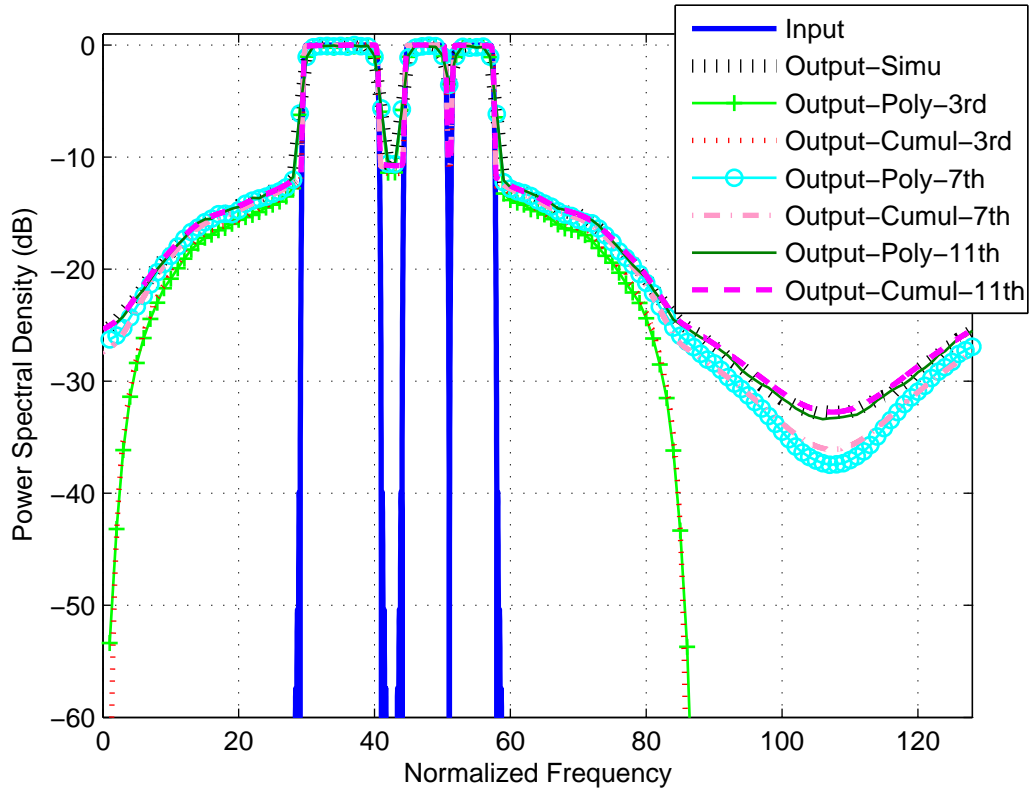


FIGURE 3.5: PSD Prediction with IBO=1 dB (3 different active Sub-bands).

to the central limit theorem, one may observe that certain aggregated signals exhibit close to Gaussian behavior. For Gaussian random process, all cumulants of order higher than 2 disappear. This is not true, in case of moments. It implies that derivation of a closed-form expression becomes much simpler. When the input to the PA is a WSS process, then its PSD can be defined as the FT of its auto-covariance function. By knowing the AM/AM and AM/PM conversion characteristics, a polynomial model can be constructed for a given polynomial order. Then, we can compute the OOB regrowth by using cumulants; thus, paving a way to derive a closed-form expression for auto-covariance function of PA output, whose FT yields the output PSD.

In this chapter, it has been demonstrated that a given IBO and a sufficient polynomial order can faithfully approximate the spectral regrowth. This polynomial order can be reduced if the PA is to be operated at a higher IBO and vice versa.

Prediction of spectral regrowth for a prescribed level of PA non-linearity can be very helpful for designing communication systems. It gives very good understanding about the severity of the PA non-linearity and its impact. Thereby, one can perform PAPR

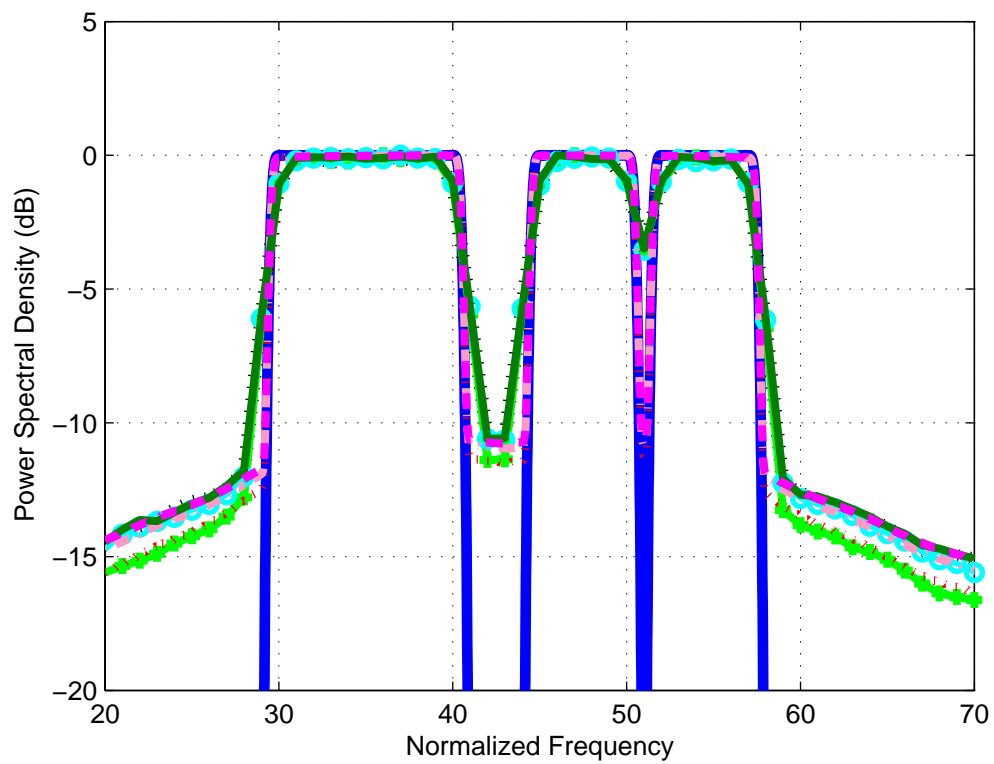


FIGURE 3.6: Zoomed version of Fig. 3.5

reduction and PA linearization in order to diminish the spectral regrowth to a level acceptable by regulatory standards. The aspect of PAPR reduction for FBMC-OQAM systems shall be elaborately dealt in detail in the forthcoming Chapter 4 and its possible application in a PMR coexistence scenario can be seen in Chapter 5.

Chapter 4

PAPR reduction techniques for FBMC-OQAM systems

4.1 Introduction

Originally, the need for PAPR reduction came into prevalence in some applications such as Radar (Radio Detection and Ranging) and Speech Synthesis. The Radar systems are limited by peak power, similar to that of communication systems. Likewise, the performance in speech synthesis applications is bound by peak power, since high peak signals lead to a hard sounding computer voice [76]. This characteristic is not desirable when simulating human speech. It is intriguing to know that the human body has also dealt with the PAPR reduction issue in a sense that in a given audible spectrum, the human speech is not as high peaked as it could be.

In MCM systems, the PAPR reduction remains to be one of the most crucial issues that need to be solved effectively with a reasonable complexity. The severity of this issue can be seen from the 3GPP specification for 4G LTE, where in the physical layer uplink (UL), the single carrier-frequency division multiple access (SC-FDMA) has been chosen instead of OFDM, owing to the high PAPR of the later. Being a MCM technique, the FBMC-OQAM system suffers from high PAPR and its frequency localization property is

no longer valid in real communication systems consisting of NL PAs leading to spectral regrowth thereby hampering much of its attractive appeal to be the ideal candidate for 5G RAT. High PAPR causes IB and OOB interferences, when the MCM signals are passed through a PA, which does not have enough linear range. With this constraint, a real communication system design needs a PA that has got longer linear region. Higher IBO results on energy wastage [39]. In order to fend off this, we ought to opt for PAPR reduction techniques, in order to operate the PA more efficiently.

This chapter is organized as follows: The Section 4.2 presents different types of PAPR reduction techniques suggested for OFDM. Section 4.3 presents the state-of-art of PAPR reduction techniques proposed for FBMC-OQAM. Later, Sections 4.4, 4.5 and 4.6, elaborate the novel PAPR reductions proposed in this thesis dissertation. Finally, the chapter is concluded in Section 4.6.

4.2 PAPR reduction techniques suggested for OFDM

4.2.1 State of the art

In multi-carrier based communication systems, the PAPR reduction remains to be one of the most crucial issues that need to be solved effectively with a reasonable complexity. Existing PAPR schemes of OFDM signals that are popular, include clipping [11], Tone Injection (TI) [12], Tone Reservation (TR) [13], Active Constellation Extension (ACE) [14], Partial Transmit Sequence (PTS) [15], Selective Mapping (SLM) [16] and block coding [17]. Comparison of most of these aforesaid schemes can be found in [18] and [19]. In general, the PAPR reduction techniques can be broadly classified into three varieties namely *clip effect transformations (clipping)*, *block coding techniques* and *probabilistic approaches*.

4.2.2 Clipping

The simplest PAPR reduction technique is clipping. In this method, the peaks of the signal $x(t)$ are clipped down whenever the peak crosses a given threshold, α_o as shown

below,

$$x_c(t) = \begin{cases} x(t) & |x(t)| \leq \alpha_o, \\ \alpha_o \cdot e^{j\angle x(t)} & |x(t)| > \alpha_o \end{cases} \quad (4.1)$$

where $\angle x(t)$ is the phase of $x(t)$. In basic form, clipping is equivalent to the SEL PA model. With this method, it's evident that no side information is required to transmit to the receiver since this is a straightforward PAPR reduction technique. However, the disadvantage is that there will be significant spectral regrowth especially when the value of α_o is small [77]. Generally, when clipping is used, it is necessary to filter the clipped signal in order to decrease out-of-band spectral regrowth. In addition to this, clipping an OFDM signal induces clipping noise, which in turn augments the error rate. In a sense, one can view the induced clipping noise as approximately independent additive white Gaussian noise (AWGN) [78], which can lead to a simple symbol error rate (SER) expression for AWGN channels. Numerous proposals have been made aiming at reducing the spectral regrowth and error rate increase due to clipping. One notable proposition is by presenting an iterative receiver design that try to negate the error rate increase induced by clipping [79].

4.2.3 Selected Mapping

SLM was introduced in [16] by Bauml, Fischer and Huber, where the term “selected mapping” was coined. SLM takes advantages of the fact that the PAPR of an OFDM signal is heavily dependent on phase shifts in its frequency-domain. Firstly, we generate U complex phase rotation vectors $\phi^{(u)}$, for $0 \leq u \leq U - 1$, of length N as:

$$\phi^{(u)} = \begin{cases} (1, \dots, 1)^T, & u = 0, \\ (\phi_0^{(u)}, \dots, \phi_{N-1}^{(u)})^T, & 1 \leq u \leq U - 1. \end{cases} \quad (4.2)$$

where, $\phi_k^{(u)}$ is the k^{th} element of $\phi^{(u)}$ defined as

$$\phi_k^{(u)} = e^{j\psi_k} \in \mathbb{C}, \quad 0 \leq u \leq U - 1, \quad 0 \leq k \leq N - 1 \quad (4.3)$$

where, ψ_k is a uniformly distributed phase between 0 and 2π . The frequency-domain input symbols \mathbf{X} with N tones, are phase rotated by U phase rotations vectors $\{\phi^{(u)}\}_{u=0}^{U-1}$,

having a size of N

$$\mathbf{X}^{(u)} = \mathbf{X} \odot \phi^{(u)}, \quad 0 \leq u \leq U - 1 \quad (4.4)$$

where, \odot denotes carrier-wise point-to-point multiplication. $\{\mathbf{X}^{(u)}\}_{u=0}^{U-1}$ carry same information and possess identical constellation as \mathbf{X} . By applying IFFT operation on $\{\mathbf{X}^{(u)}\}_{u=0}^{U-1}$, we obtain the U time-domain signal patterns $\{x^{(u)}(t)\}_{u=0}^{U-1}$. The target of the optimization problem is to identify the signal $x^{(u_{min})}(t)$ that has the least PAPR so that

$$u_{min} = \arg \min_{0 \leq u \leq U-1} \left[PAPR_{x^{(u)}(t)} \right] \quad (4.5)$$

The index of respective phase rotation vector, u_{min} is sent to receiver as side information (SI) comprising of $\log_2 U$ bits. A salient feature of SLM is that, it doesn't impact the BER. In this dissertation, we will not discuss how the transmission of SI is done. The SLM scheme performs PAPR reduction by generating U independent mappings of the time-domain signal $x(t)$ and picking the signal with lowest peak.

4.2.4 Partial transmitting sequence

In a classical PTS scheme [15], the frequency domain input symbols, \mathbf{X} are partitioned into V sub-blocks, $\{\mathbf{X}^{(v)}\}_{v=0}^{V-1}$ that are zero-padded to get a length N vectors.

$$\mathbf{X} = \sum_{v=0}^{V-1} \mathbf{X}^{(v)} \quad (4.6)$$

Every v^{th} sub-block is FBMC-OQAM modulated in order to be rotated with a phase factor $\{e^{j\omega(i,v)}\}_{i=0}^{W-1}$, where $\omega \in [0, 2\pi)$ and W is the total number of candidate phases that is to be chosen for a sub-block. The goal of the PTS scheme is to find $\{e^{j\omega(i,v)}\}_{v=0}^{V-1}$ out of W^V signal patterns such that

$$\{e^{j\omega(i,v)}\}_{v=0}^{V-1} = \arg \min_{\{e^{j\omega(i,v)}\}_{v=0}^{V-1}} \left[\max \left| \sum_{v=0}^{V-1} \mathcal{F}_N^{-1} \{ \mathbf{X}^{(v)} \} e^{j\omega(i,v)} \right| \right] \quad (4.7)$$

where, $\mathcal{F}_N^{-1}\{\cdot\}$ is a N -point IFFT transform. The PAPR reduction capability of PTS depends on the size of V and W . Totally there are W^V possible "mappings" in a PTS scheme at the cost of V IFFT operations. However, these V IFFT operations are mostly

on zero sequences, which reduces the complexity from $\mathcal{O}(VN \log N)$ to $\mathcal{O}(VN \log \frac{N}{V})$. Albeit, these mappings are not independent, since every sub-block is multiplied by same phase constant. Therefore, the PAPR of one mapping is correlated with the PAPR of another mapping whenever the mapping is not independent. This is the reason for PTS falling well behind of a scheme like SLM that test W^V independent mappings. In PTS, a side information (SI) that can distinguish W^V different mappings has to be transmitted that needs $V \log_2 W$ bits. PTS and SLM are both generalizations of each other. SLM is a PTS scheme, where only one carrier is present in each sub-block, i.e. each sub-carrier is rotated individually instead of rotation of sub-blocks of sub-carriers.

4.2.5 Tone reservation

Classical TR is an adding signal technique and was first introduced in [21]. The idea behind TR is to isolate energy used to cancel large peaks to a predefined set of tones, namely peak reserved tones (PRTs). These tones do not carry any useful information and are orthogonal to the data tones (DTs). This orthogonality makes recovering the data trivial. Stated mathematically, the resulting signal to be transmitted will be

$$x(t) = d(t) + c(t), 0 \leq t < \infty \quad (4.8)$$

where, $c(t)$ is the peak cancellation signal and $d(t)$ is the data signal (i.e. related to data only). $x(t)$ can be represented in frequency domain as $X[n]$, given by

$$X[n] = \begin{cases} D[n], & n \in \mathcal{B}^c \\ C[n], & n \in \mathcal{B} \end{cases} \quad (4.9)$$

where,

- \mathcal{B} is the set of locations of PRTs, which is of length R ,
- \mathcal{B}^c is complement set of \mathcal{B} , containing the locations of DTs and is of length $N - R$,
- $D[n]$ is DT set and $D[n] = 0$, for $n \in \mathcal{B}$,
- $C[n]$ is PRT set and $C[n] = 0$, for $n \in \mathcal{B}^c$.

The aim of TR scheme is to compute the optimal values of reserved tones subject to

$$\begin{aligned}\hat{c}(t) &= \arg \min_{c(t)} \min_{t \in [0, \infty)} PAPR_{x(t)} \\ &\equiv \arg \min_{C[n]} \left[\|d(t) + \mathcal{F}_N^{-1}\{C[n]\}\|_{\infty}^2 \right], 0 \leq t < \infty\end{aligned}\quad (4.10)$$

The aim is to select proper PRT set, so that the PAPR of the signal is reduced. Actually, it is difficult to solve the above equation even though the problem appears to be simple. Nevertheless, the optimal $\hat{c}(t)$ can be obtained by solving equation (4.10), which can be done by convex optimization algorithms such as QCQP [20], POCS [21], gradient search [20], etc. The QCQP has the computational complexity of $\mathcal{O}(RN^2)$ and yields to the optimal result. It is an optimization problem in which both the objective function and the constraints are quadratic functions. The sub-optimal approaches such as POCS and gradient search has the computational complexity of $\mathcal{O}(N \log N)$ and $\mathcal{O}(N)$ respectively. In classical TR, the reserved tones can be removed easily at the receiver side. Though impressive, TR is not without shortcomings. Since some tones are reserved for PAPR reduction, there will be loss of data rate. In [13], for TR method, nearly 20% of the total sub-carriers could be reserved.

Nevertheless, finding the optimal PRT location set, \mathcal{B} is a hard problem and it heavily impacts the performance of any TR scheme. In [13], it has been shown that the random PRTs yield very good results than equidistant or contiguous PRTs. The peak reduction kernel, \mathcal{K} design has been first suggested in [13], where, minimization of kernel side-lobes is the design criteria for choosing the optimal random PRT locations. Once \mathcal{B} with a given size R , is determined, the same can be used in solving equation (4.10). The peak reduction kernel, \mathcal{K} should be Dirac-type, i.e. as close as possible to the unit impulse symbol δ of length N , which is defined as

$$\delta[n - n_0] = \begin{cases} 1, & n = n_0, 0 \leq n < N - 1 \\ 0, & n \neq n_0, 0 \leq n < N - 1 \end{cases}\quad (4.11)$$

where, n_0 is a integer constant that can take any value between 0 and $N - 1$. In the case of OFDM, \mathcal{K} obeys circular property and hence n_0 , (the maximum of the Dirac-type kernel) can be chosen to be 0. By multiplying the PRT tones by an exponential will

change the positions of n_0 . For FBMC-OQAM, design of \mathcal{K} is subject to

$$\mathcal{K} = \arg \min_{\mathcal{B}, \mathcal{K}_0} [\|\mathcal{F}_N^{-1}(\mathcal{K}_0) - \delta[n - n_0]\|^2] \quad (4.12)$$

where \mathcal{K}_0 is any peak reduction kernel that can be generated based on a given \mathcal{B} , which obeys the conditions $\mathcal{K}_0[n] \neq 0$, for $n \in \mathcal{B}$ and $\mathcal{K}_0[n] = 0$, for $n \in \mathcal{B}^c$. For R reserved tones out of N tones, there will be $\binom{N}{R}$ possible combinations in total. For every combination of PRT locations, we compute a kernel. Out of all computed kernels, we pick the one, which has the least secondary peaks, i.e. the difference between the central peak and the secondary ones will be maximum. Once \mathcal{B} with a given size R , is determined from solution of equation (4.12), then we can use them same in solving equation (4.10).

4.2.6 Tone Injection

Prompted by data rate loss in TR, Tellado has introduced TI [12]. The idea is to enlarge the original constellation by ν times (*for e.g., from a QPSK constellation to 16 QAM or 64 QAM constellation*). By shifting the copies of the original constellation, the extra constellation points are generated. Assume d_{min} be the minimum distance between two points in the original MQAM constellation, then the constellation copies are separated by distance p in such a way that d_{min} of the enlarged constellation is same as the original d_{min} as below,

$$p \geq d_{min} \log_2 M \quad (4.13)$$

PAPR reduction is possible if the original constellation is arranged properly. The catch in this scheme is that by taking modulo p of the in-phase and quadrature phase components of the received signal, the receiver can recover the original constellation. This means that for TI, there is no need to transmit the side information (SI) to the receiver. Like TR, this scheme also involves an increase of average power since it is intuitive that any extension of the constellation will lead to increase in average power.

Arguably, there are two degrees of freedom in TI. One is the choice of tones and the other is the size of enlarged constellation which depends on ν . Searching the right possible combination involves high complexity.

4.2.7 Active Constellation Extension

This PAPR reduction technique was first proposed in [80]. Though both TI and ACE involves in extended constellation, the later differs in the manner of the constellation extension. Similar to that of TI, in ACE the minimum distance is not decreased explicitly, however in a peak power constraint system, it does. The original constellation is extended only in the regions of the signal plane where the new extended point should be further from any other points. Same methods used for TR such as POCS or gradient search algorithm, can be employed for the finding of the extension points.

4.2.8 Block coding

One of the notable techniques for reducing PAPR is Block coding. In this technique, an input data is encoded to a codeword with low PAPR. For example, in order to reduce the PAPR of OFDM signals with four sub-carriers, three-bit input data can be mapped to a four-bit codeword and a parity is added to the last bit in the frequency domain. Golay complementary sequence as codewords, can also be used to achieve the same, which can ensure that the OFDM signals with any number of sub-carriers, have PAPR of at most 3 dB [81]. A soft Reed-Muller decoding algorithm has been proposed in [82], to make this method more efficient. Another method, by constructing Golay complementary sequences with 64 QAM constellation for OFDM signals has also been proposed in [83]. Albeit, the usage of Golay complementary sequence can incur significant rate loss due to redundancy. Another disadvantage in coding methods is that they are not downward compatible since the receiver has to be modified (with a decoding algorithm).

4.3 PAPR reduction techniques suggested for FBMC-OQAM

The classical schemes, proposed for OFDM, cannot be directly applied to FBMC-OQAM. Indeed, FBMC-OQAM signals have overlapping impulse response. Of late, some PAPR schemes have been suggested for FBMC-OQAM systems. An ACE scheme based on linear programming optimization has been proposed in [28]. Iterative clipping based techniques have been proposed in [24] and [25]. ACE clubbed with TR, has

been put-forward in [29]. In [23], the authors proposed sliding window tone reservation technique for FBMC-OQAM signals, based on projection onto convex sets (POCS) method proposed for OFDM. POCS has less computational complexity; albeit, it is a sub-optimal approach.

Coming to recently proposed probabilistic schemes, in [22], an overlapped SLM (OSLM) by extending the classical SLM with consideration of overlapping nature in FBMC-OQAM signals has been proposed. Another improved SLM technique with low complexity has been put-forward by [26]. All these three schemes involve symbol-by-symbol optimization by fixing or already choosing the phase rotations of the past symbols. Symbol-by-symbol approach will lead to sub-optimal solution since, PAPR reduction obtained for a given symbol can most probably be destroyed when optimization is done for the successive symbol. In [27], a trellis-based PTS scheme with multi-block joint optimization (MBO) has been introduced, where it has been demonstrated that FBMC-OQAM system outperforms the OFDM system, if the symbol overlapping nature of the former is well exploited. In the same paper, a sub-optimal scheme with reduced complexity has been presented.

4.4 Dispersive SLM

Similar to the classical SLM scheme, in DSLM each input symbol vector \mathbf{X}_m in equation (2.7) is phase rotated with U different input vectors giving $\{\mathbf{X}_m^{(u)}\}_{u=0}^{U-1}$. The symbols, $\{a_{m',n}^{(u)}\}_{u=0}^{U-1}$ are chosen from $\{\mathbf{X}_m^{(u)}\}_{u=0}^{U-1}$ as per equation (2.8). From Fig. 2.9, it is evident that unlike OFDM, the FBMC-OQAM symbol energy spreads into its succeeding symbols rather than in its own one, which means that almost all of its energy lies in the two succeeding symbols period intervals rather than its own one. So, in order to find the optimal rotation for any m^{th} FBMC-OQAM symbol, the overlapping of its previous symbols is also taken into consideration.

The illustration of how the overlapping of previous symbols are taken into consideration in DSLM algorithm is shown in Fig. 4.1.

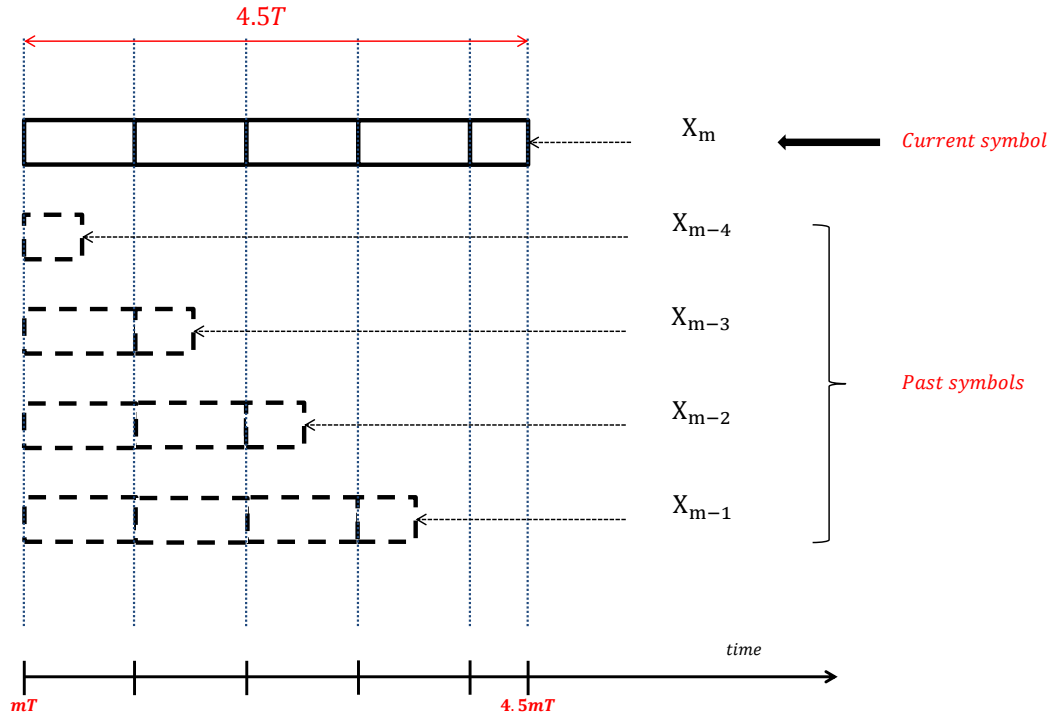


FIGURE 4.1: Illustration of past symbol overlap on the m^{th} FBMC-OQAM symbol.

4.4.1 DSLM algorithm

The DSLM algorithm involves the following steps,

Step 1 - Initialization: Firstly, we generate M complex input symbol vectors $\{\mathbf{X}_m\}_{m=0}^{M-1}$ as per equation (2.7) and U phase rotation vectors $\{\phi^{(u)}\}_{u=0}^{U-1}$ of length N as per equation (4.2). We initialize the counter m and as long as the condition $0 \leq m \leq M - 1$ is satisfied, we perform the following **Steps 2, 3, 4, 5, 6** and **7** in a repeated manner.

Step 2 - Phase rotation: The m^{th} input symbol vector \mathbf{X}_m is phase rotated with U different phase rotation vectors $\{\phi^{(u)}\}_{u=0}^{U-1}$ as per equation (4.4), giving $\{\mathbf{X}_m^{(u)}\}_{u=0}^{U-1}$. The OQAM symbols, $a_{m',n}^{(u)}$ are chosen from $\mathbf{X}_m^{(u)}$ as per equation (2.8).

Step 3 - FBMC-OQAM modulation: FBMC-OQAM modulation is done for all

patterns of m^{th} input symbol vector, is written by

$$\begin{aligned}
 x_m^{(u)}(t) = & \underbrace{\sum_{m'=0}^{2m-1} \sum_{n=0}^{N-1} a_{m',n}^{(u_{min}^m)} h(t - m'T/2) e^{j\frac{2\pi}{T}nt} e^{j\varphi_{m',n}}}_{\text{overlapping past symbols}} \\
 & + \underbrace{\sum_{m'=2m}^{2m+1} \sum_{n=0}^{N-1} a_{m',n}^{(u)} h(t - m'T/2) e^{j\frac{2\pi}{T}nt} e^{j\varphi_{m',n}}}_{\text{current symbol}}
 \end{aligned} \tag{4.14}$$

where,

- $x_m^{(u)}(t) \neq 0$ from $t = [0, (2m + 1)\frac{T}{2} + 4T)$,
- $a_{m',n}^{(u_{min}^m)}$ are from previous selected symbols $\mathbf{X}_m^{(u_{min}^m)}$,
- $m \in \{0, 1, \dots, M - 1\}$ and $0 \leq u \leq U - 1$.

From equation (4.14), it is intuitive that we have U patterns of the modulated FBMC-OQAM signal $x_m^{(u)}(t)$, for $0 \leq u \leq U - 1$.

Step 4 - Partial PAPR Calculation: Then, we compute the partial PAPR of $x_m^{(u)}(t)$ on a certain interval $T_0 = [mT + T_a, mT + T_b)$, which is any arbitrary interval within the $[mT, mT + 4.5T)$ interval:

$$PAPR_{(T_0)}^{(u)} = \frac{\max_{t \in T_0} |x_m^{(u)}(t)|^2}{\frac{1}{T_0} \int_{T_0} |x_m^{(u)}(t)|^2 . dt} \tag{4.15}$$

where $T_a \geq 0$ and $T_b < 4.5T$.

Step 5 - Selection: Among $PAPR_{T_0}^{(u)}$, the index u is chosen for the signal with least PAPR as per the below criterion:

$$u_{min}^m = \arg \min_{0 \leq u \leq U-1} \left[PAPR_{x_m^{(u)}(t)} \right], mT + T_a \leq t < mT + T_b \tag{4.16}$$

where, $t \in T_0$, $T_a \geq 0$ and $T_b < 4.5T$. The choice of interval T_0 during partial PAPR calculation plays vital role in ameliorating the peak reduction performance. It can be applied for any prototype filter.

Step 6 - Updation: We update the current overlapping input symbol vector:

$$\mathbf{X}_m^{(u_{min}^m)} = \mathbf{X}_m \cdot \phi^{(u_{min}^m)} \quad (4.17)$$

The input symbol that has been rotated with $\phi^{(u_{min}^m)}$ is considered to be optimally rotated w.r.t DSLM scheme.

Step 7 - Incrementation: Increment the value of m by 1 and go to **Step 2**.

4.4.2 Simulation results with DSLM

The objective of the simulations is to understand the impact of duration T_0 while calculating PAPR and comparison with OFDM when classical SLM scheme is used. Simulations are done for a FBMC-OQAM signal that has been generated from 10^5 4-QAM symbols with 64 sub-carriers. The PHYDYAS filter has been chosen to be the prototype filter was used in the simulation, which spans for $4T$ [41]. Nevertheless, the scheme holds for any prototype filter. The range of the complex phase rotation vector was chosen such as, $\phi^{(u)} \in \{1, -1, j, -j\}$. In general most of the PAPR reduction schemes are implemented over discrete-time signals. So, we need to sample the continuous-time FBMC-OQAM signal $x(t)$, thereby obtaining its discrete-time signal $x[n]$. In order to well approximate the PAPR, we have over sampled the modulated signal by a factor of 4 and then implemented the Dispersive SLM scheme on the discrete-time signal $x[n]$.

4.4.2.1 Impact of variation of T_0 duration

When computing the PAPR, the duration of $[T_a, T_b)$ of T_0 seems to make a significant impact in the performance of DSLM scheme as depicted in Fig. 4.2. By varying the duration over which the PAPR is calculated, we can see how it is affecting the efficiency of the DSLM scheme. ‘FBMC 1st’, ‘FBMC 23rd’ and ‘FBMC 1234th’ in the legend indicate that the duration considered for PAPR calculation of a given FBMC-OQAM symbol are $[T_a, T_b) = \{[0, T), [T, 3T), [0, 4T)\}$ respectively. The phase rotation vector size is fixed for $U = 4$.

We can infer from this figure that, when only current symbol period is considered (i.e. $[0, T)$ w.r.t the current symbol), then it won’t lead to any improvement. It implies that

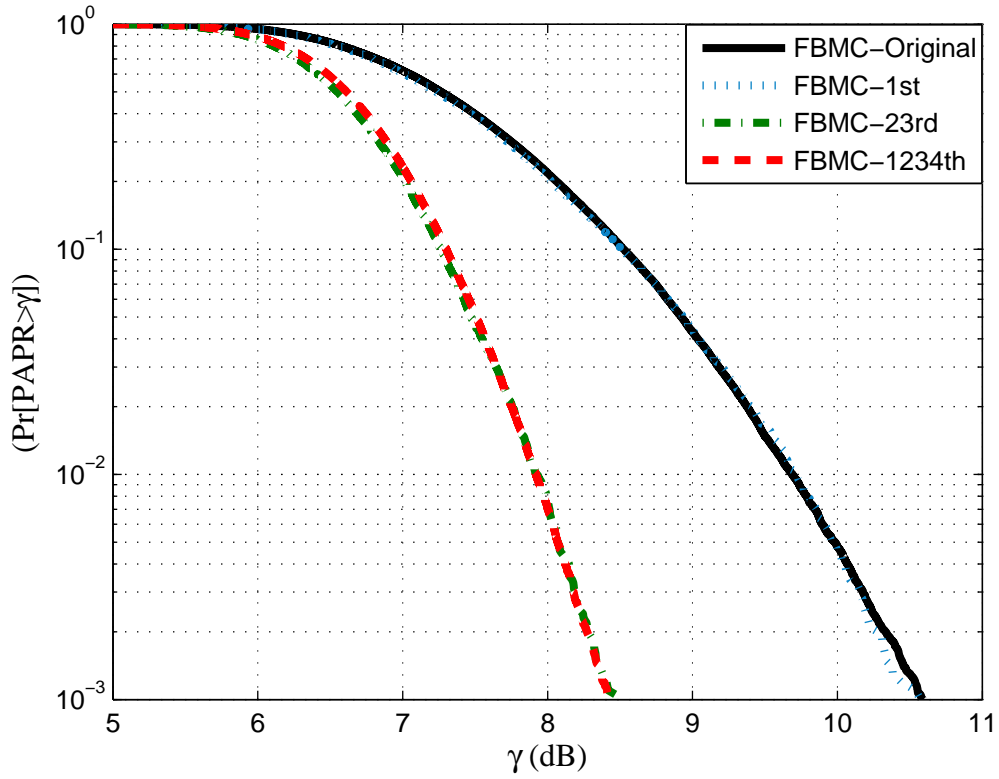


FIGURE 4.2: CCDF of PAPR plot for FBMC-OQAM symbols with partial PAPR calculated over $[T_a, T_b) = \{[0, T), [T, 3T), [0, 4T)\}$ with $U = 4$ to illustrate the impact of variation of T_0 duration on the DSLM scheme.

because of the overlapping nature of FBMC-OQAM symbols, direct implementation of classical SLM i.e. $[T_a, T_b) = [0, T)$ is ineffective.

Whereas when 2^{nd} and 3^{rd} symbol periods (i.e. $[T, 3T)$ w.r.t the current symbol) and when 1^{st} , 2^{nd} , 3^{rd} and 4^{th} symbol periods (i.e. $[0, 4T)$ w.r.t the current symbol) are taken into account, then the performance of PAPR reduction with DSLM implementation seems to be trailing very closely to that of the OFDM with classical SLM as we can see from Fig. 4.3. The reason behind this is well understood from the earlier Fig. 2.9 which shows that for a given FBMC-OQAM symbol much of its energy lies in 2^{nd} and 3^{rd} time intervals rather than in its own interval.

By taking the time dispersion of FBMC-OQAM symbols into account, $[T_a, T_b) = [0, T)$ has been varied and we have found out that intervals $[T_a, T_b) = \{[T, 3T), [T, 4T), [0, 4T)\}$ offer notable PAPR reduction when compared to the case of $[T_a, T_b) = [0, T)$.

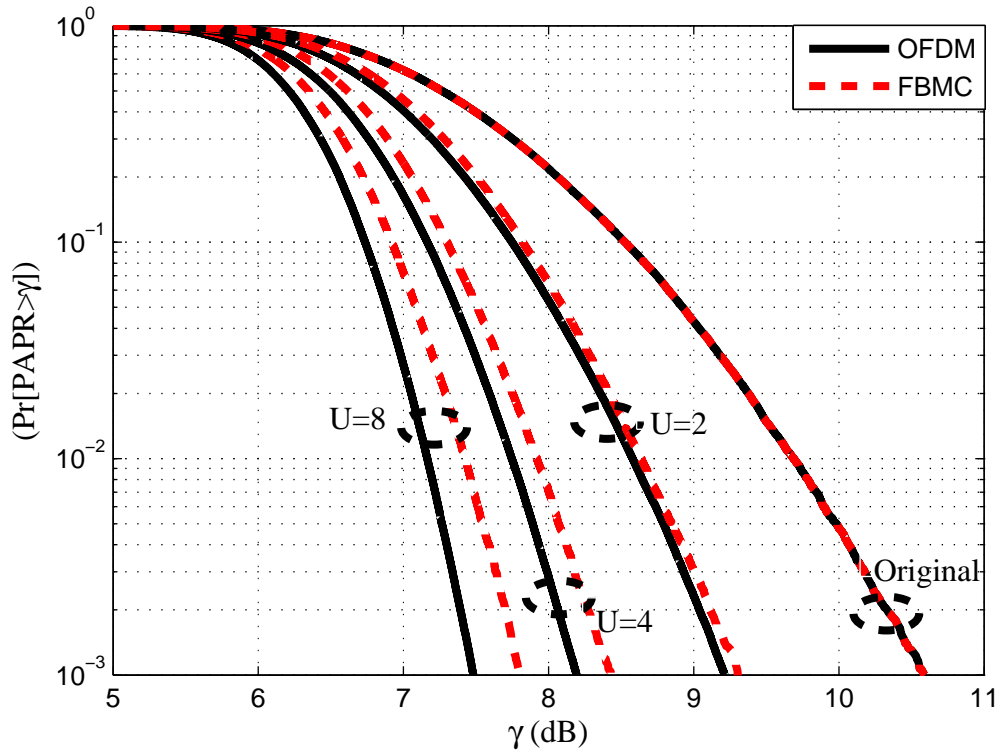


FIGURE 4.3: CCDF of PAPR plot for FBMC-OQAM symbols with PAPR calculated over $[2T, 4T)$ with $U = \{2, 4, 8\}$ to illustrate the impact of size of U on the DSLM scheme in comparison with SLM scheme for OFDM.

4.4.2.2 Impact of size of U

Like any SLM scheme, the size of phase rotation vector impacts the performance of the PAPR reduction. For an illustration of impact of the U , we have considered $[T_a, T_b) = [0, 4T)$. The different sizes considered are $U = \{2, 4, 8\}$. We can see from Fig. 4.3, that in terms of PAPR reduction, the DSLM with FBMC-OQAM is very close to the performance of OFDM with classical SLM and difference is in around of 0.05 dB, 0.25 dB and 0.32 dB at 10^{-3} value of CCDF of PAPR when $U = \{2, 4, 8\}$ respectively. It implies that when the overlapping nature of the FBMC-OQAM signals is well exploited then it can significantly impact the PAPR reduction. Another observation is that as phase rotation vector size U is getting increased; we can see the trail gap between CCDF curves of OFDM and FBMC-OQAM is getting increased.

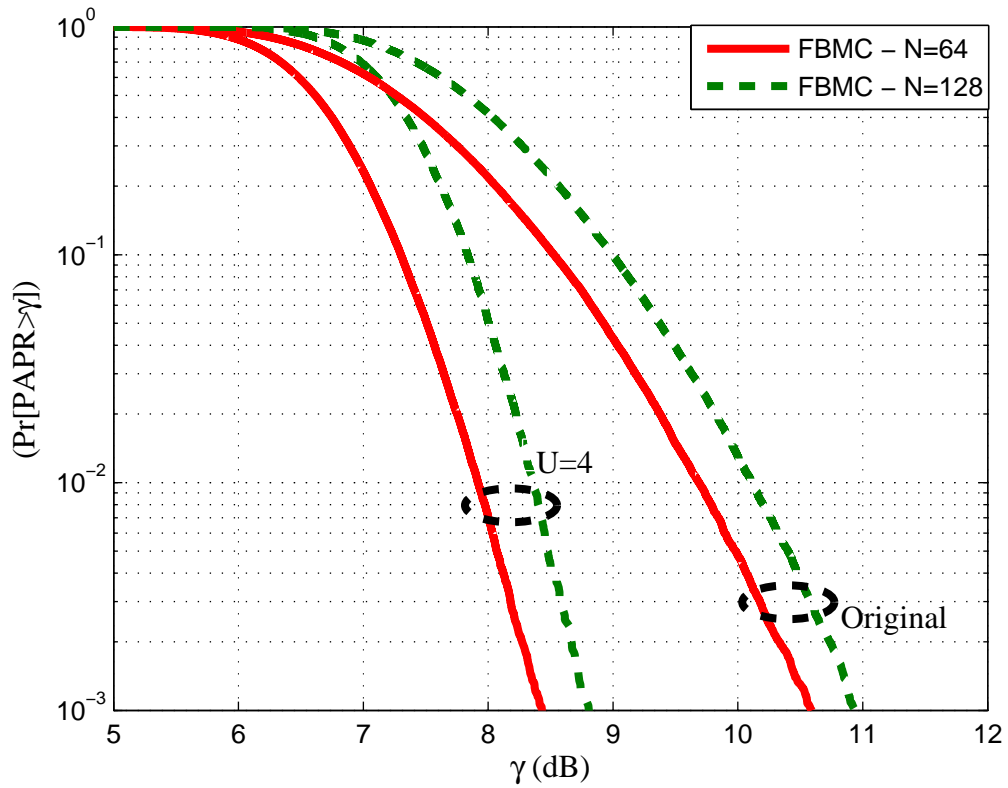


FIGURE 4.4: CCDF of PAPR plot for FBMC-OQAM symbols with PAPR calculated over $[2T, 4T)$ with $U = 4$ and $N = \{64, 128\}$ to illustrate the impact of FFT size on the DSLM scheme.

4.4.2.3 Impact of FFT size

When the FFT size is increased, then we observe that the original PAPR increases, while the PAPR reduction capability of the DSLM based scheme remains almost same as shown in Fig. 4.4. We can observe that in comparison with the original PAPR, the PAPR reduction is around 2.16 dB and 2.37 dB when N is 64 and 128 respectively.

4.4.2.4 Comparison of OSLM and DSLM

Both OSLM and DSLM schemes are compared by keeping the number of sub-carriers, modulation type and prototype filter. This is done, because, both these SLM-based schemes opt symbol-by-symbol approach. Actually, DSLM can be seen as improvised generalization of OSLM. In the implementation of OSLM [22], oversampling was not done and IOTA filter with a filter length of $4T$ has been used as the prototype filter. So, as a

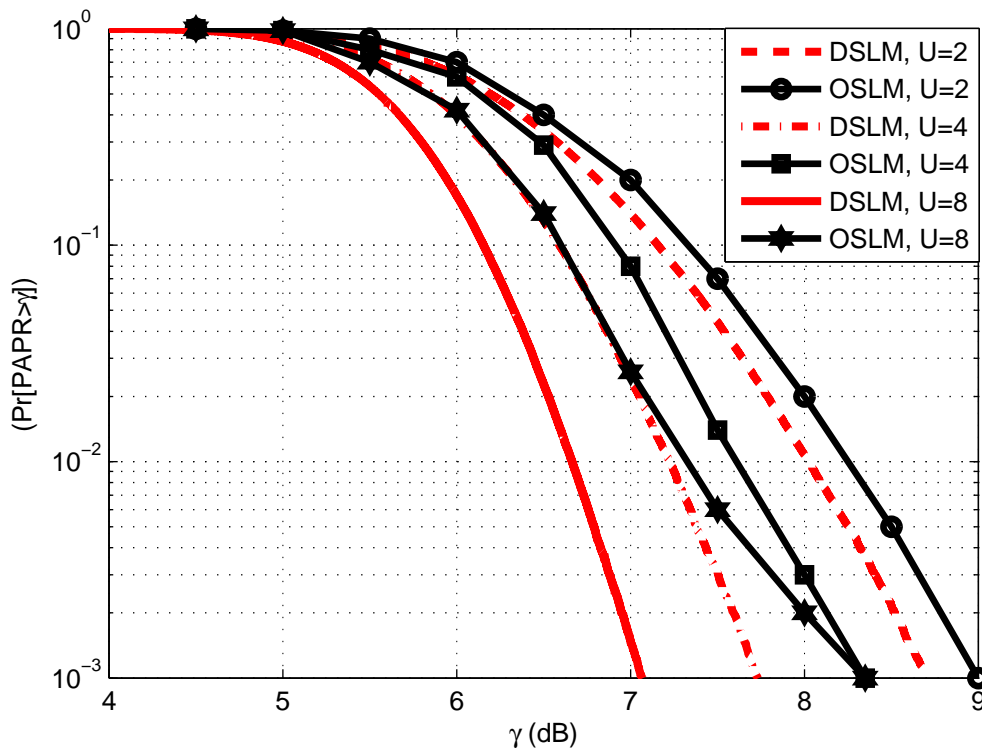
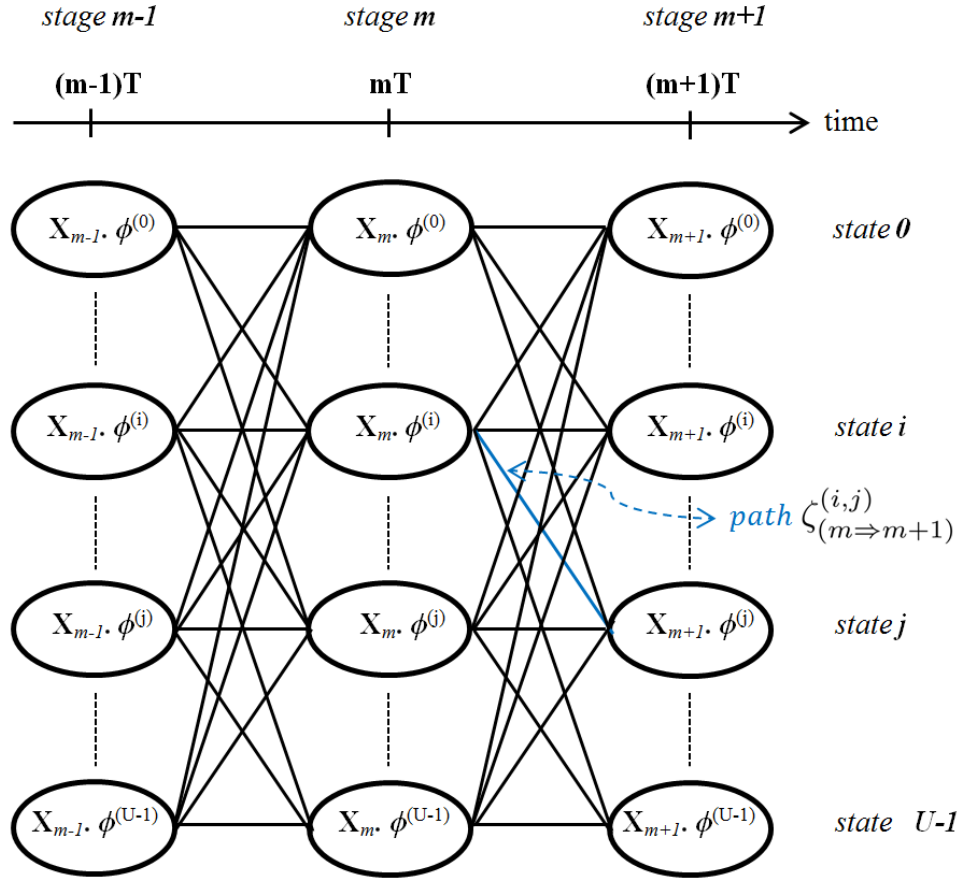


FIGURE 4.5: CCDF of PAPR plot for FBMC-OQAM symbols with PAPR calculated over $[2T, 4T)$ with $U = \{2, 4, 8\}$ with DSLM and OSLM schemes.

matter of coherence during comparison, we have implemented the DSLM scheme without oversampling and with the IOTA filter. CCDF plots with both DSLM and OSLM has been shown in Fig. 4.5. In terms of PAPR reduction, the DSLM with FBMC-OQAM outperforms the OSLM and difference is in around of 0.3 dB, 0.62 dB and 1.28 dB at 10^{-3} value of CCDF of PAPR when $U = 2$, $U = 4$ and $U = 8$ respectively. Upto 10^{-2} value of CCDF of PAPR, we can notice that DSLM with $U = 4$ and OSLM with $U = 8$, have similar performance; beyond which, we can see OSLM with $U = 8$ lagging badly behind the DSLM with $U = 4$. This lag by OSLM can be explained by the fact that in OSLM, only the current interval is considered for PAPR calculation of the phase rotated symbol.

4.4.3 Sub-optimality of the symbol-by symbol approach

From the simulation results, it can be noticed that the FBMC-OQAM with DSLM is trailing to that of OFDM with SLM in PAPR reduction performance. In Fig. 4.3, we can perceive that the trail gap in terms of PAPR reduction performance, increasing

FIGURE 4.6: Illustration of the trellis diagram between M stages composed of U states.

with size of U . The reason for sub-optimality is that, in DSLM, the phase rotations of the past symbols are fixed or already chosen since it is based on symbol-by-symbol optimization. Whatever peak reduction, we may obtain for the current symbol, can probably be hampered by its immediate next symbol.

This motivated us to investigate this sub-optimality and probe for optimal solutions. In the next section, we propose a trellis-based method that is able to obtain results very close to the optimal solution.

4.5 Trellis-based SLM

If we have to transmit M input symbol vectors $\{\mathbf{X}_0, \mathbf{X}_1, \dots, \mathbf{X}_{M-1}\}$, then we need to find Θ , which is the optimal set of M different phase rotation vectors that give the best

PAPR

$$\Theta = \{\phi^{(u_{min}^0)}, \phi^{(u_{min}^1)}, \dots, \phi^{(u_{min}^{M-1})}\} \quad (4.18)$$

where, $\{u_{min}^0, u_{min}^1, \dots, u_{min}^{M-1}\}$ are the indices of optimal phase rotation vectors for the M input symbol vectors, which are to be sent to the receiver as SI. With M FBMC-OQAM symbols and U phase rotation vectors, we need to find the best path in the trellis of Fig. 4.6 that gives the lowest PAPR. Choosing an optimal path in the trellis means finding the multiplicative vectors by solving equation (4.5), with the help of a trellis diagram.

For $0 \leq m \leq M-1$, every m^{th} FBMC-OQAM symbol $x_m(t)$, obtained from modulation of input symbol vector \mathbf{X}_m , is represented as the m^{th} stage in the trellis that will reach at time instant mT . At each stage, there will be U different states, representing the rotated FBMC-OQAM symbols. Among these states, any i^{th} trellis state indicates rotation by phase rotation vector $\phi^{(i)}$. Between every two stages, there exist U^2 number of possible paths. The joint FBMC-OQAM modulation of m^{th} and $(m+1)^{th}$ rotated input symbol vectors $\mathbf{X}_m^{(u)}$ and $\mathbf{X}_{m+1}^{(v)}$ respectively is represented in the trellis by the path $\zeta_{(m \Rightarrow m+1)}^{(u,v)}$ between u^{th} state in m^{th} stage and v^{th} state in $(m+1)^{th}$ stage; where \Rightarrow represents a transition between two successive stages.

4.5.1 Exhaustive search

In order to achieve the optimal performance in PAPR reduction, one need to consider all the possible U phase rotations for all M symbols and pick out the best one out of the U^M different combinations. In practical sense, it is meaningless to perform this exhaustive search, since it adds mammoth complexity to the implementation of any SLM-based scheme.

4.5.2 Dynamic programming

In order to circumvent the high computational complexity of exhaustive search, we opt for the dynamic programming (DP), which can help in reducing substantially, the number of paths one need to pick [84]. Actually, DP is an optimization technique of solving complex problems by breaking them down into simpler steps. It is applicable to

problems which exhibit the characteristics of overlapping subproblems. Thereby, a DP algorithm can find the optimal solution for with low computational complexity. At any transition between two stages, we have U^2 paths to compare and for M FBMC-OQAM symbols, we have totally $M - 1$ transitions. Therefore, the trellis-based SLM (TSLM) scheme needs to search only $U^2(M - 1)$ paths. This is due to eliminating certain paths by evaluating them based on a metric. The partial PAPR that has been calculated between two stages with multiple states serves as characteristic of path metric, which can aid at identifying the U optimal paths that arrive at successive stages. For the path $\zeta_{(m \Rightarrow m+1)}^{(u,v)}$, its path metric $\Gamma_{(m,m+1)}^{(u,v)}$ can be written as

$$\Gamma_{(m,m+1)}^{(u,v)} = f(PAPR_{m,m+1}^{(u,v)}) \quad (4.19)$$

where $f(\cdot)$ is any convex function and $PAPR_{m,m+1}^{(u,v)}$ is the partial PAPR of the path $\zeta_{(m \Rightarrow m+1)}^{(u,v)}$, which is to be computed over a duration T_0 as

$$PAPR_{m,m+1}^{(u,v)} = \frac{\max_{t \in T_0} |x_{m,m+1}^{(u,v)}(t)|^2}{\frac{1}{T_0} \int_{T_0} |x_{m,m+1}^{(u,v)}(t)|^2 dt}, \quad 0 \leq u, v \leq U - 1, \quad (4.20)$$

where $T_0 \in [mT + T_a, mT + T_b)$, which is any arbitrary interval within the $[mT, mT + 4.5T)$ interval. It has to be noted that $T_a \geq 0$ and $T_b < 4.5T$. Similarly, we define a state metric $\Psi_{(u,m)}$ at the m^{th} stage as a measure of optimality of cumulative path matrices of the optimal paths that arrived to the u^{th} state from previous stages through various transitions. It can be evaluated simply by adding the path metric $\Gamma_{(m-1,m)}^{(u,v)}$ of arriving optimal path $\zeta_{(m-1 \Rightarrow m)}^{(w,u)}$ from w^{th} state of the previous $(m - 1)^{th}$ stage with the state metric $\Psi_{(w,m-1)}$ of the w^{th} state from which this optimal path departs.

In fact, a FBMC-OQAM signal obtained from modulation of the M complex input symbols that are rotated with U i.i.d phase rotation vectors, can be viewed as an *overlapping Markov chain* (since the states are finite, i.e. they are countable and stages are discrete, nevertheless overlapping). So, the trellis-based schemes, optimizing more than one symbol, offer naturally very good performance in terms of PAPR reduction than symbol-by-symbol optimization schemes. The TSLM scheme tries to find the states that lead to least PAPR. The whole optimization problem in this regard can be viewed as a continuum of overlapping optimization sub-problems, i.e. finding a FBMC-OQAM signal with least PAPR is equivalent to obtaining the accumulation of the least

peaks. This is reflected in the state metric of a given state at any stage.

4.5.3 TSLM algorithm

In the TSLM, every two symbols are rotated with different phase rotation vectors that are i.i.d and are FBMC-OQAM modulated. The two optimal states between the two successive stages are chosen among others, based on least PAPR criterion that has been computed over $T_0 \in [T, 4T)$. Even though a FBMC-OQAM symbol overlaps over its next three symbols, it gets significantly impacted by its immediately preceding and succeeding symbols. Therefore, consideration of every two symbols in an overlapped manner is a necessary and sufficient condition to solve the optimization problem. The TSLM algorithm involves the following steps,

Step 1 - Initialization: Firstly, we generate M complex input symbol vectors $\{\mathbf{X}_m\}_{m=0}^{M-1}$ as per equation (2.7) and U phase rotation vectors $\{\phi^{(u)}\}_{u=0}^{U-1}$ of length N as per equation (4.2). We initialize the counter m and the state metrics for all states of the first stage as below.

$$m = 0 \quad (4.21)$$

$$\Psi_{(u,0)} = 0, \quad u = 0, \dots, U - 1 \quad (4.22)$$

As long as the condition $0 \leq m \leq M - 2$ is satisfied, we perform the following **Steps 2, 3, 4, 5** and **6** in a repeated manner.

Step 2 - Phase rotation: Two input symbol vectors $\mathbf{X}_m, \mathbf{X}_{m+1}$ are phase rotated with U different phase rotation vectors $\{\phi^{(u)}\}_{u=0}^{U-1}$ and $\{\phi^{(v)}\}_{v=0}^{U-1}$, as per equation (4.4), giving $\{\mathbf{X}_m^{(u)}\}_{u=0}^{U-1}$ and $\{\mathbf{X}_{m+1}^{(v)}\}_{v=0}^{U-1}$ respectively. The symbols, $a_{m',n}^{(u)}$ and $a_{m',n}^{(v)}$ are chosen from $\mathbf{X}_m^{(u)}$ and $\mathbf{X}_{m+1}^{(v)}$ respectively, as per equation (2.8).

Step 3 - FBMC-OQAM modulation: FBMC-OQAM modulation is done jointly

for all combination of the patterns of m^{th} and $(m + 1)^{th}$ input symbols, is written by

$$x_m^{(u)}(t) = \sum_{m'=2m}^{2m+1} \sum_{n=0}^{N-1} a_{m',n}^{(u)} h(t - m'T/2) e^{j\frac{2\pi}{T}nt} e^{j\varphi_{m',n}} \quad (4.23)$$

$$x_{m+1}^{(v)}(t) = \sum_{m'=2m+2}^{2m+3} \sum_{n=0}^{N-1} a_{m',n}^{(v)} h(t - m'T/2) e^{j\frac{2\pi}{T}nt} e^{j\varphi_{m',n}} \quad (4.24)$$

$$x_{m,m+1}^{(u,v)}(t) = x_m^{(u)}(t - T) + x_{m+1}^{(v)}(t), \quad 0 \leq u, v \leq U - 1 \quad (4.25)$$

From equation (4.25), it is intuitive that we have U^2 patterns of the modulated FBMC-OQAM signal $x_{m,m+1}^{(u,v)}(t)$, for $0 \leq u, v \leq U - 1$.

Step 4 - Path metric calculation: For each of the U^2 patterns of the modulated FBMC-OQAM signal $x_{m,m+1}^{(u,v)}(t)$, we compute partial PAPR over duration T_0 as per equation (4.20) For the path $\zeta_{(m \Rightarrow m+1)}^{(u,v)}$, we calculate its path metric $\Gamma_{(m,m+1)}^{(u,v)}$ according to equation (4.19).

Step 5 - Survivor path identification: The states for stage m that are related to the survivor paths leading to stage $m + 1$, are stored in a state matrix $\lambda(v, m)$ as given below

$$\lambda(v, m) = \min_{u \in [0, U-1]} \left[\Psi_{(u,m)} + \Gamma_{(m,m+1)}^{(u,v)} \right], \quad v = 0, \dots, U - 1 \quad (4.26)$$

Step 6 - State metric updation: The state metric $\Psi_{(v,m+1)}$, for the stage $m + 1$, can be updated as follows,

$$\Psi_{(v,m+1)} = \Psi_{(\lambda(v,m),m)} + \Gamma_{(m,m+1)}^{(\lambda(v,m),v)}, \quad v = 0, \dots, U - 1 \quad (4.27)$$

Step 7 - Incrementation: Increment the value of m by 1 and if $0 \leq m \leq M - 2$, then go to **Step 2**; Else, for $0 \leq m = M - 1$, go to **Steps 8**.

Step 8 - Traceback: Once state metrics for all the M^{th} stages has been computed, then identify the state that has the least state metric as shown below

$$\Theta(M - 1) = \min_{u \in [0, U-1]} [\Psi_{(u, M-1)}] \quad (4.28)$$

TABLE 4.1: Computational complexity comparison of the SLM algorithms

Algorithm	Complexity
Exhaustive search for a FBMC-OQAM system	$\mathcal{O}(U^M)$
Trellis-based SLM for a FBMC-OQAM system	$\mathcal{O}((M-1)U^2)$
Dispersive SLM for a FBMC-OQAM system	$\mathcal{O}(MU)$
Classical SLM for a OFDM system	$\mathcal{O}(MU)$

then start tracing back from last stage to the first one in order to find the unique survivor path Θ by identifying the optimal states at each stage as below

$$\Theta(x) = \lambda(\Theta(x+1), x) \quad (4.29)$$

where, $x = M-2, M-3, \dots, 1, 0$.

This survivor path Θ is the set of optimal phase rotation vectors, that is obtained after solving the optimization problem by DP and its indices $\{u_{min}^0, u_{min}^1, \dots, u_{min}^{M-1}\}$, are supposed to be transmitted to the receiver as SI.

4.5.4 Computational complexity analysis of DSLM and TSLM

General expressions for computational complexity have been derived. So that, for any given probabilistic scheme, one can readily derive accordingly. The computational complexity of TSLM is $\mathcal{O}((M-1)U^2)$ and the computational complexities for SLM schemes for FBMC-OQAM with different approaches along with that of classical SLM scheme for OFDM has been summarized in Table 4.1.

4.5.4.1 Derivation of computational complexities in DSLM and TSLM

In any SLM based scheme, the complexity in implementation will be due to phase rotation, FBMC-OQAM modulation and metric calculation. Let us denote the complexity related to these three in the DSLM and TSLM schemes as c_{rot} , c_{mod} and c_{met} respectively. The phase rotation of the m^{th} input symbol vector \mathbf{X}_m needs complex multiplications equal to the number of its tones N . So, the complexity c_{rot} is given as

$$c_{rot} = N \quad (4.30)$$

However, in poly-phase filtering operation, we perform IFFT and filtering with $h(t)$. OQAM mapping involves complex-to-real symbol mapping. It may seem that one has to perform two real IFFT operations. Nevertheless, it is possible to compute two real IFFTs simultaneously like a single complex IFFT operation without increasing the number of complex multiplications [85]. The same can be applied in filtering with $h(t)$. Thus, the computational complexity involved in FBMC-OQAM modulation c_{mod} is given as

$$c_{mod} = \underbrace{\frac{N}{2} \log_2 N}_{IFFT} + \underbrace{4N}_{filtering} \quad (4.31)$$

In the metric calculation operation, we need N complex multiplications to find the peak. c_{met} depends on T_0 and is given as

$$c_{met} = dN \quad (4.32)$$

where, T_0 is the duration of time in terms of N and d is a constant that represents the number of successive symbol intervals, considered for metric calculation.

The computational complexity in the case of DSLM and TSLM, in terms of complex multiplications and additions are summarized in the Tables 4.2 and 4.3. In the table, “weight”, is mentioned to calculate the complexity for M symbols and U phase rotation vectors. We multiply this weight to the respective multiplications or addition complexities related to the needed operations, namely, rotation, modulation and metric calculation. The general expressions computational complexity in terms of complex multiplications for DSLM and TSLM are given below

$$c_{DSL M} = M[U.c_{rot} + U.c_{mod} + U.c_{met}] \quad (4.33)$$

$$= MNU \left[\frac{1}{2} \log_2 N + 5 + d \right] \quad (4.34)$$

$$c_{TSL M} = M[U.c_{rot} + U.c_{mod} + (1 - \frac{1}{M})U^2.c_{met}] \quad (4.35)$$

$$= MN \left[(\frac{1}{2} \log_2 N + 5)U + d(1 - \frac{1}{M})U^2 \right] \quad (4.36)$$

TABLE 4.2: Computational complexity in DSLM

Operation	Multiplications	Additions	Weight
Rotation	N	0	MU
Modulation	$\frac{N}{2} \log_2 N + 4N$	$N \log_2 N + 3N$	MU
Metric	dN	0	MU

TABLE 4.3: Computational complexity in TSLM

Operation	Multiplications	Additions	Weight
Rotation	N	0	MU
Modulation	$\frac{N}{2} \log_2 N + 4N$	$N \log_2 N + 3N$	MU
Metric	dN	dN	$(M - 1)U^2$

4.5.4.2 Comparison of computational complexities of TSLM and MBJO-PTS

This subsection aims at fair comparison of TSLM and MBJO-PTS schemes in terms of computational complexity. MBJO-PTS scheme is a trellis-based adaption of classical PTS scheme to FBMC-OQAM system by multi-block joint optimization and is presented in [27]. In MBJO-PTS, a number of data blocks are buffered and optimized. A penalty function is defined, which represents the penalties like signal distortion, performance loss etc. The aim of MBJO-PTS is to minimize the summed penalty of the signal of all M input symbol vectors. This is done by jointly optimizing the phase factor vectors of M input symbol vectors. Unlike symbol-by-symbol approach based PAPR reduction schemes that independently optimize the data blocks, the MBJO-based scheme exploits the overlapping structure of the FBMC-OQAM signal and jointly optimizes multiple data blocks. To achieve this, A DP algorithm is used to solve the optimization problem without exhaustive search.

Since, both TSLM and MBJO-PTS have trellis-based approach, we felt it is interesting to compare both their performances. Fair comparison of any PTS and SLM scheme cannot be possible, if both schemes do not exhibit the same computational complexity [86]. The following consideration holds generally for any SLM and PTS schemes that are applied in FBMC-OQAM systems. The complexity analysis includes both complex multiplications and additions. However, in the performance comparison between the two schemes, only the complex multiplications are considered; since, they dominate the overall complexity in common hardware implementations [87].

Unlike SLM, in any PTS-based scheme, we can perform phase rotation in time-domain.

This avoids need for multiple FBMC-OQAM modulation operations. Thus, the complexity due to FBMC-OQAM modulation in a PTS based scheme \hat{c}_{mod} , can be reduced as $\frac{N}{V}$ -point IFFT is sufficient. We recall that in PTS, V is the number of sub-block partitions and W is the number of candidate phases.

$$\hat{c}_{mod} = \frac{N}{2V} \log_2 \frac{N}{V} + 4N \quad (4.37)$$

In PTS scheme, we individually perform phase rotation in time domain to the V sub-blocks and then add them, leading to W^V different signal patterns. Since, we consider a certain time duration T_0 for partial PAPR calculation, we need dN complex multiplications within that time duration. The computational complexity involved in phase rotation operation for MBJO-PTS scheme, \hat{c}_{met} is given by

$$\hat{c}_{rot} = dNV \quad (4.38)$$

The computational complexity involved in metric calculation for MBJO-PTS scheme, \hat{c}_{met} is given by

$$\hat{c}_{met} = dN \quad (4.39)$$

TABLE 4.4: Computational complexity in MBJO-PTS

Operation	Additions	Multiplications	Weight
Rotation	0	dNV	MW
Modulation	$\frac{N}{V} \log_2 \frac{N}{V} + 3N$	$\frac{N}{2V} \log_2 \frac{N}{V} + 4N$	MV
Metric	$2(V-1)dN$	dN	$(M-1)W^{2V}$

General expression for MBJO-PTS computation complexity for M symbols has been derived similarly, as summarized in the Table 4.4 and given below

$$c_{MBJO} = M[W \cdot \hat{c}_{rot} + V \cdot \hat{c}_{mod} + (1 - \frac{1}{M})W^{2V} \cdot \hat{c}_{met}] \quad (4.40)$$

$$= MN \left[\left(\frac{1}{2} \log_2 \frac{N}{V} + 4V + dVW \right) + d \left(1 - \frac{1}{M} \right) W^{2V} \right] \quad (4.41)$$

From equations (4.35) and (4.40), it is clear that, in FBMC-OQAM with TSLM and MBJO-PTS, the complexities involved in rotation and metric calculation are linear w.r.t N . Whereas, the modulation complexity with TSLM and MBJO-PTS, are of order

$\mathcal{O}(\frac{N}{2} \log_2(N))$ and $\mathcal{O}(\frac{N}{2V} \log_2(\frac{N}{V}))$ respectively. It implies that the modulation complexity dominates over remaining other complexities. From the size of phase rotation point of view, the complexity is solely dominated by U in TSLM. On the contrary, it is distributed between V and W in MBJO-PTS.

In order to avail a fair comparison, the condition for identical computation complexity in both TSLM and MBJO-PTS schemes is given by

$$c_{TSLM} = c_{MBJO} \quad (4.42)$$

By substituting equations (4.35) and (4.40) in equation (4.42), we obtain

$$\begin{aligned} & MN \left[\left(\frac{1}{2} \log_2 N + 5 \right) U + d \left(1 - \frac{1}{M} \right) U^2 \right] \\ &= MN \left[\left(\frac{1}{2} \log_2 \frac{N}{V} + 4V + dVW \right) + d \left(1 - \frac{1}{M} \right) W^{2V} \right] \end{aligned} \quad (4.43)$$

For a large value of M , the term $1 - \frac{1}{M} \rightarrow 1$ and therefore, it can be neglected. The equation (4.43) is simplified

$$dU^2 + \left(\frac{1}{2} \log_2 N + 5 \right) U - \frac{1}{2} \log_2 \frac{N}{V} - 4V - dVW - dW^{2V} = 0 \quad (4.44)$$

The possible root U in ideal case for the quadratic function equation (4.44), denoted by U_{root} is given by

$$U_{root} = \frac{-\frac{1}{2} \log_2 N - 5 + \sqrt{\Delta}}{2d} \quad (4.45)$$

where Δ is the discriminant, which is given by

$$\Delta = \left(\frac{1}{2} \log_2 N + 5 \right)^2 + 4d \left(\frac{1}{2} \log_2 \frac{N}{V} + 4V + dVW + dW^{2V} \right)$$

4.5.5 Simulation Results with TSLM

The objective of the simulations is to analyze the performance of TSLM scheme in comparison with OFDM when classical SLM scheme is used. Simulations are done for a FBMC-OQAM signal that has been generated from 10^5 4QAM symbols with 64 sub-carriers. The PHYDYAS prototype filter [41], which spans over $4T$ was used by default unless specified otherwise. The range of the complex phase rotation vector was

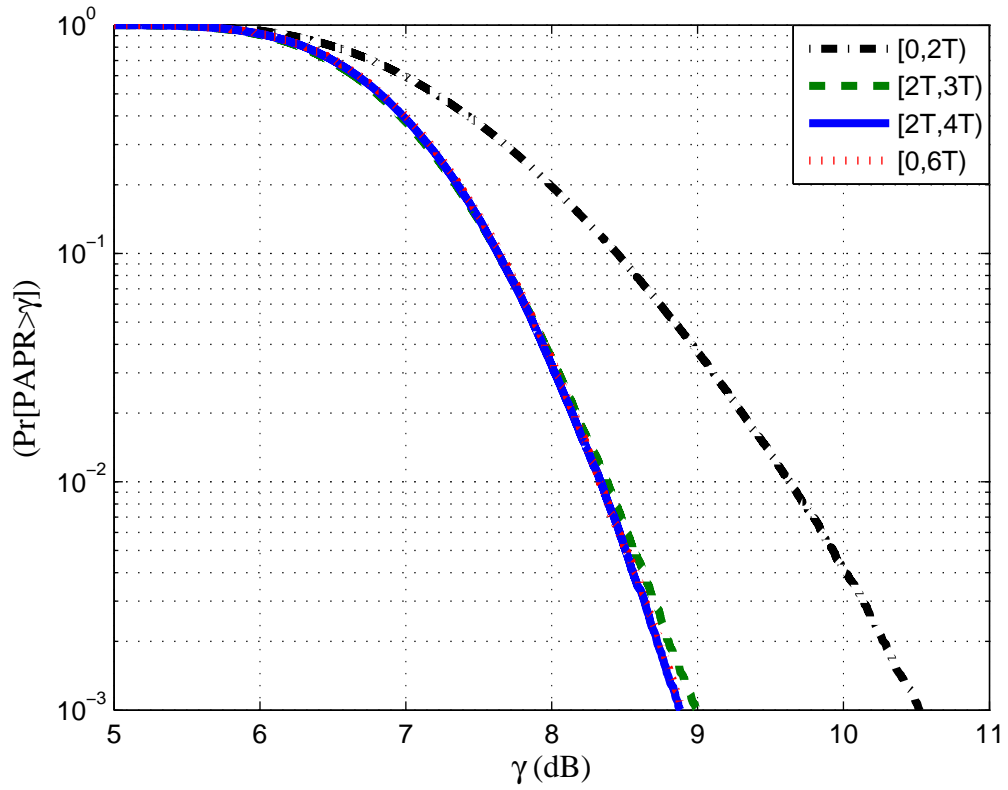


FIGURE 4.7: CCDF of PAPR for FBMC-OQAM symbols with partial PAPR calculated over different T_0 , $U = 2$ and PHYDYAS filter.

chosen such as, $\phi^{(u)} \in \{1, -1\}$. In general most of the PAPR reduction schemes are implemented over discrete-time signals. So, we need to sample the continuous-time FBMC-OQAM signal $x(t)$, thereby obtaining its discrete-time signal $x[n]$. In order to well approximate the PAPR, we have oversampled the modulated signal by a factor of 4 and then implemented the TSLM scheme on the discrete-time signal $x[n]$. Exponential function has been used as the metric function $f(\cdot)$ in equation (4.19), when calculating the path metrics.

4.5.5.1 Impact of variation of T_0 duration

When computing the PAPR, the interval $[T_a, T_b)$ of duration T_0 seems to make a significant impact on the performance of TSLM scheme as depicted in Fig. 4.7. Reducing the interval T_0 reduces the complexity of the optimization problem. Choosing $[T_a = 2T)$ and $[T_b = 4T)$ seems to be the lower bound as it yields better performance than the remaining intervals. If we choose intervals $[T_a > 2T)$ or $[T_b < 3T)$, then there is a

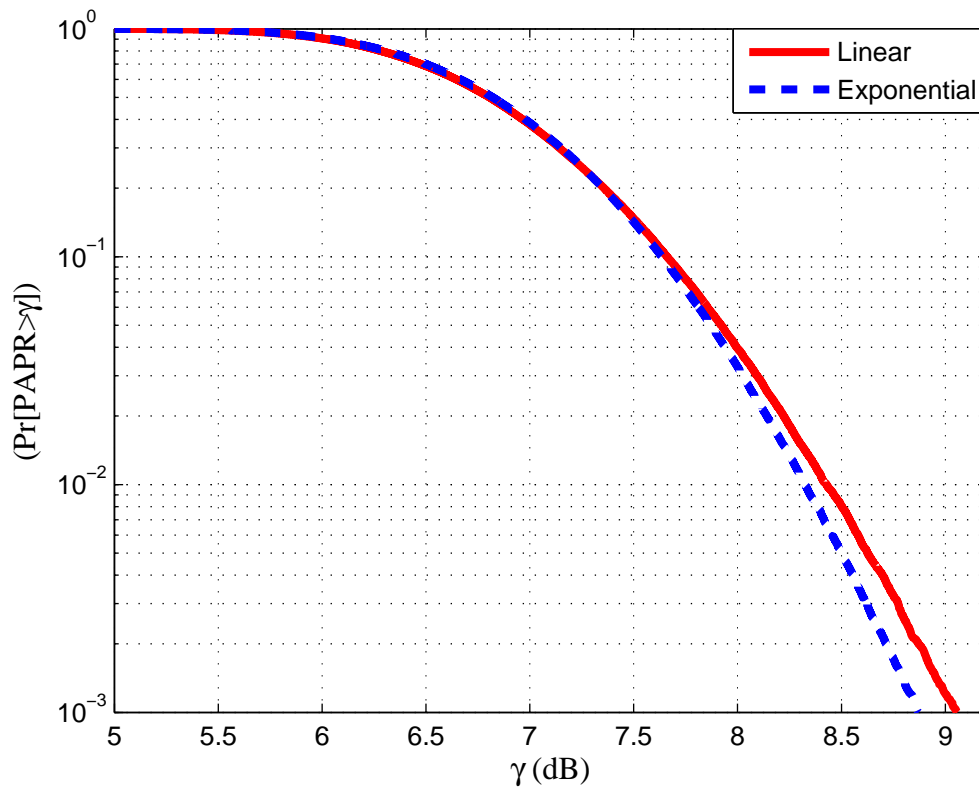


FIGURE 4.8: CCDF of PAPR for FBMC-OQAM symbols with partial PAPR calculated over $[2T, 4T)$, $U = 2$ and different metric functions.

significant degradation on the performance, because a significant part of the energy of a FBMC-OQAM symbol lies between $2T$ and $3T$ as evident in Fig. 2.9. In conclusion, it is sufficient to make the optimization problem of equation (4.26), for the intervals $[2T, 4T)$, as it seems to be an optimal choice to be considered. It is interesting to notice that the interval $[2T, 3T)$ (i.e., just one symbol period) also has performance loss of 0.08 dB and number of complex multiplications reduced by $(1 - \frac{1}{M})U^2$ w.r.t the optimal one.

4.5.5.2 Impact of choice of the metric function

The choice of metric function $f(\cdot)$ in equation (4.19) seems to have some impact on the performance in terms of PAPR mitigation. Two different functions, namely, linear and exponential functions, have been chosen to understand the impact of choice of the metric function $f(\cdot)$ on the performance of the TSLM scheme. As seen in Fig. 4.8, for low values of the PAPR, the PAPR reduction performance with exponential function is almost as same as that with the linear one, albeit, lagging minutely. Very small

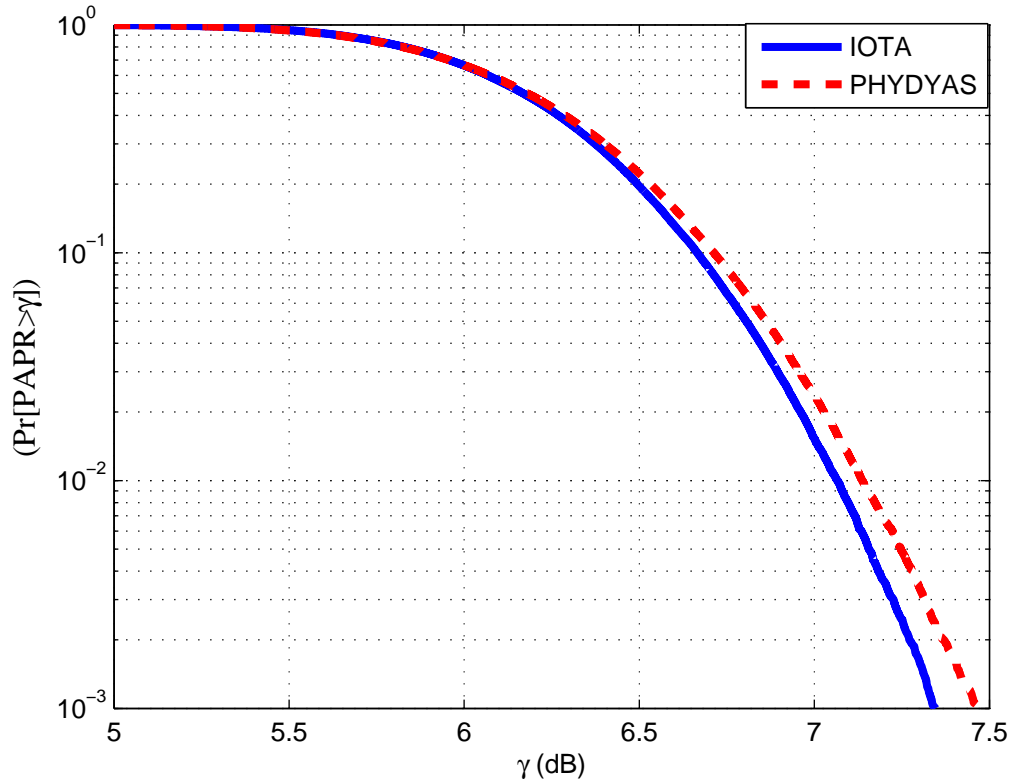


FIGURE 4.9: CCDF of PAPR plot for FBMC-OQAM symbols with PAPR calculated over $[2T, 4T)$ with $U = 8$ with PHYDYAS and IOTA filters.

performance gain can be seen at high values of the PAPR. This can be explained by the fact that as the exponential function puts more weightage to higher peaks than the linear one in identifying the set of optimal phase rotation vectors. Although, we do consider exponential function in all our simulation, we suggest that it can be sufficient to choose a linear metric function.

4.5.5.3 Impact of variation in prototype filter

In order to verify that the FBMC-OQAM with TSLM outperform over OFDM with classical SLM holds for any prototype filter, isotropic orthogonal transform algorithm (IOTA) filter is used. It has to be noted that the impulse response for both filters has length $4T$. As seen in Fig. 4.9, the performance of IOTA based FBMC-OQAM with TSLM in PAPR reduction outperforms the PHYDYAS based FBMC-OQAM with TSLM scheme. This is due to the fact that the concentration of the signal energy is

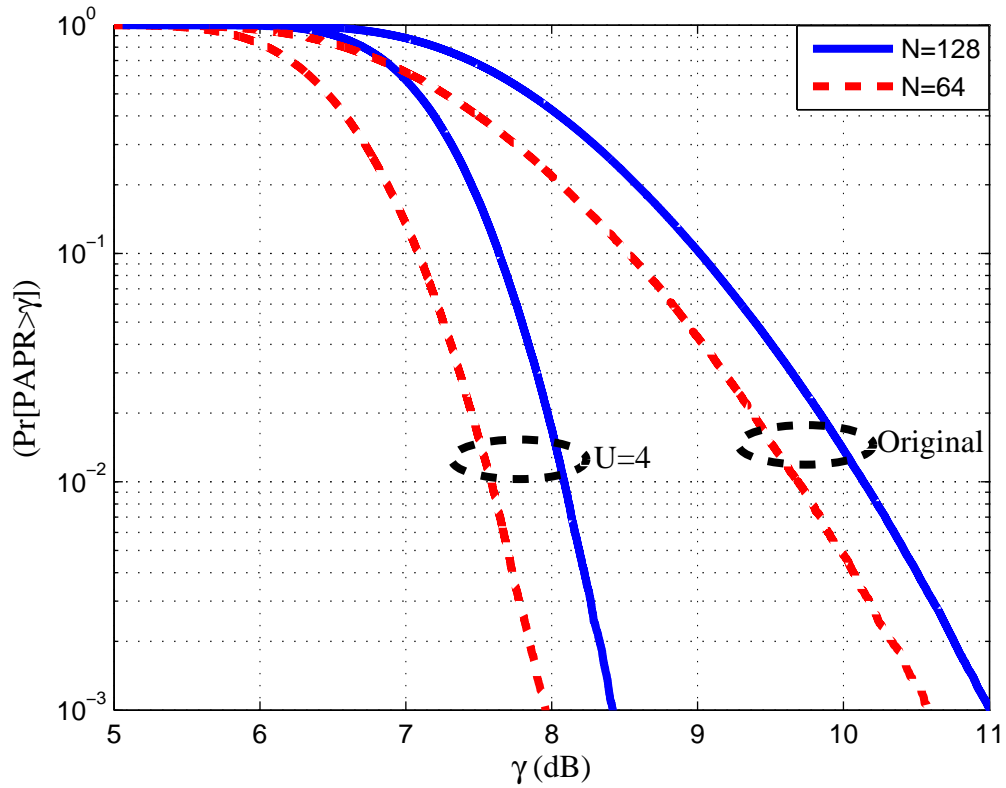


FIGURE 4.10: CCDF of PAPR plot for FBMC-OQAM symbols with PAPR calculated over $[2T, 4T)$ with $U = 4$ and $N = \{64, 128\}$ to illustrate the impact of FFT size on the TSLM scheme.

better in the case of IOTA filter leading to reduction in the symbol overlapping when compared to the PHYDYAS one.

4.5.5.4 Impact of FFT size

When the FFT size is increased, then we observe that the original PAPR increases, while the PAPR reduction capability of the TSLM scheme remains almost same as shown in figure 4.10. We can observe that in comparison with the original PAPR, the PAPR reduction is around 2.63 dB and 2.49 dB when $N = \{64, 128\}$ respectively.

4.5.5.5 Impact of size of U

Like any SLM scheme, the size of phase rotation vector impacts the performance of the PAPR reduction. For an illustration of impact of U , we have considered $T_0 = [2T, 4T)$.

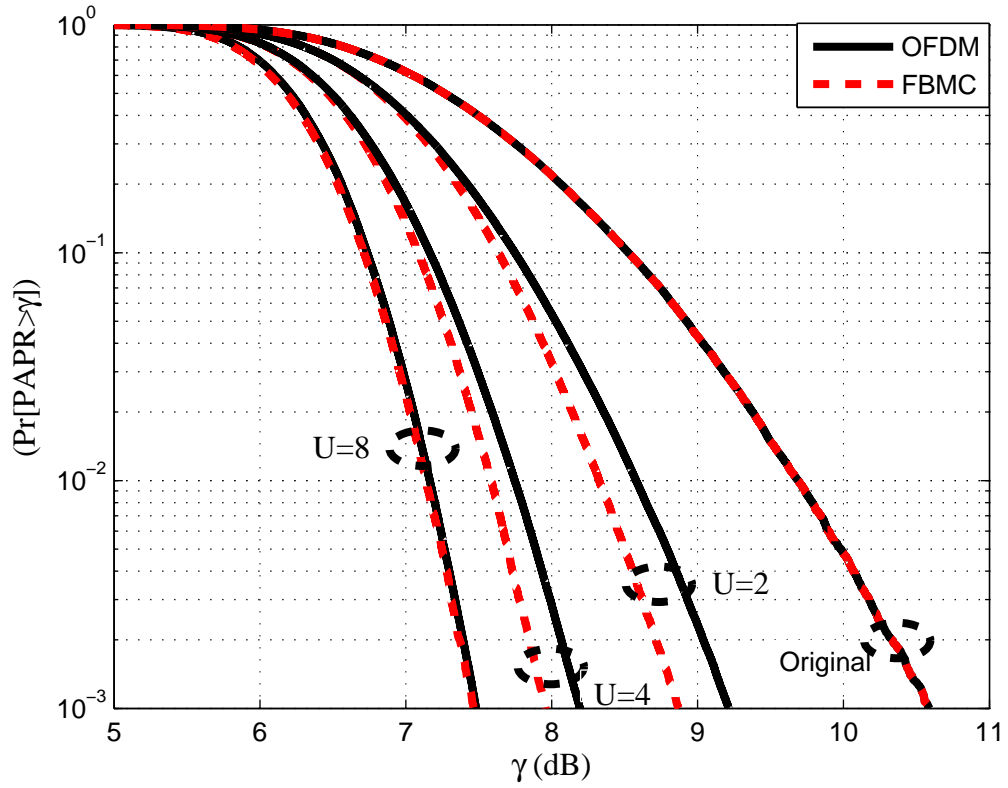


FIGURE 4.11: CCDF of PAPR for FBMC-OQAM symbols with partial PAPR calculated over $[2T, 4T)$ with $U = 2, 4, 8$ and PHYDYAS filter.

The different sizes considered are $U = \{2, 4, 8\}$. The values at 10^{-3} of CCDF of PAPR in the Fig. 4.11, has been summarized in Table 4.5. We can see from Table 4.5, that

TABLE 4.5: CCDF of PAPR at 10^{-3} value (in dB)

Modulation type	Reduction Scheme	$U = 2$	$U = 4$	$U = 8$
OFDM	Classical SLM	9.21	8.19	7.48
FBMC-OQAM	Trellis-based SLM	8.86	7.95	7.46
FBMC-OQAM	Disperive SLM	9.26	8.44	7.8

the FBMC-OQAM with TSLM has outperformed the OFDM with classical SLM by 0.35 dB, 0.24 dB and 0.02 dB at 10^{-3} value of CCDF of PAPR when $U = 2$, $U = 4$ and $U = 8$ respectively. The PAPR reduction performance of FBMC-OQAM with DSLM is also mentioned in the table, in order to show the superior performance of trellis-based approach over symbol-by-symbol one. FBMC-OQAM with DSLM. It is worth noting that at 10^{-3} value of CCDF of PAPR when $U = 2$, we are able to achieve 1.73 dB PAPR reduction from the original signal with a SI of 1 bit. This superior performance implies that when the overlapping nature of the FBMC-OQAM signals is well exploited

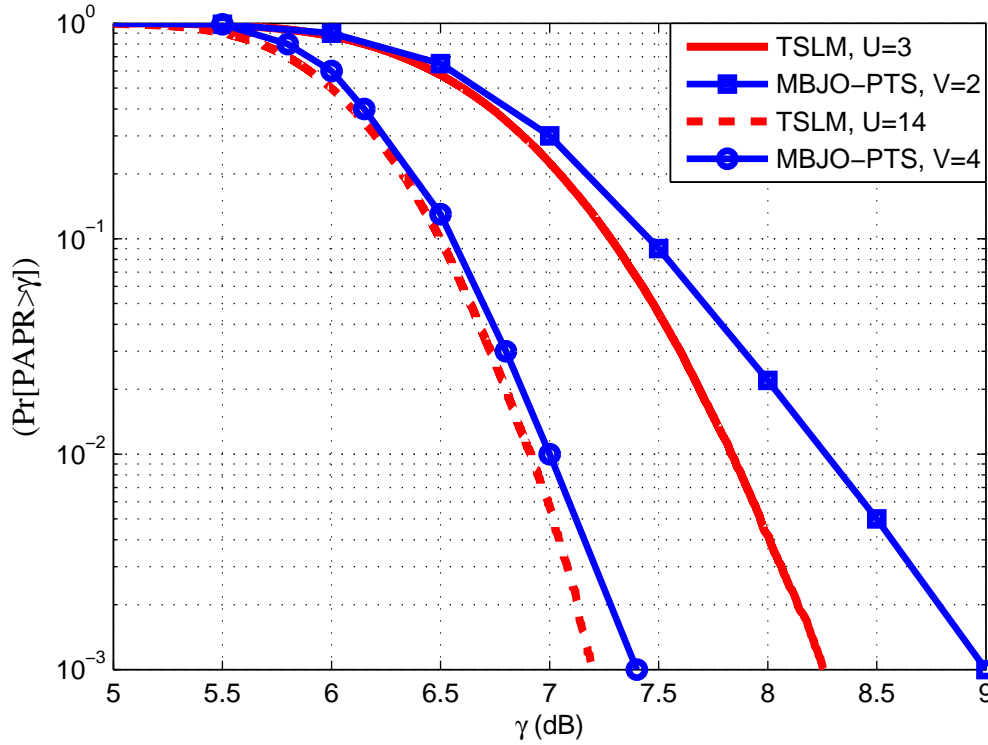


FIGURE 4.12: CCDF of PAPR for FBMC-OQAM symbols with PAPR calculated over $[2T, 4T)$ with $U = 8$ with PHYDYAS.

then it can significantly impact the PAPR reduction and such proper exploitation can be possible with trellis-based approach instead of symbol-by-symbol optimization. Another observation is that the lead gap between CCDF curves of OFDM and FBMC-OQAM gets narrowed as U increases.

4.5.5.6 Comparison of TSLM and MBJO-PTS schemes

We try to compare the computational complexity of MBJO-PTS with TSLM by keeping the number of tones, type of modulation, the prototype filter and T_0 duration identical. The value of W is 2 as per the proposed MBJO-PTS scheme [27]. The value of U_{root} calculated for $V = \{2, 4\}$ according to equation (4.45) is found to be 3.39 and 14.64 respectively. Since, these two U_{root} values respective to $V = \{2, 4\}$ are not integers, we can make a fair comparison by approximating equation (4.45) as below

$$U = \lfloor U_{root} \rfloor \quad (4.46)$$

where, $\lfloor \cdot \rfloor$ is a floor function. The value of U obtained from equation (4.46) implies that the computational complexity of TSLM scheme made marginally less to that of MBJO-PTS. The comparison of the performance of MBJO-PTS for $V = \{2, 4\}$ and $W = 2$ w.r.t. TSLM scheme for corresponding values of $U = \{3, 14\}$ that are obtained from the approximation of respective U_{root} values according to equation (4.46), can be seen in Fig. 4.12. The number of complex multiplications and additions needed for implementation of TSLM and MBJO-PTS algorithms over 10^5 FBMC-OQAM symbols, has been summarized in Table 4.6.

TABLE 4.6: Computational complexities of the TSLM and MBJO-PTS w.r.t. complex multiplications and additions

PAPR reduction scheme	Complex	
	Multiplications	Additions
TSLM ($U = 3$)	269×10^6	211×10^6
MBJO-PTS ($V = 2, W = 2$)	323×10^6	298×10^6
TSLM ($U = 14$)	3226×10^6	986×10^6
MBJO-PTS ($V = 4, W = 2$)	3494×10^6	3443×10^6

At CCDF of 10^{-3} in the Fig. 4.12, we can infer that the FBMC-OQAM with TSLM leads the MBJO-PTS scheme in PAPR reduction by roughly 0.7 dB and 0.2 dB for $U = 3$ and $U = 14$ respectively.

4.6 Dispersive TR

We have come to conclusion that probabilistic PAPR reduction schemes provide optimal results, with trellis-based approach. This has prompted us to investigate new category of PAPR reduction techniques. As a next step, we thought of studying an adding signal technique and we have chosen TR. Due to the similarity between the FBMC-OQAM and OFDM systems, it is natural to consider employing TR to reduce the PAPR of FBMC-OQAM signals. One of the subtle reason behind choosing TR is that, it is well known that in some PA linearization techniques, especially in predistortion, we can add a signal in order to the input of PA, to achieve linearized amplification. We felt, studying TR in the case of FBMC-OQAM can pave way to mitigate the NL effects of PA by adding a signal, which can achieve PAPR reduction and PA linearization. Moreover, It is very simple, agile and it does not cause any interference to the original data signal.

OFDM signals do not have overlapping nature and thus classical TR scheme is sufficient

since, $c(t)$ is determined independently for each symbol. Due to the overlapping nature of FBMC-OQAM symbols, direct implementation of classical TR scheme yields poor PAPR reduction performance.

In this section, we propose a novel scheme, namely, dispersive TR (DTR) to reduce the PAPR of the FBMC-OQAM systems. The aim of the DTR is to consider the overlap of the past symbols on the current m^{th} symbol, when solving the optimization problem. The proposed scheme deals with the time dispersive nature of the FBMC-OQAM signals and hence termed as DTR. The prototype filter considered in our analysis is PHYDYAS one. It has to be noted that the peak cancellation signals of the preceding overlapping symbols are fixed, while the current symbol's peak cancellation signal $\hat{c}_m(t)$ is obtained by solving the optimization problem.

4.6.0.1 Determination of \mathcal{B} for FBMC-OQAM

The determination of PRT locations for FBMC-OQAM is different than that of OFDM as the kernel cannot obey the circular property, due to the presence of prototype filter. The peak reduction kernel, \mathcal{K} should be Dirac-type, i.e. as close as possible to the unit impulse symbol δ of length $4.5N$, which is defined as

$$\delta[n - n_0] = \begin{cases} 1, & n = n_0, 0 \leq n < 4.5N \\ 0, & n \neq n_0, 0 \leq n < 4.5N \end{cases} \quad (4.47)$$

where, $n_0 \in [0, 4.5N)$. In the case of OFDM, \mathcal{K} obeys circular property and hence n_0 , (the maximum of the Dirac-type kernel) can be chosen to be 0. By multiplying the PRT tones by an exponential will change the positions of n_0 . In FBMC-OQAM, it is totally different. A circular shift of the kernel maximum position is not possible by a simple multiplication of the PRTs. This is due to the presence of the prototype filter. Looking at Fig. 2.9, it is clear that the maximum mean energy of the first FBMC-OQAM symbol is located at $2.25N$. In fact, the maximum of discrete impulse response of the prototype filter is at $n = 2N$ and the delay of the imaginary part (due to OQAM modulation), gives finally a maximum in $n = 2.25N$. So, we will choose $n_0 = 2.25N$ in order to generate the kernel so that, the unit impulse symbol δ defined in equation (4.47) should have its peak corresponding to the maximum mean power of the FBMC-OQAM symbol. This choice of $n_0 = 2.25N$ guarantees that we will have the minimal power on the reserved tones in

order to get a Dirac-type kernel. Choosing $n_0 = N$, for example, should result in a higher power on the PRTs for having the same maximum for the kernel. For FBMC-OQAM, design of \mathcal{K} is subject to

$$\mathcal{K} = \arg \min_{\mathcal{B}, \mathcal{K}_0} [\|\mathcal{G}(\mathcal{K}_0) - \delta[n - n_0]\|^2] \quad (4.48)$$

where \mathcal{K}_0 is any peak reduction kernel that can be generated based on a given \mathcal{B} , which obeys the conditions $\mathcal{K}_0[n] \neq 0$, for $n \in \mathcal{B}$ and $\mathcal{K}_0[n] = 0$, for $n \in \mathcal{B}^c$. For R reserved tones out of N tones, there will be $\binom{N}{R}$ possible combinations in total. For every combination of PRT locations, we compute a kernel. Out of all computed kernels, we pick the one, which has the least secondary peaks, i.e. the difference between the central peak and the secondary ones will be maximum.

Actually, in the case of OFDM, it is possible to use the peak reduction kernel \mathcal{K} , to construct the peak cancellation signal, without solving the TR optimization problem. All we have to do is to find the peaks, beyond a particular threshold and shift the kernel \mathcal{K} designed in equation (4.12), to that instant and subtract it to reach the threshold. By adding all the shifted versions of the kernel, it is possible to construct the peak cancellation signal in OFDM. Suppose, \mathbf{n}_{peak} is the set of indices of time samples, which have exceeded a particular threshold c . Then, for OFDM, the kernel-based peak cancellation signal \mathcal{K}_c can be constructed as follows

$$\mathcal{K}_c = \sum_{n_i \in \mathbf{n}_{peak}} d_{(i)} \mathcal{K}[n - n_i] \quad (4.49)$$

where, i is index in the set \mathbf{n}_{peak} , $d_{(i)}$ is a constant, that depends on the respective peak n_i and threshold c . This approach makes TR behave like a clipping method.

Where as, in the case of FBMC-OQAM, this is not possible due to presence of prototype filter. Thus, the FBMC-OQAM kernel \mathcal{K} that is computed in equation (4.48), will not be used as it is in the following; but, only the PRT locations of it will be used, deeming them as optimal PRT locations.

4.6.0.2 DTR Algorithm

The DTR algorithm is given below

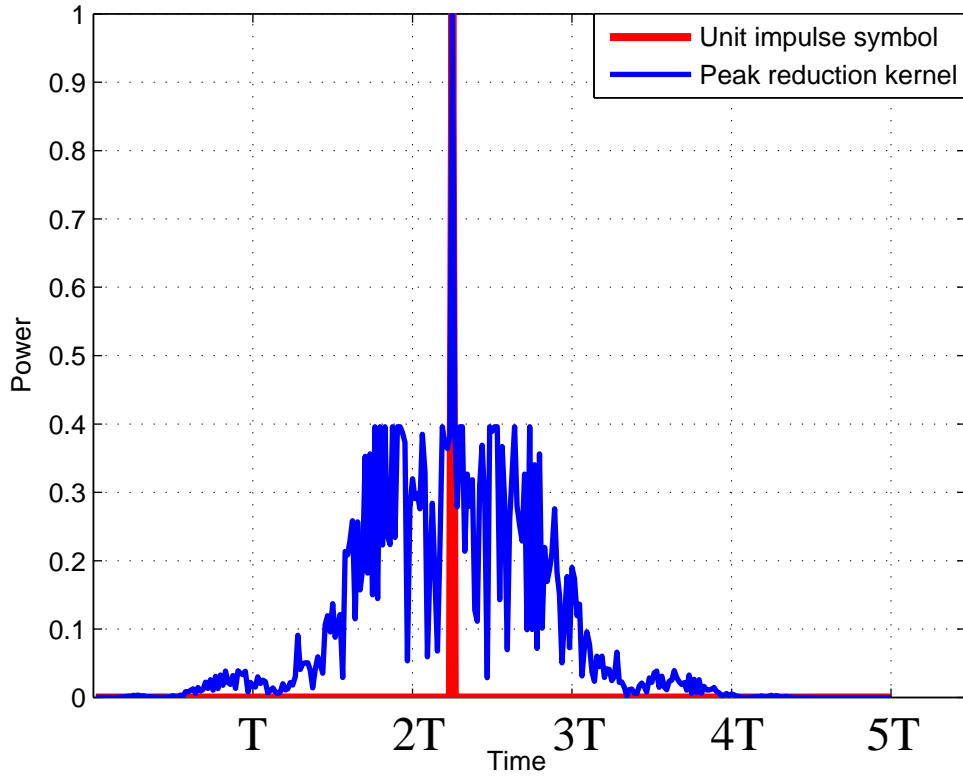


FIGURE 4.13: Illustration of DTR kernel for FBMC-OQAM with 64 sub-carriers.

Step 1 - Initialization: Firstly, we compute the PRT location set \mathcal{B} , based on the peak reduction kernel \mathcal{K} , obtained from equation (4.48). We generate M complex DT sets $\{\mathbf{D}_m\}_{m=0}^{M-1}$ as per equation (2.7) and we put zeros in the PRT locations, for $0 \leq n \leq N-1$, as shown below

$$\mathbf{D}_m[n] = \begin{cases} data, & n \in \mathcal{B}^c \\ 0, & n \in \mathcal{B} \end{cases} \quad (4.50)$$

Then, We initialize $m = 1$. We remind that we compute \mathbf{C}_m such as, $\mathbf{X}_m = \mathbf{D}_m + \mathbf{C}_m$. Our aim is to compute the optimal PRT set, \mathbf{C}_m , by solving the optimization problem of equation (4.12).

Step 2 - FBMC-OQAM modulation: The current FBMC-OQAM symbol $\tilde{x}_m(t)$, is obtained by FBMC-OQAM modulation for the m^{th} DT set \mathbf{D}_m as per equation (2.12)

and the signal generated by past symbols, denoted by $\dot{o}_m(t)$, is added to $\tilde{x}_m(t)$ as below

$$\dot{x}_m(t) = \mathcal{G}\{\mathbf{X}_0, \mathbf{X}_1, \dots, \mathbf{X}_{m-1}, \mathbf{D}_m\} \quad (4.51)$$

$$\begin{aligned} &= \underbrace{\sum_{m'=0}^{2m-1} \sum_{n=0}^{N-1} \dot{b}_{m',n} h(t - m'T/2) e^{j\frac{2\pi}{T}nt} e^{j\varphi_{m',n}}}_{\text{overlapping past symbols}} \\ &+ \underbrace{\sum_{m'=2m}^{2m+1} \sum_{n=0}^{N-1} \dot{a}_{m',n} h(t - m'T/2) e^{j\frac{2\pi}{T}nt} e^{j\varphi_{m',n}}}_{\text{current symbol}} \end{aligned} \quad (4.52)$$

$$= \dot{o}_m(t) + \tilde{x}_m(t) \quad (4.53)$$

where,

- $\dot{x}_m(t) \neq 0$ from $t = [0, (m + \frac{1}{2})T + 4T)$,
- $\dot{a}_{m',n}$ are OQAM mapped from \mathbf{D}_m ,
- $\dot{b}_{m',n}$ are OQAM mapped from $\mathbf{X}_0, \mathbf{X}_1, \dots, \mathbf{X}_{m-1}$.

Step 3 - Optimization: The peak cancellation signal of $\dot{x}_m(t)$, denoted by $\hat{c}_m(t)$ is obtained through convex optimization by solving the below optimization problem as QCQP, on a certain interval $T_0 = [mT + T_a, mT + T_b)$, which is any arbitrary interval within the $[mT, mT + 4.5T)$ interval

$$\hat{c}_m(t) = \arg \min_{\mathbf{C}_m} \left[\|\dot{x}_m(t) + \mathcal{G}\{\mathbf{C}_m\}\|_{\infty}^2 \right], mT + T_a \leq t < mT + T_b \quad (4.54)$$

where, $t \in T_0$, $T_a \geq 0$ and $T_b < 4.5T$.

Step 4 - Peak cancellation: Once $\hat{c}_m(t)$ is obtained, then construct the optimal current input symbol vector

$$\mathbf{X}_m = \mathbf{D}_m + \mathbf{C}_m \quad (4.55)$$

Step 5 - Incrementation: Increment m by 1 and go to **Step 2**, until $m = M - 1$.

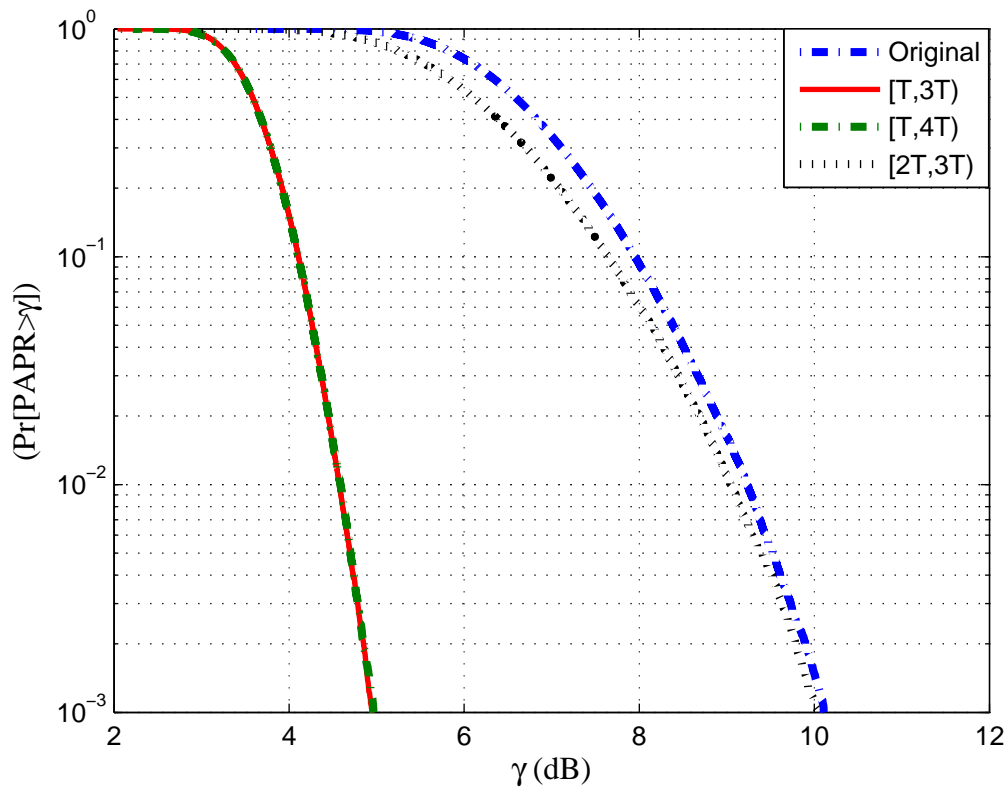


FIGURE 4.14: CCDF of PAPR plot for FBMC-OQAM symbols with PAPR calculated over $[T, 3T)$, $[T, 4T)$ and $[2T, 3T)$ with 8 PRTs (i.e. $R = 8$).

4.6.1 Simulation Results

Simulations are done for a FBMC-OQAM signal that has been generated from 10^6 4QAM symbols with 64 sub-carriers. The PHYDYAS prototype filter was used, which spans for $4T$ [41]. CCDF has been considered as the measurement of PAPR reduction performance. In the simulation figures, the curve “Original” represents the original PAPR of the FBMC-OQAM system without TR (i.e. \mathcal{B} is a null set). Where as, the “DTR” and “TR” represents the dispersive and classical TR schemes respectively. The classical TR is done by substituting $\dot{o}_m(t) = 0$ in equation (4.53).

4.6.1.1 Impact of variation of T_0 duration

When computing the PAPR, the interval $[T_a, T_b)$ of duration T_0 seems to make a significant impact on the performance of DTR scheme as depicted in Fig. 4.14. By varying the duration over which the PAPR is calculated, we can see how it is affecting the efficiency

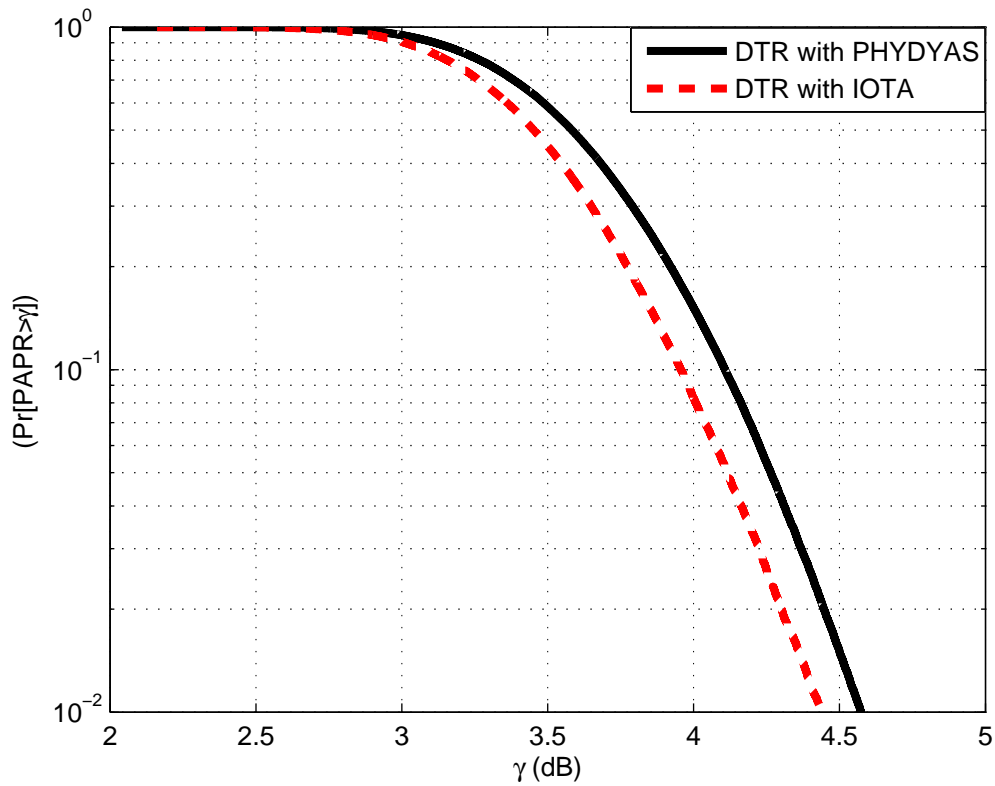


FIGURE 4.15: CCDF of PAPR plot for FBMC-OQAM symbols with PAPR calculated over $[T, 3T)$ with size of PRT set, $R = 8$.

of the DTR scheme. Looking at Fig. 2.9, it is evident that the interval T_0 goes from $T_a = 0$ to $T_b = 4.5T$. Nevertheless, because of the power profile of the prototype filter, the interval T_0 can be reduced. Reducing the interval T_0 reduces the complexity of the optimization problem.

Choosing $T_a = T$ and $T_b = 3T$ or $4T$ give the same performance because, for $t \leq T$, there is no significant contribution of $x_m(t)$ (see Fig. 2.9) and for $t \geq 3T$, it is the same. If we choose $T_a = 2T$ and $T_b = 3T$, there is a significant degradation on the performance, because a significant part of the energy of $x_m(t)$, lies between T and $2T$. In conclusion, it is sufficient to make the optimization problem of equation (4.54), for an interval T_0 going from $T_a = T$ to $T_b = 3T$.

4.6.1.2 Impact of variation in prototype filter

In order to understand the impact of variation in prototype filter over the PAPR reduction performance DTR scheme, simulation has been done by considering isotropic

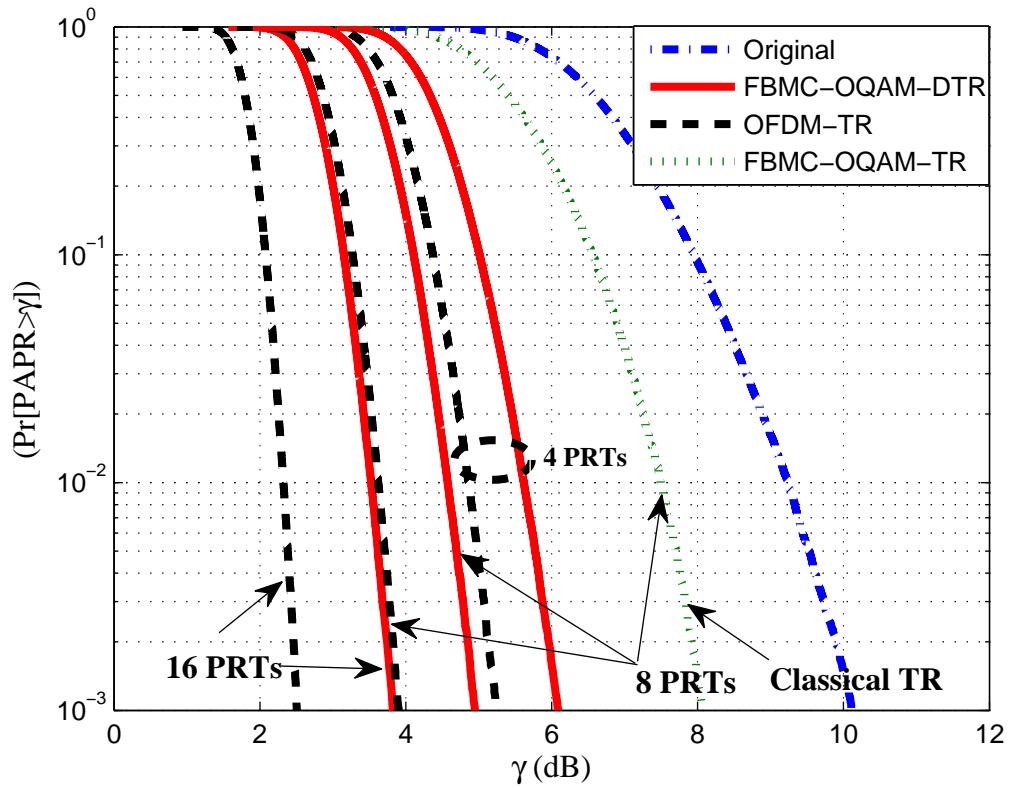


FIGURE 4.16: CCDF of PAPR plot for FBMC-OQAM symbols with PAPR calculated over $[T, 3T)$ with size of PRT set, $R = \{4, 8, 16\}$.

orthogonal transform algorithm (IOTA) filter as the prototype filter. We can notice from Fig. 4.15, that the DTR scheme fares marginally better in a FBMC-OQAM system with IOTA filter than PHYDYAS one. This is due to the fact that the signal energy spread is lower in the case of IOTA filter leading to less symbol overlapping than the PHYDYAS one.

4.6.1.3 Impact of size of \mathcal{B}

In any TR scheme, the size of \mathcal{B} , R impacts the performance of the PAPR reduction [13]. To analyze the impact of R , we have considered different sizes of $R = \{4, 8, 16\}$ and fixed $T_0 = [T, 3T)$. It means, for $R = \{4, 8, 16\}$, we have reserved 6.25 %, 12.5 % and 25 % of the total sub-carriers, respectively, for PAPR reduction by DTR. The values at 10^{-3} of CCDF of PAPR in the Fig. 4.16, have been summarized in Table 4.7. The exploitation of the overlapping nature of the FBMC-OQAM signals can significantly impact the PAPR reduction. From Table 4.7, it is clear that the PAPR reduction performance

TABLE 4.7: CCDF of PAPR at 10^{-3} value (in dB)

Modulation type	Reduction Scheme	$R = 4$	$R = 8$	$R = 16$
OFDM	Classical TR	5.3	3.9	2.5
FBMC-OQAM	Dispersive TR	6.1	4.9	3.8
FBMC-OQAM	Classical TR	—	8.1	—

of FBMC-OQAM with classical TR is outperformed by the one with DTR scheme by 3.2 dB, for $R = 8$. Also in the same figure, we can notice that the CCDF of PAPR for FBMC-OQAM with DTR is closely trailing that of OFDM with classical TR by roughly 1 dB, for $R = \{4, 8, 16\}$, respectively. Another important observation is that, as size of \mathcal{B} is getting increased; we can see the trail gap between CCDF curves of OFDM and FBMC-OQAM is getting increased. The reason for performance lag of DTR scheme is that there is a possibility that PAPR reduction done for the current symbol can be hampered by the future symbols, which is an inherent liability for schemes that opt for symbol-by-symbol approach. The probability of such occurrences increases along with the number of PRTs and this explains the increase in performance lag of FBMC-OQAM with DTR w.r.t. the OFDM with classical TR.

4.6.1.4 Impact of FFT size

Unlike probabilistic schemes, DTR seems to show impressive improvement in PAPR reduction performance, as the FFT size gets increased. We have done simulation for $N = \{64, 256\}$, by reserving 12.5% of the total sub-carriers as PRT locations. It means, we

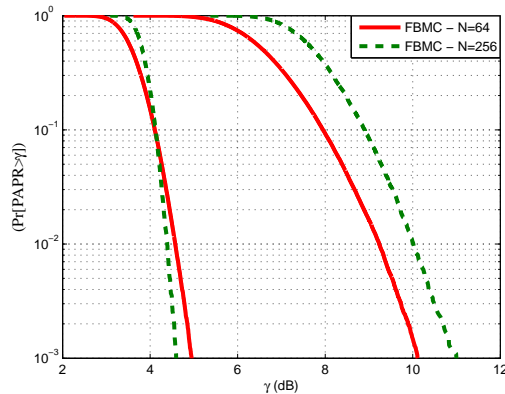


FIGURE 4.17: CCDF of PAPR plot for FBMC-OQAM symbols with PAPR calculated over $[T, 3T)$ with $R = \{8, 32\}$ for $N = \{64, 256\}$ respectively.

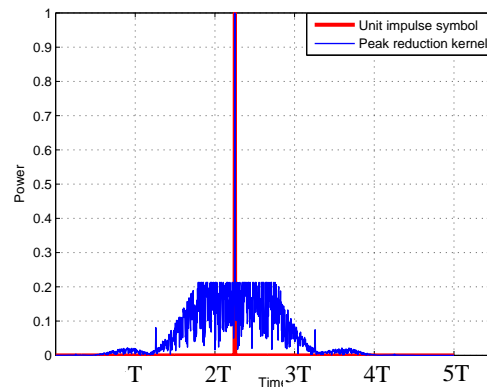


FIGURE 4.18: Illustration of DTR kernel for FBMC-OQAM with 256 sub-carriers.

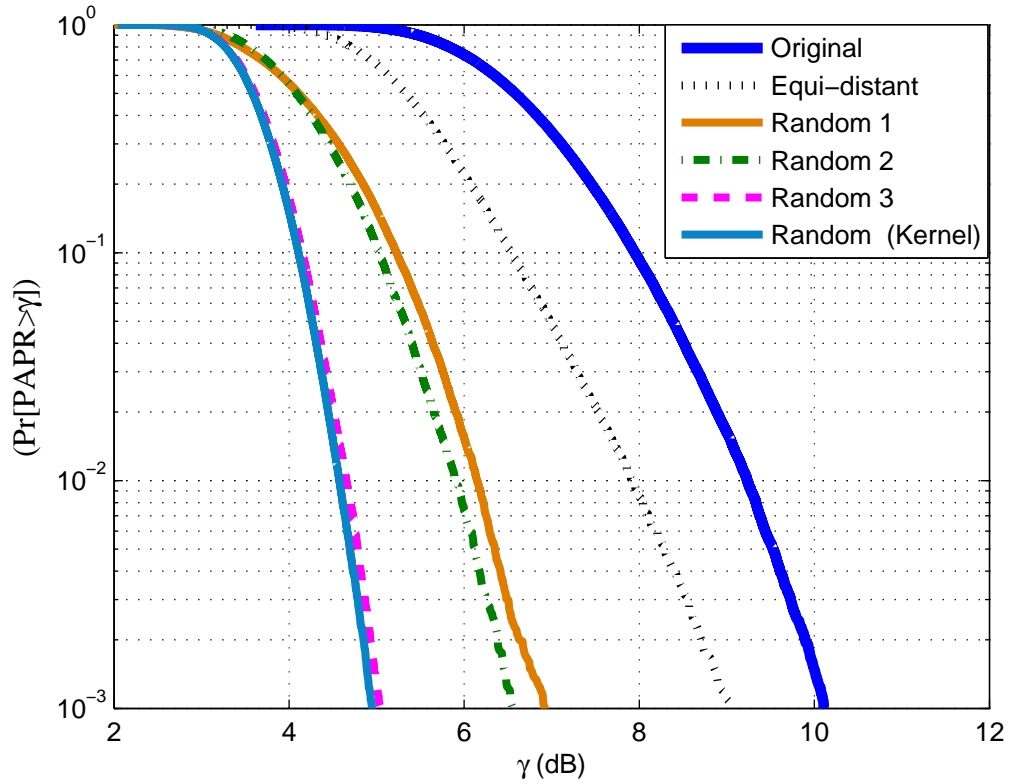


FIGURE 4.19: CCDF of PAPR plot for FBMC-OQAM symbols with PAPR calculated over $[T, 3T)$ with 8 PRTs (i.e. $R=8$) for various PRT locations.

have $R = \{8, 32\}$ for $N = \{64, 256\}$ respectively. Fig. 4.17 illustrates this simulation, we can observe that even though the original PAPR increases along with the FFT size, when DTR is applied, we see ameliorated PAPR reduction performance when $N = 256$. This phenomenon is of particular interest for broadband communication systems, where we have typically, high number of sub-carriers. This superior performance can be explained by the fact that, in the case of $N = 256$, we are able to design a better peak reduction kernel \mathcal{K} , which is illustrated in Fig. 4.18. It is interesting to notice the different in the computed kernel shown in 4.18 with that of 4.13. then we can understand We can observe that in comparison with the original PAPR, the PAPR reduction is around 5.16 dB and 6.4 dB for $N = \{64, 128\}$ respectively.

4.6.1.5 Impact of PRT locations

Simulation results show that the location of PRTs have significant impact on the PAPR reduction of the FBMC-OQAM system with DTR scheme. In the legend of Fig. 4.19,

“equi-distant” and “random (kernel)” indicate the PRT locations that are uniformly spaced, and obtained based on kernel method, respectively. Whereas “random 1”, “random 2” and “random 3” are three different randomly chosen (without kernel method) PRT locations. From Fig. 4.19, it can be inferred that the equidistant case always yields non-optimal performance and it is better to opt for random PRT locations obtained by kernel method; as the PAPR reduction performance of the DTR scheme based on the later depends on luck rather than reason. This result validates our approach of utilizing the PRT locations of the designed kernel for FBMC-OQAM.

4.7 Overview of proposed PAPR reduction schemes

Thus, in this chapter, we have three original proposals for PAPR reduction of FBMC-OQAM systems.

- Dispersive SLM
- Trellis-based SLM
- Dispersive TR

An overview of these three schemes have been provided in Table 4.8. Out of all three schemes proposed, DSLM has least computational complexity, while DTR seems to have better PAPR reduction capability. Although, none of these degrade the BER, we can notice that all three induce rate loss. The rate loss in the two probabilistic schemes is due to SI. While, in the case of DTR, it is caused by reserving sub-carriers for PRTs. The computational complexity of probabilistic schemes doesn’t depend upon number of sub-carriers N .

Nevertheless, an interesting observation is that as the FFT size increases, the PAPR

TABLE 4.8: Overview of different novel PAPR reduction techniques proposed for FBMC-OQAM

PAPR reduction technique	SI	Rateloss	BER degradation	Computational Complexity	PAPR reduction capability
DSLM	Yes	Yes	No	$\mathcal{O}(MU)$	Low
TSLM	Yes	Yes	No	$\mathcal{O}((M-1)U^2)$	High
DTR	No	Yes	No	$\mathcal{O}(MRN^2)$	Very High

reduction capability of DTR gets ameliorated. Where as, the suggested probabilistic schemes, DSLM and TSLM, doesn't almost constant PAPR reduction performance, for different FFT size.

4.8 Conclusion

Since FBMC-OQAM signals have high PAPR, there is a dire need to probe for suitable PAPR reduction schemes. Classical probabilistic schemes available for OFDM systems cannot be directly applied. By taking overlapping signal structure of FBMC-OQAM into account, initially DSLM scheme has been suggested, which is essentially a symbol-by-symbol approach. However, DSLM leads to a sub-optimal performance w.r.t the classical scheme in OFDM. However, the phase rotations of the past symbols in DSLM are fixed or already chosen, as it follows symbol-by-symbol approach. It means, the peak reduction we may obtain for the current symbol, can possibly be destroyed by the future symbol. This is the main reason for lagging performance of DSLM behind the OFDM with SLM scheme. Since trellis-based scheme involves in optimizing the PAPR for more than one symbol at a time, it naturally offers superior performance than a symbol-by-symbol approach. In fact, the proposed TSLM scheme outperforms the OFDM in terms of reduction performance for any kind of prototype filter. Nevertheless, variation in prototype filter has slight impact on the performance and it depends on the spreading extant of the filter impulse response.

Finally, a TR based scheme, namely DTR has been proposed, which seems to yield very good PAPR reduction performance. We have suggested a kernel method to identify the PRT locations, which impact heavily the PAPR reduction performance of DTR. To realize the optimal performance in a symbol-by-symbol approach, we have used QCQP. Nevertheless, any other convex optimization method can be used. Simulation results show that, although we consider the overlap of the past symbols, the duration of signal considered for optimization has significant impact on the PAPR reduction performance and the proposed DTR scheme is quite effective in reducing the PAPR of the FBMC-OQAM signal and the PRT locations also play vital role in that aspect. Albeit, this scheme is closely lagging behind the OFDM with classical TR in terms of PAPR reduction performance.

Chapter 5

Coexistence capability of FBMC-OQAM

Systems with PMR Systems

5.1 Introduction

The public protection and disaster relief (PPDR) agencies in Europe are relying on digital PMR narrowband networks for mission-critical voice and data communications. The PMR networks are used nowadays for voice communications, where voice data occurs at low rate [88] and they are highly resilient and properly dimensioned to cope with crisis and emergency handling, and are well protected against monitoring and intrusion by means of encryption, authentication and integrity. Lately, there are increasing attempts to enhance its scalability, in order to support high-rate applications and broadband services [30]. TETRA (TERrestrial Trunked RAdio) and TETRAPOL are the two main standards for digital PMR networks in Europe. The Tetra enhanced data service (TEDS) is a new TETRA High Speed Data (HSD) service using different RF channel bandwidths and data rates for flexible use of PMR frequency bands. TEDS is capable of providing HSD in 150 kHz RF channels. However, the current limitation caused by insufficient RF spectrum to support the growth of TETRA will probably limit early deployments. So, PMR system need to coexist with a broadband system that can fit

perfectly within the PMR–TEDS harmful interference protection requirements. Notwithstanding by this, in general, there is a dire need for a new 5G radio waveform that can be narrowband-friendly. Even though conventional LTE broadband system, can cope with the ever increasing demands for wireless bandwidth, its coexistence with the narrow band systems, while retaining its normal performance without comprising on throughput, is one of the crucial challenges in 5G RAT. Broadband systems such as LTE stand as one of the most attractive candidates that can achieve very high data rates. Since the 3GPP LTE is supposed to dominate in the forthcoming years, it is natural to consider the LTE system as a reference basis in the PMR system development.

The advent of the cognitive radio (CR), Ad-hoc networks, device-to-device (D2D) and the expected explosion of Machine Type Communication (MTC) are posing new and unexpected challenges such as asynchronism and low latency in communications. 5G RAT is supposed to deal with these serious challenges especially for MTC, D2D as it would be interesting for not to have a very tight synchronization, which is costly in terms of energy consumption. The current generation of cellular physical layers such as used by LTE and LTE Advanced requires strict synchronism and orthogonality between users within a single cell. Fast dormancy necessary for these types of equipment to save battery power can result in significant control signaling growth in a synchronized network. Even while there is no traffic between the network and user equipment (UE), who has to keep listening to network, which would drain the battery. For OFDM-based conventional LTE has latency of around 10 *ms*. In general, low latency is desirable for user experiences; albeit, with more power consumption at the terminal side. So, the future MCM technique should tolerate not only the asynchronism but also support low latency. Furthermore, as the availability of large amounts of contiguous spectrum is getting more and more difficult to guarantee, the aggregation of non-contiguous frequency bands has to be considered. Therefore, some key parameters for future generations of wireless networks are, energy efficiency, low carbon emission, low latency, relaxed synchronization constraint and access to fragmented spectrum (i.e. allow coexistence).

Precisely, in the context of PMR systems, it has been recently shown that a LTE-like broadband system based on OFDM lack coexisting capability, even in the absence of RF impairments [89]. This implies the dire need in the context of 5G PMR systems, to probe for new MCM waveforms that can: i) support user aysnchronism and low latency, ii) permit coexistence with narrowband systems and iii) be capable to be operated with NL devices with high energy efficiency. In this regards, a genuine attempt has been done

in this chapter, to address the hitherto mentioned issues. Although, OFDM is the first choice for next generation communications; still it is not considered the optimal MCM technique for PMR coexistence. The principal reason is the lack of sub-channels' spectral confinement, making it especially inapplicable to non-synchronized mobile networks. This chapter investigate the coexistence capabilities of OFDM and FBMC-OQAM systems. A PMR system that operates on licensed narrowband located in 380-400 MHz, 410-430 MHz, or 450-470 MHz is considered in our analysis.

This chapter is organized as follows: The section 5.2 discuss about PMR system. In the section 5.3, TEDS standard mask defined in the ETSI TETRA standard is discussed. Section 5.4 introduces a LTE-like FBMC-OQAM system model in a typical coexistence scenario and defines some key parameters related to the LTE system that are used for the context analysis. In section 5.5, the co-existence capabilities of FBMC-OQAM system will be examined in the case of ideal PA and then taking into account the NL nature of PA based on a behavioral model. Later, in the same section, the impact of PAPR reduction on the interference analysis is studied. In section 5.6, we summarize the observations from the previous analysis and propose a possible solution for the considered coexistence scenario. Finally, section 5.7 concludes this chapter.

5.2 PMR systems

PMR systems are fundamentally used for low-rate data transmission like voice communications in public safety services by public and private organizations alike. In order to cope up with the broadband data communication services in the future generations, a remarkable transformation is going on for PMR-based PPDR communications such as TETRA, TETRAPOL, TETRA/TEDS, APCO in US and others [30]. One among the earliest critical communication systems is the TETRA, which was mature and established TDMA digital voice trunked and data radio technology used around the world. TETRA is an open standard developed by the European Telecommunications Standards Institute (ETSI), which was introduced in the market in 1997. It has significantly evolved into TEDS, in order to integrate the wide-band data. By supporting around several hundred kbit/s data rates, TEDS fits well into the PMR frequency spectrum. The narrowband PMR is designed to be in accordance with the channels used for analog PMR networks with typical channel width of 12.5 or 25 kHz . Especially public safety

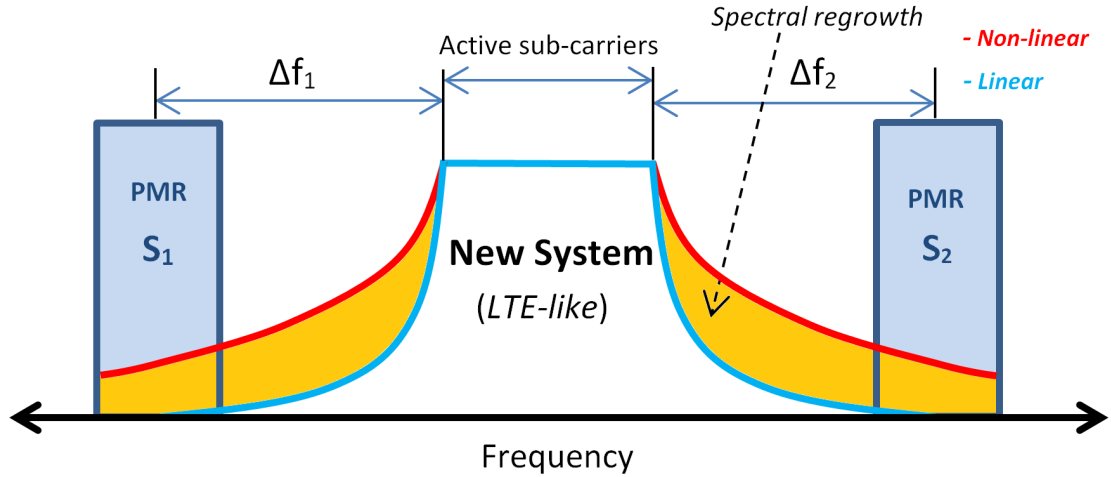


FIGURE 5.1: Coexistence of a LTE-like broadband system with narrowband PMR users.

organizations are investigating in LTE as basis for future broadband data standard for their applications.

5.3 TEDS reception mask

The focus shall be on a 25 kHz TEDS system and the extension to other PMR standards is straightforward. The interfering signal powers can be represented as function of frequency offsets between the nominal carrier frequency (i.e. center frequency) of the TEDS system and the closest adjacent interfering channel.

In the scientific literature, PSD is commonly used for interference analysis. Interference evaluation involves the calculation of spectral distance of the OOB radiation value between a designed carrier and its spectral distance from the primary band. The resulting interference power in a given bandwidth $[f_1, f_2]$ is defined by

$$I = \int_{f_1}^{f_2} \Phi(f) df \quad (5.1)$$

where, $\Phi(f)$ is the PSD of the MCM waveform of the broadband system.

The overall interference level can be defined as the maximum interference level that should be tolerated by the TEDS receiver in order to guarantee a given quality of service. Mathematically, the overall interference level I , expressed in dBm, is the difference

between the receiver's sensitivity S_{dBm} and the signal-to-noise ratio E_S/N_0 .

$$I = S_{\text{dBm}} - E_S/N_0 \quad (5.2)$$

Finally, the TEDS reception mask R_m in dBc, for a given frequency offset, is the difference between the overall residual interference levels I and the blocking levels B .

$$R_m = I - B \quad (5.3)$$

The value of E_S/N_0 can be computed in dB as below

$$\begin{aligned} \frac{E_S}{N_0} &= S_{\text{dBm}} - 10 \log_{10}(kT_0W) - NF - \nu_{\text{dB}} - 30 \\ &= S_{\text{dBm}} - 10 \log_{10}(1.38 \times 10^{-23} \times 290 \times 25000) - NF - \nu_{\text{dB}} - 30 \\ &= S_{\text{dBm}} + 160 - NF - \nu_{\text{dB}} - 30 \end{aligned} \quad (5.4)$$

- $k = 1.38 \times 10^{-23} \text{ J/K}$ is the Boltzmann constant,
- $T_0 = 290 \text{ K}$ is the reference temperature for receiver noise,
- $W = 25 \text{ kHz}$ is the total bandwidth of the TEDS receiver,
- NF is the noise figure,
- ν_{dB} is the efficiency loss (in dB).

As per the TEDS standard [88], S_{dBm} is -113 dBm , NF is 11 dB for mobile station in downlink for 4 QAM constellation. For 16 QAM and 64 QAM constellations, the receiver sensitivity levels are -106 dBm and -101 dBm respectively. Also, the efficiency loss ν_{dB} is computed as

$$\begin{aligned} \nu_{\text{dB}} &= 10 \log_{10} \left(\frac{N_d}{N_t} \times \frac{R_s S_c}{W} \right) \\ &= 10 \log_{10} \left(\frac{204}{272} \times \frac{2400 \times 8}{25000} \right) \\ &= 10 \log_{10}(0.576) \\ &= -2.4 \text{ dB} \end{aligned} \quad (5.5)$$

- $N_d = 208$ is the number of data symbols in a TEDS slot,
- $N_t = 272$ is the number of total symbols in a TEDS slot,

- $R_s = 2400$ bauds is the symbol rate,
- $S_c = 8$ is the number of subcarriers in the considered bandwidth.

The OOB radiation of the LTE system should respect the reception mask levels specified as per the TEDS standard. Based on the blocking level B given in Table 5.1, we can compute the 25 kHz-TEDS reception mask R_m as

$$\begin{aligned}
 R_m &= 10 \log_{10}(kT_0W) + NF + \nu_{\text{dB}} + 30 - B \\
 &= -160 + 11 - 2.4 + 30 - B \\
 &= -121.4 - B
 \end{aligned} \tag{5.6}$$

TABLE 5.1: 25 kHz-TEDS receiver blocking levels and mask

Offset nominal Rx freq.	Blocking level, B	Mask level, R_m
50 kHz to 100 kHz	-40 dBm	-81.4 dBc
100 kHz to 200 kHz	-35 dBm	-86.4 dBc
200 kHz to 500 kHz	-30 dBm	-91.4 dBc
> 500 kHz	-25 dBm	-96.4 dBc

5.4 System model in a typical coexistence scenario

We analyze the possibility to deploy a LTE-like MCM system in a 1.4 MHz PMR channel (located in the 400 MHz band) in presence of a NL PA. As illustrated in the Fig. 5.1, a typical coexistence issue can be a situation where the broadband system should respect the constraints imposed by the already existing and operational PMR communication devices, S_1 and S_2 that are situated in a frequency spectrum with a given spectral gap. So, the spectral gap of 1.4 MHz PMR band between S_1 and S_2 , has to be filled with a new system, which can be a LTE-like broadband system. Actually, we have chosen spectral gap, just to illustrate a typical LTE-like broadband system. However, this gap can vary. 1.4 MHz spectral gap, just to illustrate a typical LTE-like broadband system. However, this gap can be vary Depicted systems S_1 and S_2 , in Fig. 5.1 are two TEDS of 25 kHz bandwidth each. Δf_1 and Δf_2 are the frequency offsets, i.e. distances between the nearest adjacent interferer channels and the nominal carrier frequencies of the existing active users in the band. The PMR systems considered for the analysis are defined by

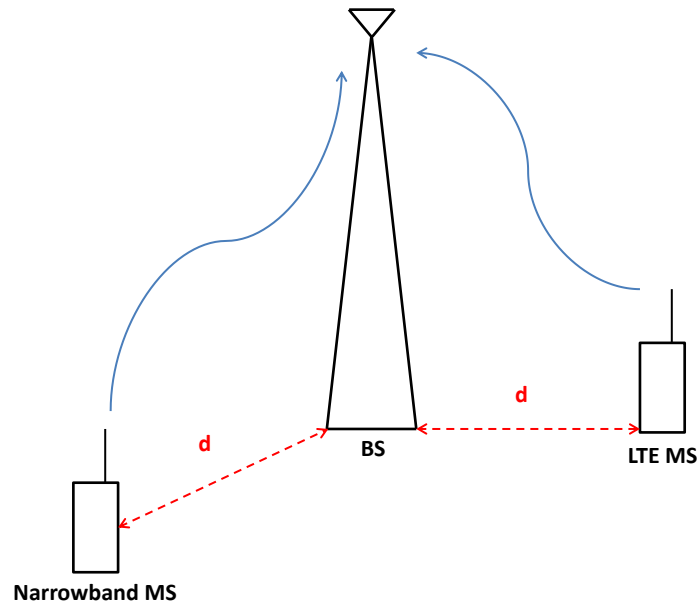


FIGURE 5.2: The location of LTE mobile station and narrowband mobile station near a base station in our coexistence scenario.

ETSI TEDS standard [88]. It has been proposed in [89], that a LTE-like system can be deployed in the spectrum holes of the PMR bands by strictly respecting the reception masks of the currently active PMR systems as per the PMR standard's interference blocking recommendations. The characteristic parameters of a 1.4 MHz LTE system, are shown in Table 5.2 [90]. The OOB radiation of the LTE-like system should be below a particular level such that the destructive interference level of this system will be below the mask level given in Table 5.1.

TABLE 5.2: LTE Physical layer parameters

Transmission bandwidth	1.4 MHz
Sub-carrier spacing	15 kHz
Size of FFT	128
Useful subcarriers (with DC)	73
Effective bandwidth	1.08 MHz

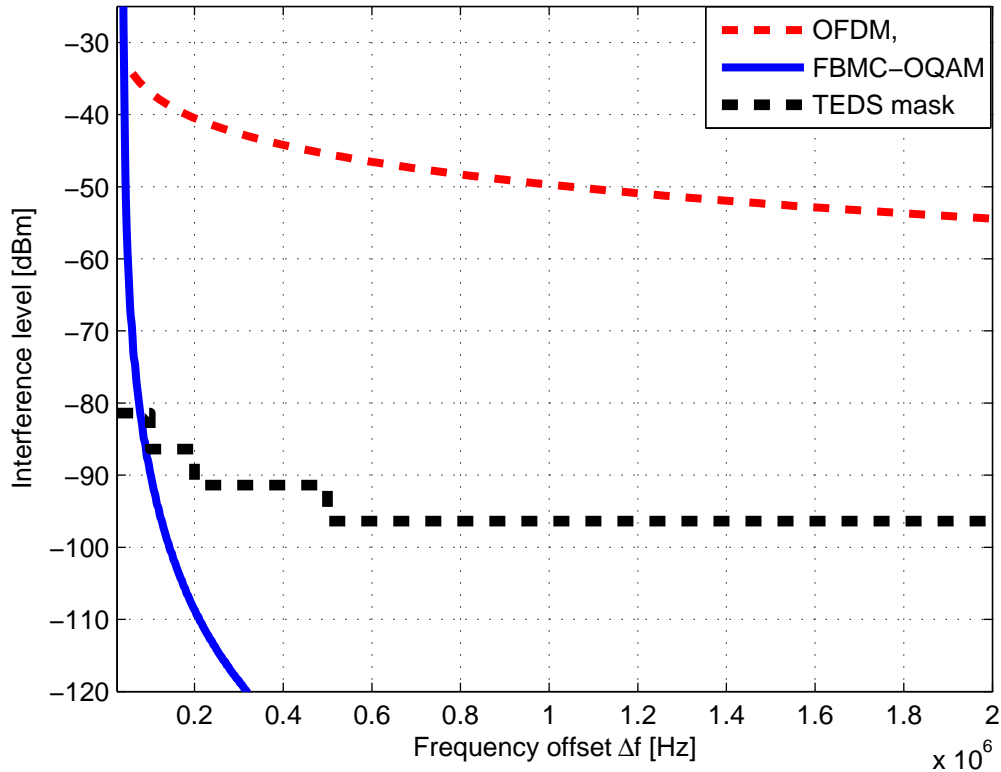


FIGURE 5.3: Interference performances for OFDM and FBMC-OQAM with linear PA.

5.5 Interference analysis of the coexistence scenario

The simulations are done with 128 subcarriers for 4 QAM symbols in a LTE-like MCM system in a 1.4 MHz PMR band, coexisting with 25 kHz narrowband PMR legacy systems. The oversampling factor L is 4. As illustrated in Fig. 5.2, it is assumed that the base stations of narrowband systems and the LTE one are situated next to each other so that there is no path loss (i.e. the transmitters of PMR users and the LTE-like system are equi-distant from the PMR-receiver). It has to be noted that the LTE-like system transmit power is fixed to 0 dBm.

5.5.1 Coexistence scenario in a linear case

We have tested the capability of the FBMC-OQAM system to fulfill the TEDS mask, first assuming a hypothetical linear case with an ideal PA, where the output signal is nothing but an amplified input signal with a linear gain (i.e. no amplitude or phase distortion). The power spectral density (PSD) of each waveform is integrated over a

25 kHz bandwidth and compared with the TEDS mask in Fig. 5.3. It is clear from this figure that FBMC-OQAM is able to satisfy the TEDS mask and not the OFDM one. Even without taking the energy efficiency constraint and assuming an ideal amplification scenario, only FBMC-OQAM can fulfill the TEDS mask. It means, when PA non-linearity is taken into account, it is meaningless to consider OFDM as the effective interference will be increased, due to possibly induced spectral regrowth. So, we consider only FBMC-OQAM, hereafter in our analysis.

5.5.2 Coexistence scenario in a NL case

Since, energy efficiency is a serious issue, it is vital to analyze the coexistence scenario, taking into account the PA non-linearities. To meet the energy efficiency requirements, it is necessary to operate the PA in the NL region, which induces spectral regrowth resulting in OOB radiation in FBMC-OQAM. The PA behavioral model used in our analysis is the Rapp model behaving with conversion characteristics given in equations (2.54) and (2.55).

5.5.2.1 Scenario 1: Realistic model without PAPR reduction

We consider a realistic case of the Rapp model with $p = 2.25$, as in the case of PHYDYAS project, where the PA model shows severe non-linear nature. Impact of the IBO on the effective interference has been simulated and the results are shown in Fig. 5.4. In the legend, “Linear” indicates a hypothetical ideal PA, “IBO” indicates the presence of NL PA w.r.t a given IBO, “TEDS mask” indicate the 25 kHz TEDS reception mask given in Table 5.1. As evident from this figure, the IBO has to be greater than 21 dB in order to respect the TEDS mask, which is practically non-feasible, as the energy efficiency will be terribly low.

5.5.2.2 Scenario 2: Perfectly linearized model without PAPR reduction

The analysis of the previous scenario prompted us to investigate an ideal case where perfect linearization of PA is assumed. This can be done by fixing $p = \infty$ in equation (2.54), where the performance of PA converges to that of a SEL. Fig. 5.5 summarizes the impact of IBO on the effective interference, when no PAPR reduction is done and

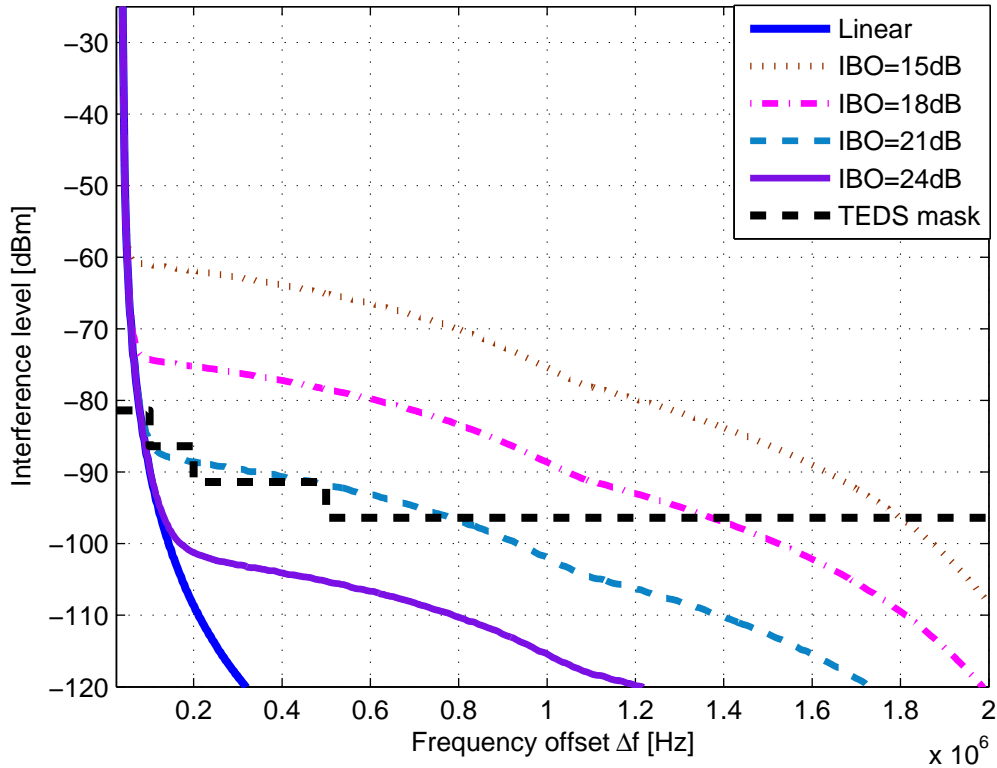


FIGURE 5.4: Impact of IBO on the effective interference of FBMC-OQAM system with a realistic PA model (Rapp model with $p = 2.25$).

IBO of 11.7 dB is needed to adhere the TEDS mask. This implies that even when a PA is perfectly linearized, the energy efficiency cannot be completely assured, which is a serious criterion as stated earlier.

5.5.2.3 Scenario 3: Perfectly linearized model with PAPR reduction

To understand the impact of PAPR reduction, we have implemented DTR scheme in the perfectly linearized PA case and the interference analysis results are shown in the Fig. 5.6. In the legend, “IBO...with PAPR redn” indicates the presence of NL PA w.r.t a given IBO with PAPR reduction for a given value of R (we recall that R is the number of reserved tones). As predicted, the PAPR reduction seems to have significant impact on the coexistence scenario. In Fig. 5.6 it can be noticed that for $R = \{8, 16\}$, the TEDS mask can be obeyed for IBO values of 6.7 dB and 5.6 dB respectively. While observing the performance of DTR scheme, one must take into account the IBO value also, which explains the apparent better performance of $R = 8$ than $R = 16$. So, there is a tradeoff

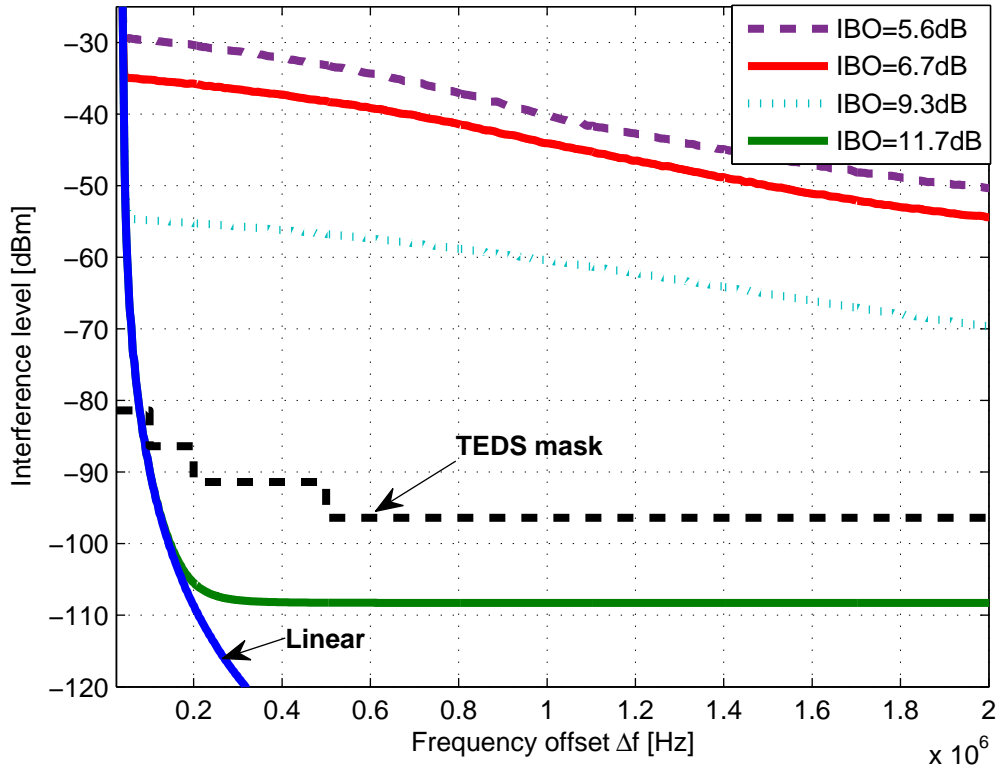


FIGURE 5.5: Impact of IBO on the effective interference of FBMC-OQAM system with a perfectly linearized PA.

between the rate loss (due to PRTs) and power loss (due to IBO). But, the coexistence seems to be possible; if a judicious choice of IBO and R is achieved.

5.5.2.4 Scenario 4: Moderately linearized model with PAPR reduction

Now, we assume that some linearization of PA has been done, making the PA model moderately linear by choosing a higher value of $p = 6$ compared to that of the model in Scenario 1 (refer 5.5.2.1). The extent of moderate linearization can be understood from the AM/AM conversion characteristic in Fig. 2.12. From Fig. 5.7, it can be noticed that for $R = 16$, the TEDS mask can be obeyed for IBO values of 9.2 dB with DTR scheme, which saves around 4.7 dB when compared to the case without PAPR reduction. Though not plotted, it has been found that an IBO of 13.9 dB is needed to adhere the TEDS mask; without any PAPR reduction.

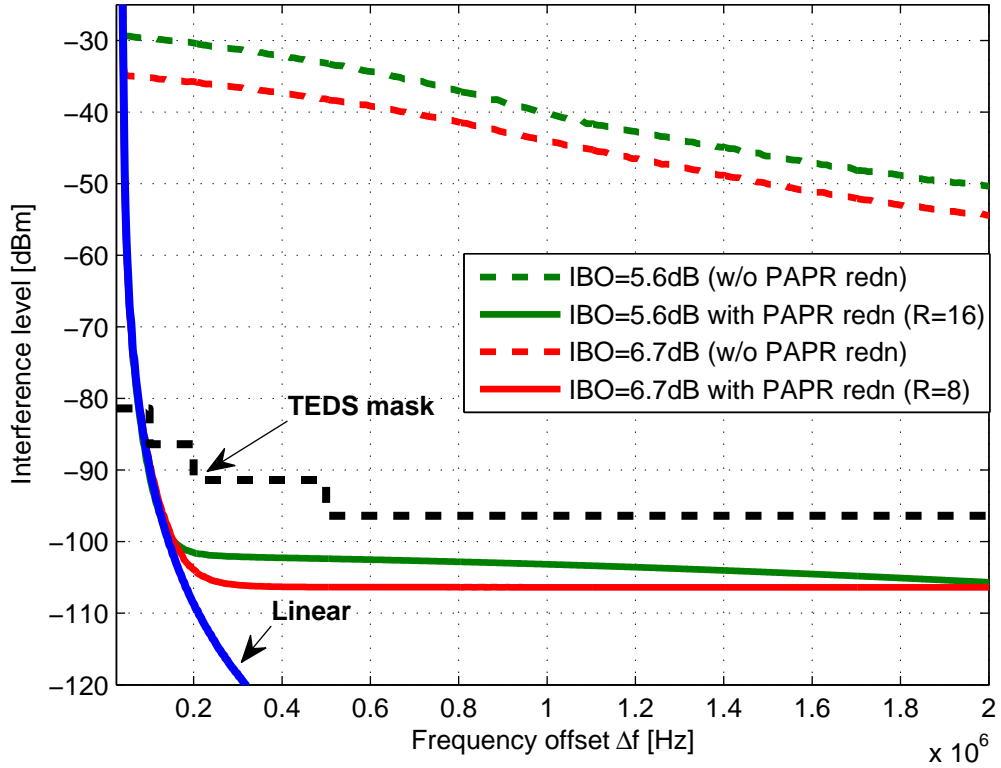


FIGURE 5.6: Impact of PAPR reduction on the effective interference of FBMC-OQAM system with a perfectly linearized PA.

5.6 Proposed solution for PMR coexistence

Merely increasing IBO to respect the mask is not an optimal approach as it results in higher energy wastage. The IBO needed to fit into TEDS mask in these scenarios has been summarized in Table 5.3. By analyzing the three scenarios, we can conclude that the impact of NL effects of PA can be decisively mitigated by: (i) linearization of NL PA, (ii) operating the NL PA with high IBO and (iii) PAPR reduction of the input signal. Therefore, we conclude that for a LTE-like FBMC-OQAM system to coexist with

TABLE 5.3: IBO requirements to reach the TEDS spectrum mask for FBMC-OQAM system with bandwidth corresponding to 72 active LTE subcarriers. SSPA model with different values of knee factor p with and without DTR based PAPR mitigation.

SSPA model p -factor	Minimum IBO in dB without PAPR mitigation	Minimum IBO in dB with DTR mitigation
2.25	> 21	–
6	13.9	9.2
300	11.7	5.6

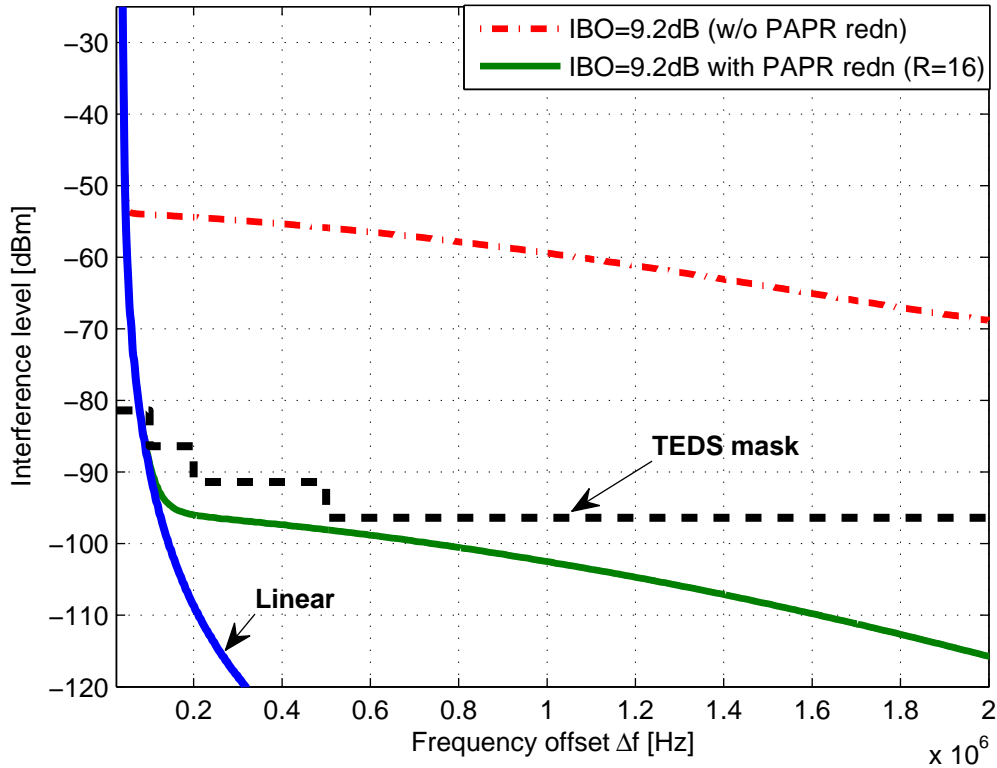


FIGURE 5.7: Impact of PAPR reduction on the effective interference of FBMC-OQAM system with a moderately linearized PA.

already existing narrowband PMR/PPDR systems, it is mandatory to have both PA linearization and PAPR reduction along with sufficiently moderate IBO. Linearization of NL PA can be achieved by techniques such as digital pre-distortion techniques and shall be duly considered in the next Chapter 6.

5.7 Conclusion

The PPDR agencies in Europe are relying on digital PMR narrowband networks for mission-critical voice and data communication, which adhere to the TETRA standard in Europe. TEDS is the new HSD service in this regard, which is capable of providing broadband service. Albeit, the insufficient spectrum remains to be a stumbling block for the growth of TETRA. There is a serious need to probe for a post-OFDM waveform that can: i) support user asynchronism and low latency, ii) permit coexistence with narrowband systems and iii) be capable to be operated with NL devices with high energy

efficiency. It can be noticed that FBMC-OQAM system seems to be a promising candidate satisfying first two aforementioned constraints, while their operation on NL devices is a severe hindrance due to the induced spectral regrowth. This chapter investigates the impact of PA non-linearities to comprehend the arising challenges and to find means to overcome those. Merely increasing IBO to respect the mask is not an optimal approach as it results in poor efficiency. Different scenarios of PA non-linearity have been studied. The simulation results suggest that it is mandatory to have both PA linearization and PAPR reduction along with sufficiently moderate IBO and it has been concluded that a FBMC-OQAM system can still coexist with PMR/PPDR systems.

Chapter 6

PA linearization techniques for FBMC-OQAM systems

6.1 Background

As energy efficiency communications is the need of hour, it is essential to mitigate NL effects. Thus, in modern wireless communication systems, it is very important to realize simultaneously high-efficiency and linear operation of the power amplifiers. PA linearization has become a subject in its own right in recent years, and has seen a large investment of research and development funding in both the industrial and academic sectors. Every few months, it seems, a new start-up company lets out a press release proclaiming their totally new, disruptive linearized PA technique which will revolutionize the industry; another heavily patented area [91].

It is often necessary in a communication system, to suppress spectral regrowth, contain adjacent channel interference, and reduce BER. In order to ensure linear amplification of a signal, a PA with a power higher than required is usually selected such that the input signal fits into the linear region of the PA. This “back-off” approach can result in a significant increase in PA power specification as well as reduced efficiency. This is due to the fact that the PA is using a high DC power; but, is utilizing only a small portion

TABLE 6.1: Impact of Digital Predistortion

PARAMETERS	Digital Predistortion	
	No	Yes
PA power rating	160 W	80 W
Peak power	80 W	80 W
Average power	10 W	10 W
PAPR	9 dB	9 dB
IBO	12 dB	9 dB
Efficiency	9 %	18 %
Power dissipation	101 W	45 W

of its allowed input range. Thus, PA linearization approach offers a good remedy to this problem. With PA linearization the PA linearity is improved and extended so that the PA can be operated at lower IBO. This means that a lower-power lower-cost linearized PA can be used in place of a higher-power higher-cost PA. Furthermore, the linearized PA operates more efficiently since it is operated closer to saturation. The benefits are compounded because a lower-power PA operating more efficiently consumes substantially less power than an inefficient higher-power PA.

Among all linearization techniques, digital base-band predistortion is one of the most cost effective techniques. A predistorter, which (ideally) has the inverse characteristic of the PA, is used to compensate for the non-linearity in the PA. The benefits of digital predistortion (DPD) are even more pronounced for multi-carrier applications where the PAPR is large. With industry trends towards multi-carrier cellular base stations increasing, digital predistortion is certain to be a critical technology in the future.

To elucidate this concept, a typical example has been shown in Table 6.1 [92], where, a linearized 80 W PA is compared to an unlinearized 160 W PA. The linearized 80 W PA can be operated in the linear zone with a peak power of 80 W. Where as, in order to ensure linear operation, the unlinearized 160 W PA may only be utilized up to a peak power of 80 W. Since, only half of its power is utilized, i.e., the 160 W PA uses additional 3 dB IBO, its efficiency is lower than that of the 160 W PA. From the Table 6.1, it can be noticed that the power dissipation of this later is more than twice than that of the 80 W PA. This means, using the linearized 80 W PA is more advantageous, as it can be smaller and cheaper than the 160 W PA; since, both price and size generally increase with the PA power specification. The power consumption of the linearized 80 W PA is less; implying that, it requires less energy to operate. Alternatively, if the PA is operating using a battery, then the battery will last longer. Since, it has less power

consumption and thereby, dissipating less heat; which, in turn reduces the cooling costs. In this dissertation, the PA linearization aspects have been briefly dealt with an aim to propose some DPD techniques for FBMC-OQAM. A novel DPD technique, termed as overlapped recursive error correction has been proposed in this chapter for linearization of non-linearly amplified FBMC-OQAM signals.

This chapter is organized as follows: The Section 6.2 presents different types of PA linearization techniques suggested for OFDM. Section 6.3 presents the state-of-art of digital predistortion techniques proposed for FBMC-OQAM and the adding signal based predistortion approach. Later, in the same Section 6.3, novel predistortion technique proposed in this thesis dissertation is presented. In, Section 6.4, the PA linearization analysis with the newly proposed technique shall be duly dealt with simulation results. Finally, the chapter is concluded in Section 6.5.

6.2 Introduction to PA linearization techniques

Generally, PA linearization techniques rely on the amplitude and phase of the input RF envelope as a template, for comparing with output; and thereby generate appropriate corrections. The main distinction in linearizing techniques is formed by the manner in which the correction is applied. These two approaches are input and output correction [91]. The correction is applied at the input cannot increase the PA peak power; while, the one applied at output increases the peak power capability of PA. There are many different linearization systems described in the open literature: power backoff, feedback, feedforward, dynamic biasing, envelope elimination and restoration (EER), predistortion, linear amplification with NL components (LINC) and adaptive predistortion. Predistortion, which can be either analog or digital. In this thesis, we focus primarily on digital predistortion.

6.2.1 Power backoff

Power backoff exploits the observation that any amplifier appears linear for sufficiently small departures from its bias condition. Power backoff is not really true to the spirit of linearization techniques, because no attempt is made to beat the linearity-vs.-efficiency tradeoff. The input drive is simply reduced until linearity requirements are met, and

the resulting efficiency is accepted, which can be extremely low as it is not uncommon to hear figures on the order of 5%. It is mentioned here because it is so commonly used, and because it is, in fact, the best solution in some cases.

6.2.2 Feedback

The use of feedback techniques to reduce or eliminate the quirky and unpredictable behavior of electronic devices has been standard practice for just about the full duration of the electronic era. Fundamentally, the concept behind this technique is a negative feedback [93]. It runs into problems, however, when the time delay of the propagating signals becomes significant in comparison to the timescale on which the signals themselves are changing. Some categories of feedback techniques are direct, indirect, Cartesian loop and polar loop. The feedback technique is used in some narrow band applications in order to improve the linearity. The improvement is about 3 dB to 5 dB and depends on the bandwidth and frequency of operation. The phase and amplitude flatness are the major items affecting the improvement especially the phase flatness.

6.2.3 Feedforward

The feedforward configuration consists of two circuits, the signal cancellation circuit and the error cancellation circuit. The purpose of the signal cancellation circuit is to suppress the reference signal from the main power amplifier output signal leaving only amplifier distortion, both linear and nonlinear, in the error signal. Linear distortion is due to deviations of the amplifier's frequency response from the flat gain and linear phase [94]. Distortion from memory effects can be compensated by the feedforward technique, since these effects will be included in the error signal. The purpose of the error cancellation circuit is to suppress the distortion component of the PA output signal leaving only the linearly amplifier component in the linearizer output signal.

The feedforward structure is very complicated but it still be widely used in the narrow band wireless market because of its dramatic improvement on the linearity of the amplifier. The efficiency of the classical feedforward structure is only about 6% to 7% [95].

6.2.4 Dynamic biasing

In some cases, an amplifier exhibits good linearity over a wide range of input signals. In that scenario, the focus of the linearization effort shifts away from making great gains in linearity. Instead, one thinks of trading the excess linearity for a boost in power efficiency. A strategy for doing this is called dynamic biasing [96]. In a dynamic biasing scheme, the gate (or base) bias voltage of the amplifying device is varied according to the known statistics of the transmitted signal. The goal, at all times, is for the amplifier to use the minimum bias current needed for a given level of linearity. While it is difficult to achieve this ideal in practice, substantial gains in efficiency are nevertheless possible.

6.2.5 Envelope elimination and restoration

The unmatched efficiency of switching power amplifiers has prompted efforts to utilize them for linear amplification purposes. EER falls into the category of one such effort [97]. The basic idea is to typically use a switching, DC-DC feedback power converter in order to impose the varying envelope on the power supply of the switching PA. The DC-DC converter represents a design issue that can make EER and polar feedback systems difficult to implement.

6.2.6 Linear amplification with NL components

LINC is another approach to harnessing the efficiency benefits of switching PA. It is a linearization technique, whereby, a linear modulation signal is converted into two constant envelope signals that are independently amplified by power-efficient Class D amplifiers and then combined using a hybrid coupler [98]. The most obvious hindrance to this technique might be the complexity in generation of the two constant envelope signals, although it can be achieved with sufficient computing power. Another very serious difficulty is managing the phase and gain mismatch between these two signal paths, and the drift thereof. The most prohibitive hurdle is implementing the summation in a way that is low loss and maintains high isolation between the two PAs.

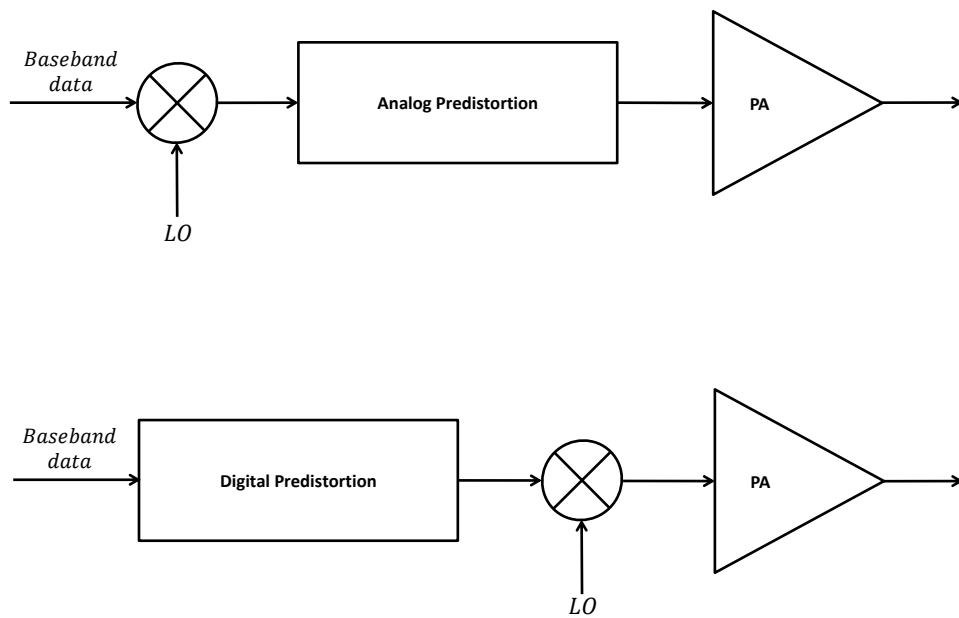


FIGURE 6.1: Illustration of analog and digital predistortion scheme to linearize a PA, where LO is the local oscillator.

6.2.7 Predistortion

Analog predistortion techniques have a long history, having been used extensively to correct the nonlinear characteristics of TWTAs, for high power amplifications in the upper GHz frequency [99]. Predistortion is the generic term given to techniques, which seek to linearize a PA by making suitable modifications to the amplitude and phase of the input signal. A typical illustration of analog and digital predistortion is shown in Fig. 6.1. The first implementation, known as analog predistortion, is applied to the RF signal itself; as illustrated in the upper half of the figure. This predistortion is applied to the analog signal by cleverly realizing the NL inverse of the PA conversion characteristic [100, 101]. The second type of predistortion, namely DPD, is applied to the baseband symbols before upconversion, and is shown in the lower half of the Fig. 6.1 [102]. In this implementation, the predistorting function is typically maintained as a digital look-up table. By posing the digital predistortion as an adding signal technique, a new scheme has been proposed for OFDM signals in [103].

The main advantage of predistortion is its conceptual simplicity. It also does not suffer a bandwidth limitation that is as stringent as some feedback techniques. Nevertheless, its

main liability is that, it is helpless in the face of variations in the PA. Apart from aging, the exact NL characteristic of a PA varies with temperature and process variations. This implies that, as conditions change, a fixed predistorter will gradually tend to become misaligned with the nonlinearity of the PA, resulting in a suboptimal performance. Another serious drawback to predistortion is its heavy dependence on a good model of the PA. It is notoriously difficult to model the PAs, and predistortion immerses the designer directly into this thorny issue.

6.2.8 Adaptive predistortion

As discussed, the greatest weakness of predistortion is its inability to cope with variations in the PA characteristics. Adaptive predistortion is a logical evolutionary step forward from ordinary predistortion in this regard, by trying to solve this issue [104]. An adaptive predistortion system maintains a dynamically updated model. Based on the parameters of this model, and on comparisons between the transmitted data and the PA output, a predistortion table is computed. By periodically updating the predistortion table, the system is able to react to changes due to process variations, temperature, etc. Thus, a substantial improvement comes without incurring a bandwidth limitation. Albeit, the main disadvantage of adaptive predistortion is its complexity. This is due to the fact that its strategy is implemented with considerable computing power, often in the form of a digital signal processor, which requires enormous power. Thereby, effectively ruling out adaptive predistortion as an option for portable transceivers. For adaptive predistortion, the difficulty is compounded by the discrete-time stability problem associated with convergence of the model parameters according to the adaptive algorithm.

6.3 Digital predistortion techniques suggested for FBMC-OQAM

6.3.1 State of the art

Recently, for FBMC-OQAM systems, an adaptive DPD based on neural networks, has been proposed in [31]. Because of the imaginary interference of FBMC-OQAM system,

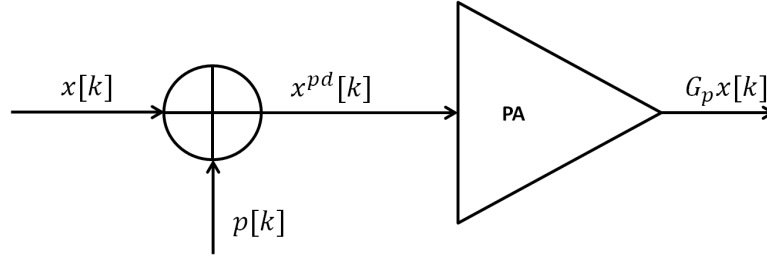


FIGURE 6.2: Illustration of DPD as an adding signal method.

careful implementation has to be done, especially for the phase (AM/PM) correction. Also, in [31], it has been shown that the FBMC-OQAM signals are more sensitive to phase error than OFDM signal and two linearizing solutions have been proposed. Experimental evaluation of DPD with FBMC-OQAM systems has been done in [32]. Therein, the authors have experimentally proved that using FBMC signals, lower ACP can be achieved. Also, it has been shown that FBMC-OQAM signals show lower resistance than OFDM signals to NL distortions and that DPD is even more important for FBMC than for OFDM signals.

6.3.2 Predistortion by signal addition

If the memory effects of the PA are negligible, the predistortion is therefore based on a non-linear and non-memory function. In such case, it has been shown in [103], that the Bussgang's theorem facilitates for formulation of predistortion as an adding signal technique for OFDM signals. The idea behind any adding signal DPD technique is that, we add a predistortion signal $p[k]$ to the signal $x[k]$ to compensate the PA non-linearity. The predistorted signal $x^{pd}[k]$ can be expressed as

$$x^{pd}[k] = \mathcal{P}\{x[k]\} \quad (6.1)$$

$$= x[k] + p[k] \quad (6.2)$$

where $\mathcal{P}\{\cdot\}$ is the predistortion function. Details about predistortion principle and benefits can be found in [105]. The aim of a DPD technique is to obtain a \mathcal{P} such that:

$$\mathcal{A}\{\mathcal{P}\{x[k]\}\} = G_p x[k] \quad (6.3)$$

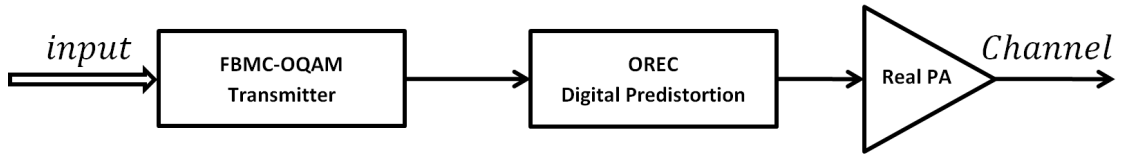


FIGURE 6.3: Illustration of a FBMC-OQAM system along with OREC-DPD scheme.

where G_p is a linear gain and we recall that $\mathcal{A}\{\cdot\}$ is the amplification function of PA. Illustration of DPD as signal adding technique is displayed in the Fig. 6.2. One can solve equation (6.3) with low complexity, by a recursive error correcting (REC) approach. The advantage in this approach is that, it opens a way to joint optimization of PAPR reduction and PA linearization; since, there exists some PAPR techniques such as ACE, TR, which are also signal adding techniques. In [106], the objective was to propose joint optimization for OFDM signals.

6.3.3 Overlapped-Recursive Error Correcting Digital Predistortion

Pioneering ahead in the direction of posing DPD as an adding signal method as suggested in [103], in this chapter we propose a novel DPD technique, to linearize FBMC-OQAM signals. It is termed as overlapped-recursive error correcting-digital predistortion (OREC-DPD), because it takes into account the overlapping nature of the FBMC-OQAM symbols. The manner in which the overlapping of previous symbols are taken into consideration is similar to that of the proposed PAPR reduction techniques and can be understood from Fig. 4.1. However, the DPD is done in baseband, which implies that first we model the real PA and then we perform linearization. Illustration of a FBMC-OQAM system along with OREC-DPD scheme is shown in Fig. 6.3. The implementation of OREC-DPD is displayed with much detail in Fig. 6.4.

The OREC-DPD algorithm is given below

Step 1: Step 1a - FBMC-OQAM signal generation - Firstly, we generate M complex input symbol vectors as per equation (2.7) and oversample them by L times as per equation (2.18) to obtain $\{\hat{\mathbf{X}}_0, \hat{\mathbf{X}}_1, \dots, \hat{\mathbf{X}}_{M-1}\}$. Then, for $0 \leq k < (M + K - 0.5)LN - 1$, we perform discrete-time FBMC-OQAM modulation for these as per equation (2.16) to obtain the FBMC-OQAM signal $x[k]$.

Step 1b - Predistortion signal initialization - Then, we reinitialize $m = 0$ and initialize

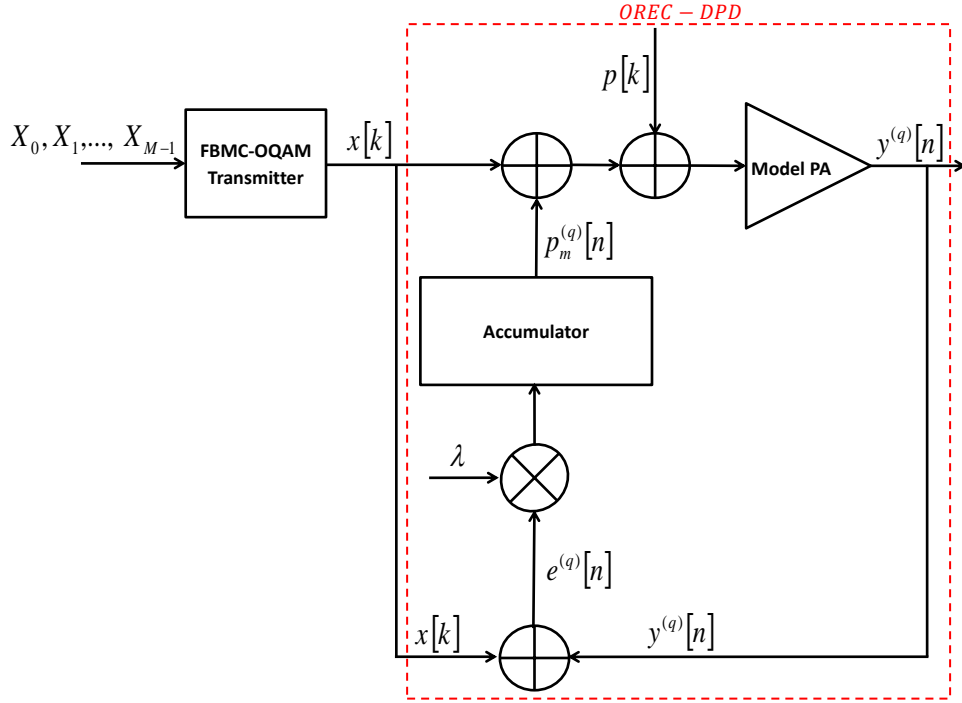


FIGURE 6.4: Detailed illustration of OREC-DPD block.

predistortion signal $p[k]$ as zero

$$p[k] = 0 \quad (6.4)$$

Step 2: We initialize iteration counter $q = 1$ and then, initialize the accumulative partial predistortion signal $p_m^{(0)}[n]$ that is related to the m^{th} signal $x_m[k]$ to be zero.

$$p_m^{(0)}[n] = 0, mLN \leq n < (m + K + 0.5)LN - 1 \quad (6.5)$$

Step 3: For $mLN \leq n < (m + K + 0.5)LN - 1$, we perform the following substeps:

Step 3a - Amplification - The predistortion signal $p[k]$ should be added to the FBMC-OQAM signal $x[n]$ along with the current accumulative predistortion signal upto q^{th} iteration $p_m^{(q)}[n]$ and amplify this with a model PA as shown below

$$y^{(q)}[n] = \mathcal{A}\left\{x[n] + p[k] + p_m^{(q)}[n]\right\} \quad (6.6)$$

we remind $0 \leq k < (M + K - 0.5)LN - 1$.

Step 3b - Recursive error computation - The recursive error signal $e^{(q)}[n]$ at iteration q ,

is the difference between amplified signal $y^{(q)}[n]$ and the input signal $x[k]$ as done below

$$e^{(q)}[n] = y^{(q)}[n] - x[n] \quad (6.7)$$

Step 3c - Recursive error correction - The accumulative partial predistortion signal $p_m^{(q)}[n]$, is updated through recursive accumulation as below

$$p_m^{(q)}[n] = p_m^{(q-1)}[n] + \lambda e^{(q)}[n] \quad (6.8)$$

where, λ is the convergence rate.

Step 4: If $q \leq Q$, we increment q by 1 and go to **Step 3**. Else, we update the predistortion signal $p[k]$ by concatenating with the latest accumulated partial predistortion signal $p_m^{(Q)}[n]$ as follows

$$p[k] = p[k] + p_m^{(Q)}[n] \quad (6.9)$$

we remind $0 \leq k < (M + K - 0.5)LN - 1$ and $mLN \leq n < (m + K + 0.5)LN - 1$.

Step 5: If $m \leq M - 1$, we increment m by 1 and go to **Step 2**. Else, we proceed to next step.

Step 6: Add the obtained predistortion signal $p[k]$ to the FBMC-OQAM signal $x[k]$ to obtain the predistorted input signal $x^{pd}[k]$, which shall be fed into the real PA.

$$x^{pd}[k] = x[k] + p[k] \quad (6.10)$$

We have kept λ as constant. However, there are enough methods in the literature to calculate the λ for each iteration, which varies accordingly with number of iterations Q , smoothing factor p and IBO.

6.3.4 Non-collaborative PAPR reduction

It is of great interest for us to comprehend the impact of PAPR reduction before linearizing the FBMC-OQAM signal. By intuition, we consider a situation, where, the PA linearization is preceded by PAPR reduction, which is non-collaborative in nature. The non-collaborative approach is a cascaded combination without exchanging information of the PAPR-reduction technique and the linearization one. It means, PAPR reduction

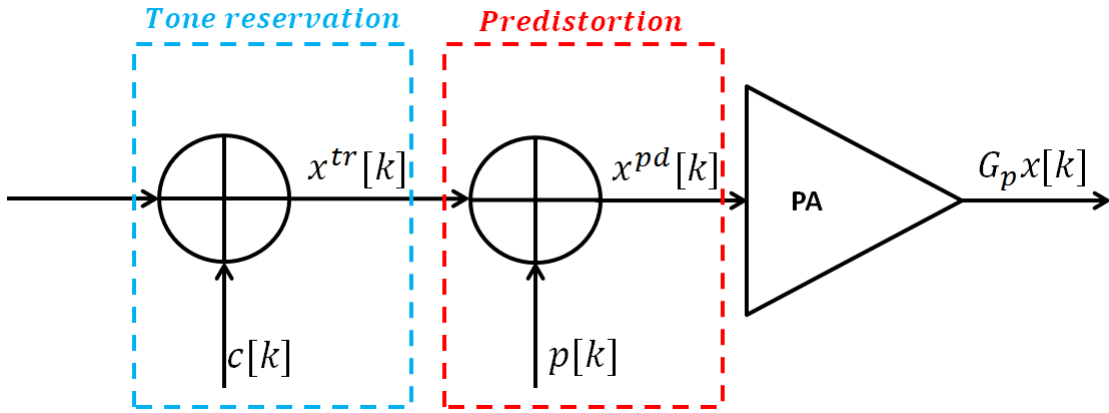


FIGURE 6.5: Illustration of PAPR reduction by DTR followed by OREC-DPD.

or linearization doesn't share any information between them and act independently as shown in Fig. 6.5. Therefore, The parameters for reducing the PAPR can be selected and adjusted independently of the linearization and vice versa. In [107, 108], it has been shown that reducing the PAPR improves efficiency of linearization and the same is observed in our analysis, which we shall demonstrate in the simulations later. The reason for considering a non-collaborative approach is that it already exists in the literature many techniques for linearization and PAPR reduction. Most of these techniques are already implemented or implementable in real systems. Since OREC-DPD is an adding signal technique, we thought that it would be interesting to use DTR, which is also an adding signal technique, for the PAPR reduction.

We recall that both PA linearity and its efficiency are mutually complimentary. After PAPR reduction, we can observe that the peaks are reduced. However, the predistortion increases the peaks. Even if the non-collaborative approach helps in understanding the amelioration of linearization, with PAPR reduction; it would be of great interest, if a single treatment, such as adding a signal, can possibly reduce both the PAPR and also linearize the PA, which we term as joint optimization. It has to be noted that joint optimization has not been performed in our linearization analysis. But, can be seen as preliminary step towards that direction.

6.4 Linearization analysis

The simulations are done for 10^5 FBMC-OQAM 4QAM symbols that are to be transmitted over 64 sub-carriers. The oversampling factor of $L = 4$ has been chosen. The

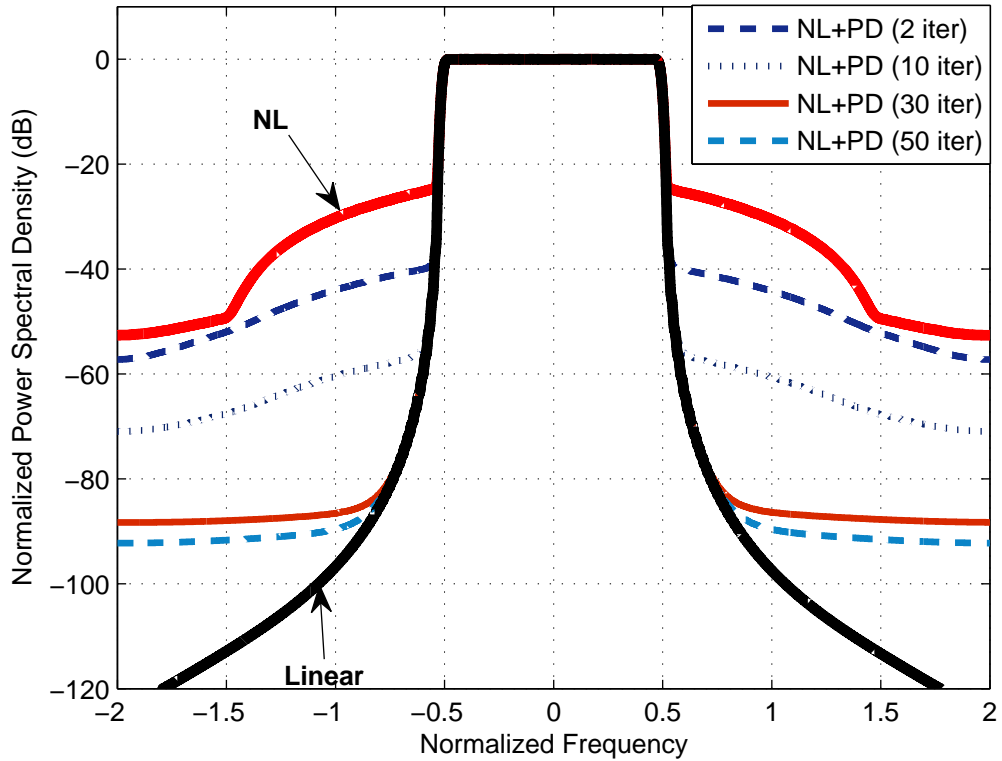


FIGURE 6.6: Impact of number of iterations on the OREC-DPD algorithm with $\lambda = 0.1$ and IBO=5 dB.

prototype filter used is the PHYDYAS one. In the analysis, we consider a SSPA, which is modeled by Rapp model with $p = 2.25$. Also, we fix $\lambda = 0.1$ in our linearization analysis.

6.4.1 Impact of number of iterations Q

Though it is imperative that more iterations yield to better result, we perform this to understand its quantitative impact on the algorithm. Initially, the convergence rate λ is fixed as 0.1. the IBO is 5 dB. The algorithm has been run with $Q = \{2, 10, 30, 50\}$ iterations and we can see how the sidelobe reduction is seen in the normalized PSD shown in the Fig. 6.6. In the legend, “Linear” and “NL” indicates normalized PSD at the input and output of the Rapp model of PA, without any predistortion. “NL+PD (2 iter)” indicate that predistortion has been applied with 2 iterations and then nonlinearly amplified. We can notice in the Fig. 6.6 that, for $Q = \{2, 10, 30, 50\}$, the spectral regrowth of the predistorted and NL amplified signals in the OOB w.r.t. the linear

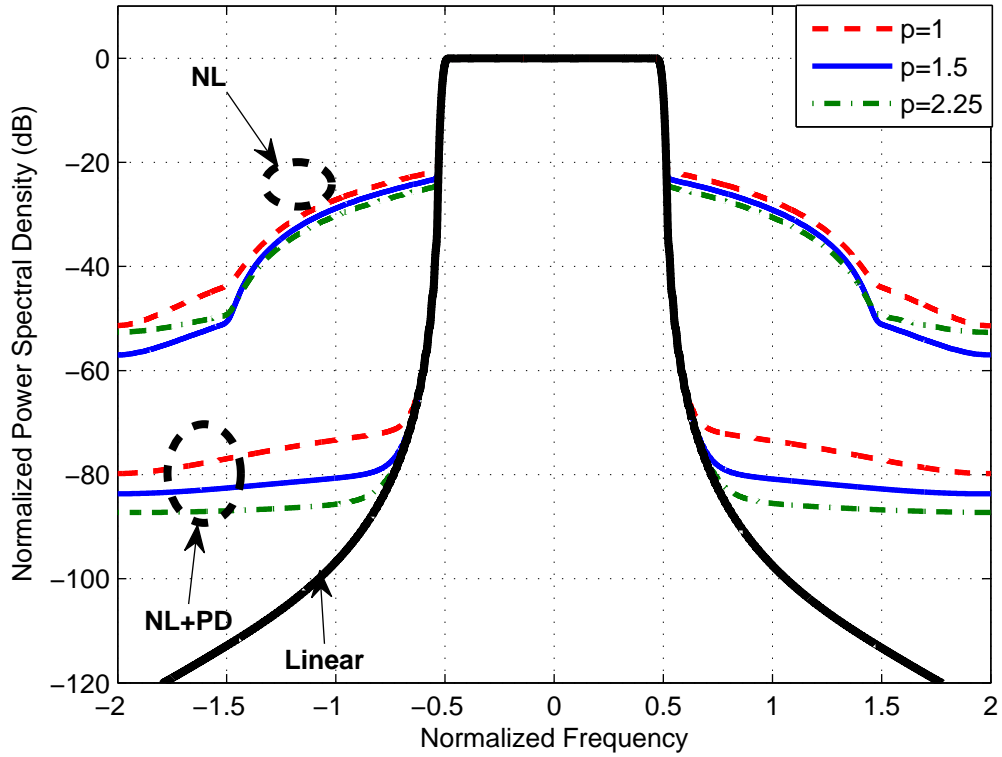


FIGURE 6.7: Impact of PA non-linearity on the OREC-DPD algorithm, for $p = \{1, 1.5, 2.25\}$ and IBO=5 dB.

case, roughly present at -57.26 dB, -70.97 dB, -88.31 dB and -92.26 dB respectively at normalized frequency of 2. In the same figure, initially, with 2 iterations itself, we can observe some reduction in the spectral regrowth. However, with a constant convergence rate, we see that there is need for exponential increase in number of iterations, to expect much better performance.

6.4.2 Impact of knee factor p

We have done simulations with different values of p as it is imperative to understand the linearization capability of OREC-DPD algorithm, when the PA is severely NL. The simulation results are shown in Fig. 6.7. The chosen simulation parameters are IBO=5 dB, $p = \{1, 1.5, 2.25\}$, $Q = 30$ and $\lambda = 0.1$. It can be noticed from the same figure, that the induced spectral regrowth in OOB, for $p = \{1, 1.5, 2.25\}$ is -79.81 dB, -83.69 dB and -87.27 dB respectively at normalized frequency of 2. It shows that

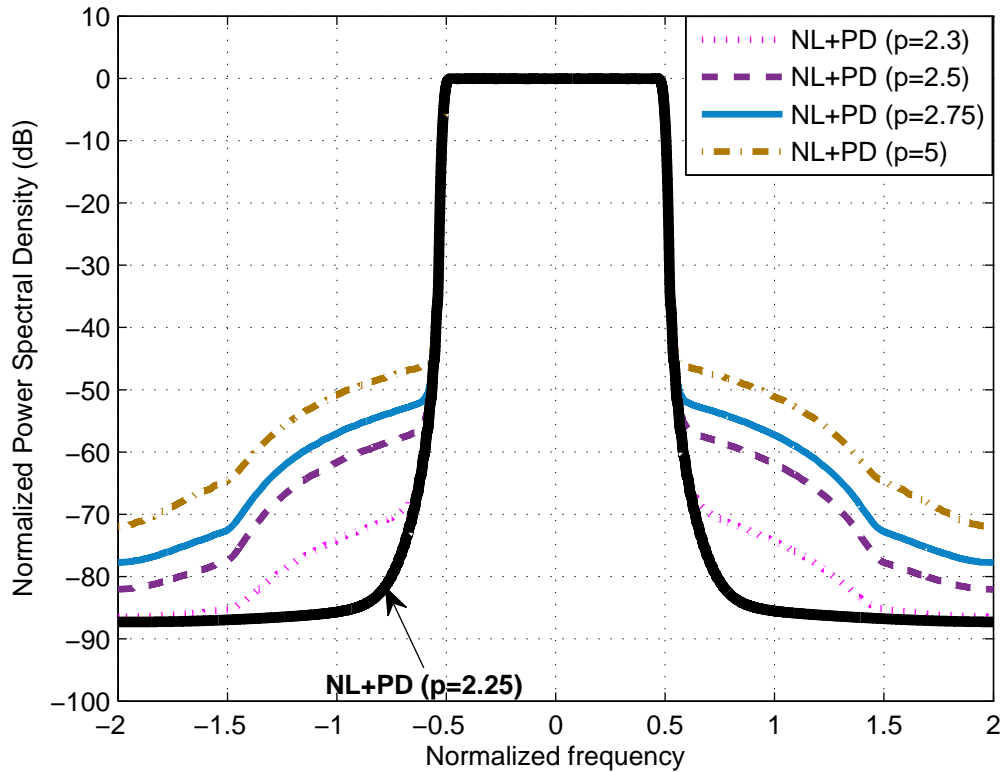


FIGURE 6.8: Impact of negative mismatch of PA modeling on the OREC-DPD algorithm, for $p_{real} = 2.25$ and IBO=5 dB.

OREC-DPD is effective in linearizing the PA; but, for severe PA, the IBO should be higher to have similar spectral regrowth.

6.4.3 Impact of polynomial model mismatch

Perhaps the most important weakness of predistortion is its loss of linearization performance when there is a mismatch between the real PA and the PA model of Fig. 6.4 due variations of PA characteristics or improper modeling. By intuition we can anticipate the performance loss; but, our simulation putforward some intriguing observations. Let us assume that the real SSPA is supposed to be modeled perfectly with $p_{real} = 2.25$. So, as a metric of model mismatch, we vary p_{model} . We define that negative and positive mismatch are cases when $p_{model} > p_{real}$ and $p_{model} < p_{real}$ respectively. We fix the IBO=5 dB, $\lambda = 0.1$ and $Q = 30$.

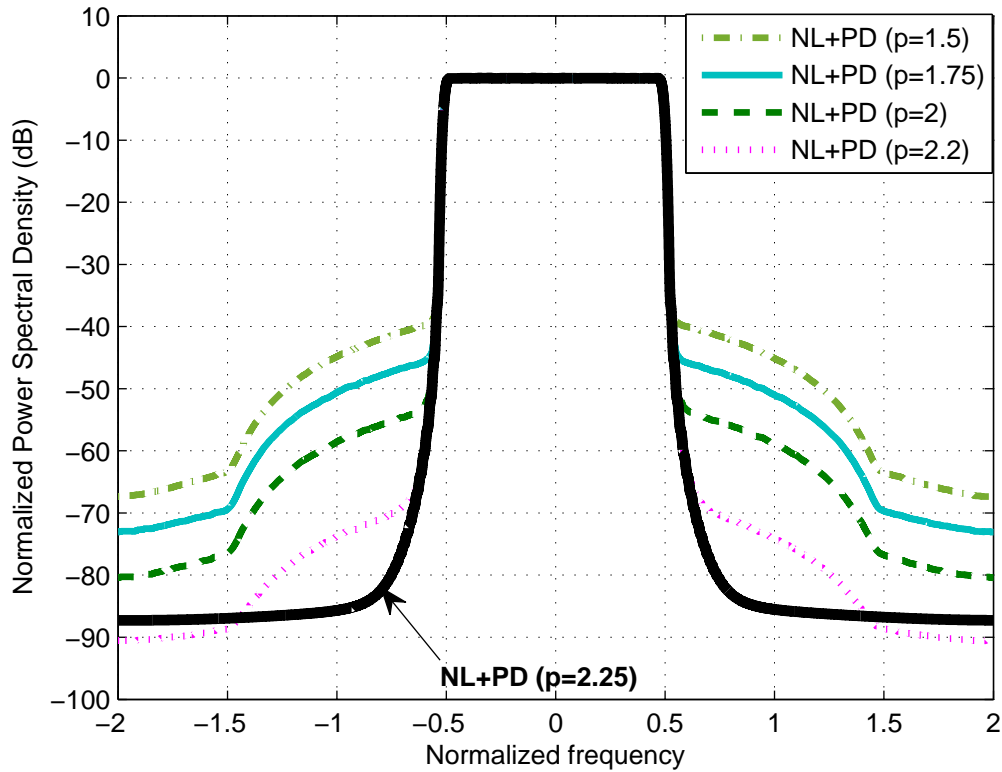


FIGURE 6.9: Impact of positive mismatch of PA modeling on the OREC-DPD algorithm, for $p_{real} = 2.25$ and $IBO=5$ dB.

6.4.3.1 Negative mismatch ($p_{real} - p_{model} < 0$)

Suppose, the real PA tends to behave more NL as the time passes, then if modeling is done much earlier and the same is still being used then negative mismatch occurs. Even though, the PA is more NL, we underestimate its non-linearity and perform pre-distortion. Higher value of knee factor p is indirectly equivalent to a PA model that is more linearized. So, in the simulation we have chosen the different knee factors, $p_{model} = \{2.3, 2.5, 2.75, 5\}$ for model PA in the predistortion algorithm and the result is plotted in Fig. 6.8. The thick black curve refers to the predistorted signal without any mismatch i.e. $p_{model} = p_{real} = 2.25$. We can infer from the figure that a slight mismatch with an error of 0.05, induces significant spectral regrowth. Higher the model mismatch, greater the increase in spectral regrowth in OOB w.r.t. the perfect match case, which is around 0.83 dB, 5.22 dB, 9.52 dB and 15.3 dB for $p_{model} = \{2.3, 2.5, 2.75, 5\}$ respectively, at normalized frequency of 2.

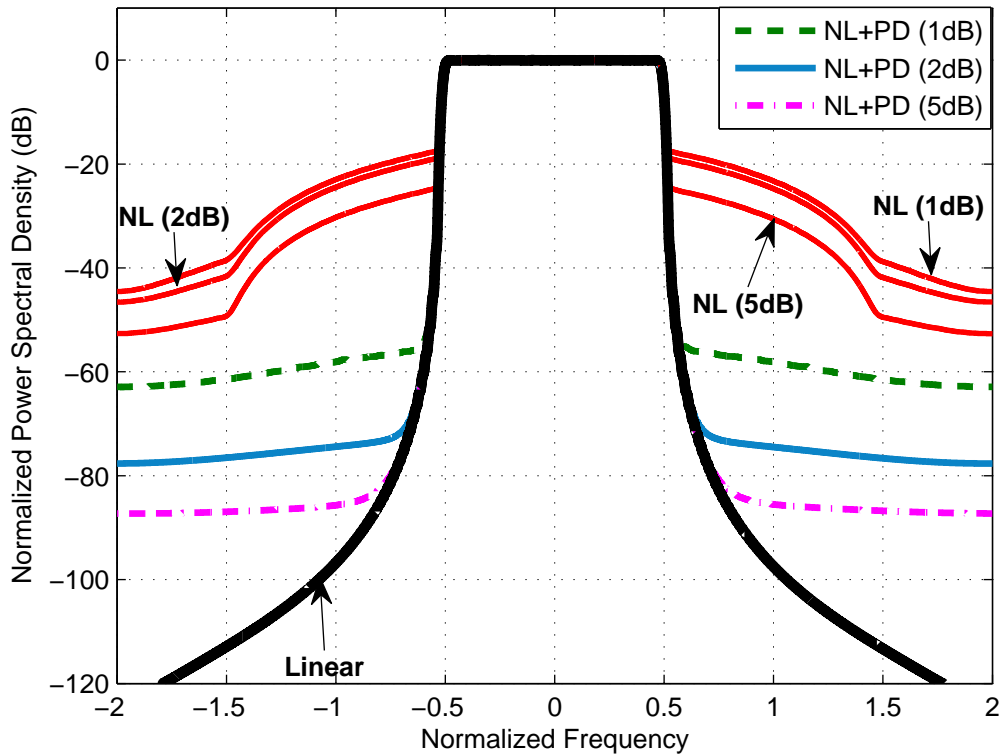


FIGURE 6.10: Illustration of IBO on OREC-DPD scheme with $p = 2.25$ dB.

6.4.3.2 Positive mismatch ($p_{real} - p_{model} > 0$)

Suppose, the real PA is mistaken to be more NL, and it is modelled with this error, then positive mismatch occurs. It means we are inducing unwanted non-linearity into the system; instead of minimizing the non-linearity of PA. Different knee factors, $p_{model} = \{2, 2.2, 1.75, 1.5\}$ for model PA has been chosen for simulation of positive mismatch and the results are plotted in Fig. 6.9. It can be noticed that the increase in spectral regrowth in OOB, for $p_{model} = \{2, 2.2, 1.75, 1.5\}$ is around -3.29 dB, 6.86 dB, 14.19 dB and 19.89 dB respectively, at normalized frequency of 2.

6.4.4 Impact of IBO

The main aim of PA linearization is to increase energy efficiency; which means to operate the PA at much lower IBO. The impact of IBO on the OREC-DPD scheme has been simulated for values of $IBO = \{1 \text{ dB}, 2 \text{ dB}, 5 \text{ dB}\}$ with $Q = 30$ and presented in Fig. 6.10. The PA is assumed to be modeled perfectly without any mismatch and knee factor

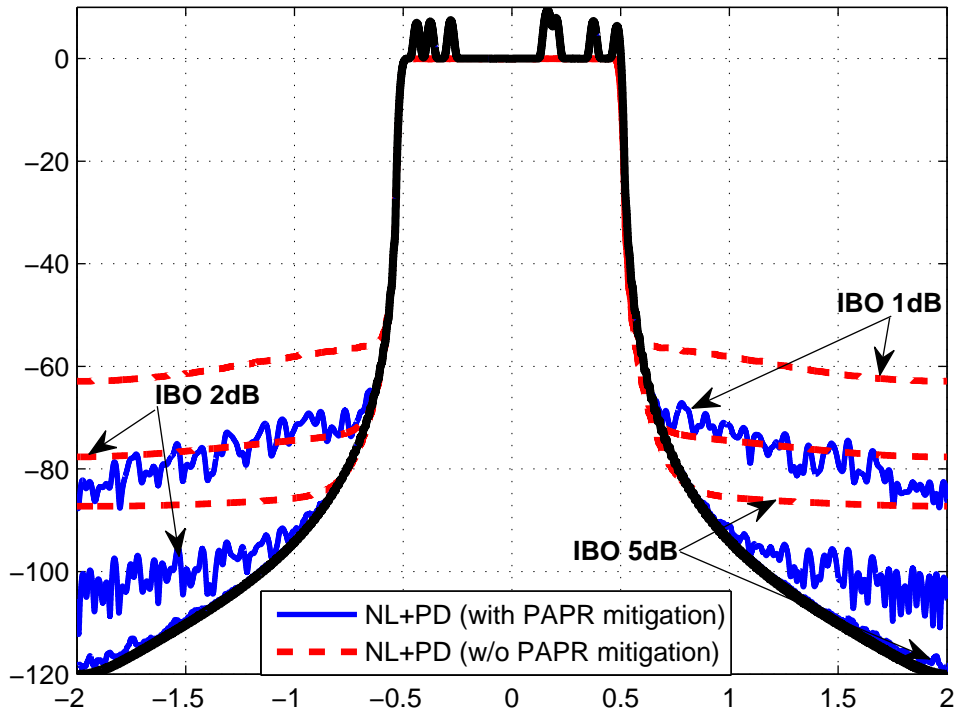


FIGURE 6.11: Illustration of impact of PAPR (DTR with $R = 8$) on OREC-DPD scheme with $p = 2.25$ dB.

of $p = 2.25$ is used. From Fig. 6.10, it can be noticed that there is a decrease in spectral regrowth at OOB, for $\text{IBO} = \{1 \text{ dB}, 2 \text{ dB}, 5 \text{ dB}\}$ w.r.t. their respective to their original NL spectral regrowth without any predistortion. This relative decrease is found to be around 18.35 dB, 31.12 dB and 34.62 dB respectively, at a normalized frequency of 2.

6.4.5 Impact of non-collaborative PAPR reduction

In a non-collaborative PAPR reduction preceding the linearization, we can choose the parameters of PAPR reduction and linearization separately in an independent manner. DTR with $R = 8$ has been performed before linearization. If we can recall from the previous Chapter 5, we have not done any linearization in our coexistence analysis and assumed some moderate linearization. There, we have studied the impact of PA linearization on PAPR reduction. In this simulation, we try to understand the impact of non-collaborative PAPR reduction upon the spectral regrowth of a predistorted FBMC-OQAM signal. The PA parameters are $\text{IBO} = \{1 \text{ dB}, 2 \text{ dB}, 5 \text{ dB}\}$ and $p = 2.25$. The

TABLE 6.2: Spectral regrowth for FBMC-OQAM when OREC-DPD is implemented with and without DTR based PAPR mitigation, before amplified by a Rapp model PA with $p = 2.25$.

IBO value (in dB)	Spectral regrowth in dB without PAPR mitigation	Spectral regrowth in dB with DTR mitigation
1	-66.28	-86.3
2	-77.65	-105.4
5	-87.27	-118.3

DPD parameters are $Q = 30$. From the Fig. 6.11 and Table 6.11, it can be noticed that by reducing the PAPR of the signal before OREC-DPD has decreased the spectral regrowth in OOB, for IBO={1 dB, 2 dB, 5 dB} by 20.02 dB, 27.75 dB and 31.03 dB respectively, at normalized frequency of 2 w.r.t the scenario where there is no PAPR reduction before OREC-DPD. Though, this kind of result is expected, it shows the effective mitigation of spectral regrowth even when we perform non-collaborative PAPR reduction. Also, this analysis will serve as the first step towards joint optimization of PAPR reduction and PA linearization.

In the Fig. 6.11, we can notice that there is no IB distortion induced by OREC-DPD; but, there seems to be some due to DTR. However, it will not have negative impact at the receiver, provided it knows beforehand, the PRT locations. Then, the retrieval of information from the DT locations can be done without any difficulty.

6.5 Conclusion

The wireless communications market has experienced significant growth in the past decade. The RF power amplifier represents a critical component in the design of the transmitter. It is typically the most costly item and consumes most of the DC supply. The purpose of the work described in this chapter is to contribute to the field of PA linearization. In DPD, the input signal is distorted before feeding into the PA, in order to minimize the non-linear effects induced by it. A novel DPD technique, namely OREC-DPD has been suggested for FBMC-OQAM systems and the simulation results suggest that it is very efficient in PA linearization. It has been found that erroneous modeling of the PA can induce significant OOB in OREC-DPD. It was observed that even a 5% error in knee factor p , induces non-negligible spectral regrowth. It has been found that it is better to have negative mismatch for the PA model. This is the inherent weakness in any

predistortion technique and necessary precautions has to be taken. Notwithstanding by this, we conclude that symbiotic combination of PAPR reduction and PA linearization leads to high energy efficiency of PA with reduced non-linearity that is tolerable. The use of adding signal techniques for PAPR reduction and linearization, opens a possibility to investigate joint optimization.

Chapter 7

Conclusion

7.1 Background and motivation

Single carrier modulation was used in the early digital communication systems. Especially, during last two decades, the demand for multimedia wireless communication services has grown tremendously and this trend is expected to continue in the near future. This high demand of multimedia wireless communication services force the development of advanced digital wireless communication system which can provide high data rate transmission at low cost to as many as users with high reliability, large bandwidth, and with great flexibility for varying traffic condition. To support these types of services, for large number of users and with limited spectrum, current wireless communication system adopted MCM technologies, which are bandwidth efficient and robust to multipath channel condition.

OFDM, which is the most popular and most widely used MCM, has indeed become part of new emerging standards for broadband wireless access. However, it suffers from some inherent disadvantages such as high sensitivity to residual frequency and timing offsets, bad frequency localization and need for CP, etc. These shortcomings has instigated the researchers to probe for alternate solutions and some enhanced physical layers based on filter-bank processing, have been proposed.

FBMC-OQAM is one of such MCM techniques, which have attracted vast research attention from academician, researchers and industries since last two decades. Moreover, FBMC-OQAM have recently been considered for the emerging wireless communication systems as a means to improve the utilization of the physical resources in asynchronous transmissions. FBMC-OQAM divides the overall frequency channel in a set of subchannels of bandwidth proportionally decreasing with the number of subchannels. If the number of subchannels is high enough, the bandwidth of each subchannel is small enough to assume that it is approximately flat.

The most attractive feature of FBMC-OQAM is its excellent frequency localization. This is indeed much needed; because, the emerging wireless communication systems are carefully designed to simultaneously optimize the delivered user capacity, the average spectral efficiency and the cell coverage. Adding to these, the energy crisis and global warming problems became primordial issue in almost every sector of development and is of very serious concern. Its a worrying concern that ICT industry has emerged as one of the major contributors to the CO₂ emission and world power consumption. Reducing the energy consumed by radio base stations and mobile equipments, will definitely reduce the environmental impact of the RAT. The RF PAs consume large amounts of energy, dissipate heat, and take up space in base stations. The main objective of PA research is to increase efficiency while maintaining linearity and broadening the operating bandwidth.

Being inherently NL, the PAs could induce serious damage to the transmitted signals. However, FBMC-OQAM system suffers from high PAPR by being a MCM technique and it's frequency localization property takes off beat in real communication systems consisting of NL PAs leading to spectral regrowth thereby abrogating much of it's attractive appeal to be a serious candidate for emerging communications. This crucial reason coerces us to probe for mitigating techniques to combat the effects of PA non-linearity.

7.2 Contributions

This thesis is part of the European FP7 project EMPHATIC. Throughout this dissertation, we have reviewed some important aspects related to the study of NL effects of PA on FBMC-OQAM signals in the OOB. Eventhough, the main intention of this dissertation is to propose novel PAPR reduction techniques; on the other hand, some aspects of PA

linearization has been briefly discussed towards the end. The review of formal aspects of FBMC-OQAM signal generation and the development of expressions for the continuous and discrete modeling of the transmission chain, allowed us to explore different aspects of FBMC-OQAM signals such as, real-domain orthogonality, frequency localization, overlapping nature. Then, we also reviewed different memoryless PA models, the impact of their non-linearities and means to mitigate them such as PAPR reduction and PA linearization.

The main contributions in this dissertation are enlisted below

- While, **Chapter 1** provided background motivation, in **Chapter 2** we have given the theory and aspects of FBMC-OQAM systems, PA non-linearities, memoryless PA models and means to mitigate PA NL effects. Actually, **Chapter 2** serves an overture into the actual contribution of this dissertation.
- **Spectral regrowth prediction:** In, **Chapter 3**, we have introduced cumulants and by using them, we have shown how prediction of the spectral regrowth in non-linearly amplified FBMC-OQAM systems can be done. This chapter demonstrates the severity of spectral regrowth induced by PA in real communication systems.
- **PAPR reduction for FBMC-OQAM:** **Chapter 4** is the core of this dissertation, dealing with the PAPR reduction for FBMC-OQAM systems. Different PAPR reduction techniques have been presented for both OFDM and FBMC-OQAM. We have shown that it is imperative to consider the overlapping nature of FBMC-OQAM, when proposing PAPR reduction; else, any attempt shall be futile.

We have proposed three novel PAPR reduction techniques suited for FBMC-OQAM systems and studied their computational complexities. Two of them are DSLM and TSLM, which come under the category of probabilistic approach. While the former has a symbol-by-symbol approach, the later treads a trellis-based one. We have demonstrated that any probabilistic scheme with symbol-by-symbol approach yield to sub-optimal PAPR reduction performance and trellis-based ones can supersede even OFDM techniques in PAPR reduction. One observation common to both these probabilistic approaches is that as the number of multiplicative phase rotation vectors increase, their superior performance in PAPR reduction performance w.r.t. OFDM techniques gets narrowed. Finally, we have proposed DTR,

which is an adding signal technique. We have suggested a method to identify the optimal PRT locations, which ensure excellent PAPR reduction for FBMC-OQAM signals.

- **Coexistence capabilities of FBMC-OQAM:** In **Chapter 5**, we have investigated the co-existence capabilities of a FBMC-OQAM system working on non-linear devices in the case of PMR/PPDR systems. The current limitation caused by insufficient RF spectrum hinders the growth of PMR/PPDR systems, which need new MCM waveforms that can: i) support user asynchronism and low latency, ii) permit coexistence with narrowband systems and iii) be capable to be operated with NL devices with high energy efficiency. Without RF impairments, the FBMC-OQAM seems to be promising in this aspect. However, with introduction of PA non-linearity, we have shown that FBMC-OQAM suffers from severe spectral regrowth. By analyzing different scenarios, we have shown that it is possible for FBMC-OQAM system to coexist with PMR/PPDR systems. Albeit, it is mandatory to have both PA linearization and PAPR reduction along with sufficiently moderate IBO.
- **Linearization of FBMC-OQAM:** Actually, the **Chapter 5** have motivated us to study the aspects of PA linearization. Thus in **Chapter 6**, we have made a genuine attempt to showcase the importance of linearization, with or without PAPR reduction. We have introduced briefly different PA linearization techniques. We have understood that we need to take into consideration the overlapping signal structure of FBMC-OQAM when proposing any PA linearization technique. Then, we have proposed a novel DPD technique for FBMC-OQAM systems.

7.3 Future Perspectives

In this thesis dissertation some effort was made to study the impact of PA non-linearity on MCM signals using OFDM or FBMC-OQAM and solutions that one can use to reduce these impacts. For sure, many ideas appeared as the time progressed and we think that it would be interesting for example to consider the following listed aspects:

In **Chapter 3**, we have studied the spectral regrowth prediction using cumulants. In our analysis, we have made the hypothesis that the input HPA signal was Gaussian. This

hypothesis is verified if the number of subcarriers is sufficiently large and furthermore, if no PAPR reduction technique is applied to the input HPA signal. If some PAPR reduction technique is used, the input signal is no more Gaussian and a perspective could be to study spectral regrowth using cumulants when the input signal is PAPR reduced. In the same way, it would be of interest to predict the spectral regrowth when the PA model shows memory effects.

Concerning **Chapter 4** and PAPR reduction, a trellis quasi-optimal procedure has been studied using selective mapping. One perspective could be to study other PAPR techniques for FBMC-OQAM using such trellis processing. It could be interesting to compare the performance of DTR to a trellis-based DTR.

Another perspective for **Chapter 4**, is related to the complexity of the DTR algorithm. Computation of the reserved tones is done by an optimal optimization procedure using QCQP algorithm. This technique is highly complex and sub-optimal techniques using POCS or gradient algorithms could be compared to the optimal DTR procedure. Concerning DTR, no power limitation is put on the reserved tones. So, it should be interesting to study the impact of a power limitation on the reserved tones and to compare the performances of DTR with and without power limitation. Influence of the number of sub-carriers on PAPR reduction algorithm performances could also be studied more deeply.

In **Chapter 5**, we have examined the coexistence capabilities of FBMC-OQAM systems working on NL devices, to coexist with legacy PMR system, which have licensed spectrum. However, it would be a perspective to study the coexistence capability in unlicensed bands.

In **Chapter 6**, we have studied linearization of the PA using DPD. The adopted DPD technique has been an “adding signal” technique. Because PAPR reduction using DTR is also an “adding signal” technique, one very important perspective could be to realize the joint optimization of the added signal suited for both PAPR reduction and DPD.

In this dissertation, much emphasis has been given to OFDM and FBMC-OQAM waveforms. Nevertheless, it would be of equal interest to study other post-OFDM waveforms and compare them with FBMC-OQAM, in the 5G context.

Bibliography

- [1] Y. Zhao and S.-G. Haggman. Sensitivity to doppler shift and carrier frequency errors in ofdm systems-the consequences and solutions. *IEEE Vehicular Technology Conference*, 3:1564–1568, May 1996.
- [2] J. Armstrong. Analysis of new and existing methods of reducing intercarrier interference due to carrier frequency offset in ofdm. *IEEE Transactions on Communications*, 47(3):365–369, Mar. 1999.
- [3] B. Saltzberg. Performance of an efficient parallel data transmission system. *IEEE Transactions on Communication Technology*, 15(6):805–811, Dec. 1967.
- [4] Global eSustainability Initiative. *SMART 2020: Enabling the low carbon economy in the information age*. The Climate Group, 2008.
- [5] G. Plan. *An inefficient truth*. Global Action Plan, 2009.
- [6] H. Bogucka and A. Conti. Degrees of freedom for energy savings in practical adaptive wireless systems. *IEEE Communications Magazine*, 49(6):38—75, Jun. 2011.
- [7] P. Siohan, C. Siclet, and N. Lacaille. Analysis and design of ofdm/oqam systems based on filter bank theory. *IEEE Trans. on Signal Processing*, 50:1170–1183, May 2002.
- [8] H. E. Rowe. Memoryless nonlinearity with gaussian inputs: elementary results. *BELL Systems Technical Journal*, 61(7):1519–1526, 1982.

- [9] A. A. Saleh. Frequency-independent and frequency-dependent nonlinear models of twt amplifiers. *IEEE Transactions on Communications*, 29(11):1715–1720, Nov. 1981.
- [10] S. Benedetto and E. Biglieri. *Principles of Digital Transmission with Wireless Applications*. Kluwer Academic/Plenum Publishers, New York, 1999.
- [11] H. G. Ryu, B. I. Jin, and I. B. Kim. Papr reduction using soft clipping and aci rejection in ofdm system. *IEEE Transactions on Consumer Electronics*, 48(1):17–22, Aug. 2002.
- [12] J. Tellado. *Multicarrier Modulation with Low PAR: Applications to DSL and Wirelless*. Kluwer Academic Publishers, 2000.
- [13] J. Tellado. *Peak to Average Ratio Reduction for Multi-carrier Modulation*. PhD thesis, Stanford University, Stanford, CA, USA, Sep. 1999.
- [14] Z. X. Yang, H. D. Fang, and C. Y. Pan. Ace with frame interleaving scheme to reduce peak-to-average power ratio in ofdm systems. *IEEE Transactions on Broadcasting*, 51(41):571–575, Mar. 2005.
- [15] S. H. Muller and J. B. Huber. Ofdm with reduced peak-to-average power ratio by optimum combination of partial transmit sequences. *IEEE Electronics Letters*, 33(5):368—369, Feb. 1997.
- [16] R. W. Bauml, R. F. H. Fischer, and J. B. Huber. Reducing the peak-to-average power ratio of multicarrier modulation by selected mapping. *IEEE Electronics Letters*, 32(22):2056–2057, Oct. 1996.
- [17] T. A. Wilkinson and A. E. Jones. Minimisation of the peak-to-mean envelope power ratio of multicarrier transmission schemes by block coding. *IEEE Vehicular Technology Conference*, 2:925–829, Feb. 1995.
- [18] H. S. Hee and L. J. Hong. An overview of peak-to-average power ratio reduction techniques for multicarrier transmission. *IEEE Transactions on Wireless Communications*, 12(2):56–65, Apr. 2005.
- [19] T. Jiang and Y. Wu. An overview: Peak-to-average power ratio of ofdm signals. *IEEE Transactions on Broadcasting*, 54(2):257–268, Jun. 2008.

- [20] J. Tellado and J. Cioffi. Peak power reduction for multicarrier transmission. *IEEE CTMC, GLOBECOM*, Nov. 1998.
- [21] A. Gatherer and M. Polley. Controlling clipping probability in dmt transmission. *Asilomar Conference record*, 1:578—584, Nov. 1997.
- [22] A. Skrzypczak, P. Siohan, and J. P. Javardin. Reduction of the peak-to-average power ratio for ofdm-oqam modulation. *IEEE Vehicular Technology Conference*, 4(841680):2018–2022, May 2006.
- [23] S. Lu, D. Qu, and Y. He. Sliding window tone reservation technique for the peak-to-average power ratio reduction of fbmc-oqam signals. *IEEE Wireless Communication Letters*, 4(1):268–271, Aug. 2012.
- [24] Z. Kollar and P. Horvath. Papr reduction of fbmc by clipping and its iterative compensation. *Hindawi Journal of Computer Networks and Communications*, 2012 (382736), May 2012.
- [25] Z. Kollar, L. Varga, B. Horvath, P. Bakki, and J. Bitó. Evaluation of clipping based iterative papr reduction techniques for fbmc systems. *Hindawi Scientific World Journal*, 2014(841680), Jan. 2014.
- [26] G. Cheng, B. Dong, H. Li, and S. Li. An improved selective mapping method for papr reduction in ofdm/oqam system. *Scientific Research Communications and Network Journal*, 5(3C):53–56, Jun. 2013.
- [27] D. Qu, S. Lu, and T. Jiang. Multi-block joint optimization for the peak-to-average power ratio reduction of fbmc-oqam signals. *IEEE Transactions on Signal Processing*, 61(7):1605–1613, Apr. 2013.
- [28] N. van der Neut, B. Maharaj, F. de Lange, G. Gonzalez, F. Gregorio, and J. Cousseau. Papr reduction in fbmc using an ace-based linear programming optimization. *EURASIP Journal on Advances in Signal Processing*, 2014(172), Dec. 2014.
- [29] B. Horvath and P. Horvath. Establishing lower bounds on the peak-to-average-power ratio in filter bank multicarrier systems. *IEEE European Wireless Conference*, pages 1–6, May 2015.

- [30] ETSI TR 102 580 V1.1.1. *Designer's Guide; TETRA High-Speed Data (HSD); TETRA Enhanced Data Service (TEDS)*. TETRA, 2007.
- [31] R. Zayani, Y. Medjahdi, H. Bouhadda, H. Shaiek, D. Roviras, and R. Bouallegue. Adaptive predistortion techniques for non-linearly amplified fbmc-oqam signals. *IEEE Vehicular Technology Conference*, pages 1–5, May 2014.
- [32] T. Gotthans, R. Marsalek, J. Blumenstein, and G. Baudoin. Experimental evaluation of digital predistortion with fbmc and ofdm signals. *IEEE Annual Wireless and Microwave Technology Conference*, pages 1–3, Apr. 2015.
- [33] T. H. Stitz. *Filter Bank Techniques for the Physical Layer in Wireless Communications*. PhD thesis, Tampere University of Technology, Tampere, Finland, 2010.
- [34] G. Cherubini, E. Eleftheriou, and S. Olcer. Filtered multitone modulation for vdsl. *IEEE Global Telecommunications Conference*, 2:1139–1144, 1999.
- [35] G. Cherubini, E. Eleftheriou, S. Oker, and J.M. Cioffi. Filter bank modulation techniques for very high speed digital subscriber lines. *IEEE Communications Magazine*, 38(5):98–104, May 2000.
- [36] G. Cherubini, E. Eleftheriou, and S. Olcer. Filtered multitone modulation for very high-speed digital subscriber lines. *IEEE Journal on Selected Areas in Communications*, 20(5):1016–1028, Jun. 2002.
- [37] B. F. Boroujeny and C. H. Yuen. Cosine modulated and offset qam filter bank multicarrier techniques: a continuous-time prospect. *EURASIP Journal on Advances in Signal Processing*, 2010(6):1–6, Jan. 2010.
- [38] R. W. Chang. High-speed multichannel data transmission with bandlimited orthogonal signals. *Bell System Technology Journal*, 45:1775–1796, Dec. 1966.
- [39] L. Lin and B. F. Boroujeny. Cosine-modulated multitone for veryhigh-speed digital subscriber lines. *EURASIP Journal on Applied Signal Processing*, 2006(6):1–6, Jan. 2006.
- [40] B. Hirosaki. An orthogonally multiplexed qam system using the discrete fourier transform. *IEEE Transactions on Communications*, 29(7):982–989, Jul. 1981.

- [41] M. Bellanger. Specification and design of prototype filter for filter bank based multi-carrier transmission. *IEEE International Conference on Acoustic, Speech and Signal Processing*, 4:2417–2420, May 2001.
- [42] L. E. Larson. Radio frequency integrated circuit technology for lowpower wireless communications. *IEEE Personal Communications Magazine*, 5(3):11—19, Jun. 1998.
- [43] P. Mogensen et al. 5g small cell optimized radio design. *IEEE Globecom Workshops*, pages 111–116, Dec. 2013.
- [44] B. F. Boroujeny. Ofdm versus filter bank multi-carrier. *IEEE Signal Processing Magazine*, 8(3):92–112, May 2006.
- [45] M. Bellanger and J. Daguët. Tdm-fdm transmultiplexer: Digital polyphase and fft. *IEEE Transactions on Communications*, 22(9):1199–1205, Sep. 1974.
- [46] T. Strohmer and S. Beaver. Optimal ofdm design for time-frequency dispersive channels. *IEEE Transactions on Communications*, 51(7):1111–1122, Jul. 2003.
- [47] B. L. Floch, M. Alard, and C. Berrou. Coded orthogonal frequency division multiplex. *IEEE Proceedings*, 83(6):982–996, Jun. 1995.
- [48] L. Crislin. *Méthodes d’Estimation de Canal, et Combinaison avec l’Accès Multiple CDMA ou les Systèmes Multi-Antennes*. PhD thesis, Conservatoire National des Arts et Métiers, Paris, France, 2008.
- [49] A. Viholainen, M. Bellanger, and M. Huchard. Prototype filter and structure optimization. *website: www.ict-phydyas.org: Document D5.1 deliverable*, Jan. 2009.
- [50] H. Zhang, D. Le Ruyet, and M. Terre. Spectral efficiency comparison between ofdm/oqam and ofdm based cr networks. *Wireless Communications and Mobile Computing Wiley*, 9:1487–1501, Nov. 2009.
- [51] B. Boashash. *Time frequency signal analysis and processing: a comprehensive reference*. Elsevier, 2003.
- [52] P. Siohan and C. Roche. Cosine-modulated filterbanks based on extended gaussian functions. *IEEE Transactions on Signal Processing*, 48(11):3052–3061, Nov. 2000.

- [53] H. G. Feichtinger and T. Strohmer. *Gabor analysis and algorithms: theory and applications*. Birkhäuser, 1998.
- [54] G. T. Zhou, H. Qian, L Ding, and R. Raich. On baseband representation of a bandpass nonlinearity. *IEEE Transactions on Signal Processing*, 53(8):2953–2957, 2005.
- [55] C. Rapp. Effects of hpa nonlinearity on 4-dpsk-ofdm signal for digital sound broadcasting systems. *2nd European Conference on Satellite Communications*, pages 38–45, Oct. 1991.
- [56] R. Zayani, R. Bouallegue, and D. Roviras. Adaptive predistortions based on neural networks associated with levenberg-marquardt algorithm for satellite down links. *EURASIP Journal on Wireless Communications and Networking*, 2008(132729), 2008.
- [57] L. E. Larson. Radio frequency integrated circuit technology for lowpower wireless communications. *IEEE Personal Communications Magazine*, 5:11–19, Jun. 1998.
- [58] H. Bogucka and A. Conti. Degrees of freedom for energy savings in practical adaptive wireless systems. *IEEE Communications Magazine*, 49(6):38–45, Jun. 2011.
- [59] L. Hanzo, M. Manster, B. J. Choi, and T. Keller. *OFDM and MC-CDMA for broadband Multi-Users communications, WLANs and Broadcasting*. IEEE press. Wiley Series, 2003.
- [60] Y. Louet and J. Palicot. Power ratio definitions and analysis in single carrier modulations. *European Signal Processing Conference*, Sep. 2005.
- [61] T. Ihalainen, T. H. Stitz, and M. Renforce. Channel equalization in filter bank based multicarrier modulation for wireless communications. *EURASIP Journal on Advances in Signal Processing*, 2007(049389), 2007.
- [62] A. Skrzypczak, P. Siohan, and J.-P. Javardin. Power spectral density and cubic metric for the ofdm/oqam modulation. *Proceedings of ISSPIT*, Sep. 2006.
- [63] J. Nsenga, W. Van Thillo, A. Bourdoux, V. Ramon, F. Horlin, and R. Lauwereins. Spectral regrowth analysis of band-limited offset-qpsk. *IEEE International*

- Conference on Acoustics, Speech and Signal Processing*, pages 3593–3596, Apr. 2008.
- [64] S. Sall, H. Shaiek, D. Roviras, and Y. Medjahdi. Analysis of the nonlinear spectral re-growth in FBMC systems for cognitive radio context. *IEEE International Symposium on Wireless Communications Systems*, pages 1–5, Aug. 2013.
- [65] G. T. Zhou and R. Raich. Spectral analysis of polynomial nonlinearity with applications to rf power amplifiers. *EURASIP Journal on Applied Signal Processing*, 2004(256395):1931–1840, 2004.
- [66] H. Cramer. *Mathematical Methods of Statistics*. Princeton University Press, 1946.
- [67] J. John Wishart R.A. Fisher. The derivation of the pattern formulae of two-way partitions from those of simpler patterns. *Proceedings of the London Mathematical Society*, 1932.
- [68] H. D. Ursell. The evaluation of gibbs phase-integral for imperfect gases. *Mathematical Proceedings of the Cambridge Philosophical Society*, 23(6):685–697, Apr. 1927.
- [69] D. R. Brillinger. *Time Series: Data Analysis and Theory*. Holden-Day. Inc, San Francisco, 1981.
- [70] I. S. Reed. On a moment theorem for complex gaussian process. *IRE Transactions on Information Theory*, pages 194–195, Apr. 1962.
- [71] S. P. Stapleton, G. S. Kandola, and J. K. Cavers. Simulation and analysis of an adaptive pre-distorter utilizing a complex spectral convolution. *IEEE Transactions on Vehicular Technology*, 41(4):387–394, Nov. 1992.
- [72] K. G. Gard, H. M. Gutierrez, and M. B. Steer. Simulation and analysis of an adaptive pre-distorter utilizing a complex spectral convolution. *IEEE Transactions on Microwave Theory and Techniques*, 47(7):1059–1069, Jul. 1999.
- [73] P. Banelli and S. Cacopardi. Theoretical analysis and performance of ofdm signals in nonlinear awgn channels. *IEEE Transactions on Communications*, 48(3):430–441, Mar. 2000.

- [74] J.M. Mendel. Tutorial on higher-order statistics (spectra) in signal processing and system theory: theoretical results and some applications. *Proceedings of the IEEE*, 79:78–305, Mar. 1999.
- [75] G. T. Zhou and J. Stevenson Kenney. *Predicting spectral regrowth of nonlinear power amplifiers*. Georgia Institute of Technology, 2001.
- [76] M. R. Schroeder. *Number theory in science and communication*. Springer, 1962.
- [77] R. O'Neil and L.B. Lopes. Envelope variations and spectral splatter in clipped multicarrier signals. *IEEE PIMRC*, pages 71–75, Sep. 1995.
- [78] H. Ochiai and H. Imai. Performance analysis of deliberately clipped ofdm signals. *IEEE Transactions on Communications*, 50:89–101, Jan. 2002.
- [79] D. Kim and G.L. Stuber. Clipping noise mitigation for ofdm by decision-aided reconstruction. *IEEE Communication Letters*, 3:1–4, 2008.
- [80] B.S. Krongold and D.L. Jone. Papr reduction in ofdm via active constellation extension. *IEEE Transactions on Broadcasting*, pages 258—268, Sep. 2003.
- [81] J.A. Davis and J. Jedwab. Peak-to-mean power control in ofdm, golay complementary sequences, and reed-muller codes. *IEEE Transactions on Information Theory*, 45(7):2397—2417, Nov. 1999.
- [82] Y. Louet and A. Le Glaunec. Peak-factor reduction in ofdm by reed-muller channel coding a new soft decision decoding algorithm. *IEEE MELECON*, pages 872—875, May 2000.
- [83] H. Lee and S.W. Golomb. A new construction of 64-qam golay complementary sequences. *IEEE Transactions on Information Theory*, 52(4):1663—1670, Apr. 2006.
- [84] R. Bellamen. *Applied Dynamic Programming*. Princeton, 1962.
- [85] E. Chu and A. George. *Inside the FFT Black Box: Serial and Parallel Fast Fourier Transform Algorithms*. Computational Mathematics Series, 1999.
- [86] C. Siegl and R. F. H. Fischer. Comparison of partial transmit sequences and selected mapping for peak-to-average power ratio reduction in mimo ofdm. *IEEE International ITG Workshop on Smart Antennas*, 52:324—331, Feb. 2008.

- [87] A. Burg. *VLSI Circuits for MIMO Communication Systems*. PhD thesis, ETH Zurich, Zurich, Switzerland, 2006.
- [88] ETSI TS 100 392-2. *Voice plus Data (V+D); Part 2: Air Interface (AI)*. TETRA, 2011.
- [89] Y. Medjahdi, D. Le Ruyet, F. Bader, and L. Martinod. Integrating lte broadband system in pmr band: Ofdm vs. fbmc coexistence capabilities and performances. *IEEE International Symposium on Wireless Communication Systems*, pages 643–648, Aug. 20014.
- [90] 3GPP TR 25.814. *Physical layer aspects of evolved Universal Terrestrial Radio Access (UTRA)*. 3GPP, 2006.
- [91] S. C. Cripps. *RF Power Amplifiers for Wireless Communications*. Artech house, 2006.
- [92] Application note AN1022. *Operation and Performance of the ISL5239 Pre-distortion Linearizer*. Intersil, 2002.
- [93] V. Petrovic. Reduction of spurious emission from radio transmitters by means of modulation feedback. *IEEE Conference on Radio Spectrum Conservation Techniques*, pages 44–49, Sep. 1983.
- [94] H. Seidel. A microwave feed-forward experiment. *Bell Systems Technical Journal*, 50(9):2879–2918, Nov. 1971.
- [95] S. P. Stapleton. *Presentation on Adaptive Feedforward Linearization for RF Power Amplifiers-Part 2*. Agilent Technologies, Inc, 2001.
- [96] A. A. M. Saleh and D. Cox. Improving the power-added efficiency of fet amplifiers operating with varying-envelope signals. *IEEE Transactions on Microwave Theory and Techniques*, 31(1):365–369, Mar. 1983.
- [97] D. Su and W. McFarland. An ic for linearizing rf power amplifiers using envelope elimination and restoration. *ISSCC Digest of Technical Papers*, 22(12):54—55, Dec. 1998.
- [98] D. K. Su and M. J. McFarland. Linear amplification with nonlinear components. *IEEE Journal of Solid-State Circuits*, 22(12):2252–2258, Dec. 1974.

- [99] A. Katz et al. Passive fet mmic linearizers for c, x, and ku-band satellite applications. *IEEE International Microwave Symposium*, pages 353–356, 1993.
- [100] R. C. Tupynamba and E. Camargo. Mesfet nonlinearities applied to predistortion linearizer design. *IEEE MTT-S Digest*, 2:955—958, Jun. 1992.
- [101] N. Imai, T. Nojima, and T. Murase. Linear amplification with nonlinear components. *IEEE Transactions Microwave Theory and Techniques*, 37(8):1237–1243, Aug. 1989.
- [102] G. Karam and H. Sari. Implementation and performance of data predistortion with memory in digital microwave radio. *IEEE Global Telecommunications Conference*, 1:400—405, Nov. 1989.
- [103] O. A. Gouba and Y. Louet. Digital predistortion expressed as an adding signal technique in ofdm context. *IEEE International New Circuits and Systems Conference*, pages 1–4, Jun. 2013.
- [104] H. W. Kang, Y. S. Cho, and D. H. Youn. On compensating nonlinear distortions of an ofdm system using an efficient adaptive predistorter. *IEEE Transactions on Communication*, 47(4):522–526, Aug. 1999.
- [105] P. B. Kenington. *High-linearity RF amplifier design*. Artech house, 2000.
- [106] O. A. Gouba. *Approche Conjointe de la Reduction du Facteur de Crete et de la Linearisation dans le contexte OFDM*. PhD thesis, École supérieure d’électricité, Rennes, France, 2010.
- [107] R. Sperlich, Y. Park, G. Copeland, and J. S. Kenney. Power amplifier linearization with digital pre-distortion and crest factor reduction. *IEEE MTT-S International Microwave Symposium Digest*, 2:669–672, Jun. 2004.
- [108] J. S. Kenney and Jau-Horng Chen. Power amplifier linearization and efficiency improvement techniques for commercial and military applications. *IEEE International Conference on Microwaves, Radar Wireless Communications*, pages 3–8, May 2006.

Vita

BULUSU Sri Satish Krishna Chaitanya was born in Kakinada, India, on *September*17, 1984. In 2001, he started B.Tech in electronics and communications engineering at Pondicherry Engineering College, India, which he completed with first class in 2005. He finished his M.S in mobile communications from Institute Eurecom, France, in 2009. In 2013, he has started Ph.D at Conservatoire National des Arts et Métiers, France. His research interests include digital signal processing, digital communications, embedded systems, PA linearization and PAPR reduction techniques.

Résumé

Cette thèse a été effectuée dans le cadre du projet européen FP7 - ICT 318362 EMPHATIC (Enhanced Multicarrier Techniques for Professional Ad-Hoc and Cell-Based Communications). Plusieurs universités européennes et deux partenaires industriels: THALES Communications Security et CASSIDIAN ont participé à ce projet. L'objectif de ce projet est de développer, d'évaluer et de démontrer les apports des techniques multi-porteuses avancées, permettant une meilleure utilisation des bandes de fréquences radio existantes en fournissant des services de données à large bande, en coexistence avec les services traditionnels à bande étroite. Le projet porte sur l'application de radiocommunications mobiles professionnelles (Professional Mobile Radio : PMR). L'idée principale de ce projet est d'analyser la viabilité des systèmes à large bande utilisant des bancs de filtres (Filter Bank Multi Carrier : FBMC) conjointement avec une modulation d'amplitude en quadrature avec décalage (Offset Quadrature Amplitude Modulation : OQAM) dans le cadre de la 5ème génération (5G) des systèmes radio-mobiles.

La modulation FBMC-OQAM se positionne comme candidate potentielle pour les futurs systèmes de communication. Cette modulation avancée offre de nombreux avantages tels que l'excellente localisation fréquentielle de sa densité spectrale de puissance (DSP), une robustesse au bruit de phase, aux décalages de fréquence ainsi qu'à l'asynchronisme entre les utilisateurs. Ces atouts, la rendent plus attrayant qu'OFDM pour l'application PMR, la radio cognitive (CR) et la 5G. Cependant, comme toute autre technique de modulation multi-porteuses, FBMC-OQAM souffre d'un facteur de crête ou d'un PAPR (pour Peak to Average Power Ratio) élevé. Lorsque l'amplificateur de puissance (AP), utilisé au niveau de l'émetteur, est opéré proche de sa zone non-linéaire (NL), ce qui est le cas dans la pratique, la bonne localisation fréquentielle de la DSP du système FBMC-OQAM est sérieusement compromise, en raison des remontées spectrales.

Le premier objectif de cette thèse est de prédire l'étendue des remontées spectrales dans les systèmes FBMC-OQAM, introduites par la non-linéarité de l'AP. Le deuxième objectif de ce travail est de proposer des techniques, pour les systèmes FBMC-OQAM, permettant la réduction du PAPR et la linéarisation de l'AP, afin d'atténuer les effets NL. L'utilisation des cumulants, a permis de prédire les remontées spectrales pour les signaux FBMC-OQAM après amplification NL. En outre, certains algorithmes de réduction du PAPR, basés sur des approches probabilistes et des techniques d'ajout de signaux, ont été proposés. La capacité de coexistence du système à large bande utilisant FBMC-OQAM avec des systèmes PMR à bande étroite en présence de PA a été analysée et il a été démontré que la coexistence est possible, à condition qu'il y ait une bonne combinaison entre le recul du signal à l'entrée de l'AP (Input Back-Off : IBO), la réduction du PAPR et la linéarisation de l'AP. Enfin, une nouvelle technique de linéarisation de l'AP a été proposée pour le système FBMC-OQAM.

Mots clés : FBMC, OQAM, AP, DSP, PAPR, PTS, SLM, TR, PMR, PPDR, 5G, Co-existence, Linearisation, Bande étroite, Remontées spectrales.

Abstract

This thesis is part of the European FP7 - ICT 318362 EMPHATIC project (Enhanced Multicarrier Techniques for Professional Ad-Hoc and Cell-Based Communications) including various European universities and two main industrial partners: THALES Communications Security and CASSIDIAN. The EMPHATIC objective is to develop, evaluate and demonstrate the capability of enhanced multi-carrier techniques to make better use of the existing radio frequency bands in providing broadband data services in coexistence with narrowband legacy services. The project addresses the Professional Mobile Radio (PMR) application. The main idea is to analyze the viability of broadband systems based on filter bank multi-carrier (FBMC) clubbed with offset quadrature amplitude modulation (OQAM) in the context of the future 5th Generation (5G) radio access technology (RAT).

Increasingly, the FBMC-OQAM systems are gaining appeal in the probe for advanced multi-carrier modulation (MCM) waveforms for future communication systems. This advanced modulation scheme offers numerous advantages such as excellent frequency localization in its power spectral density (PSD), a robustness to phase noise, frequency offsets and also to the multi-user asynchronism; making it more appealing than OFDM for PMR, cognitive radio (CR) and 5G RAT. However, like any other MCM technique, FBMC-OQAM suffers from high PAPR. When the power amplifier (PA) non-linearity, which is realistic radio-frequency impairment, is taken into account; the good frequency localization property is severely compromised, due to the spectral regrowth.

The first objective of this PhD thesis is, to predict the extent of the spectral regrowth in FBMC-OQAM systems, due to the PA non-linearity. The second objective is to probe techniques for FBMC-OQAM systems, such as PAPR reduction and PA linearization, in order to mitigate the NL effects of PA. By cumulant analysis, spectral regrowth prediction has been done for FBMC-OQAM systems. Also, some algorithms for PAPR reduction, which are based on probabilistic approach and adding signal methods, have been proposed. The coexistence capability of the FBMC-OQAM based broadband system with the narrowband PMR systems in the presence of PA has been analyzed and it has been found that coexistence is possible, provided there is a symbiotic combination of PA Input Back-off (IBO), PAPR reduction and PA linearization. Finally, a novel PA linearization technique has been proposed for FBMC-OQAM.

Index Terms—FBMC, OQAM, PSD, PAPR, PTS, SLM, TR, PMR, PPDR, 5G, DPD, Non-linear PA, Spectral regrowth, Cumulants, Co-existence, Narrowband-friendly, Trellis-based, PA linearization and Digital predistortion.